CHARACTERIZATION AND MODELING OF ELECTROSTATICALLY ACTUATED POLYSILICON MICROMECHANICAL DEVICES

A DISSERTATION

SUBMITTED TO THE DEPARTMENT OF ELECTRICAL ENGINEERING

AND THE COMMITTEE OF GRADUATE STUDIES

OF STANFORD UNIVERSITY

IN PARTIAL FULFILLMENT OF THE REQUIREMENTS

FOR THE DEGREE OF

DOCTOR OF PHILOSOPHY

Edward Keat Leem Chan

November 1999

Email: edward_chan@stanfordalumni.org

Prepared under the support of the

Defense Advanced Research Projects Agency (DARPA)

Composite CAD Program (F30602-96-2-0308-P00001)

Integrated Circuits Laboratory

Center for Integrated Systems

Stanford University, Stanford, CA 94305-4075

I certify that I have read this dissertation and that in my opinion it is fully adequate, in scope and quality, as a dissertation for the degree of Doctor of Philosophy.

Robert W. Dutton (Principal Adviser)

I certify that I have read this dissertation and that in my opinion it is fully adequate, in scope and quality, as a dissertation for the degree of Doctor of Philosophy.

Umran S. Inan

I certify that I have read this dissertation and that in my opinion it is fully adequate, in scope and quality, as a dissertation for the degree of Doctor of Philosophy.

John C. Bravman

Approved for the University Committee on Graduate Studies:

Dean of Graduate Studies

Abstract

Sensors, actuators, transducers, microsystems and MEMS (MicroElectroMechanical Systems) are some of the terms describing technologies that interface information processing systems with the physical world. Electrostatically actuated micromechanical devices are important building blocks in many of these technologies. Arrays of these devices are used in video projection displays, fluid pumping systems, optical communications systems, tunable lasers and microwave circuits.

Well-calibrated simulation tools are essential for propelling ideas from the drawing board into production. This work characterizes a fabrication process — the widely-used polysilicon MUMPs process — to facilitate the design of electrostatically actuated micromechanical devices. The operating principles of a representative device — a capacitive microwave switch — are characterized using a wide range of electrical and optical measurements of test structures along with detailed electromechanical simulations. Consistency in the extraction of material properties from measurements of both pull-in voltage and buckling amplitude is demonstrated. Gold is identified as an area-dependent source of nonuniformity in polysilicon thicknesses and stress. Effects of stress gradients, substrate curvature, and film coverage are examined quantitatively.

Using well-characterized beams as in-situ surface probes, capacitance-voltage and surface profile measurements reveal that compressible surface residue modifies the effective electrical gap when the movable electrode contacts an underlying silicon nitride layer. A compressible contact surface model used in simulations improves the fit to measurements. In addition, the electric field across the nitride causes charge to build up in the nitride, increasing the measured capacitance over time. The rate of charging corresponds to charge injection through direct tunneling.

A novel actuator that can travel stably beyond one-third of the initial gap (a trademark limitation of conventional actuators) is demonstrated. A “folded capacitor” design, requiring only minimal modifications to the layout of conventional devices, reduces the parasitic capacitances and modes of deformation that limit performance. This device, useful for optical applications, can travel almost twice the conventional range before succumbing to a tilting instability.

Acknowledgements

It is difficult to spend nine years in school at one place and not have a lot of people to thank and to blame. Two groups of people have contributed much to my cherished years here at Stanford – those who helped me in my professional development, and those who contributed to my personal development. Of course there is much overlap, but since this is my Ph.D. thesis, and not my wedding bulletin, I'll emphasize the first group. I hate leaving people out of my acknowledgments, but that's rather likely since I've been here a long time and might forget those who've helped me a great deal years ago during my undergraduate days.

First of all, I have to thank Professor Robert Dutton, whom I called "Bob" only after managing the group's softball team for over a year. I finally decided yelling, "Hey Professor Dutton, earn your pay..." or things like that on the field was just too formal. Bob taught me how to look for buried bodies, how to declare victory when I found one, and how not to disturb other bodies nearby. He's incredibly accessible for someone so incredibly busy. And he's always been willing to sacrifice his shins to block softballs that I throw in the dirt. The turning point in my Ph.D. came on October 21, 1997, when I stopped by Bob's office the day before a DARPA site visit. I pretty much said that my work over the past year was junk and I didn't have anything to show for the next day. But just one hour later, he steered me towards making measurements and examining material properties, ultimately leading to a rewarding thesis. Those of us in the group realize just how good we have it when we hear high praise for Bob from students in other research groups.

Professor Inan taught me to love divergence and curl at an early age, and both challenged and encouraged me as an undergraduate. Dr. David Burns has been a tremendous resource for both technical and business advice. He's certainly gone above the call of duty of a consulting professor, and has forced me to think through many of my ideas more carefully. Professor Gill taught me digital design years ago and came to my rescue when I needed someone to chair my orals committee. Professor Bravman, who introduced me to Materials Science as a sophomore, always asked the toughest but best questions during our group meetings.

Acknowledgements

I would like to thank DARPA for supporting this contract, code-named ACADEMIA (αχαδεμια), and for bringing together the community of CAD developers. It was great having the freedom to define what we wanted to do, and also to interact with others in the field of sensors, actuators, MEMS etc. I would like to thank the many people associated with ACADEMIA– Guido Cornella, Brian Eplett, Krishna Garikipati, Ken Honer, Kai Hsiau, Edwin Kan, Greg Kovacs, Hoo Jeong Lee, Chris Storment, Rick Vinci, Nathan Wilson, and Ping Zhang – who have provided ideas, advice and fun discussions. Group meetings were usually fun, lot's of cut-up, yet good technical content. The extended family of the TCAD group – Fely Barrera, Tao Chen, Choshu Ito, Jaejune Jang, Atsushi Kawamoto, Michael Kwong, Aon Mujtaba, Miho Nishi, Maria Perea, Xiaoning Qi, Francis Rotella, Olof Tornblad, Ken Wang, Dan Yergeau, Zhiping Yu, and Xin Yi Zhang – has helped me in much the same way. Random questions, either from me or asked of me, really helped the thinking process. They've been a good group to bounce things off, both ideas and softballs. In addition, the computer (Dan) and administrative (Fely, Maria, Miho) support has been nothing short of phenomenal.

Further along the line are the various people in CIS that I've gotten to know along the way, especially those from the Kovacs, Harris and Wong groups, who've helped me make sense of many mysteries and miseries. The very first MEMS devices I measured were from Professor Harris' group. People from the Kovacs group really helped me get up to speed on the field of MEMS, sensors, and actuators in general. Those from the Wong group were exceptionally helpful with processing and fabrication information. I am indebted to the professors in Materials Science and Mechanical Engineering who were so generous with their time in helping fill in the many blanks in my knowledge. I'm grateful to the folk at the Stanford Linear Accelerator Center who gave me my first taste of research, and extra pocket money for three years.

I'd like to thank all my friends for their friendship and support throughout the years, especially those from Campus Crusade for Christ. They have made my experience at Stanford everything it was meant to be. Finally, I want to thank my family for their love and support, giving me the opportunity to go to the best schools, or at least the best schools I could get into. They've provided for me in ways that I will probably never understand until and unless I have a family of my own. And even then…

A passage in the book of Psalms says:

> "*Unless the Lord builds the house, the builders labor in vain. Unless the Lord watches over the city, the watchmen stand guard in vain. In vain you rise up early and stay up late toiling for food to eat – for He grants sleep to those He loves*."

I thank God that I've gotten enough sleep most of the time, and that my labor has not been in vain.

Table of Contents

List of Tables

List of Figures

Chapter 1 Introduction

Chapter 2 Simulation Models and Techniques

Chapter 3 Metrology

Chapter 4 Characterization of Pull-in

Chapter 5 Characterization of Contact Electromechanics

Chapter 6 Electrostatic Actuator with Extended Travel

List of Figures

Chapter 1 Introduction

1.1 Hello, World!

"Hello, world!" The ubiquitous words that pop up on the computer screen as the first outputs of an introductory computer program. The computer screen, along with keyboards and disk drives, has been the primary means for a computer or information processing system to interact with humans and the physical world. Sensors, actuators, transducers, microsystems and MEMS are some of the technologies that promise to greatly improve such interaction, especially when large numbers of these devices are assembled into interconnected systems, somewhat like the World Wide Web or VLSI electronics. These systems can sense and create motion, reflect and direct light and electromagnetic waves, and control chemical and biological fluid flow and interactions [1], [2]. Paul Saffo of the Institute for the Future – a strategic planning organization – calls sensors the "foundational technology of the next decade" [3]. The director of Sandia National Laboratories' micromachining program declares in Fortune magazine that "a second silicon revolution is under way in the electronics world" [4]. Clearly, there is potential for spectacular achievements. Figure 1-1 gives a flavor of what some of these devices look like – the Scanning Electron Micrograph (SEM) on the top left is of a gear system, the top right is of a hinged reflector that can pop off the surface of a silicon

wafer, the bottom left is of an electrostatic motor, and the world's smallest steam engine is on the bottom right.

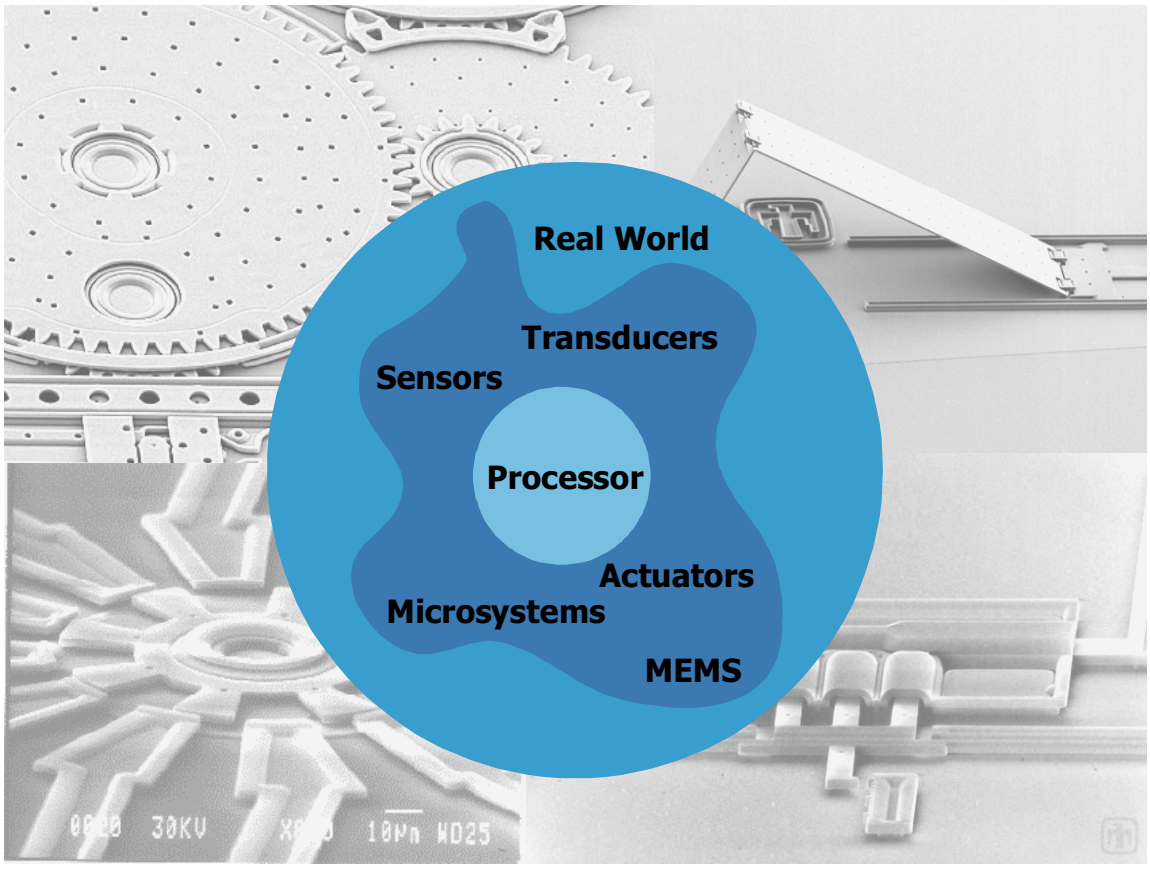

Figure 1-1. MEMS, microsystems, sensors, actuators, and transducers are some of the technologies that interface computers and information processors with the physical world. The fours SEMs (courtesy of Sandia National Laboratories and the Microelectronics Center of North Carolina/Cronos Integrated Microsystems, Inc.) show examples of these microdevices. The top left is a gear system (Sandia), the top right is a hinged reflector (Sandia), the bottom left is an electrostatic motor (MCNC/Cronos), and the bottom right is a steam engine (Sandia).

How small really is "micro"? On the high end of the spectrum of everyday things shown in Figure 1-2, in the meter range, stands a typical human being. On the lower end are atoms and molecules that are fractions to several tens of nanometers. Further up are integrated circuit technologies with critical dimensions from about one-tenth of a micron to several microns. Protozoa and amoeba are roughly tens or hundreds of microns long, comparable in size to the micromechanical devices studies in this thesis. Man-made devices still lag far behind in complexity, however.

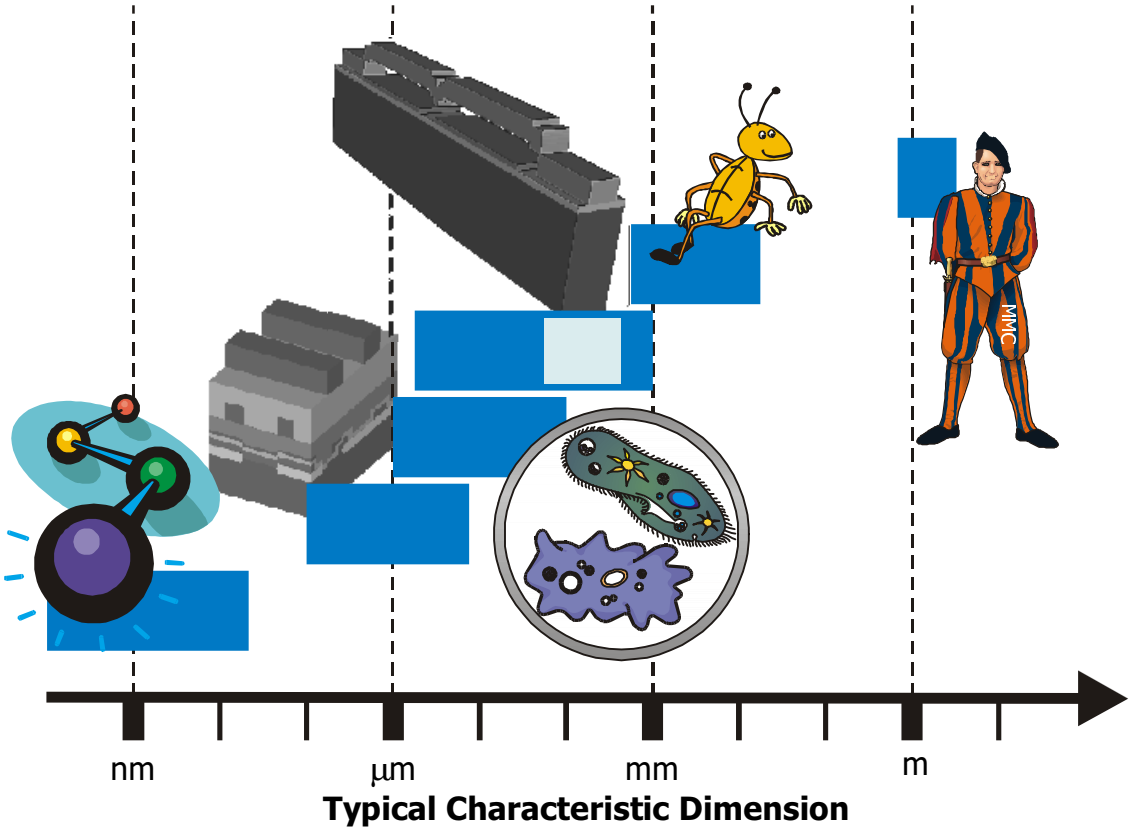

Figure 1-2. The scale of micromechanical devices compared to the rest of the world. The bars indicate the ranges of typical characteristic dimensions of atoms and molecules, integrated circuit technologies, amoeba and protozoa, micromachines, insects, and humans. The range of lengths of the micromechanical devices studied in this thesis is shown by the lighter shaded region of the range-indicator bar.

While the field of sensors, actuators, transducers, microsystems and MEMS encompasses the domains of mechanics, electronics, heat transfer, optics, fluidics, biology, chemistry, magnetics and more, this thesis focuses on coupled electromechanical devices, an important building block that can be considered the granddaddy of the field. Examples of electromechanical devices are two elements of a Deformable Mirror Display from Texas Instruments shown in Figure 1-3 [5]. With proper voltage signals, large arrays of these pixels reflect light at different angles to form projected images. One pixel is interesting and useful but thousands of these devices working in concert can achieve much more than might be imagined of a single device. Another interesting example of an electromechanical application is a BEAD mesopump being developed at the Honeywell Technology Center [6]. When a voltage is applied between the top and bottom of this bellows-like pump, the diaphragm approaches the bottom electrode and squeezes the

liquid out from the outlet in the center. Several of these pumps can be arranged in series to generate higher pressures, or configured in parallel for higher throughput.

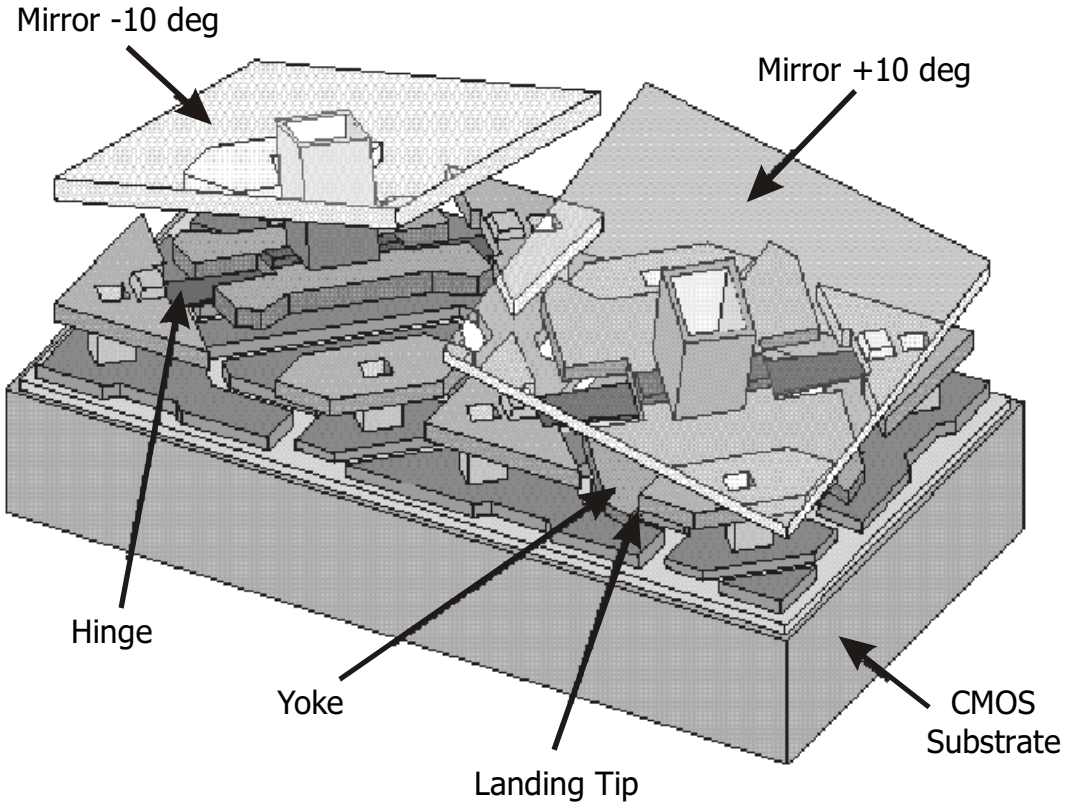

Figure 1-3. Two elements of a Deformable Mirror Display (DMD) from Texas Instruments (courtesy of Texas Instruments, Inc.).

The electrostatically actuated device that motivates this work is the micromachined capacitive microwave switch developed at Raytheon (in a division formerly of Texas Instruments) [7]-[9]. The device is shown in the Scanning Electron Micrograph (SEM) of Figure 1-5. Representative drawings of the device operating as a shunt switch are shown in Figure 1-6(a) and (b) to illustrate the operating principles more clearly. The vertical scale is grossly exaggerated in this and all other drawings so that geometric features can be seen more clearly. When the plate is up as in Figure 1-6(a), the coupling capacitance between the deformable plate (top electrode) and transmission line (bottom electrode) is small, and the microwave signal propagates unimpeded along the transmission line at the bottom. When a dc voltage is applied between the top and bottom electrodes, the applied voltage generates electrostatic forces that pull the top plate down until it contacts the dielectric, creating a dielectric sandwich – a large capacitance. Thus

the microwave signal is shunted to ground instead of continuing down the transmission line. This micromechanical device has very desirable microwave characteristics, primarily excellent linearity at very high – 100's of GHz – frequencies, and low static power dissipation. Four operating domains are of interest for modeling and characterization. The first is the microwave domain that is relatively mature with many excellent commercial simulators available such as XFDTD [10] and Ansoft HFSS [11]. The second is the static electromechanical domain that is the main focus of this work. The third domain is dynamic electromechanics that is more difficult to characterize and simulate accurately. Dynamic operation is usually analyzed using simplified models. Reliability is the fourth domain of interest, which is receiving ever more attention from the research community [12]. One aspect of reliability – drift in performance over time due to charging – is described in this thesis.

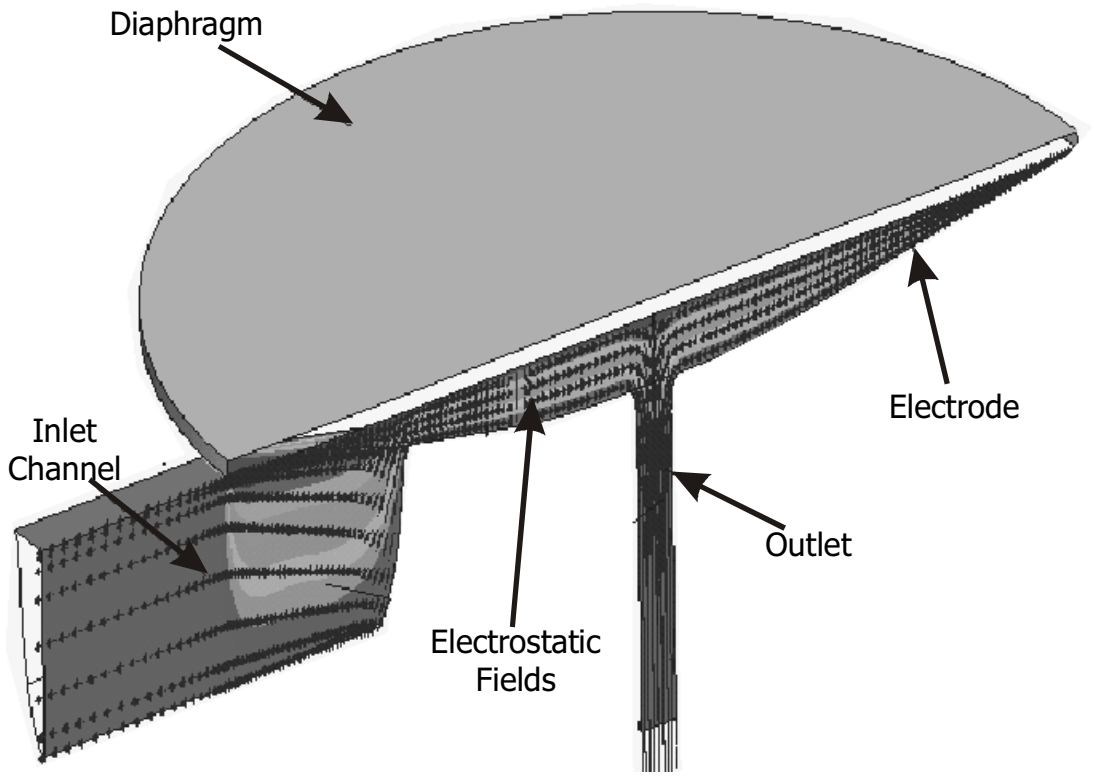

Figure 1-4. BEAD mesopump developed at the Honeywell Technology Center (courtesy of Computational Fluid Dynamics Research Corporation).

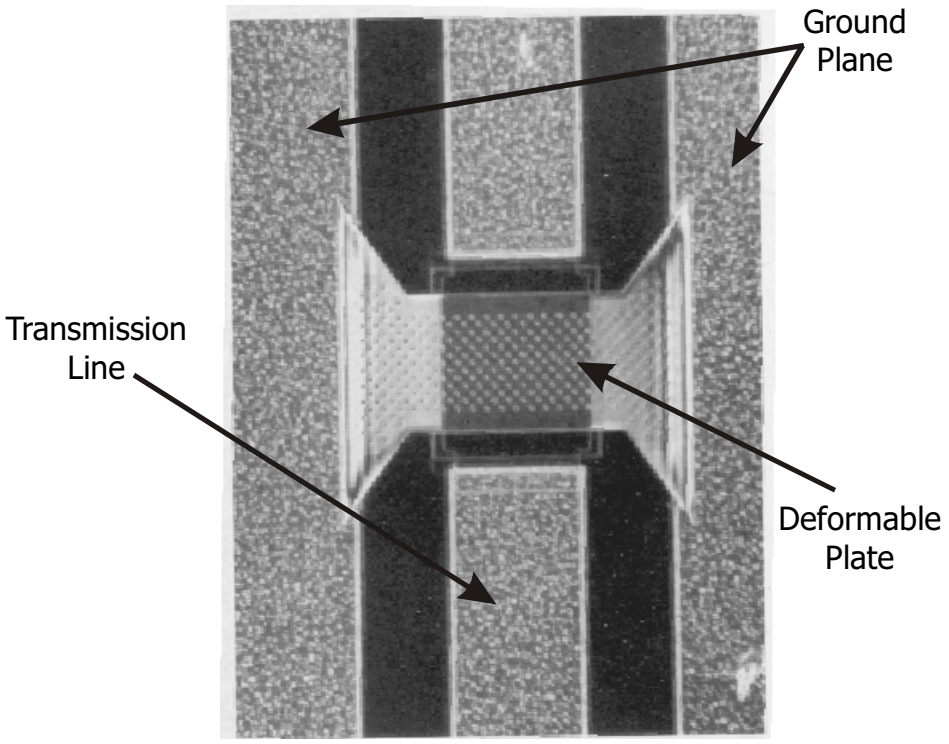

Figure 1-5. SEM of micromachined microwave switch by Raytheon (Courtesy Raytheon Systems Company). Microwave signal propagates down coplanar transmission line. With the deformable plate up, the signal propagates unimpeded. When a voltage is applied to pull the plate down, the large capacitive coupling shunts the microwave signal to ground.

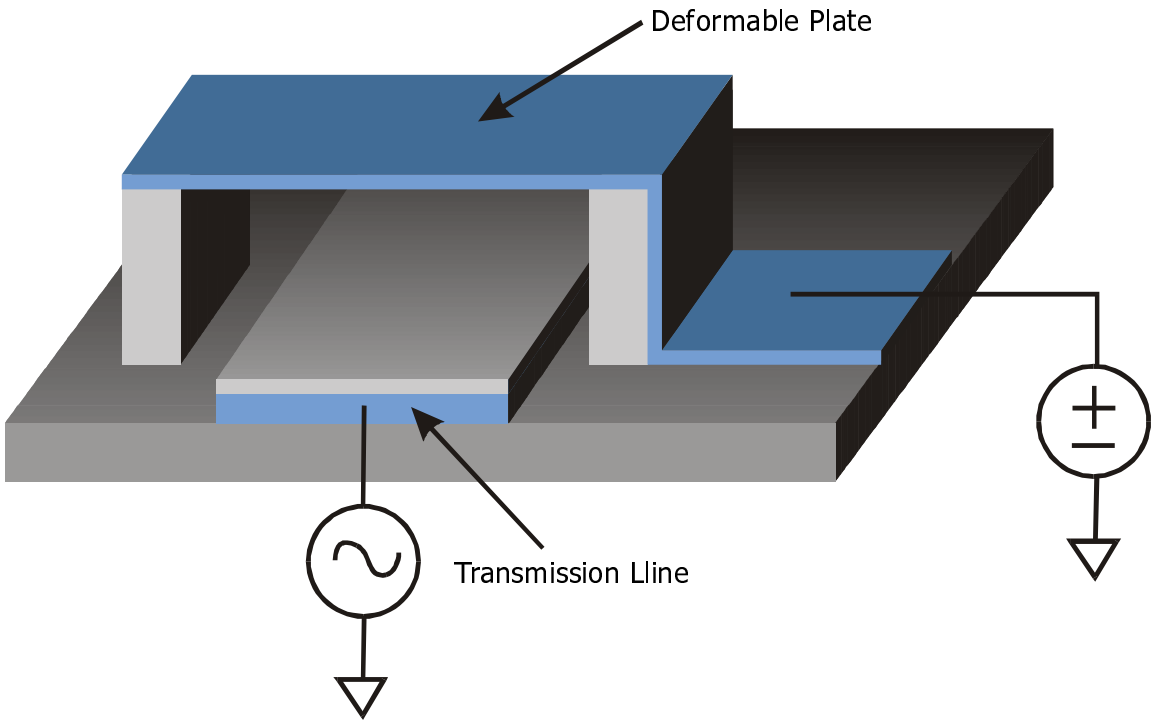

(a)

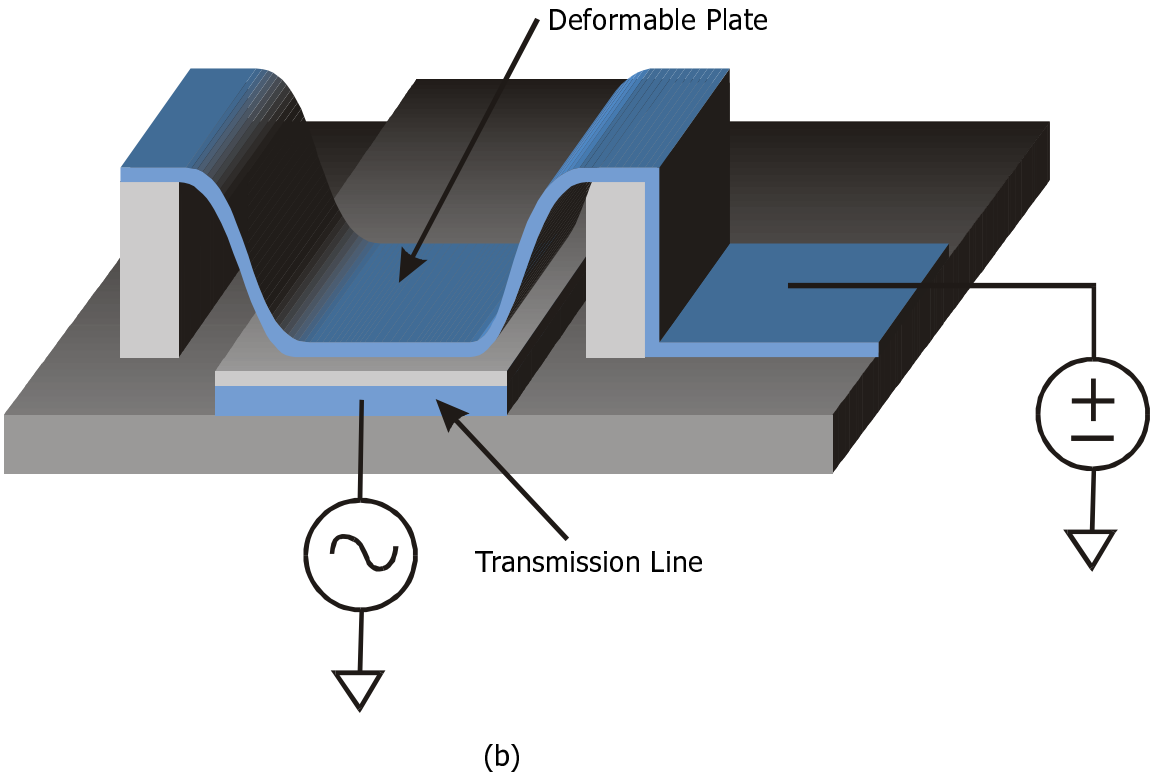

Figure 1-6. Drawing of micromachined microwave switch showing deformation characteristics in more detail. The vertical scale is grossly exaggerated in this and most of the other drawings in this thesis to show device details more clearly. **(a)** Initial state – microwave signal propagates unimpeded. **(b)** Down/actuated state – microwave signal is shunted to ground.

1.2 Outline of Thesis

Computer design and simulation tools are essential in accelerating the field of sensors, actuators, transducers, microsystems and MEMS towards fulfilling its promise of becoming the "next big thing" [13]. Currently, such computer tools are not as widely used as in the integrated circuit arena because designers are often skeptical of the reliability and accuracy of computer simulations. The almost mind-boggling expansive range of fabrication processes, physical domains and applications makes the task of developing general purpose simulation tools very difficult.

Simulation tools are required at several stages in the design process including:

- systems level simulation using fast behavioral models
- device level simulation comprising 2-D or 3-D solutions of Partial Differential Equations (PDEs)

- geometry generation from etching and deposition steps

This thesis looks primarily at device-level simulations.

All these modeling and simulation steps require varying degrees of user-intervention and user-expertise although more and more sophistication is being built into commercial simulation packages. This thesis tackles one corner of the modeling pie to show in detail how, and how well, computer simulations work, and where they must be used with caution. The general areas of modeling and characterization of micromechanical devices are too broad to summarize in this introductory chapter, therefore specific overviews and reviews of prior work are deferred to the beginnings of each chapter.

Chapter 2 describes a range of computer models that simulate the behavior of electrostatically actuated micromechanical devices. These models that trade off between simulation speed and accuracy are tailored towards fixed-fixed beams. Mechanics, electrostatics, damping, and contact are discussed, with particular attention given to accuracy in modeling the electrostatics. Sources of error in the 2-D simulation model are eliminated to obtain a good simulation basis for the characterization work in Chapters 4 and 5. The MUMPs fabrication process which underlies this thesis is introduced in Chapter 3. Techniques for obtaining accurate measurements of geometry and thicknesses in the face of overetch and the stress in PSG are explained. The design-dependent influence of gold is described along with a model that captures the observed effects. The scope of the calibration work is defined clearly, avoiding highly variable nonuniformities, especially among cantilever beams.

The characterization of electromechanical beams up until the point of instability or pull-in is presented in Chapter 4. Material properties are extracted using measurements of both buckling amplitude and pull-in voltages. The expansion of PSG is shown to affect beams with backfilled step-up anchors. Three distinct pull-in behaviors are identified. Issues related to multiple mechanical discontinuities, stress gradients, substrate curvature, and film coverage are discussed quantitatively. The well-calibrated simulation model is then used to extrapolate the behavior of a benchmark verification problem. Chapter 5 discusses the details of contact electromechanics where contact surface compressibility, and dielectric charging come into play. The fixed-fixed beam, well-characterized in

Chapter 4, serves as an in-situ contact surface probe. Charge buildup in the nitride is measured and shown to correspond to direct injection of carriers into the nitride. Apparent compressibility of the contact surface is measured using a surface profiler and a specially-designed test structure, and incorporated into the simulations of capacitance-voltage characteristics.

Chapter 6 presents an electrostatic actuator that can travel beyond the limited range of conventional actuators. The practical issues of parasitics, nonuniform deformation, and tilting due to asymmetry are addressed. A "folded capacitor" design is shown to mitigate most of the effects of parasitics. Limits in performance due to tilting are analyzed. Conclusions, and opportunities for further investigation are presented in Chapter 7.

The major contributions of this work are summarized in the list below. More thorough descriptions are given at the end of each chapter, and in Section 7.1.

- **Simulation models and techniques**
  - Improved and verified the accuracy and range-of-applicability of the coupled electromechanical simulation model for parameter extraction purposes.
- **Metrology**
  - Measured thicknesses accurately in the presence of nonuniformities due to overetch and PSG encapsulation.
  - Identified and modeled the design-dependent effects of gold on polysilicon layer thicknesses and stress.
- **Characterization of pull-in**
  - Demonstrated consistency in the extraction of material properties from both pull-in voltage and buckling amplitude measurements.
  - Showed that the expansion of PSG increases the stress significantly in beams with backfilled anchors.
  - Identified, measured and simulated three distinct types of pull-in behavior, including post-buckled behavior.
  - Examined the effects of dimples and steps.
  - Proposed a benchmark verification case to evaluate the accuracy of coupled electromechanical simulators.

- Demonstrated that stress gradients do not affect fixed-fixed beams appreciably, that buckling amplitude is affected by probe pressure, and that the coverage of deposited films affects the behavior of composites.

❖ **Characterization of contact electromechanics**

- Designed test structures to eliminate zipping in order to measure contact surface properties accurately through capacitance-voltage measurements.
- Established, through surface profile and capacitance-voltage measurements, that the contact surfaces between the nitride layer and polysilicon beams exhibit apparent compressibility.
- Incorporated a compressible contact surface model into simulations that improves the simulation fit to measurements.
- Utilized electrostatically actuated beams as electrometers to measure charge buildup in dielectrics.
- Identified charge injection through direct tunneling as a source of charging.

❖ **Electrostatic actuator with extended travel**

- Showed the effects of parasitic capacitances, both from layout and from operation, on the performance of an electrostatic actuator that can travel beyond the conventional range.
- Proposed and fabricated "folded capacitor" designs that are compact, limit parasitics, and are straightforward to implement.
- Demonstrated the first devices incorporating series capacitor feedback.
- Showed, through measurements and simulation, that tilting due to asymmetry is a fundamental limit to performance.

Using computer simulations in conjunction with careful physical measurements is one of the best ways to understand device behavior and physical properties. The work in the upcoming chapters is guided by this principle.

Chapter 2 Simulation Models and Techniques

2.1 Overview

The first step in performing a computer simulation of a device is determining what physical effects are important, and which of these effects are coupled. This usually determines the choice of the simulator that can be used. Then the geometry of the device must be built and meshed. The geometry can either be crafted from purely geometric operations resulting in boxy and sharp-angled shapes [14], or from process simulation resulting in accurate geometries that capture the effects of conformal and nonconformal deposition [15], [16]. Input parameters – loads, boundary conditions, and material properties – are included next. Material properties should ideally be obtained from characterization of simplified test structures as detailed in this thesis. Simulations of device behavior can then be performed using traditional mechanical simulation tools such as Abaqus [17], or multi-physics simulation tools such as MEMCAD [18], IntelliCAD [19], Solidis [20], Ansys [21] and CFD-ACE+ [22]. These simulation tools use finite-element, boundary-element, finite-difference, or finite-volume methods to solve PDEs. The multi-physics tools MEMCAD and IntelliCAD are built upon the mechanical simulation tool Abaqus. Simplified models are then extracted from the detailed device simulations for use in higher-level systems design. System-level performance can be analyzed using some flavor of the circuit simulator SPICE [23], or more general

simulators such as Simulink [24], and Saber [25] which implements a version of the VHDL-AMS modeling language standard. Hybrid device-system simulations, where some inner workings of a device are simulated explicitly within a system-level simulation, can be performed in SUGAR [26], Saber, or Working Model Motion [27]. Working Model Motion is particularly useful for multi-body contact simulations. Pseudo-rigid-body concepts [28]-[29] can be used to model compliant structures within rigid-body frameworks.

The goal of this work is to characterize a fabrication process, and calibrate and configure a computer simulator to help a designer optimize device designs. More than just extracting basic material parameters, this thesis shows what it takes to perform accurate simulations, highlighting the effects of geometry, and pointing out interesting new phenomena and potential pitfalls.

This chapter begins with an introduction to the fundamentals of electrostatically actuated micromechanical devices. The details of physical and computer simulation models used in this work are described next. While the models are general and suitable for a wide range of electromechanical devices, this chapter tailors models from prior work toward the simulation of electrostatically actuated micromechanical beams. Improvements in accuracy, completeness, and simulation efficiency are incorporated. A one degree-of-freedom (1-DOF) model offers quick yet accurate and scalable results because it is physically-based. The effects of damping on chattering at contact are shown. A 2-DOF model is introduced that offers better performance for devices with distinct tethers and centerpieces. The electrostatic fringing field model [30]-[31] in quasi-2-D and 2-D Abaqus [32] simulations is augmented to include the effects of finite conductor thickness. The accuracy of the parallel plate electrostatic approximation in 2-D is confirmed by field solver results. Potential sources of error in the 2-D Abaqus model are identified and eliminated so that the characterization work of Chapters 4 and 5 have a solid simulation basis. Quasi-3-D and full 3-D simulations are shown for completeness. The accuracy and applicability of the various simulation models are compared and contrasted.

2.2 Coupled Electromechanical Behavior

The simple one-dimensional (1-D) spring-mass-capacitor model of Figure 2-1(a) illustrates the basic principles of an electrostatically actuated micromechanical device. It consists of a movable top plate suspended by flexible tethers above a fixed bottom plate. An applied voltage generates an electrostatic force that tries to pull these plates together. As a result, the top plate moves downwards as shown in Figure 2-1(b). By controlling the voltage, the plate can be positioned accurately within the gap or pulled all the way down into contact with the bottom plate. While moving, the plate squeezes air out from between the plates. This is a significant source of damping. At one-third of the initial gap, the plate is at the threshold of instability. There is no static equilibrium position beyond this point (until contact) because the increase in electrostatic forces due to further displacement overwhelms the mechanical restoring forces. Positive feedback snaps the movable plate down all the way to the bottom plate. Contact, adhesion, surface topography and charging come into play at this point (Figure 2-1(c)).

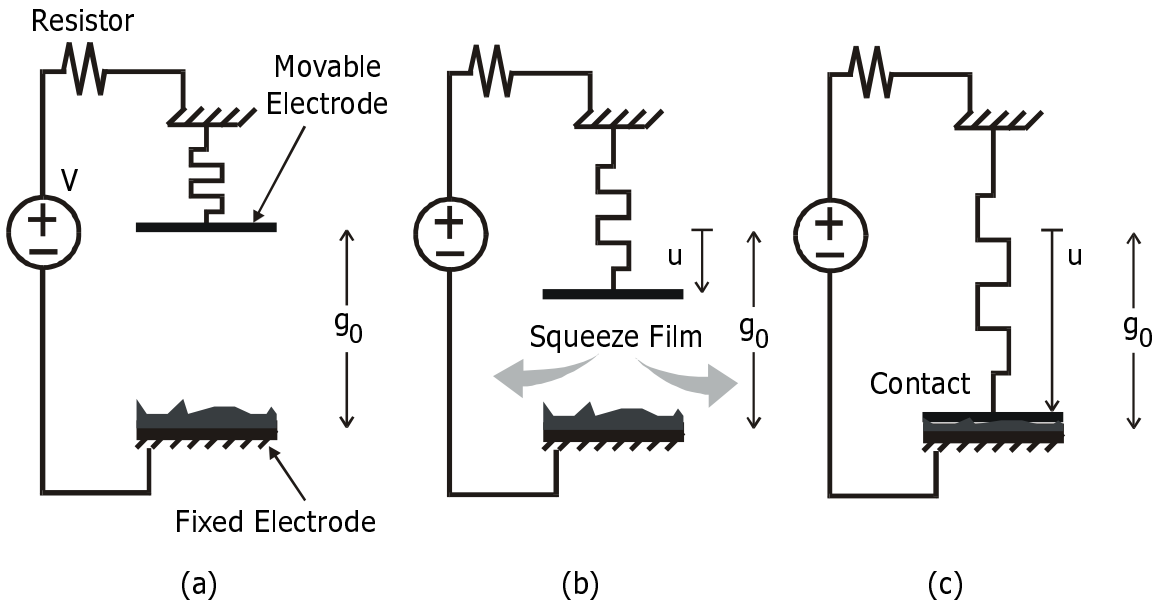

Figure 2-1. Simple spring-mass-capacitor model of an electrostatically actuated micromechanical device. **(a)** Initial position. **(b)** Applied voltage generates electrostatic force that actuates the movable electrode. Air is squeezed out from between the electrodes. At 1/3 of the initial gap, the plate is at the threshold of pull-in. **(c)** Plate makes contact with bottom as voltage is increased further. A thin dielectric layer prevents fusing due to conductor-to-conductor contact. Adhesion, charging, compression, and other surface effects come into play.

An analysis using simple 1-D models for the mechanical and electrostatic forces illustrates the fundamentals of static coupled electromechanical behavior. The mechanical restoring force is given by (2-1) where *u* is the displacement of the top plate and *k* is the spring constant.

$$F_{mechanical} = -ku \tag{2-1}$$

The electrostatic force is proportional to the square of the applied voltage, *V*, and inversely proportional to the square of the gap as shown in (2-2) where g_0 is the initial gap, *A* is the area of the plate and ε_0 is the permittivity of the gap. The thin dielectric coating the bottom electrode is neglected for now.

$$F_{electrostatic} = \frac{A\varepsilon_0 V^2}{2(g_0 - u)^2} \tag{2-2}$$

Equating the mechanical and electrostatic forces and solving for displacement as a function of voltage produces the curve in Figure 2-2. It is shown in Figure 2-2 and derived below that once the plate moves beyond $g_0/3$, there is no stable static equilibrium solution.

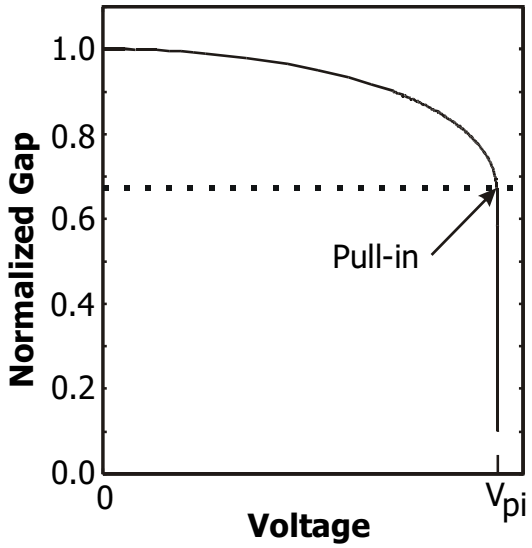

Figure 2-2. Normalized gap as a function of applied voltage. As the deflection reaches 1/3 of the initial gap, the system is at the threshold of instability or pull-in.

At equilibrium, the total force on the top plate is zero i.e.

$$F_{total} = F_{mechanical} + F_{electrostatic} = -ku + \frac{A\varepsilon_0 V^2}{2(g_0 - u)^2} = 0. \tag{2-3}$$

For stable equilibrium,

$$\frac{\partial^2 U_{total}}{\partial u^2} > 0 \tag{2-4}$$

where U_{total} is the potential energy, therefore requiring

$$\frac{\partial F_{total}}{\partial u} < 0 . \tag{2-5}$$

Taking the derivative and setting it to zero to obtain the threshold of instability results in

$$-k + \frac{A\varepsilon_0 V^2}{(g_0 - u)^3} = 0 \tag{2-6}$$

whereby substituting (2-3) into (2-6) gives

$$-k + \frac{2ku}{g_0 - u} = 0. \tag{2-7}$$

Solving for u at the threshold of instability gives the desired conclusion for the maximum stable displacement

$$u_{\max} = \frac{g_0}{3}. \tag{2-8}$$

Substituting this expression for u back into (2-3) gives the voltage at this threshold, known as the pull-in voltage (V_{pi})

$$V_{pi} = \sqrt{\frac{8kg_0^3}{27A\varepsilon_0}}. \tag{2-9}$$

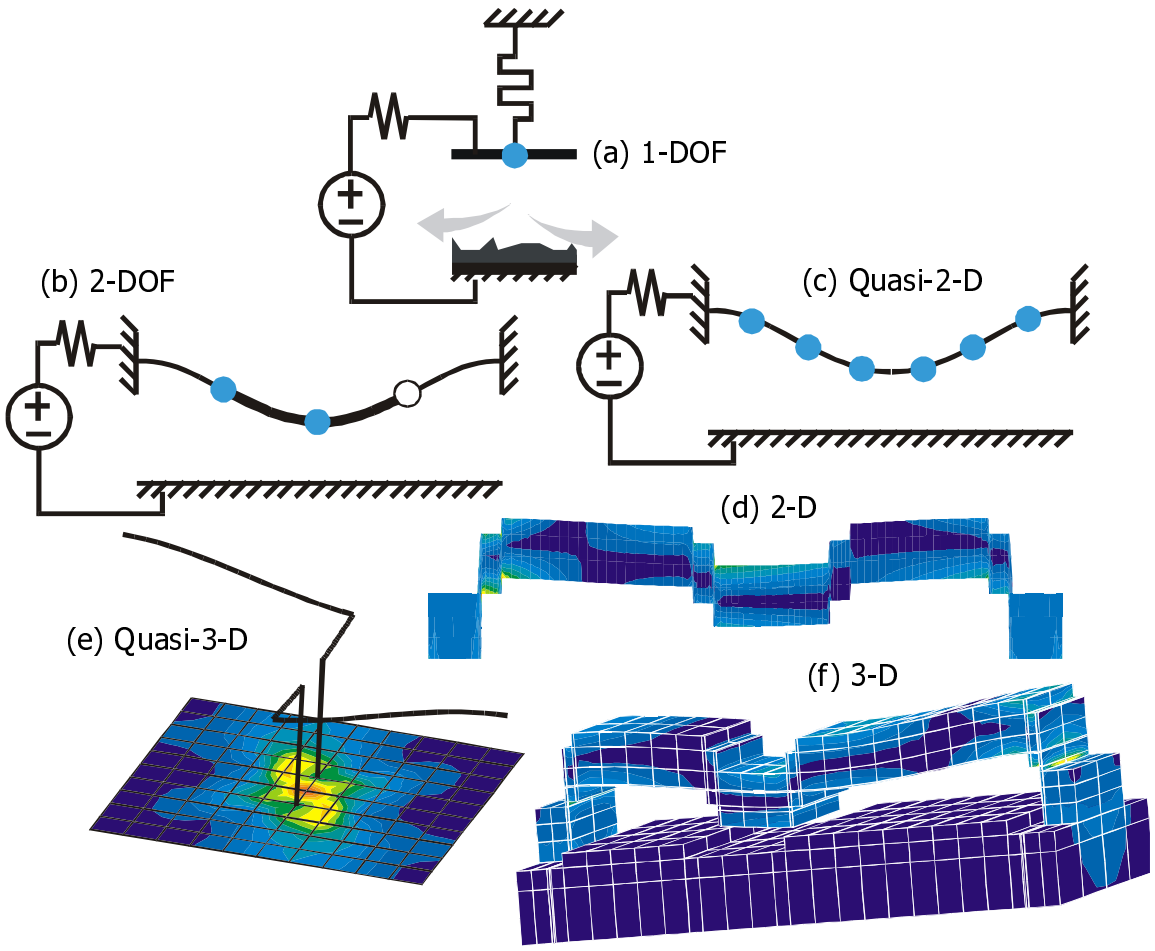

Figure 2-3. Collage of various computer simulation models. **(a)** 1-DOF model. **(b)** 2-DOF model. **(c)** Quasi-2-D finite-difference model. **(d)** 2-D finite-element model. **(e)** Quasi-3-D finite-element model. **(f)** Full 3-D finite-element-boundary-element model.

Building upon this simplest of 1-D models, computer simulation models of varying detail and sophistication, shown in Figure 2-3, were used to understand and characterize the behavior of electrostatically actuated micromechanical devices, specifically microbeams. The first is the simple one degree-of-freedom (DOF) 1-D model (Figure 2-3(a)) introduced in this section. The next is a two-DOF 1-D model (Figure 2-3(b)) which allows the tethers and centerpiece to have different properties and somewhat more independent motion. The third model (Figure 2-3(c)) is a quasi-2-D finite-difference model in which each node has a vertical displacement degree-of-freedom. Figure 2-3(d) shows the 2-D Abaqus simulation model which is the workhorse of this thesis. Each node in the mesh has vertical and horizontal displacement degrees-of-freedom. A simple 3-D model consisting of beam and shell elements is shown in Figure

2-3(e). Finally, a full 3-D simulation model is shown in Figure 2-3(f). Here, both the solid mechanics and electrostatics are solved in the full three dimensions. In all the previous models, the electrostatics are approximated by parallel plate models, which are excellent for many micromachined structures that are wide, flat and have closely spaced actuating electrodes. Each model is now described in more detail.

2.3 One-DOF 1-D Model

The equation of motion describing the displacement, u, of the center of an electrostatically actuated beam (Figure 2-1) is

$$F_{mechanical} + F_{electrostatic} + F_{damping} + F_{contact} = m\frac{d^2u}{dt^2} \tag{2-1}$$

where m is the effective mass of the beam, and $F_{<physics>}$ are the forces acting on the beam.

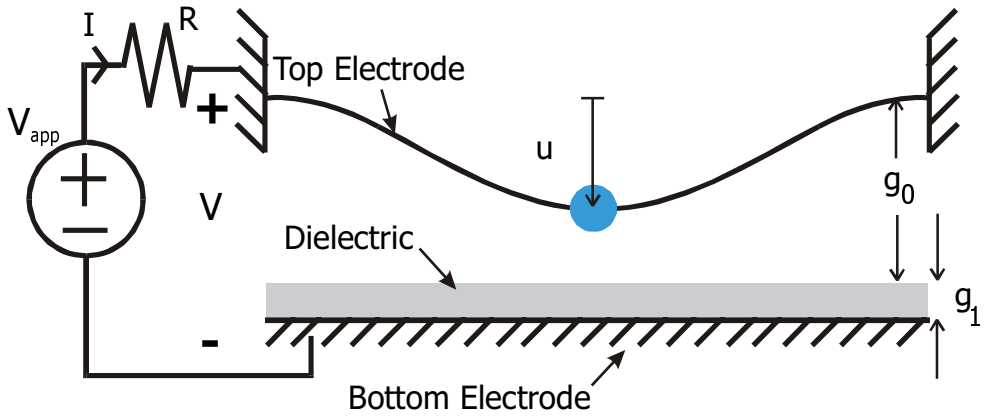

Figure 2-1. Electrostatically actuated beam modeled with a single DOF. The initial gap is g_0 and the dielectric thickness is g_1. A resistor in series with the voltage source provides damping.

The mechanical force is made up of three components related to the deformation of the beam. Assuming that the beam is loaded at the center, which is a good approximation given that electrostatic forces tend to concentrate where the gap is smallest, the first component is the linear bending force given by

$$F_{bend} = -\frac{\pi^4 E h^3 W}{6L^3}u\,. \tag{2-2}$$

E is the Young's modulus of the beam, h is the thickness of the beam, W is the width, and L is the length [33]. The bending force varies linearly with Young's modulus and beam width, and cubically with beam thickness and the inverse of beam length. In the case of wider beams, as the width becomes many times the thickness, the Young's modulus should be modified to asymptotically approach the plate modulus

$$E_{plate} = \frac{E_{beam}}{1-\nu^2} \tag{2-3}$$

where ν is Poisson's ratio. A wide plate is more resistant to bending than a slender beam. Initial stress in the beam due to deposition conditions presents another linear force given by

$$F_{stress} = -\frac{\pi^2 hW\sigma}{2L}u \tag{2-4}$$

where σ is the initial uniaxial stress (positive for tensile stress and negative for compressive stress). This time, the force varies linearly with thickness and inversely with beam length. The third mechanical restoring force is due to the stretching of the beam at large displacements, similar to the restoring force in a stretched rubber band. This force, also known as stress stiffening, varies cubically with displacement, with the other dependencies on beam properties given by

$$F_{stretch} = -\frac{\pi^4 EhW}{8L^3}u^3. \tag{2-5}$$

The relative contributions of bending, stress and stretching for a particular beam are shown in Figure 2-2 to provide an idea of when the different components are most significant. The beam is 300 μm long, 30 μm wide, and 2 μm thick. Young's modulus is 140 GPa, and the beam has an initial uniaxial compressive stress of 6.16 MPa (corresponding to an equivalent biaxial stress for a uniform film of 8 MPa). Since F_{stress} reduces the total restoring force when the stress is compressive, the simulations are only valid for

$$\left|F_{stress}\right| < \left|F_{bend}\right| \tag{2-6}$$

i.e. before buckling occurs. The critical buckling length can be obtained by equating (2-2) and (2-4) and solving for *L*. This gives exactly the same buckling criterion for fixed-fixed beams as shown in Section 4.5.1 from an alternate derivation.

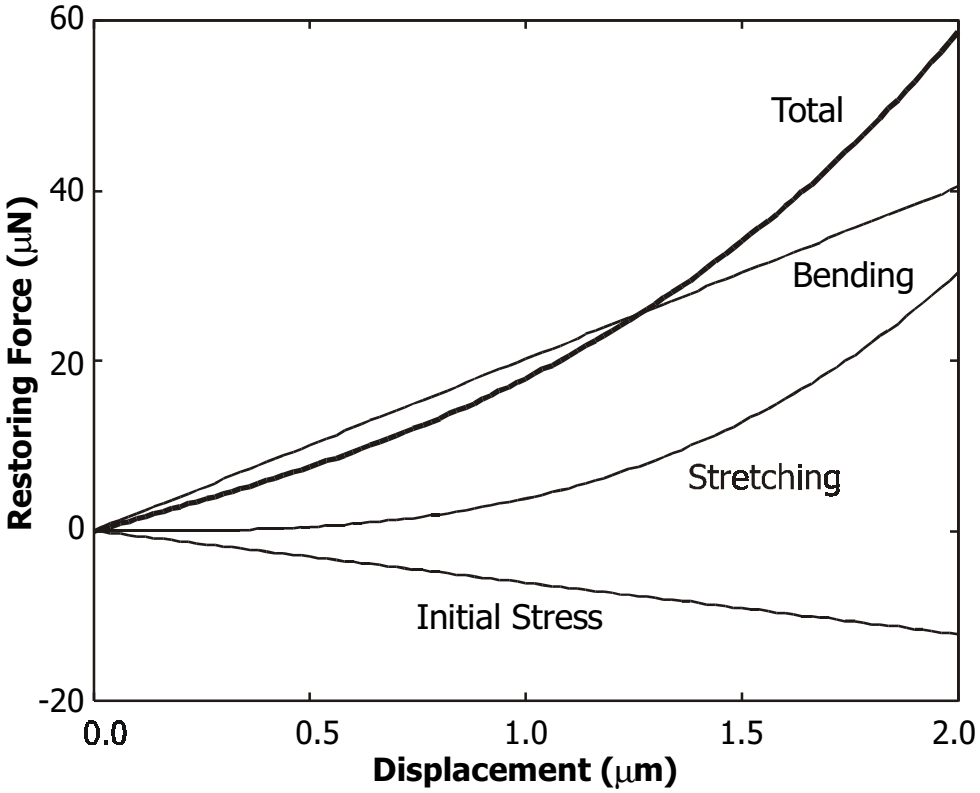

Figure 2-2. Relative magnitudes of the components of restoring force due to bending, initial stress, and stretching, as a function of displacement. Beam is loaded at the center.

The electrostatic force model utilizes a parallel plate approximation

$$F_{electrostatic} = \frac{\varepsilon_0 A V^2}{2\left(g_0 + g_1/\varepsilon_r - u\right)^2}\left[a + \frac{g_0 + g_1/\varepsilon_r - u}{b}\right] \tag{2-7}$$

where *A* is the effective area of the beam attracted by electrostatic forces, *V* is the effective voltage between the electrodes, and *a* and *b* are form factors to account for fringing fields. Only two fitting constants are actually required but *A* is kept explicitly because it signifies the portion of the beam that is being attracted by the electrostatic forces. g_1/ε_r is the electrical thickness of the dielectric coating the bottom electrode. The

form of (2-7) was derived from the analytic expression for the capacitance of an infinitesimally thin beam over an infinite ground plane incorporating the effects of fringing fields [30]. The adjustment factors *a* and *b* can further account for the fact that the effective area of concentrated electrostatic forces decreases as the beam gets closer and closer to the bottom.

With the additional non-linear mechanical force (2-5), and the form factors for fringing effects, an exact analytic expression for the pull-in voltage is impossible to derive although researchers have developed fitted expressions for specific ranges of beam dimensions and properties [30], [34]. Due to the many approximations, this 1-DOF model is suitable primarily for fast simulations of a few specific devices rather than for parameter extraction and device characterization. After calibrating the model to the first two data points obtained from quasi-2-D simulations (described in Section 2.5), the model can be used to examine the parametric dependence of pull-in voltage. As shown in Table 2-1, the predictive capability of the model is good because it is physically based. Using the constants A = 0.39, a = 1, and b = 20 μm produces results within 3% of the quasi-2-D simulations.

In transient simulations, the speed of actuation is often determined primarily by damping rather than by mechanical stiffness or inertia. For devices operated in air or other gases, squeeze film damping, expressed as

$$F_{damping} = -\frac{\mu L W^3}{(g_0 - u + \lambda)^3}\frac{du}{dt} \tag{2-8}$$

dominates. μ is the viscosity of the gas whereas λ is a factor that accounts for slip flow and is about twice the mean free path of the gas. This is a rough model which illustrates general principles, but approximations such as effective length, L, limit generality and accuracy. This damping is a viscous force that increases as the beam moves downwards and the gap becomes smaller. The model works for continuum gases and is valid for small Reynolds numbers. The model was originally derived only for small displacements [35], where the damping factor did not vary with displacement. However, comparisons with 2-D finite-difference simulations of the isothermal Reynold's equation [36]-[37]

show that an instantaneous-gap-dependent model works well, even for large displacements.

The resistor in series with the voltage source in Figure 2-1 presents another source of damping. The time constant, *RC*, to charge up the system increases as the beam deflects because of the increase in capacitance – the electrostatically actuated system is a voltage-controlled variable capacitor. The voltage, V, across the actuator with capacitance, *C*, is

$$V = V_{app} - IR \tag{2-9}$$

where

$$I = C\frac{dV}{dt} + V\frac{dC}{dt}. \tag{2-10}$$

Other interesting damping characteristics are discussed in Section 6.5.

Contact forces due to interatomic repulsion are modeled by a high-order inverse power law [38]

$$F_{contact} = -\frac{K_2 A}{(g_0 - u)^{10}}. \tag{2-11}$$

Attractive forces such as Van der Waals and capillary forces can also be included. This is the most approximate of all the models in this section because contact forces are very difficult to measure accurately and repeatably. In micromechanical devices, the exact equilibrium positions at contact are often determined more by residue and surface roughness than by the forces of an atomically smooth surface.

Residual charge can accumulate in electrostatically actuated devices containing dielectrics, or electrically isolated nodes. Net residual charge can be modeled by a sheet of charge between two voltage-driven plates as shown in Figure 2-3. According to Gauss' law, the charge sheet modifies the electric field on each side of the sheet from simply V/d_1 to be

$$E_1 = \frac{V - \frac{d_2 \rho}{\varepsilon}}{d_1}, \text{ and} \tag{2-12}$$

$$E_2 = \frac{V + \frac{(d_1 - d_2)\rho}{\varepsilon}}{d_1} \tag{2-13}$$

where ρ is the areal charge density of the charge sheet and ε is the permittivity of the region between the plates. Plate 1 in Figure 2-3 represents the actuated beam. In this case, the electric field, and hence the electrostatic force on the beam, is simply shifted by a voltage offset of $\frac{d_2\rho}{\varepsilon}$ which scales according to the amount of charge. Note that the shift does not depend on the gap between the beam and charge sheet and is thus constant throughout the entire beam regardless of the deformed shape of the beam. Therefore, the only change required in the electrostatic force expression, (2-7), is

$$V \to V - \frac{d_2\rho}{\varepsilon}. \tag{2-14}$$

Further influences and effects of residual charge are described in Sections 5.4 and 6.4.

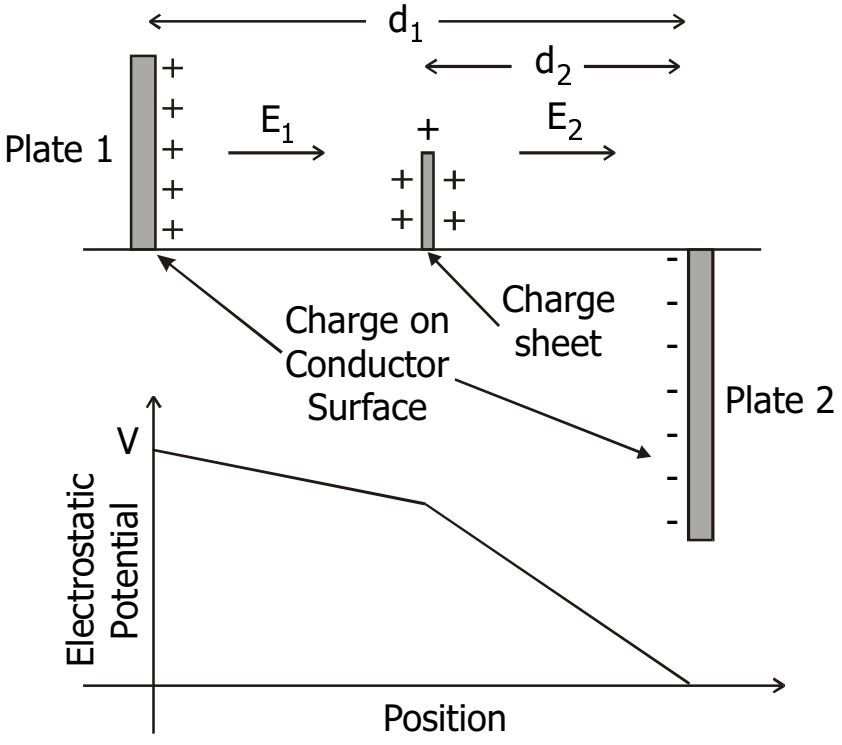

Figure 2-3. Effect of residual charge on the electrostatic field and potential distribution between two conducting plates.

The equation of motion incorporating all these expressions is simulated in Matlab using stiff ordinary differential equation (ODE) solvers. The particular solver that works best is a quasi-constant step size implementation of Numerical Differentiation Formulas (NDF) in terms of backward differences [39]. Steady-state solutions are obtained from quasi-static simulations using a very gradual voltage ramp to actuate the beam, and a mild damping force to minimize transient effects. Unlike for simulations of transient behavior, the damping force used for quasi-static simulations should not vary with the instantaneous gap to prevent severe slowing down near contact.

Figure 2-1(a) shows an ON-OFF transient simulation using a viscosity 3% that of atmospheric pressure air. The nominal system parameters shown on the first line of Table 2-1 are used. The approach to contact is slowed down by the rapid increase in damping forces. The solution at contact is computationally intensive and requires a smooth expression for the contact force to aid convergence. The small viscosity was used so that results could be compared to the next example on the same time scale. If the dependence of squeeze-film damping on instantaneous gap is removed, chattering at contact occurs as shown in Figure 2-1(b). The viscosity used in this example was 10% that of air. Such contact behavior is difficult to characterize because measuring chattering in real life is very difficult. However, hard impacts are known to shatter micromechanical devices in vacuum environments [40].

Table 2-1. V_{pi} of 1-DOF and 2-DOF models compared to quasi-2-D simulations

L	E	h	g_0	σ_u	1-DOF 1-D	2-DOF 1-D	Quasi-2-D
300	140	2	1.5	6.16	21.51	21.31	21.44
400	140	2	1.5	6.16	10.07	10.14	10.06
500	140	2	1.5	6.16	4.31	buckled	4.20
300	**100**	2	1.5	6.16	16.64	16.65	16.67
300	**200**	2	1.5	6.16	27.22	26.93	27.06
300	140	**1.5**	1.5	6.16	12.21	13.42	12.27
300	140	2	**2.0**	6.16	33.93	35.60	34.35
300	140	2	1.5	**3.16**	23.51	23.21	23.33

Variations from nominal case are in bold. L is beam length (in μm), E is Young's modulus (in GPa), h is beam thickness (in μm), g_0 is the initial air gap (in μm), and σ_u is the uniaxial compressive stress (in MPa).

2.4 Two-DOF 1-D Model

To model inhomogenous devices – plates suspended by slender tethers, or beams with distinct variations in cross-section – a two-DOF model, still in 1-D, is shown in Figure 2-2. The beam is divided into two parts – a center-loaded portion called the centerpiece, and cantilever-like tethers that are loaded at their tips by the centerpiece. Assuming symmetry, only one-half needs to be modeled thus only 2 DOFs are required. The equation of motion is modified to become

$$F^{t}_{mechanical} - F^{c}_{mechanical} = m_t \frac{d^2 u_t}{dt^2} \tag{2-1}$$

for the motion of the tether, and

$$F^{c}_{mechanical} + F^{c}_{electrostatic} + F^{c}_{damping} + F^{c}_{contact} = m_c \frac{d^2 u_c}{dt^2} \tag{2-2}$$

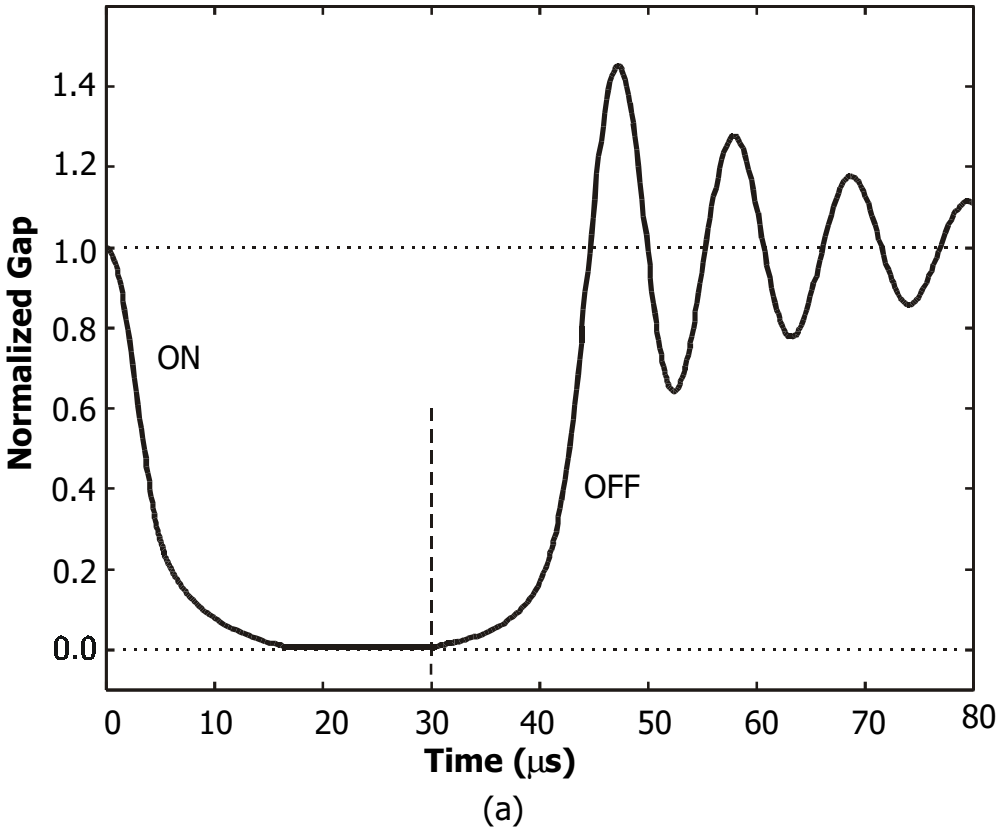

(a)

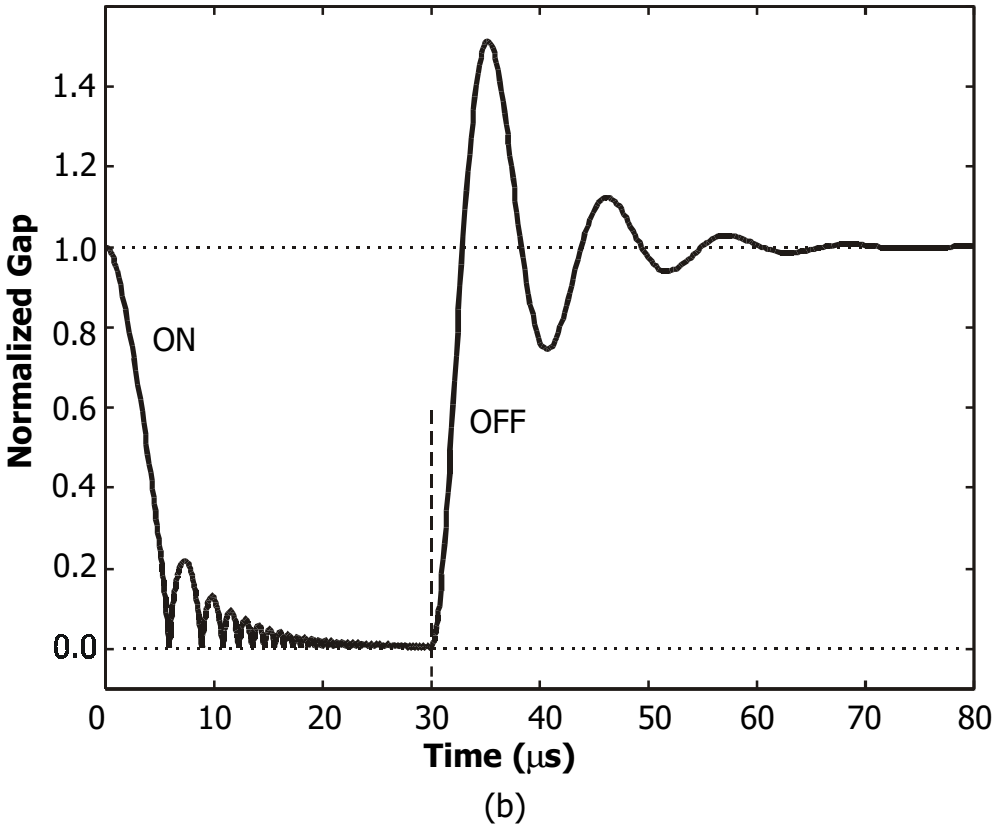

Figure 2-1. Transient simulation using 1-DOF model. 25 V is applied at t = 0 μs and then removed at t = 30 μs. **(a)** This model uses an instantaneous-gap-dependent damping model with a viscosity constant 3% that of air. The approach to contact is slowed down considerably by the squeeze-film damping. **(b)** The viscosity constant is 10% of air, and the damping factor remains constant as the gap changes. Chattering occurs upon contact.

for the motion of the centerpiece. The superscripts and subscripts *t* and *c* denote "tether" and "centerpiece", respectively. Note that the displacement of the centerpiece is measured relative to the position of the tip of the tether. This two-lump model is particularly good for designs where the tethers are flexible compared to the centerpiece and should be modeled separately. It is assumed that the electrostatic forces on the tethers are negligible compared to the mechanical forces transmitted by the centerpiece. The mechanical forces are similar in form to those described in Section 2.3 with slight modifications in the scaling constants. For the tethers, which are modeled as end-loaded cantilevers with guided tips (vertical motion only with no rotation), the mechanical restoring forces (total of both the tethers) are [33]

$$F_{bend} = -\frac{\pi^4 E_t h_t^3 W_t}{48 L_t^3} u_t, \tag{2-3}$$

$$F_{stress} = -\frac{\pi^2 h_t W_t \sigma_t}{4 L_t} u_t, \tag{2-4}$$

and

$$F_{stretch} = -\frac{\pi^4 E_t h_t W_t}{64 L_t^3} u_t^3. \tag{2-5}$$

These are essentially the same as the restoring forces of a fixed-fixed beam with twice the length of the tethers. Additional analyses of the characteristics of various tethers, including those with folded flexures can be found in [41].

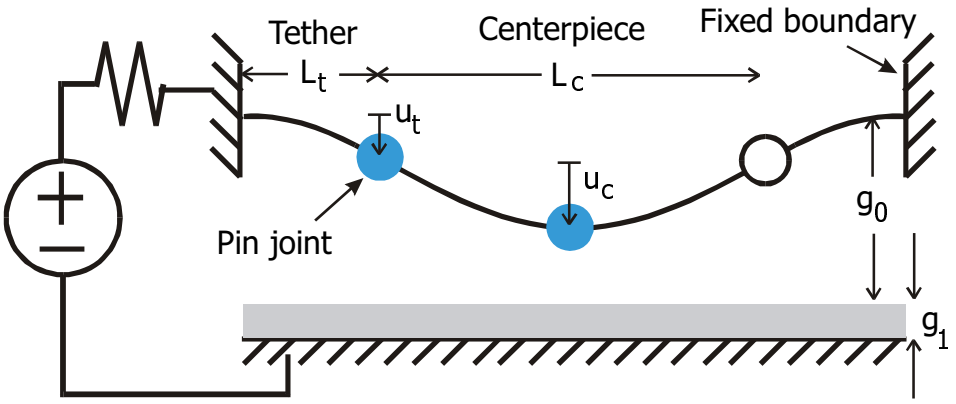

Figure 2-2. Two-DOF model of an electrostatically actuated device consisting of tethers and a centerpiece. The centerpiece is connected to the tethers by a pin joint. Only one tether node is required due to symmetry. The tethers are loaded only by the centerpiece and not by any other loads. Centerpiece displacement is measured relative to tether position.

The centerpiece is modeled as a center-loaded beam with pin joint connections to the tethers resulting in forces given by

$$F_{bend} = -\frac{\pi^4 E_c h_c^3 W_c}{24 L_c^3} u_c, \tag{2-6}$$

$$F_{stress} = -\frac{\pi^2 h_c W_c \sigma_c}{2 L_c} u_c, \tag{2-7}$$

and

$$F_{stretch} = -\frac{\pi^4 E_c h_c W_c}{8 L_c^3} u_c^3 . \tag{2-8}$$

The forces on the centerpiece can also be modeled assuming fixed-fixed boundary conditions, or distributed loading, depending on the structure and operation of the actual device.

Comparisons to quasi-2-D simulations are shown in Table 2-1. The fit is good, but not as good as the 1-DOF model for uniform beams because the partitioning between the tethers and centerpiece is not well defined. That choice of partitioning ratio – the centerpiece was assumed to be 56% of the beam with the tethers making up the rest of the beam – is the only fitting factor of the 2-DOF model. The 500-μm-long beam buckled because the pin joint boundary conditions of the centerpiece erroneously allow buckling at shorter beam lengths than fixed boundary conditions.

2.5 Quasi-2-D Model

A natural extension of the two-lump model is the increasing of the number of degrees of freedom resulting in the finite-difference quasi-2-D model shown in Figure 2-1. While the beam is discretized in 2-D space, each node in the finite-difference model has only the vertical displacement degree of freedom – hence the name quasi-2-D – which moves according to the same 1-DOF equation of motion given by (2-1). 2-D simulations in Abaqus show that horizontal displacement is negligible for the typical range of dimensions studied here. Horizontal motion is significant in cantilevers with large stress gradients, however.

The dependence of the mechanical forces on beam properties is similar to that in Section 2.3 except that the length parameter is not explicitly included. The bending force is described by the Bernoulli-Euler beam equation

$$F_{bend} = -\frac{\partial^2}{\partial x^2}\left(\frac{E h^3 W}{12}\frac{\partial^2 u}{\partial x^2}\right) \tag{2-1}$$

which is valid for only small rotations where the curvature of the beam can be approximated by the second derivative of displacement, and does not account for shear.

This approximation is valid for the long dimensions and small range of travel of many micromechanical devices. The component due to stress is given by

$$F_{stress} = hW\sigma \frac{\partial^2 u}{\partial x^2} \tag{2-2}$$

where σ is the uniaxial stress in the beam. This equation has the same restrictions as (2-1). The stretching component is calculated by computing the stress due to the change in beam length as given by

$$F_{stretch} = hW\left\{E\left[\frac{1}{L}\int_0^L \frac{1}{2}\left(\frac{\partial u}{\partial x}\right)^2 dx\right]\right\}\frac{\partial^2 u}{\partial x^2}. \tag{2-3}$$

This equation has the same form as (2-2) with the term in the square brackets being the computed strain, resulting in the term in the curly braces being the effective uniaxial stress due to stretching. (2-1) is valid for beams with longitudinally varying properties and cross sections but (2-2) and (2-3) are only valid for beams with uniform properties, because longitudinal uniaxial stress is not uniform throughout the beam cross-section otherwise. Hence, the quasi-2-D model is used mainly to simulate the behavior of long, uniform beams.

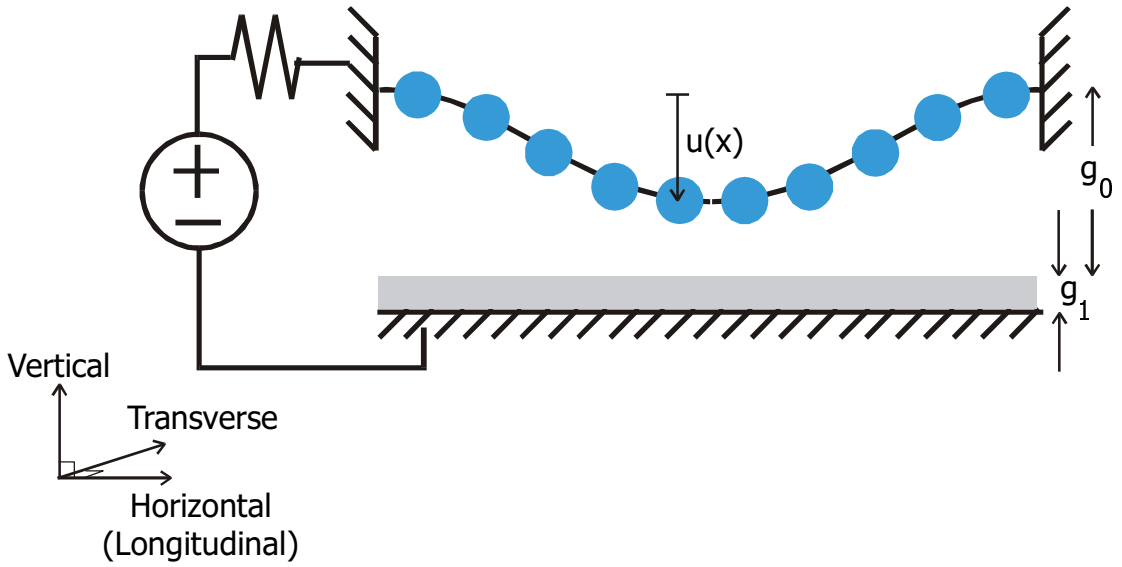

Figure 2-1. Quasi-2-D finite-difference model. Entire beam is discretized. Each node only has a vertical degree of freedom.

The electrostatics model for the centerpiece is exactly the same as in the one-lump case. If the centerpiece is rigid compared to the tethers, most of the deformation occurs at the tethers. As such, the electromechanical system resembles a 1-D system more closely, and the parallel plate approximation is more accurate. The same is true for the 1-D approximations of the damping and contact models which are approximate curve fits anyway.

The most common step-up boundary condition is the ideally fixed boundary condition where the curvature (proportional to $\frac{\partial^2 u}{\partial x^2}$) at the boundary is fixed at zero. Details of the first-order-accurate finite-difference implementation can be found in Appendix A. A more sophisticated boundary condition includes the effects of compliance by iteratively solving for the rotation at the boundary due to the moment induced by the deformation of the beam [42]. Iterative solutions such as these are best left to dedicated solvers such as Abaqus, which is described in the next section. A simpler method to account for the compliance of step-up boundaries is to extend the beam length by an additive offset [34]. Nevertheless, initial buckling of long beams with compressive stress is difficult to simulate in this 2-D finite-difference formulation with whichever boundary condition due to numerical instabilities.

The 1-D electrostatics, damping, contact and residual charge models of Section 2.3 can be easily converted into models for each node in the quasi-2-D model. Noting that displacement, *u*, is now a function of position, *x*, and removing the *L* (length) term from (2-8) gives the damping force per unit length

$$F_{damping} = -\frac{\mu W^3}{(g_0 - u + \lambda)^3}\frac{du}{dt}. \tag{2-4}$$

In a similar manner, dividing (2-11) through by *L* gives the contact force per unit length

$$F_{contact} = -\frac{K_2 W}{(g_0 - u)^{10}}. \tag{2-5}$$

Electrostatic force per unit length becomes

$$F_{electrostatic} = \frac{\varepsilon_0 W V^2}{2\left(g_0 + g_1/\varepsilon_r - u\right)^2}\left[a + \frac{g_0 + g_1/\varepsilon_r - u}{b}\right] \tag{2-6}$$

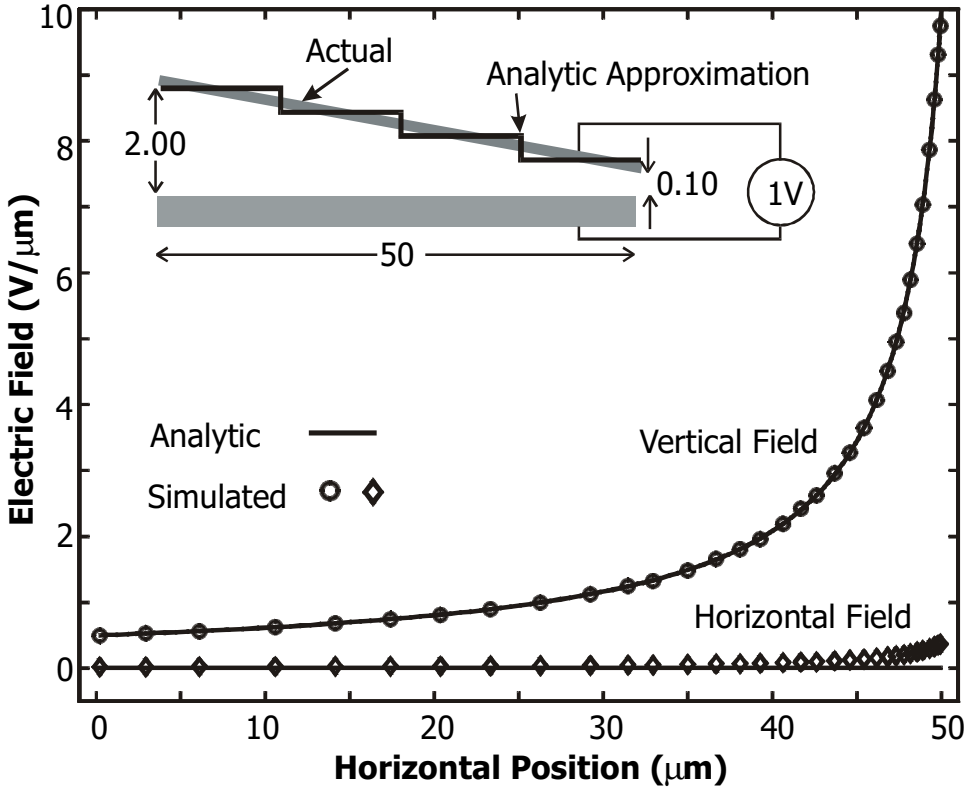

Figure 2-2. Electric field configuration on sloping beam. The beam is 50 μm long and has a 2-μm gap on the left tapering down to a 0.1-μm gap on the right. That is the steepest slope encountered in the electrostatically actuated devices studied. Reflective boundary conditions are applied to the left and right boundaries to maintain vertical electric fields there. Analytic curves using the staircase-like approximation (with many more panels than drawn here) match simulation results very well indicating that the parallel plate approximation holds. The horizontal fields are small compared to the vertical fields and have negligible effect on deflection. Simulations were performed using the Matlab PDE Toolbox [43]

where the constants *a* and *b* are modified to account for only 2-D fringing fields in the transverse plane. An effective area approximation is no longer needed. A long beam suspended above an infinite plate can be approximated by many horizontal-plate-to-ground-plane capacitors connected in parallel along the length of the beam, creating a staircase-like electrostatics model. This approximation is examined in two orthogonal planes. Considering the longitudinal plane that spans the length of the beam first, the

electrostatic forces on the underside of a sloping beam are shown in Figure 2-2. The beam is assumed to be infinitely wide. A simple parallel plate approximation for electric field,

$$E = \frac{V}{g} \tag{2-7}$$

where g is the gap at any position along the beam, matches the simulated results very well, rendering form factors unnecessary to model electrostatic fields in this plane. The horizontal electric field is small compared to the vertical field justifying the use of only the vertical electrostatic force component on surfaces with slopes up to the steepness shown. Furthermore, the horizontal forces do little to influence beam displacement.

Figure 2-3 shows the electric fields near an open end of a beam, such as at the tip of a cantilever, and the converse situation of a beam overhanging a finite ground plane, for several gap distances. The fringing fields near the tip of the beam are difficult to model because they depend strongly on not just the gap, but on the thickness and angle of the beam because of the forces on the vertical wall. Modeling fringing fields at corners is more complex in 3-D but is necessary for cantilevers. Cantilever beams are studied in less detail in this thesis for that reason, and for other reasons described in Section 3.6. The electrostatic forces on the underside of a beam that extends beyond a finite ground plane drop off very quickly beyond the edge of the ground plane, with the abruptness increasing with decreasing gap. As such, simulations of devices over finite ground planes should have electrostatic loads applied only to the portions of the beam directly above the bottom electrodes. Such a situation is shown in Figure 4-1.

To account for fringing fields in the other orthogonal plane i.e. on the cross section of a beam as shown in the inset of Figure 2-4, electrostatic simulations in Raphael [44] were performed. The simulated capacitance and electrostatic force on a 30-μm-wide by 2-μm-thick beam as a function of the gap between the beam and ground plane are plotted in Figure 2-4. The capacitance and force on a very thin beam are also plotted to indicate the contribution due to finite plate thickness, which was neglected in prior work. The fitting parameters in (2-6) were adjusted to match the simulated values – a = 1.006 and b = 31.6 μm. As a result, the electrostatics model for fixed-fixed beams is excellent.

The accuracy of fields near step-ups is not important because the forces and deflection are smallest there.

The equations of motion from each node result in a system of coupled ODEs that can be solved using Matlab's ODE integrators [39] to produce both quasi-static and transient solutions. The damping model in the system helps improve simulation speed by reducing the occurrence of high-frequency vibrations. As for the 1-D case, instantaneous-gap-independent damping is used for quasi-static solutions. The finite-difference discretization of a beam produces a stiff system of ODEs [45] which is computationally expensive to solve. Symmetry can be exploited to solve for only one-half of the beam. Care must be taken to ensure that the symmetry boundary condition is correctly enforced at the center as shown in Figure 2-1. The two centermost points are mirrored about the axis of symmetry to allow the finite-difference computation of the forces described by (2-1), (2-2) and (2-3). If an alternate boundary condition is used where a node is placed directly on the axis of symmetry, only half the total load (electrostatic forces, damping etc.) should be applied to that node.

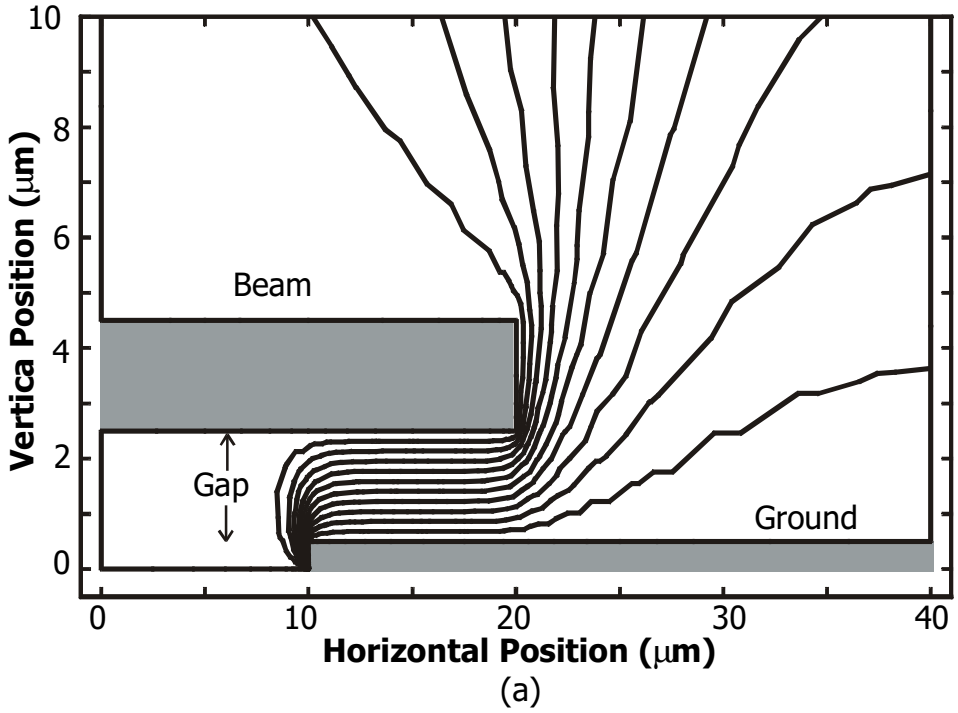

(a)

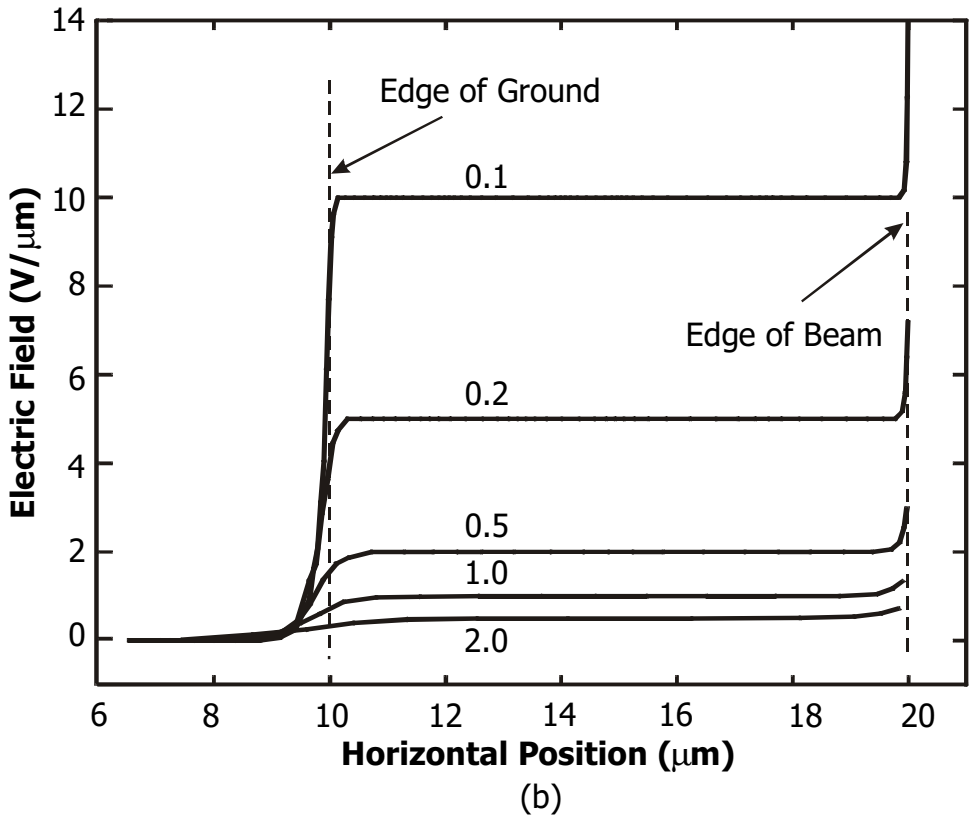

Figure 2-3. Electric field configuration near the edges of a beam/cantilever and a finite ground electrode. **(a)** Electrostatic potential contours from Matlab PDE Toolbox simulations. **(b)** Vertical electric field variation along the underside of the beam, parameterized by the gap (in μm) between the beam and ground. The field drops off very quickly at the edge of the ground electrode, with the abruptness increasing with smaller gaps. The electric fields increase rapidly towards the tip of the beam, especially for smaller gaps.

The stiffness matrix of a system of ODEs generated by a finite-difference discretization is usually diagonally dominant, allowing for sparse matrix techniques that greatly speed up computation. In this case, however, the stretching term (2-3) depends on the global solution, not just on the nearest neighbors, thus destroying the sparsity of the matrix. Nevertheless, numerical experiments show that forcing the solver to assume a diagonally dominant matrix with a bandwidth of 5 gives results that are very close to the results assuming a fully populated matrix. Both quasi-static and transient simulations up until pull-in are very efficient, faster than the relaxation coupling algorithm used in previous work, which could only obtain steady-state solutions [30], [34]. However, due to the positive feedback nature of pull-in, the ODE integrators get mired in the divergent behavior of the system beyond pull-in and take some time to arrive at the subsequent in-contact solution. The extreme behavior of the contact forces – large changes in force over

a small displacement range – also bogs down the simulator. Since transient contact behavior is difficult to measure and characterize, only static contact solutions in 2-D are discussed in this thesis. These solutions are most easily obtained using the simulation model described in the next section.

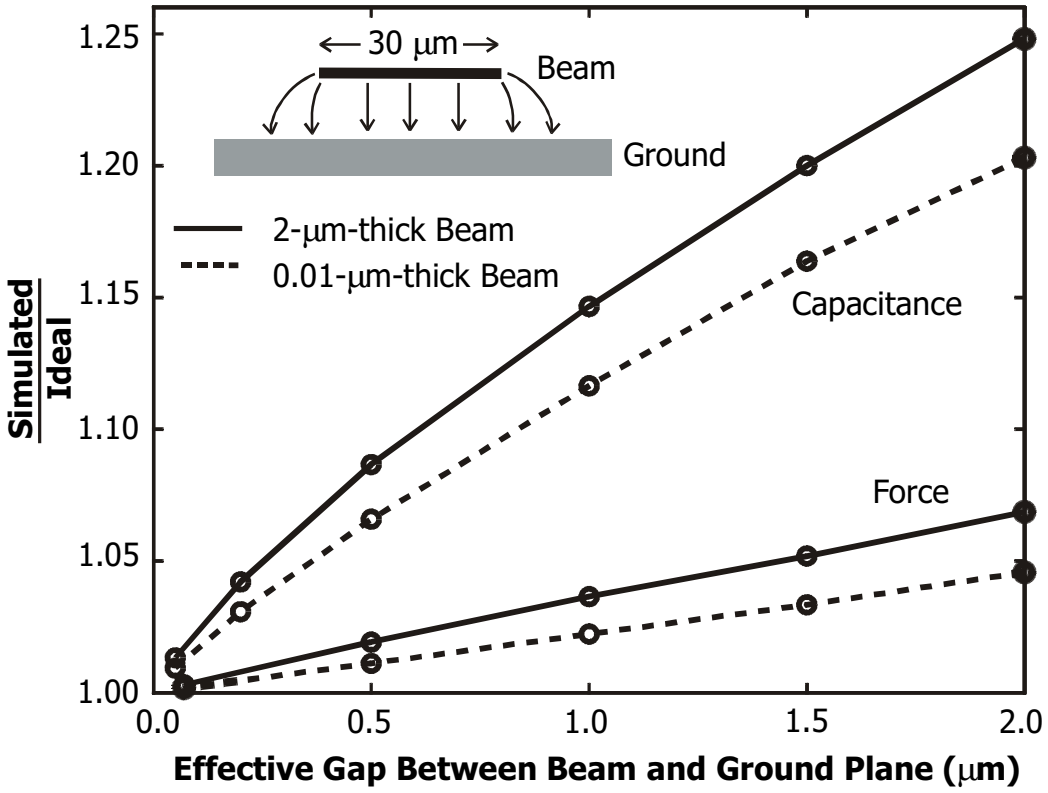

Figure 2-4. Simulated 2-D fringing effects of a 30-μm-wide beam suspended above a ground plane, as a function of gap. The deviation from an ideal parallel plate capacitor model (without fringing fields) increases as the gap increases. The contribution due to the finite thickness of the beam is also shown.

2.6 Abaqus 2-D Model

Accuracy can be further improved by utilizing the commercial finite-element package Abaqus [17] to solve the mechanical portion of the coupled electromechanical system. A simple 2-D simulation model is shown in Figure 2-2. The beam can have topography more complicated than can be captured in any of the previous simulation models, incorporating step-ups and other mechanical discontinuities explicitly, precluding the need for ad hoc mechanical form factors. The Abaqus model captures all the mechanics accurately, including the effects of stress stiffening or stretching, finite

deformation, large rotations, stress gradients, buckling, stress relaxation and compliant step-ups simply as a matter of course. This model supports the analysis of post-buckled structures in Chapter 4.

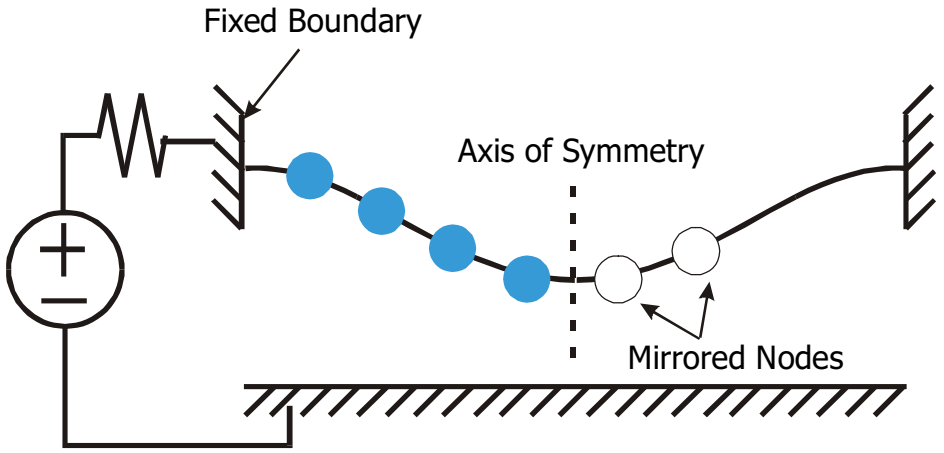

Figure 2-1. Symmetry boundary condition for quasi-2-D system. The two centermost nodes are reflected about the axis of symmetry. The spacing between all the nodes is constant.

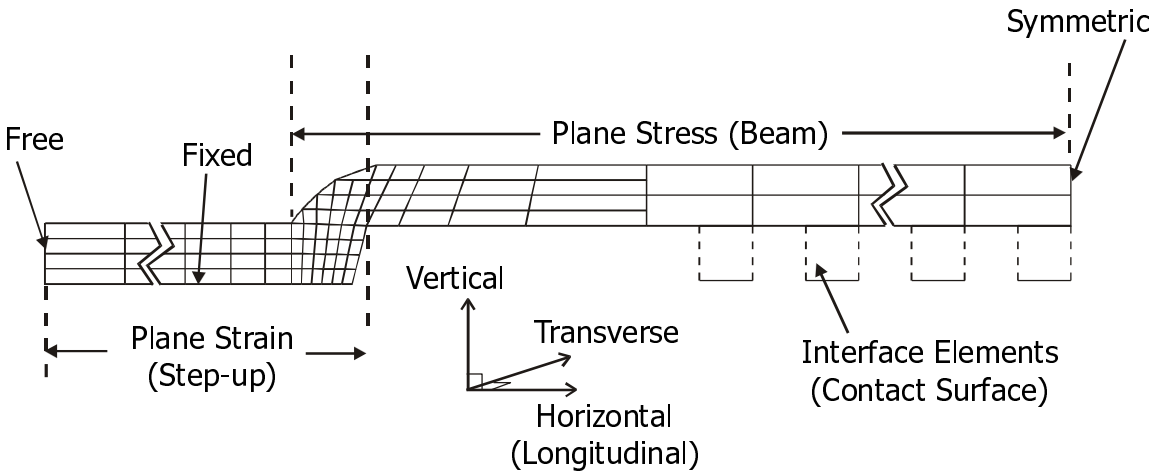

Figure 2-2. 2-D Abaqus model of a beam, capturing the geometry of the anchor step-up. Quadrilateral and triangular elements are used. Symmetry is exploited requiring that only one-half of the beam be modeled.

The model uses 2-D reduced-integration quadratic elements, with plane strain elements for the portion of the step-up anchor which adheres to the bottom surface, and plane stress elements for everything else. Residual stress in the system is quantified in terms of a thermal expansion coefficient, α. The resultant uniaxial stress, σ, is simply

αE if the temperature change is unity. The resultant biaxial residual stress in a uniformly deposited film constrained in the horizontal plane is

$$\sigma_{biaxial} = \frac{\alpha E}{1-\nu}. \tag{2-1}$$

This allows the system to be ramped up gradually to the correct initial stress state before an electrostatic load is applied. Incorporating a large residual stress as an initial condition in a single step can introduce error in simulations — underestimating the initial deflection, or deforming the beam into an incorrect buckling mode. In pre-buckled beams, compliant step-up boundaries cause the final stress state to vary according to beam length because of longitudinal stress relaxation.

The plane stress elements of the beam enforce the assumption that all the transverse stresses perpendicular to the plane of the beam shown in Figure 2-2 relax. 3-D simulations using brick (3-D quadratic) elements validate this assumption, showing that for 300-μm-long, 2-μm-thick and 30-μm-wide beams, most of the transverse stress relaxes within 10 μm of the anchors. Buckling amplitudes in 2-D simulations are also verified by 3-D simulations. To further validate the 2-D model, 3-D pressure-loading simulations of fixed-fixed beams with initial biaxial stress, which relaxes to primarily uniaxial stress in these beams, were performed. For 2-μm-thick and 30-μm-wide beams of various lengths, 2-D models using plane stress elements are more compliant than 3-D models by less than 1% if the step-up anchors are included. The error is slightly higher for beams with perfectly clamped boundary conditions. The match is also especially good for the larger deformations encountered in the contact simulations of the Chapter 5. Since the match is good, the plate-effect adjustment factor suggested by Gupta [34] is not used. Interface elements are used to model contact between the beam and the underlying surface. Complex surface conditions including compressibility can be modeled. More details are given in Section 5.3.2.

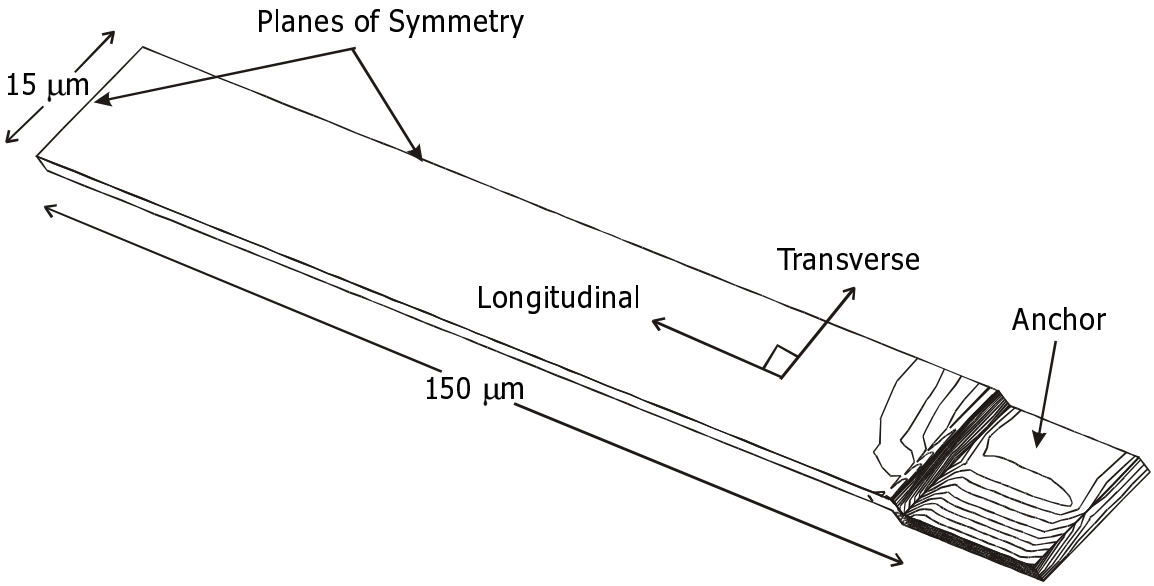

Figure 2-3. 3-D simulation of stress relaxation of a 300-μm-long, 30-μm-wide and 2-μm-thick beam including step-up anchor. Contours of transverse stress show that all the transverse stress relaxes except within 10 μm of the step-up, and in the anchor itself, which is constrained to the substrate. Quadratic brick elements are used throughout the model, and symmetry is exploited, requiring simulation of only one quarter of the fixed-fixed beam.

Electrostatic forces described by (2-6) are applied to the bottom surfaces of the beam as user-defined pressure loads [17], [32]. The pressure load is always normal to the surface of the underside of the beam and, hence, is slightly closer to reality in large rotation deformation cases than the vertical-only electrostatic fields used previously. Nevertheless, the results shown in Figure 2-2 indicate that lateral electric fields are small compared to vertical fields and have little effect. Using an analytic expression for the electrostatic force allows Abaqus to use gradient methods to find the equilibrium electromechanical solution instead of having to rely on slower relaxation methods. In addition, a numerical electrostatics solution tends to deteriorate if the mesh is kept unchanged as the gaps between the voltage-driven elements close. In fact, at the very small gaps encountered in the contact problems of Chapter 5, the analytic approximation is more reliable than numerical solutions.

Only static simulations were performed because transient contact simulations encountered convergence difficulties due to the acceleration induced by the positive feedback in the unstable pull-in regime. It is important to prevent Abaqus from checking for the convergence rate near pull-in. Otherwise, the nonlinear solver will abort the

simulation when the solution appears to diverge in the unstable positive feedback regime before finally reaching the correct in-contact solution. In addition, the divergent behavior precludes automatic step sizing. Thus the precision of the V_{pi} simulations is simply the minimum step size used (0.1 V steps are used throughout this thesis unless noted otherwise). For accurate resolution of pull-in voltages, the actuation voltage should be ramped up gradually, with finer steps closer to the expected pull-in voltage. Further simulation details – element types, solver parameters and boundary conditions – can be found in Appendix B.

2.7 Quasi-3-D Model

Extending the Abaqus model of the previous section into three dimensions gives the quasi-3-D model shown in Figure 2-1. The electrostatic forces on the faces of the mechanical structures are still approximated by parallel plate models, hence the name quasi-3-D. Fringing fields in 3-D are more difficult to characterize, generalize and model than in 2-D. In addition, it is difficult to apply electrostatic pressure loads within Abaqus that vary depending on whether the load is located near the edge of a plate or beam where fringing effects are largest, or near the center where the parallel plate approximation is very good. This method is most useful for simulating the behavior of 3-D structures where good 3-D mechanical accuracy is required but electrostatic fringing fields are not very significant. For example, devices comprising tethers with various flexures can be modeled.

2.8 Full 3-D Model

The full 3-D model of a vertical electrostatically actuated device generated in IntelliCAD [19] is shown in Figure 2-2. In theory, the model can be generated automatically from a layout but in practice, many manual adjustments are needed to obtain the correct geometry and appropriate mesh. In all the previous models, parallel plate electrostatic approximations were used, and for good reason. The parallel plate approximation is extremely fast and very accurate for the vertical electrostatically actuated devices studied in this thesis. The approximation is poor, however, for devices with pointed 3-D features such as the tips of cantilevers or comb fingers. In 3-D coupled

electromechanical simulations, the electrostatics computation usually takes much longer than the mechanical simulation, even using accelerated boundary-element techniques [46]. As noted in Section 2.6, the electrostatics solution tends to deteriorate if the boundary-element surface mesh is kept unchanged as the gaps between the actuated elements close. Coupling between the electrostatics and mechanics is usually done using relaxation methods because gradients are expensive to compute numerically – such gradient methods are more efficient only near pull-in where relaxation methods approach the converged solution very slowly [47]-[49].

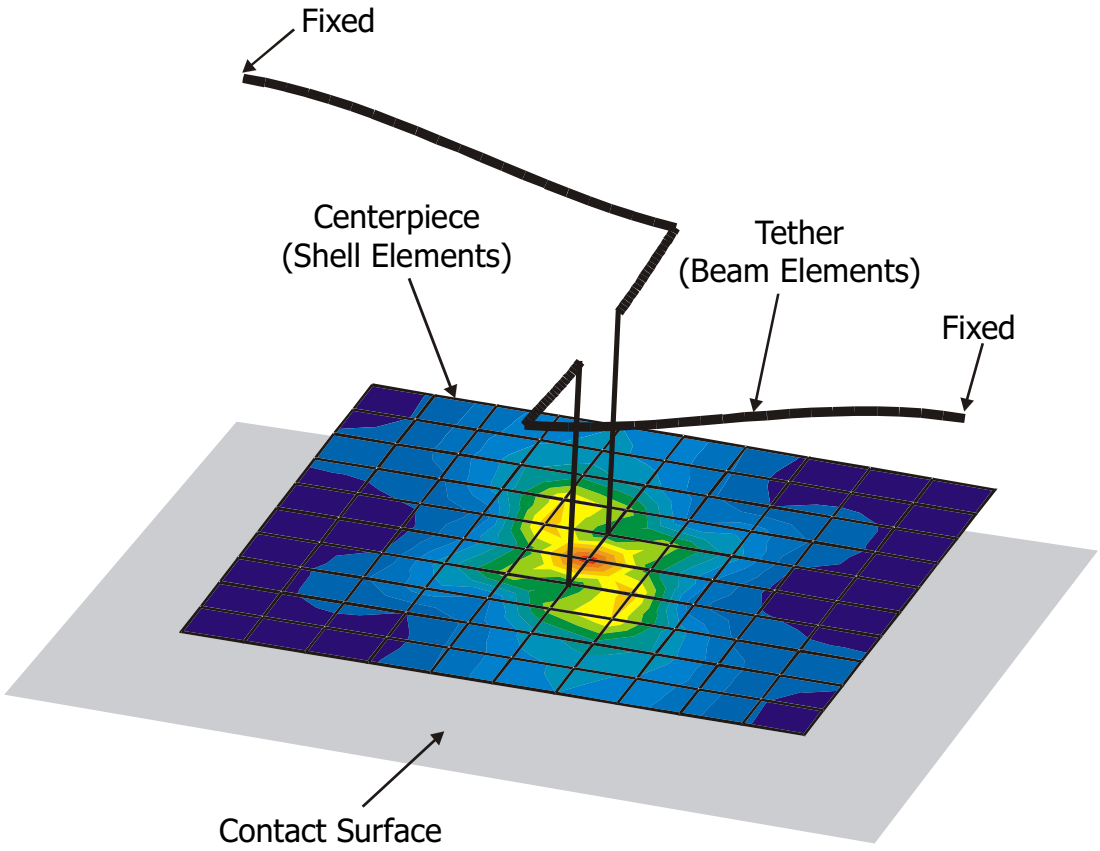

Figure 2-1. Quasi-3-D model in Abaqus. Beam elements are used for the tethers whereas shell elements are used to model the centerpiece. Electrostatic loads are applied to the underside of the centerpiece. A rigid contact surface is used, instead of interface elements, to handle contact. Van Mises stress contours are shown.

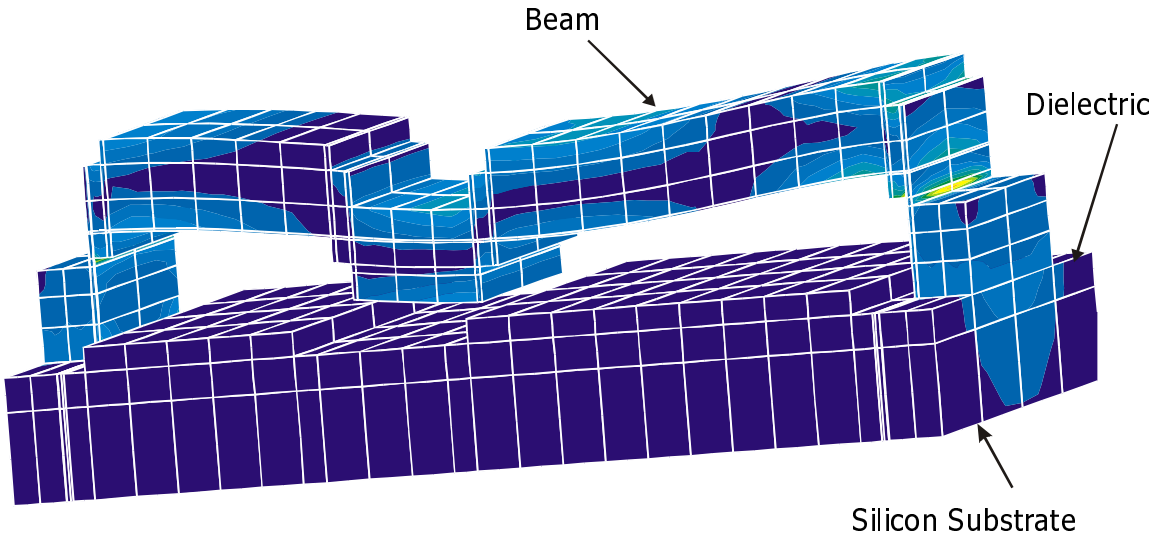

Figure 2-2. Full 3-D IntelliCAD model of a beam suspended above two bias electrodes (see Chapter 4 for more details). Vertical dimension is scaled up for clarity. Quadratic brick elements are used throughout. Electrostatic forces are applied to all exterior surfaces.

2.9 Comparisons Among Simulation Methods

Comparisons of static V_{pi} between the 1-D simulation models and quasi-2-D model for fixed-fixed beams were presented in Table 2-1. Figure 2-1(a) and (b) now compares the accuracies of a 2-D Abaqus simulation, a quasi-2-D simulation performed in Matlab, and a 3-D simulation done in IntelliCAD. The system again consists of a beam 300-μm-long, 30-μm-wide and 2-μm-thick, suspended 1.5 μm above a ground plane. The ends of the beam are ideally clamped. The beam has a Young's modulus of 140 GPa and an effective initial compressive biaxial stress of 8 MPa. A contact surface is placed 0.5 μm above the ground plane leaving a 1 μm travel gap. Capacitances from the quasi-2-D and 2-D simulations are computed using

$$C = \frac{\varepsilon_0 W}{g}\left[c + \frac{2g}{d} + \frac{2g}{d}\ln\left(\frac{d}{g}\right)\right] \tag{2-1}$$

for capacitance per unit length [50] where

$$g = g_0 + g_1/\varepsilon_r - u \tag{2-2}$$

and the constants *c* and *d* are 1.004 and 75.4 μm, respectively. These constants were obtained by fitting to Raphael simulations using a 2-μm-thick beam cross section (see Figure 2-4).

The results of the 2-D Abaqus simulation are shown as the solid lines in the displacement-voltage curve of Figure 2-1(a), and the capacitance-voltage curve of Figure 2-1(b). The computed pull-in voltage is 21.7 V. Convergence studies indicate that even a single layer of just 15 reduced-integration quadratic plane stress elements is sufficient to model one-half of the beam accurately. The quasi-2-D model is slightly more compliant than the Abaqus model, giving a pull-in voltage of 21.4 V. The quasi-2-D results are shown as the dotted lines which are almost entirely overlaid by the solid lines of the 2-D Abaqus simulation. Half the beam was simulated using 300 nodes.

The beam mesh in IntelliCAD consists of 30 × 3 × 1 quadratic brick elements. This model is slightly stiffer than the 2-D Abaqus model, giving a pull-in voltage somewhere between 21.8 and 22 V. The longitudinal mesh density for the mechanical model in IntelliCAD is the same as that used in the Abaqus model. The mesh for electrostatics on the underside of the beam and on the top of the ground plane were manually refined to obtain the necessary accuracy. The final electrostatics mesh consists of triangular surfaces with edge lengths of 5 μm and 7.5 μm on the beam and ground plane, respectively. The contact capacitances are lower than in the 2-D simulations, possibly due to the deterioration of the electrostatics solution at small gaps. The IntelliCAD computation consumes well over two orders of magnitude more time (about 30 minutes per data point on a SUN UltraSparc 2 with 1 GB main memory) than the Abaqus simulation, especially near pull-in and beyond, with most of the time spent in the electrostatics solutions. Very little transverse bending is observed in 3-D confirming that the problem is essentially two-dimensional i.e. the beam hardly deforms along the direction of the width of the beam. Hence electrostatic forces along the width can be lumped together, as in the 2-D models, assuming that the beam is rigid in that direction even though the forces are non-uniform and concentrated towards the edges of the beam.

Table 2-1 summarizes some of the pros and cons of the various simulation models, especially with the goals of this thesis in mind.

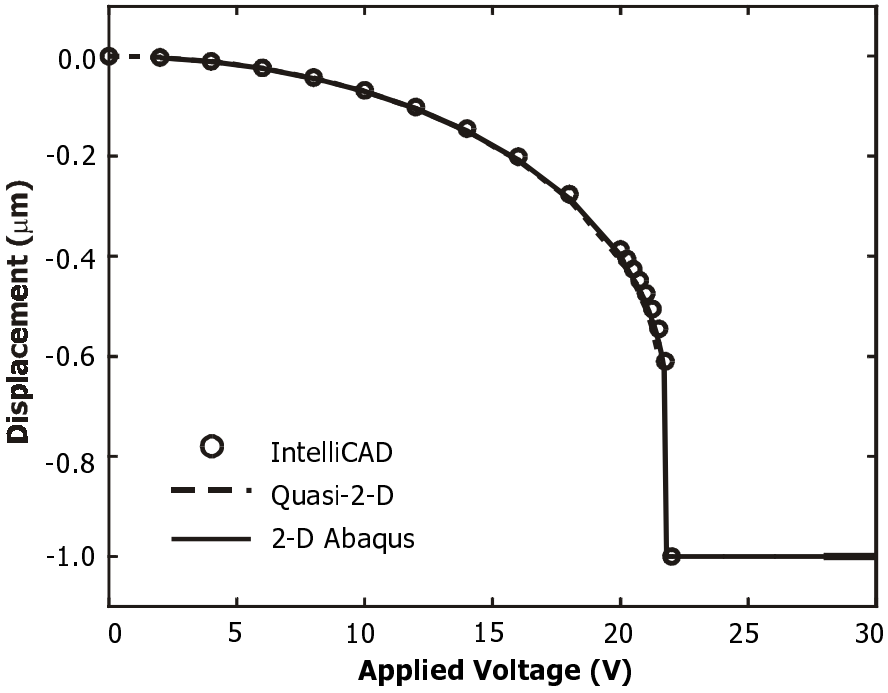

(a)

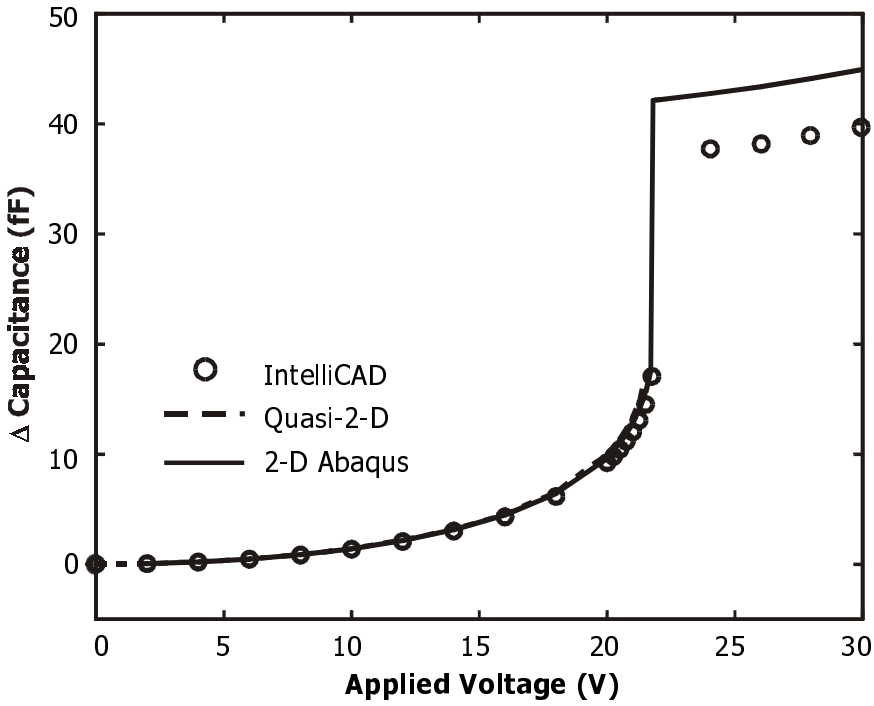

(b)

Figure 2-1. Comparison among Abaqus 2-D, Matlab quasi-2-D, and IntelliCAD 3-D simulations for a simple nominal system. **(a)** Displacement as a function of voltage. **(b)** Change in capacitance as a function of voltage.

Table 2-1. Comparison of simulation models

Method	Pros	Cons
One-DOF 1-D	• Very fast • Many physical effects/models can be simulated together • Reasonable predictive power when well-calibrated • Static and transient simulations	• Coarse approximations
Two-DOF 1-D	• Improved accuracy over one-DOF model for devices with distinct tethers and centerpieces	• Still coarse approximations
Quasi-2-D	• Fast • Good accuracy for long, uniform beams • Integrated into Matlab environment • Static and transient simulations	• For uniform beams only • Contact simulations difficult • Cannot simulate buckling
Abaqus 2-D	• Reasonably fast • Great mechanical accuracy for extruded 2-D profiles • Can incorporate complex contact conditions	• Static only • Mainly for extruded 2-D profiles
Abaqus quasi-3-D	• Reasonably fast, especially as far as 3-D simulations go • Great 3-D mechanical accuracy	• Static only • Electrostatic fringing fields are complicated to incorporate
Full 3-D	• Solves true 3-D electrostatics • Most general	• Very slow • Electrostatics solution can deteriorate with deformation • Transient simulations are only just becoming available

2.10 Summary

Computer simulation models spanning 1-D to 3-D, tailored particularly towards electrostatically actuated micromechanical beams, were compared and contrasted. Improvements in simulation efficiency, and model accuracy, especially in electrostatics, were incorporated. An engineer or designer must decide on the tradeoffs between accuracy and simulation speed when choosing among the different models. Simplified models with only 1 or 2 DOFs are often sufficient for design because the performance of the final product is usually determined by fabrication process parameters which can be highly variable. These models are also suitable for simulating the system performance of several interconnected devices. More accurate models, with improvements mainly in geometrical accuracy, are appropriate for the fine-tuning of designs and for checking for subtleties that might have been obscured by model approximations. These models should

also be used for parameter extraction to obtain better parameter accuracy and to limit the need for rather ad hoc form factors. Possible sources of error in 2-D simulations were carefully identified and eliminated to obtain a good simulation basis for parameter extraction and the investigation of physical phenomena later in this thesis.

Chapter 3 Metrology

3.1 Overview

Process technologies and the range of applications in micromechanics are developing so rapidly that it is difficult for materials characterization work to keep up. In fact, it is a very challenging task even to comprehensively characterize the widely used MUMPs (Multi User MEMS Processes) [51] surface micromachined polysilicon process which is the backbone process of this thesis. Metals are more suitable than the polysilicon of MUMPs for electrical switching applications such as the capacitive microwave switch because of their much higher electrical conductivity. Nevertheless, this thesis investigates polysilicon because the main goals are to characterize coupled electromechanical behavior, and to address the large audience of polysilicon users, by far the largest community in MEMS.

Extracted material parameters vary widely from researcher to researcher, and from extraction method to extraction method [52], often due to a lack of rigor in making measurements of geometry and thicknesses. In addition, the simulation material parameter set is often incomplete, assuming uniformity where it is lacking, leading to discrepancies between measurements and simulations. After introducing a comprehensive characterization methodology, this chapter describes the MUMPs surface micromachining process. Then the details of making accurate geometrical measurements

in the presence of overetch are presented. Although NIST has been interested in providing guidelines for determining the thickness of micromachined structures, especially released layers [53], no comprehensive study has been performed to identify and quantify sources of overetch and nonuniformity in thicknesses. The presence of gold is shown to affect the final thicknesses of layers by affecting the electrochemistry of the HF release etch. As a consequence, the stress of released polysilicon structures is also modified. Several other interesting phenomena and nonuniformities, especially among cantilever beams, are reported.

3.2 Facts of Life

The calibration steps shown in Figure 3-1 consist of identifying relevant simulation model parameters, designing suitable test structures, extracting parameters using detailed yet fast simulations, and finally extrapolating the behavior of an actual complex device. The calibration procedure starts with a designer who has a nascent idea for a device. The critical parameters such as thicknesses, geometry or shape, and material properties that determine the performance of this device are then identified. The set of critical parameters usually is application- and process-specific because it is impossible in practice to define and characterize a universal parameter set. Test structures that isolate these critical parameters to allow accurate and straightforward measurements and parameter extraction are then designed and fabricated. The parameters are stored in a detailed simulation model which can then be used to design or extrapolate the performance of an actual device. A well-calibrated simulation model, preferably in the form of an input deck template, an example of which is given in Appendix B, serves as an unambiguous and comprehensive repository of geometrical and material property information. Finally the physical device is fabricated, measured and compared to simulations. This thesis demonstrates that if the procedures are followed conscientiously, the final simulation accuracy can be within 2% of the measurements.

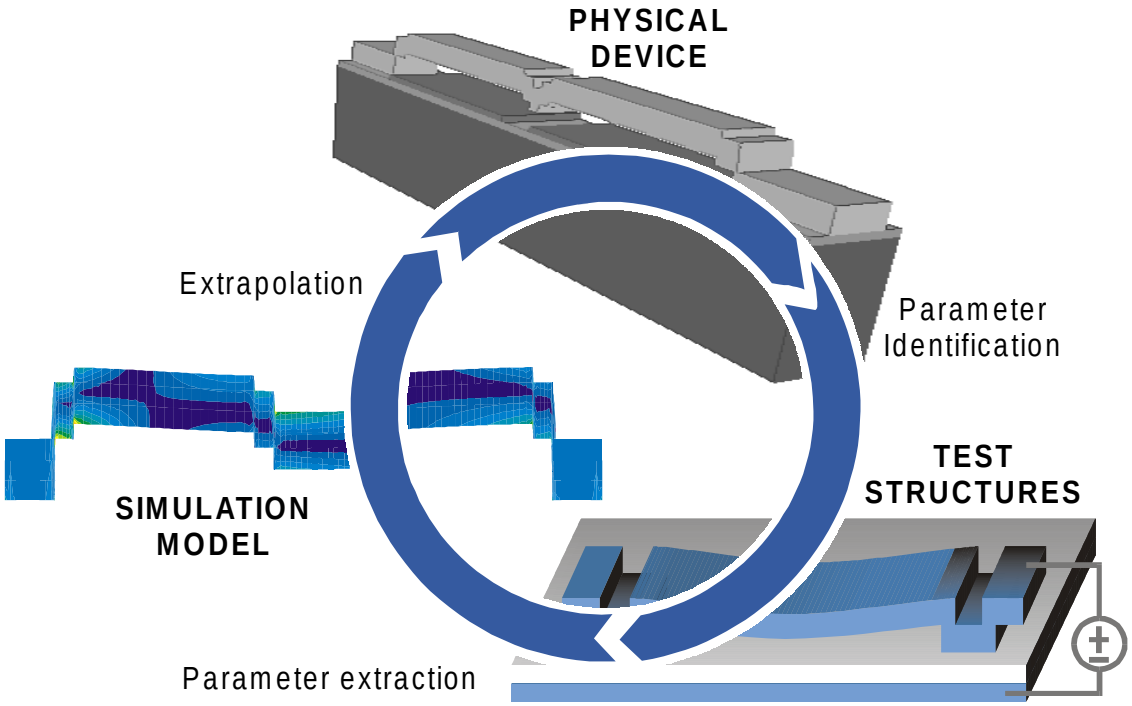

Figure 3-1. Steps required for a consistent calibration cycle: device parameter identification; test structure design; parameter extraction or simulation model calibration; extrapolation/design.

This procedure is straightforward but often engineers and researchers stop at various points in the cycle. Either they perform parameter extraction without demonstrating consistency in the design and extrapolation step, or perform simulations without using calibrated parameters, just hoping to be lucky. All the steps must flow consistently to be confident that we know what is really going on. The use of rather ad hoc and often cryptic parametric adjustments and simplifying assumptions should be avoided because they can lead to inaccurate simulations and even obscure subtle physical phenomena. Buckling, for example, is difficult to characterize using models with an additive offset to account for step-up compliance [34].

This paper targets vertical electrostatically actuated micromechanical beams fabricated in MUMPs although the extracted properties can be used to simulate other devices. However, one must be cautious whenever simulating different modes of actuation or regimes of operation, or devices with dimensions beyond the range of the calibration. Uniformity and extensibility of material and geometrical properties cannot always be assumed. For example, the performance of a device that is actuated vertically such as a microwave switch will depend on a different set of critical parameters than a

device that is actuated laterally such as a comb drive. Material anisotropy and multicrystalline behavior, rather than polycrystalline behavior, might also be factors. Measurements in this chapter and the next show possible nonuniformities in material properties with variations in width, length, and underlying materials.

Figure 3-2 is a schematic drawing that shows some other major reasons why computer simulations might not match experimental measurements. Disregarding easily avoidable errors in measurements and simulations, a primary source of discrepancies is conscious modeling approximations, such as ignoring the effects of compliant boundary conditions, etch holes, or stress variations through the film thickness (commonly known as stress gradients) for the sake of simplicity. Some effects of boundary conditions were analyzed theoretically in [54] whereas the effects of etch holes were discussed in [55], [56]. More effects of boundary condition geometry on beam behavior are discussed in the next chapter whereas stress gradients are examined and shown to be relatively unimportant to the class of MUMPs devices studied in this thesis. A second source of discrepancies is unanticipated anomalies such as nonuniformities in material properties due to gold connections, and the effects of surface residue and asperities – two effects which this work uncovers. Finally, device performance can drift over time due to factors such as fatigue or charge buildup whereas simulation results usually do not unless time-dependent properties are included explicitly.

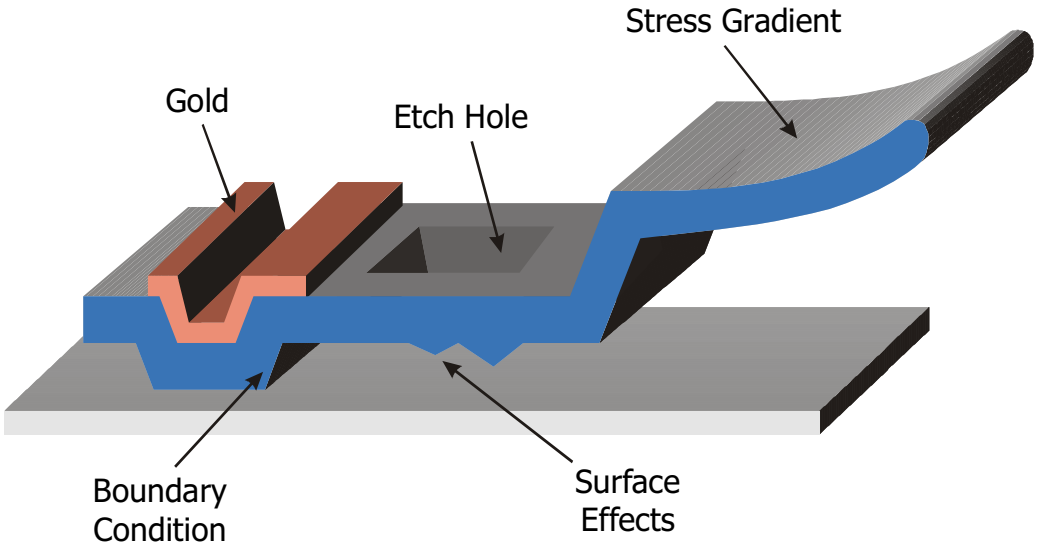

Figure 3-2. Sources of discrepancies between simulations and measurements: boundary conditions, etch holes, direction of actuation, protrusions, gold etc.

3.3 MUMPs

The Multi User MEMS Processes (MUMPs) of the Microelectronics Center of North Carolina (now Cronos Integrated Microsystems, Inc.) is a widely-used foundry process for prototyping and developing sensors, actuators and microelectromechanical devices. It is a three layer – two are released – polysilicon surface micromachining process based on the process developed at the Berkeley Sensor and Actuator Center (BSAC) of the University of California [57]. A thorough description of the process parameters and design rules can be found in the MUMPs handbook [51]. In this section, the effects of etching and deposition on the final thicknesses of films, and the topography of devices are highlighted.

In MUMPs, a nominally 0.6-μm film of silicon nitride is first deposited on a heavily-doped silicon substrate as shown in Figure 3-1(a). The nitride serves as a dielectric isolation layer. The first layer of polysilicon, 0.5-μm-thick, named POLY0 is then deposited via LPCVD and patterned using Reactive Ion Etching (RIE) as shown in Figure 3-1(b). This patterning step thins down (by about 0.03 μm [58]) and roughens exposed areas of silicon nitride. 2 μm of conformal PhosphoSilicate Glass (PSG) is put down next as the first sacrificial layer. Portions of the PSG are then etched so that polysilicon deposited subsequently can be anchored to the nitride or POLY0 layers (Figure 3-1(c)). This anchor etch overetches about 0.08 μm of nitride and about 0.04 μm of POLY0. A shorter, well-controlled PSG etch of about 0.75 μm creates dimples, and also increases the roughness of the surface of the PSG. Figure 3-1(d) shows the first structural layer, 2 μm of conformal polysilicon (POLY1), being subsequently deposited and patterned. This is the structural layer that will be examined closely in this thesis. In addition to the topography of the step-up anchors, the conformal polysilicon layer can have steps over POLY0 pads, and steps down into dimples. Another sacrificial PSG layer and another polysilicon layer (POLY2) are deposited and patterned after this but are not shown in the figures. Gold is the final layer, deposited for probing, electrical routing and to provide highly reflective surfaces (Figure 3-1(e)). At the end, the sacrificial PSG layers are etched away in an HF solution releasing the POLY1 and POLY2 layers, leaving freestanding beams anchored to the nitride, POLY0 or POLY1 layers (Figure 3-1(f)).

This is the final result – an electrostatically actuated beam with complex topographical features.

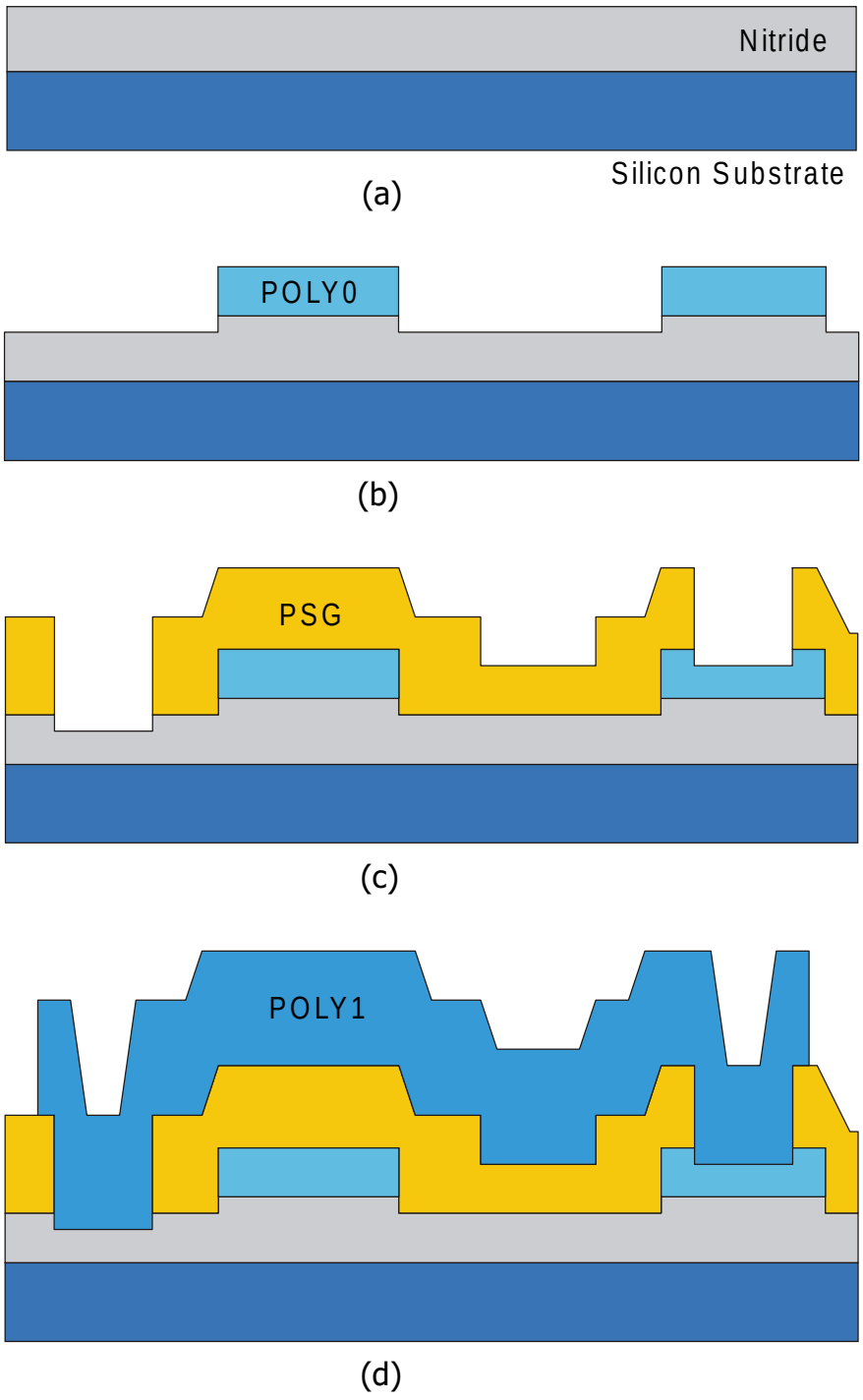

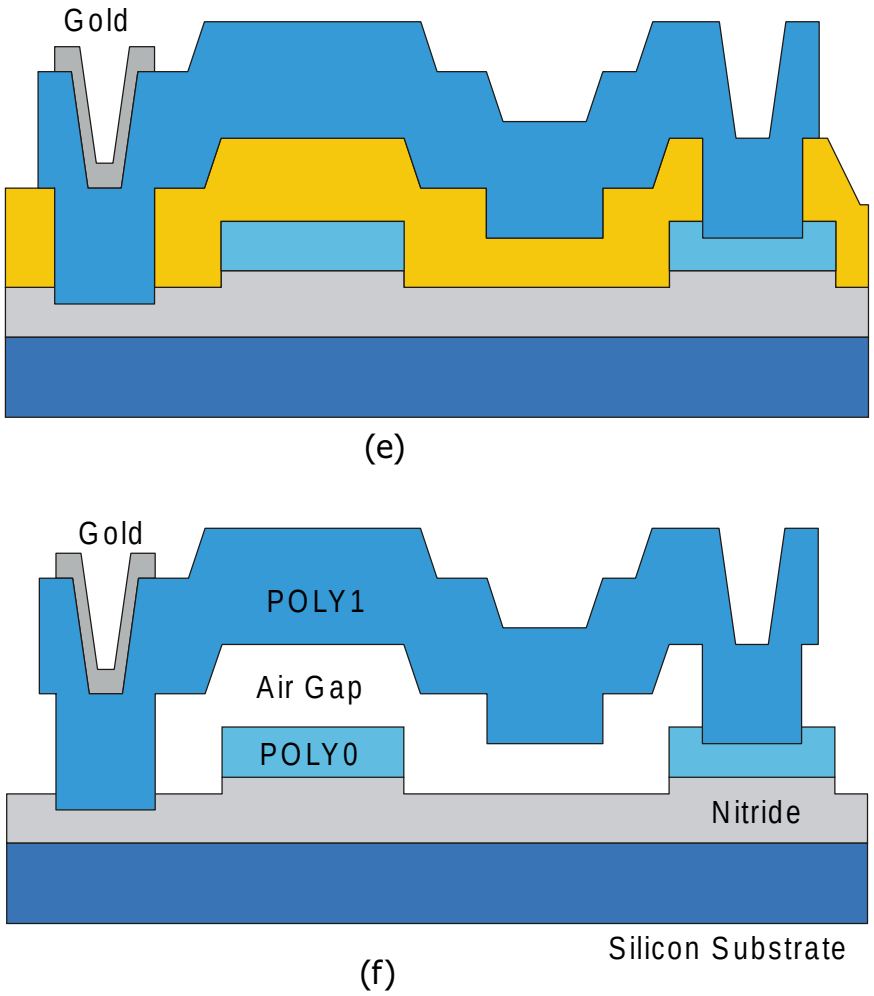

Figure 3-1. Cross-sections at various junctures during the MUMPs process showing nonuniformities in film thicknesses due to overetch. **(a)** Nitride deposited on silicon substrate. **(b)** POLY0 deposited and patterned. **(c)** Sacrificial PSG deposited and patterned. **(d)** POLY1 deposited and patterned. **(e)** Gold deposited and patterned. **(f)** PSG etched away to release POLY1 structures.

3.4 Device Parameters

The geometric properties of interest in this thesis are the thicknesses of the POLY0, POLY1, nitride and sacrificial PSG layers, and the depth of the dimple and the shape of the step-up anchors and other steps. The material properties of interest are Young's modulus (E), initial stress (σ) and stress gradient, and Poisson's ratio, ν. The geometrical measurements are described here whereas the material properties are extracted in the subsequent chapters. Accurate measurements of true final thicknesses are challenging because of overetching, and can be significantly different from

measurements of blanket films deposited on a silicon wafer. Since the goal of this thesis is to demonstrate a very accurate calibration and extrapolation methodology, and to uncover and understand physical phenomena, all of the measurements were made on a single die on the MUMPs 29 run unless noted otherwise. This eliminates run-to-run or even die-to-die variations and focuses on deterministic accuracy rather than statistical bounds. Measurements made on other dies are used only to highlight specific independent phenomena. Please refer to Appendix C for an overview of the devices and measurements of dies from the various MUMPs runs used in this thesis.

Figure 3-1 is the layout of a set of devices designed to facilitate accurate measurements of geometric parameters. The average of thickness measurements at several sites on a single die on the MUMPs 29 run are shown in Table 3-1. The electrical thickness of the nitride, $d_{electrical}$, is determined from the capacitance between a polysilicon pad and the substrate using

$$d_{electrical} = \frac{\varepsilon_0 A}{C} \tag{3-1}$$

where A is the area of the polysilicon pad and C is the measured capacitance. This parallel plate approximation is excellent for the very small electrical gaps encountered here. The capacitance between a POLY0 pad and the silicon substrate was measured with an HP 4275A LCR meter using a sensing signal of 50 mV at 100 kHz. The thickness under the POLY0 is an upper bound since the nitride everywhere else has been thinned down during the patterning of the POLY0. Similarly, the capacitance between a POLY1 pad and the silicon substrate was measured. This pad was deposited directly on the nitride in a region where the sacrificial PSG was etched away before the POLY1 was deposited. The nitride under the POLY1 pad is significantly thinner than anywhere else because the anchor etch of the PSG overetches the nitride significantly. The capacitance was measured as the voltage bias was swept from –35V to +35V to investigate if polysilicon depletion or changes in dielectric polarizability are significant issues. There were no measurable variations in capacitance throughout that voltage range for both the POLY0 and POLY1 capacitors. In Chapter 1, the possible effects of unpassivated surfaces on capacitance measurements are investigated. As can be seen in Figure 3-1(f), the thickness of the nitride under the actuated or released portion of the POLY1 beam is impossible to

measure accurately using fixed, immovable structures because of overetch. In Chapter 5, measurements using actuated plates and beams are shown. These measurements are influenced heavily by contact surface conditions, however.

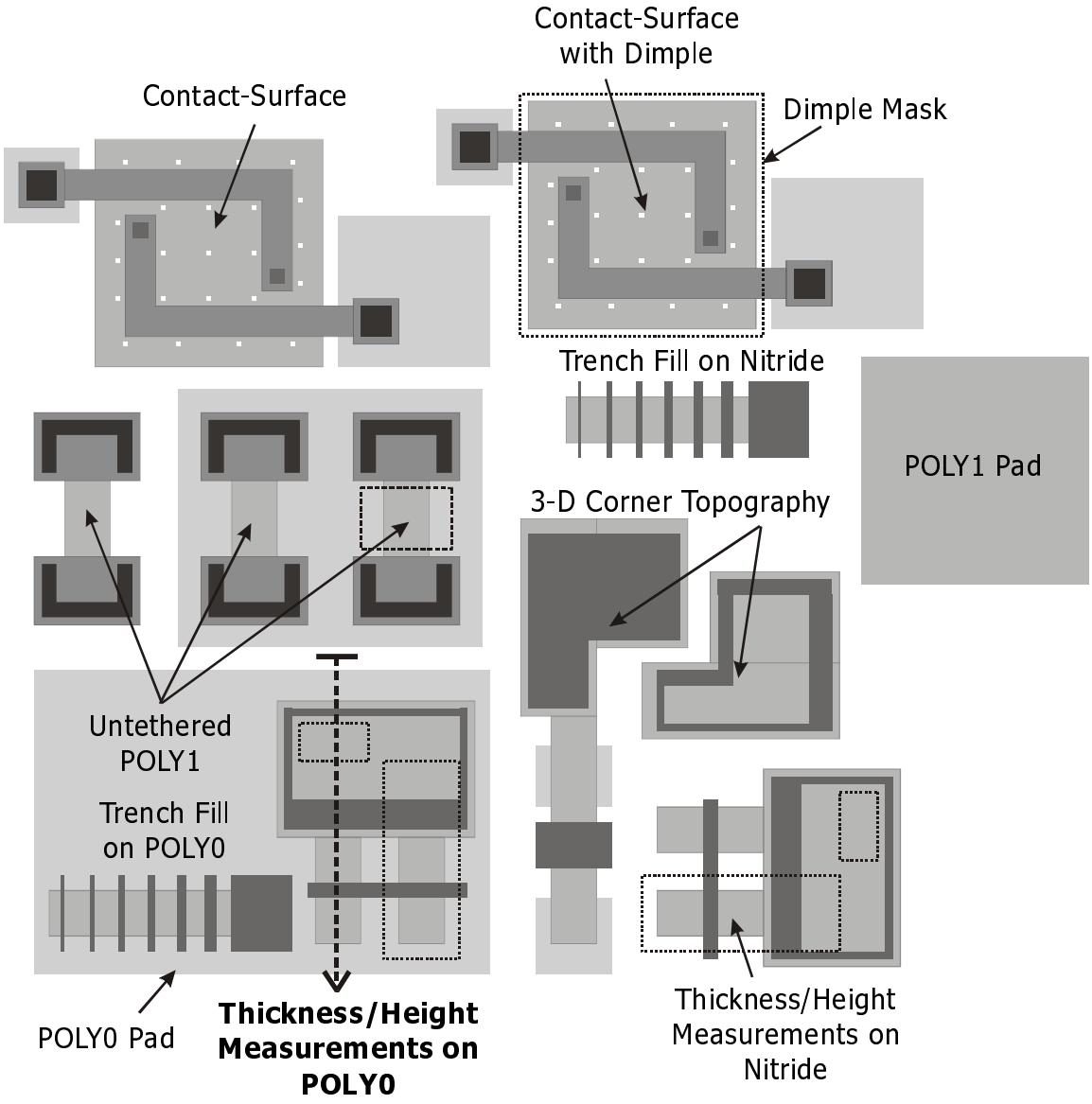

Figure 3-1. Layout of structures used to measure thicknesses and shape. The cross-sectional profile of the thickness/height measurement site indicated by the dotted line is drawn in Figure 3-2. The contact-surface test structures are tethered at the center to eliminate zipping for measurements in Section 5.3.2. Untethered POLY1 beams also eliminate zipping but uneven probe pressure can affect the accuracy of capacitance measurements. Capacitance measurements of POLY0 and POLY1 pads provide the electrical thickness of the underlying silicon nitride. Trench fill arrays are used to investigate the effects of conformal deposition in trenches with sloping sidewalls.

Table 3-1. Measured geometry

Layer	Thickness (μm)
POLY0 (with gold)	0.52
POLY0 (without gold)	0.53
POLY1 (without gold)	1.97
Dimple depth	0.67
Sacrificial PSG	1.79
Nitride under POLY0 (electrical)	0.077
Nitride under POLY1 (electrical)	0.065
Step-up sidewall thickness	2.10
Step-up sidewall angle	76°

The thickness of the POLY0 layer was measured using a Zygo NewView 200 white-light interferometer or surface profiler which, from experience, has a repeatable accuracy of about 0.01 μm [59]. Surface roughness, vibrations, and variability in reflectance limit the repeatability of measurements at different sites on the same device. With careful nulling and leveling, measurements at exactly the same site are repeatable to a precision of 0.002 μm. The interferometer was calibrated to a step height standard to ensure absolute accuracy [60]. Since the interferometer can only image the top surfaces of structures, all the thickness and height measurements have to be made with respect to known surface reference levels in the vicinity. Measurements of POLY0 which use the nitride layer – which is nearly transparent – as the reference require enough light to illuminate the nitride surface so that the reflected light can be processed by the interferometer.

The POLY1 thickness, PSG thickness, and dimple depth are determined from interferometric measurements of the cross section shown in Figure 3-2, using the POLY0 surface as the reference level. The POLY1 thickness measured here is a lower bound of the actual thickness of a released POLY1 beam because of the overetch (about 0.04 μm or less) of the underlying POLY0 due to the PSG anchor etch. This discrepancy is offset in part by the slight etching of the underside of a POLY1 beam during the HF release, and by surface roughness which adds more to optical thickness than to structural rigidity [61]. The thickness of a released POLY1 beam that was pegged to the silicon nitride after

being pulled-in was also measured and found to be 0.03 μm higher than the prior alternate measurement. This is an upper bound because surface residue can add to the true thickness. The average of those two POLY1 measurements is shown in Table 3-1.

The dimple depth is easily measured as shown in Figure 3-2. The thickness of the gap is determined by subtracting the thickness of POLY1, measured earlier, from the thickness of a POLY1-sacrificial gap stack. The thickness of a POLY1-sacrificial gap stack is actually slightly lower (by about 0.01 μm) than a POLY1-PSG stack, as shown schematically in Figure 3-2, because the encapsulated PSG is compressively stressed and expands against the POLY1. This expansion also influences the behavior of backfilled step-up anchor structures as shown in the next chapter.

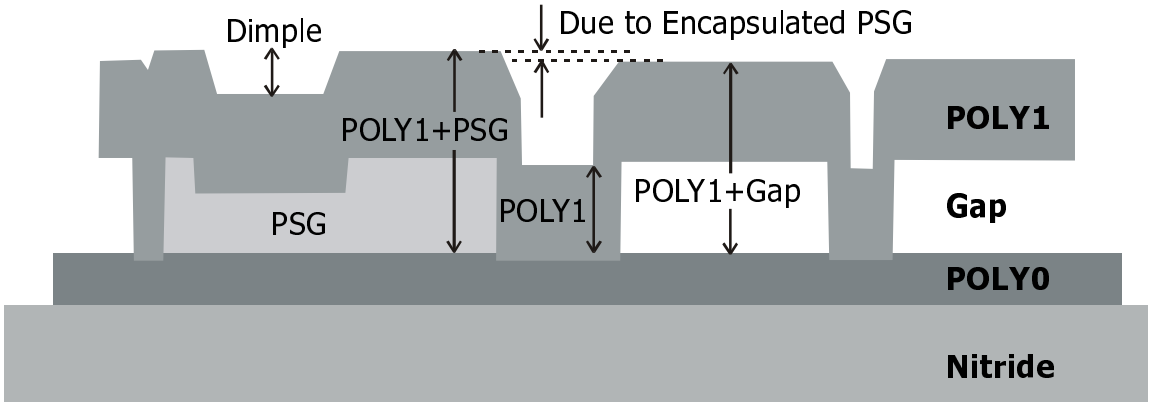

Figure 3-2. Cross section of structure indicated by the heavy dotted line in Figure 3-1, showing thickness measurements sites, with POLY0 as the reference level for the Zygo surface profiler. Overetch affects the accuracy of the measurements. The expansion of the encapsulated PSG causes the POLY1+PSG stack to be higher than the POLY1+Gap stack.

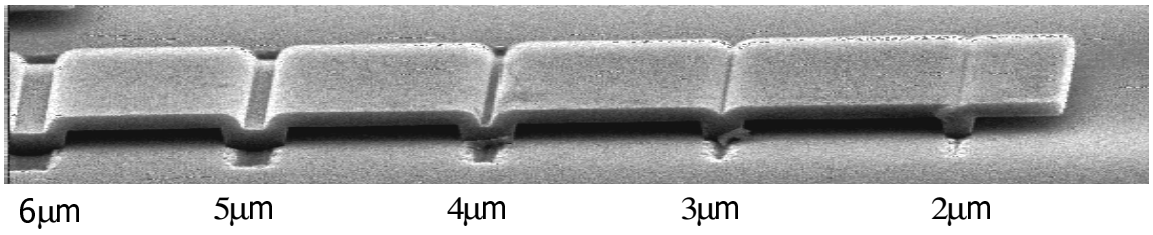

Figure 3-3. SEM of an array of trenches. The 2- and 3-μm trenches are completely filled by the conformal polysilicon whereas the larger ones are not.

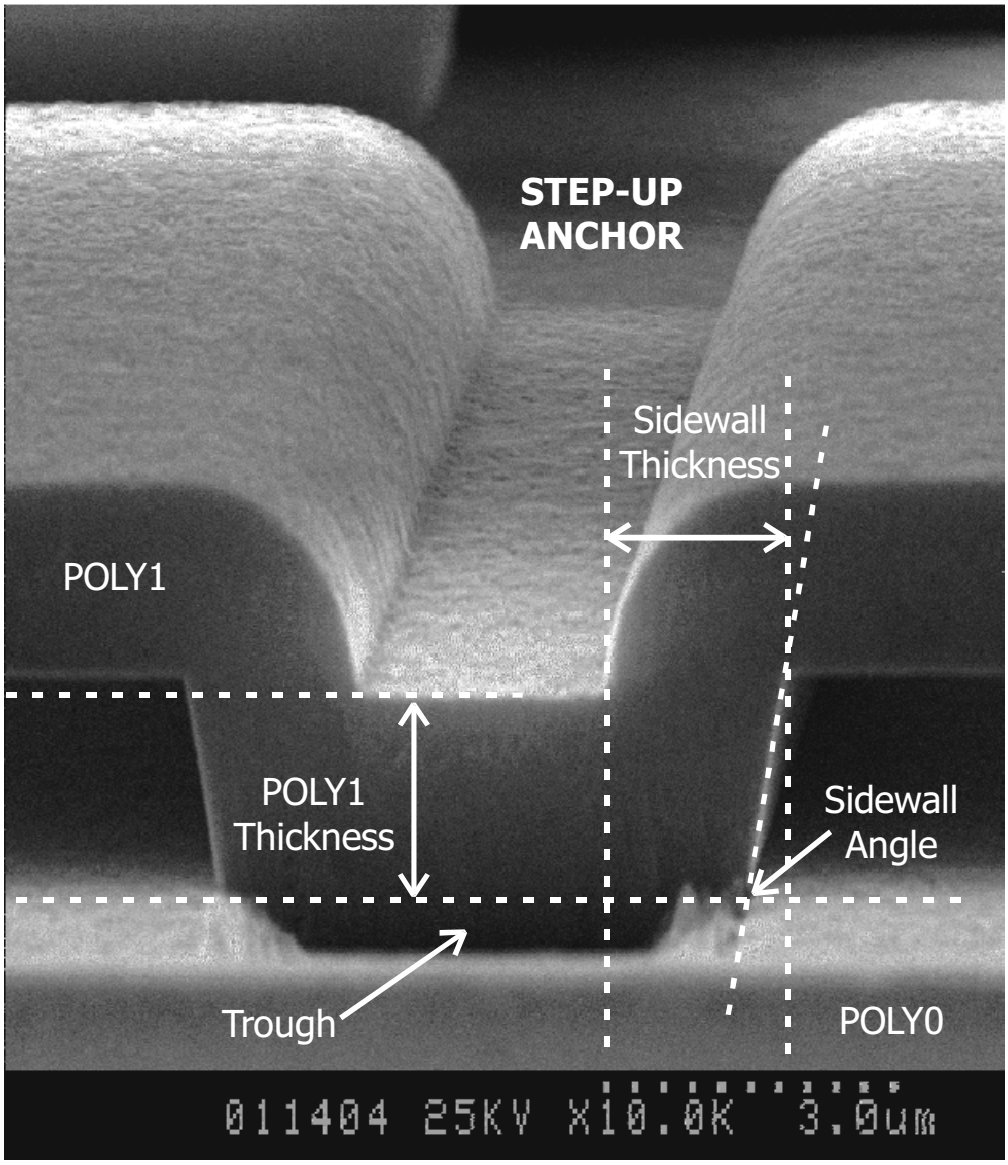

Figure 3-4. SEM of anchor step-up showing sloping sidewalls due to the overetch of the PSG, curved geometry due to conformal deposition, and the POLY1 thickness measurement site with POLY0 as the reference. The lack of a surrounding enclosure lip around the anchor trench results in the etched trough in the foreground.

POLY1 was deposited in anchor trenches of various sizes to determine the trench filling properties of polysilicon and the effect of overetch on the shape of the anchor. The trenches in the SEM of Figure 3-3 are nominally 2, 3, 4, 5 and 6-μm wide and are on POLY0. The 2- and 3-μm trenches were filled up but the 4-μm trench was not filled completely even though the thickness of the conformal polysilicon is nominally 2 μm. This is due to overetching of the PSG which results in sloping sidewalls and an increase

in the opening of the trench by about 0.5 μm on each side. These features are shown more clearly in the closeup SEM of a step-up anchor (Figure 3-4). Figure 3-5 shows the shape of conformal polysilicon deposited into a dimple and over a POLY0 layer. The dimple sidewall is angled just like the step-up anchor. The step over POLY0 is rather gradual because the conformal POLY1 is itself deposited over a conformal layer of PSG.

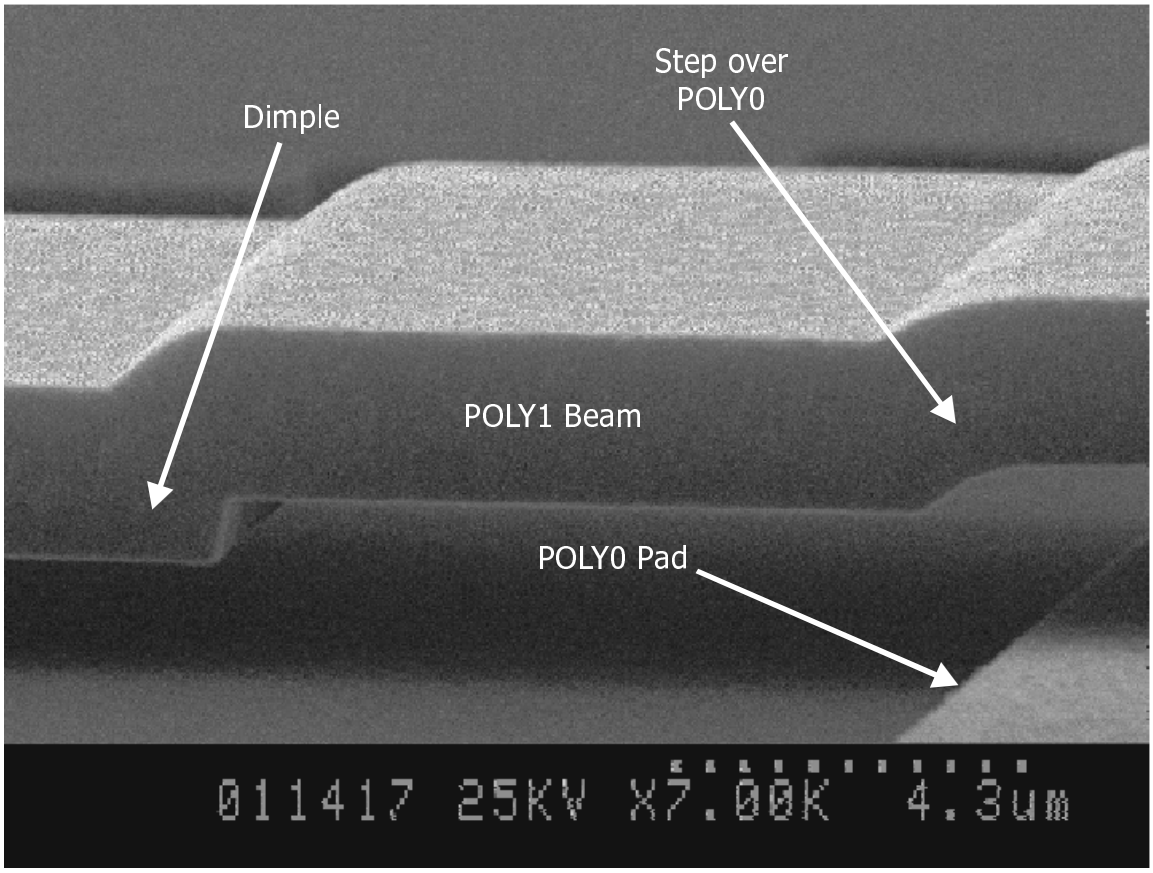

Figure 3-5. SEM of a dimple with angled sidewalls, and a gradual step over POLY0.

3.5 Effects of Gold

Observations of several MUMPs dies under an optical microscope reveal that POLY0 lines connected to gold are darker than POLY0 lines that have no gold connections. The gold connections are 100-μm by 100-μm bonding pads, not entire coatings over the POLY0 lines. The shorter the POLY0 lines, the darker the lines. Differences in shading have also been observed among lines of different characteristic impedances [40]. Surface profile measurements show that the POLY0 lines with gold are

also slightly thinner than the lines without gold. The facts that gold is the last layer deposited, and that the POLY0 is encapsulated by PSG until the HF release etch indicate that gold influences the HF etch, which in turn affects the properties of polysilicon. The gold-polysilicon-HF system sets up an electrochemical circuit which increases the etch rate of polysilicon surfaces connected to gold pads [62]. After a 2.5 minute HF etch, the nominally 0.5-μm-thick POLY0 lines with gold were 0.01 to 0.02 μm thinner than lines without gold. Consequently, the gap between a POLY1 line and an underlying POLY0 layer would be 0.01 to 0.02 μm larger than the gap between a POLY1 line and the surface of the silicon nitride because of this overetch of POLY0. Presumably, POLY1 beams with gold connections are also overetched, and on both the exposed top and bottom surfaces. The exact difference in final thickness due to gold connections is more difficult to determine among freestanding beams because thickness measurements are hampered by surface residue.

This overetching also affects the stress state of ostensibly similar POLY1 cantilevers and fixed-fixed beams. The interferometric image of Figure 3-1 shows that a cantilever connected to gold behaves differently from structures without gold. The layout of these three 300-μm cantilevers, fabricated in MUMPs 27 and released in a 2.5 minute HF etch, is shown in the inset of Figure 3-1 where only the center beam is connected to gold. To reiterate, gold is deposited only on POLY0 which is in turn connected to the anchor of the POLY1 beam, not deposited on the released portion of the beam. The center beam curls up more than the two beams alongside it.

The average stress (which is compressive) also increases causing the center beam of a three-beam array to buckle higher that the neighboring beams as shown in the interferometric image of Figure 3-2. These three 700 μm fixed-fixed beams are connected to gold in the same configuration as the three cantilevers. The increase in buckling amplitude from 0.91 μm to 1.55 μm can be attributed to an increase in average stress and a slight reduction in beam thickness. Assuming that the reduction in thickness of the POLY1 beam is only about 0.03 μm, the connection to gold increases the average uniaxial compressive stress of the beam from 4.9 MPa to 5.9 MPa. The extraction of average stress from buckling amplitude measurements is detailed in the next chapter.

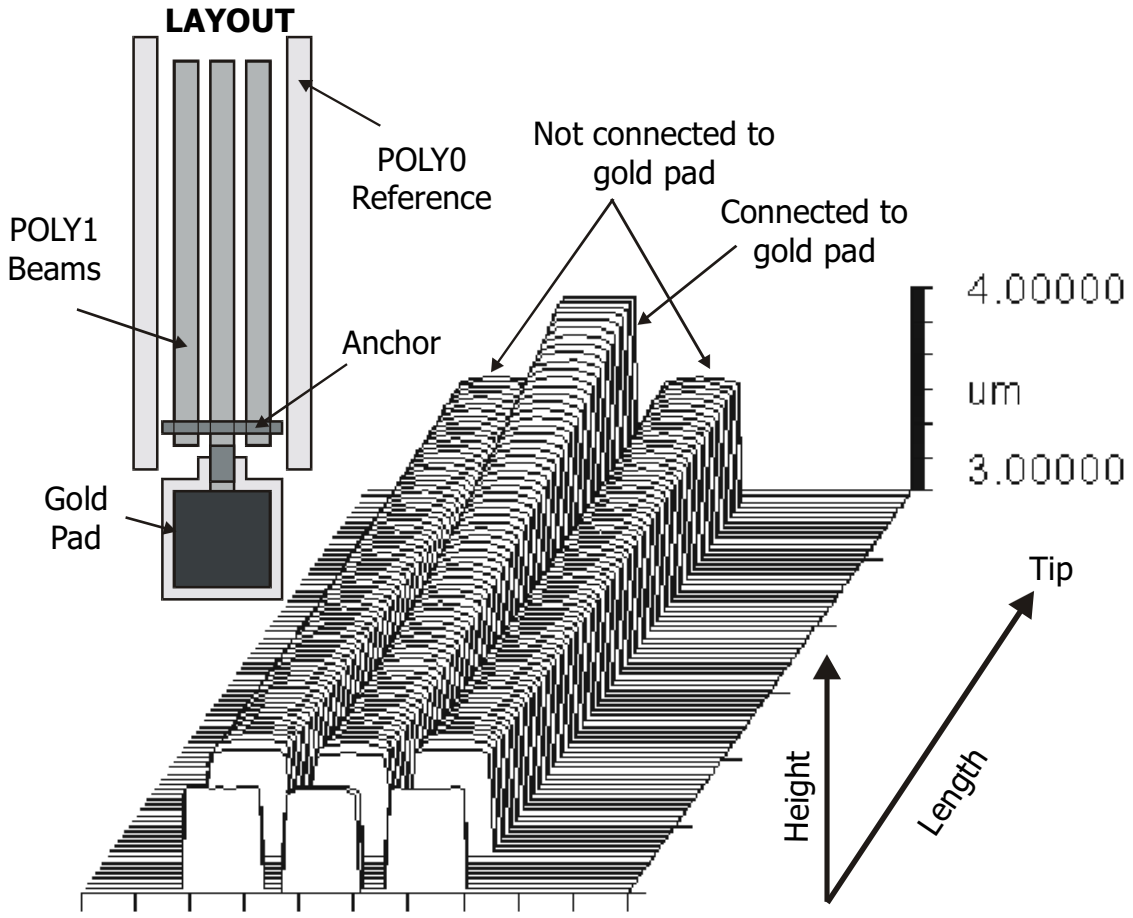

Figure 3-1. Interferometric image of three 300-μm-long cantilevers. The center cantilever is connected to a gold pad as shown in the inset layout. That center cantilever curls up more than the other two.

Figure 3-3 shows a proposed through-thickness stress profile that captures the gold-related effects. The stress profile must produce beams that meet the following four conditions:

- Cantilever beams are initially quite flat
- All modifications in behavior are due to etching of surfaces
- The final fixed-fixed beams have increased average stress
- The final cantilever beams curl up

The profile has an overall compressive average. The moment due to the highly tensile bottom surface is counterbalanced by the gradient of the rest of the beam. Such a highly tensile surface layer of only a few tens of nanometers can be due to crystallite coalescence [63]. When the top and bottom surfaces, which are more tensile than the

average, are overetched away, the average stress increases. The removal of the bottom surface layer also causes cantilevers to curl up due to the stress gradient of the bulk of the beam. The stress profile can only be approximated because the exact amount of overetch of the top and bottom surfaces is difficult to determine.

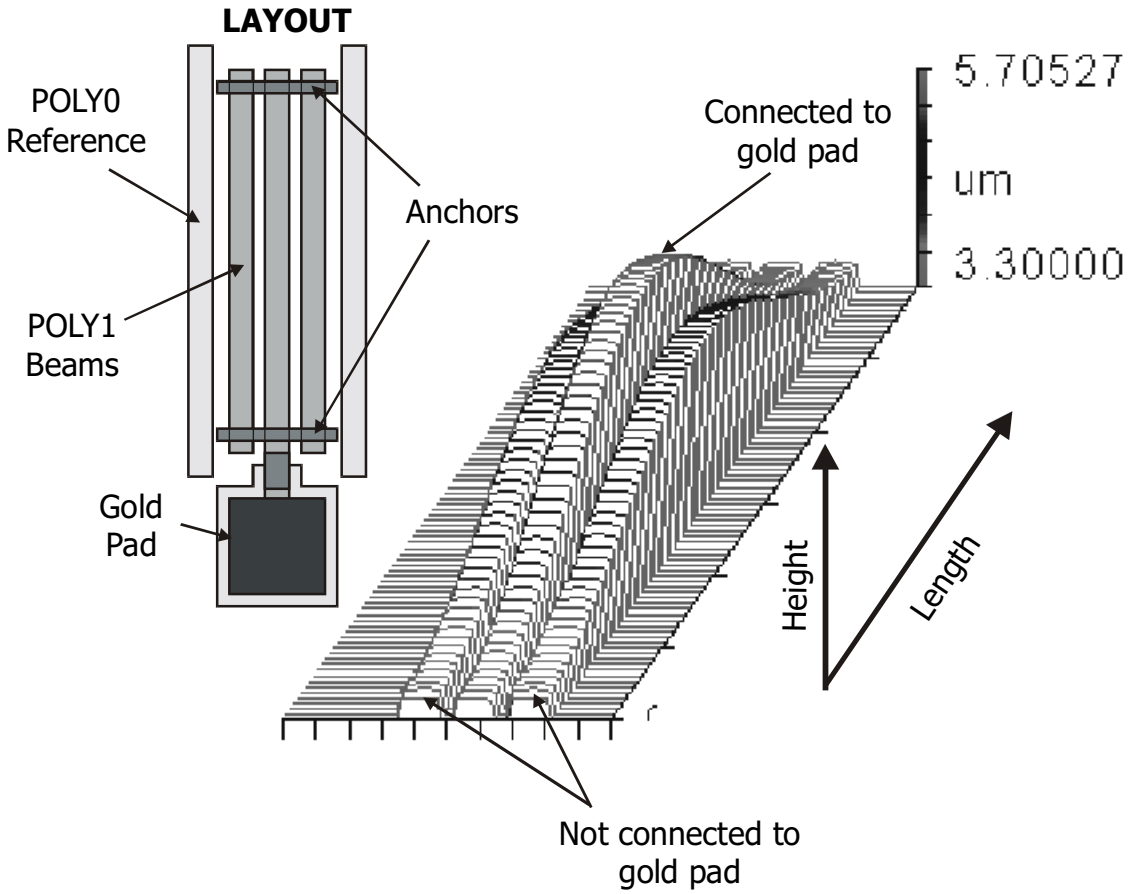

Figure 3-2. Interferometric image of three 700-μm-long fixed-fixed beams, with the center beam connected to a gold pad as shown in the inset layout. That center beam buckles higher than the other two beside it.

Since the influence of gold depends on the ratio of the area of exposed polysilicon surfaces to the area of the gold pad, the influence of gold causes a design-dependent variation in material properties. A beam in an array would have different properties than a lone beam. A short beam would have slightly higher compressive stress than a longer beam. To avoid such beam-to-beam variations in stress or thickness, most of the calibration work in the subsequent chapters is on structures without gold connections.

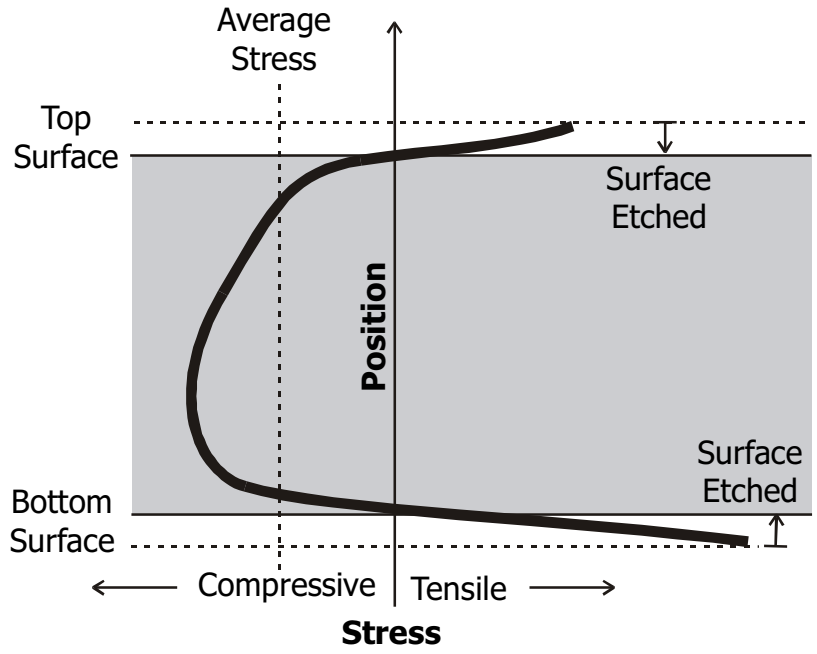

Figure 3-3. Proposed through-thickness stress profile leading to observed behavior of beams before and after the top and bottom surface layers are overetched.

3.6 Additional Nonuniformities

The behavior of the beams also shows a dependence on their widths. Figure 3-1 is an interferometric image of an array of cantilevers of similar lengths but of varying widths, fabricated in MUMPs 25 and released in a 2.5 minute HF etch with critical-point drying. The beams, all without connections to gold, curl down, each with different degrees of curvature, with the exception of the anomalous 10-μm-wide beam which actually curls up. Figure 3-2 shows the longitudinal profiles of the cantilevers more clearly. All the beams have overall downwards deflections due to rotations at the step-up boundaries. The 50- and 70-μm-wide beams appear to curl down near the anchor before curling up slightly near the suspended tips.

In addition, each of the beams exhibits variations in height along its width as shown in the cross-sectional profile of Figure 3-1. The top surfaces of the narrower beams (30-μm-wide or less) are rounded. This roundedness is probably due to uneven etching of the surface during the patterning or release etch rather than due to stress-induced bending. Bending in such a deformation mode – widthwise curling without significant curling along the length – cannot be simulated using isotropic stress gradients.

The wide beams show saddle-like height variations along their widths with rounded ridges near each edge. It is possible that the two ridges of the wider beams coalesce into one mound in the case of the narrower beams.

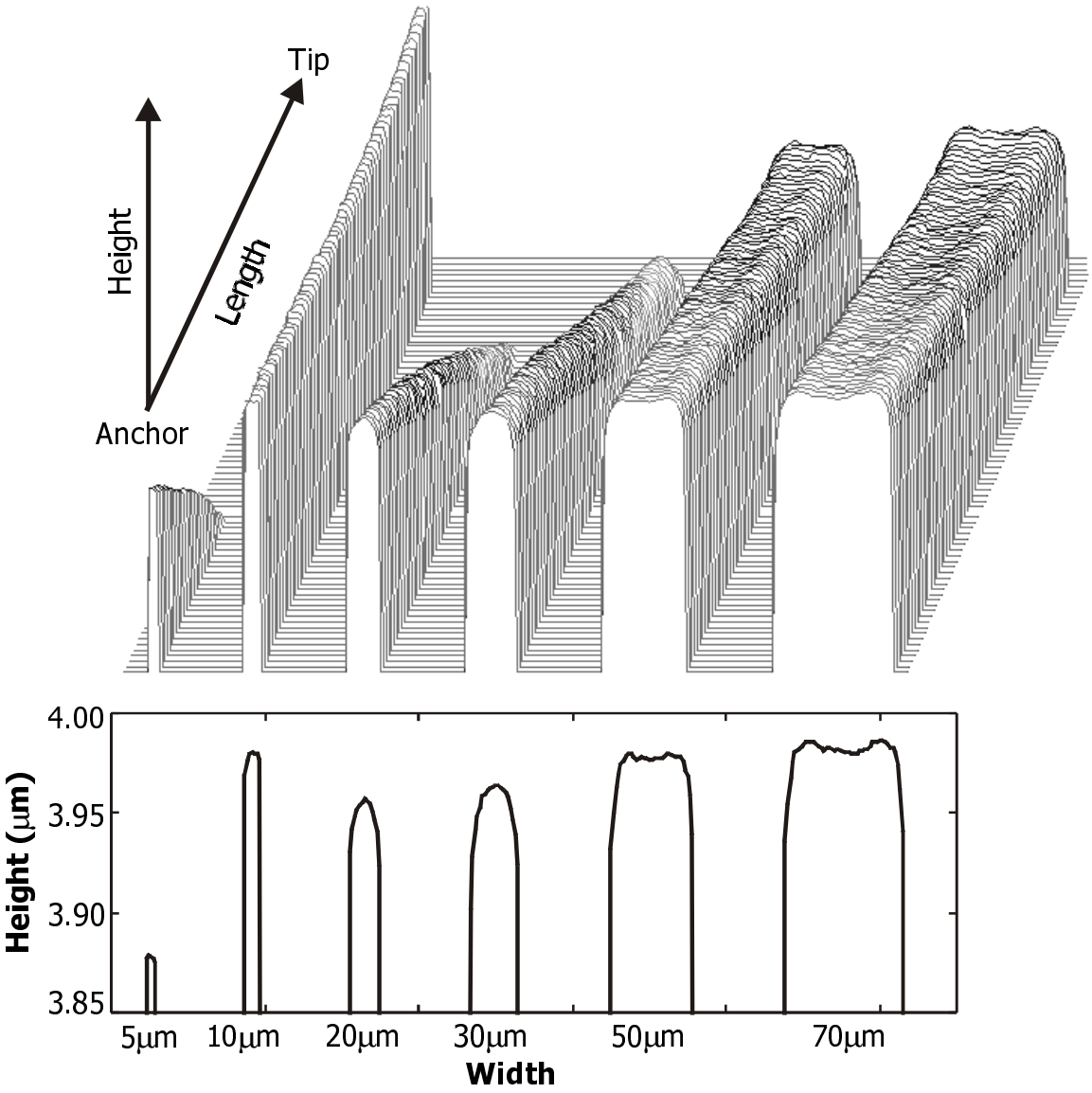

Figure 3-1. Interferometric image of 440-μm-long cantilevers of various widths, showing different degrees of curling, and height variations across the width. Corresponding lengthwise profiles are shown in Figure 3-2. Beams were fabricated in MUMPs 25 and do not have gold connections.

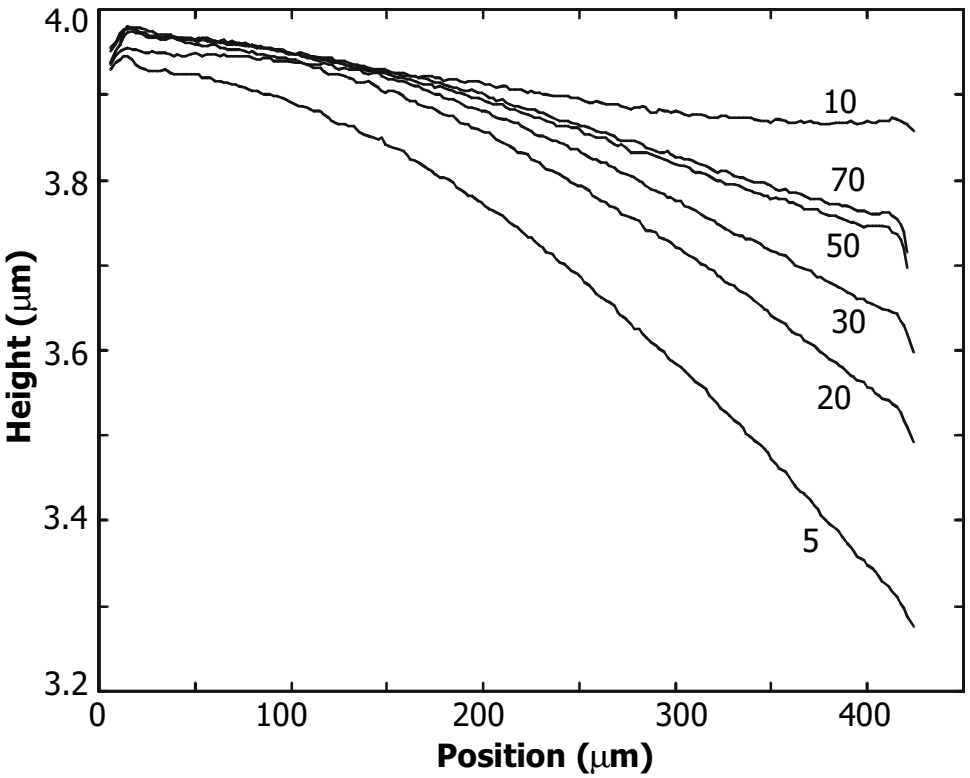

Figure 3-2. Profile of 440-μm-long cantilevers of various widths (as labeled in figure). The beams all have different degrees of curvature, with the 10-μm-wide beam differing from the norm and curling upwards. The overall downward deflection of all the beams is due to rotation at the step-ups. Beams were fabricated in MUMPs 25 run.

Variations due to width among fixed-fixed beams is less pronounced – only the 5 and 10-μm beams stand out as being different in Figure 3-3 which plots the profile of 780-μm-long beams. Since the source of such widthwise variations is unclear, only 30-μm-wide beams are used for the calibration to minimize the effects of non-ideal cross-sections while avoiding the saddle-like height variations. The narrower the beams, the more susceptible the behavior of the beams are to small deviations in the cross-section from an ideal rectangular shape, as evidenced by the large measurement scatter in [64].

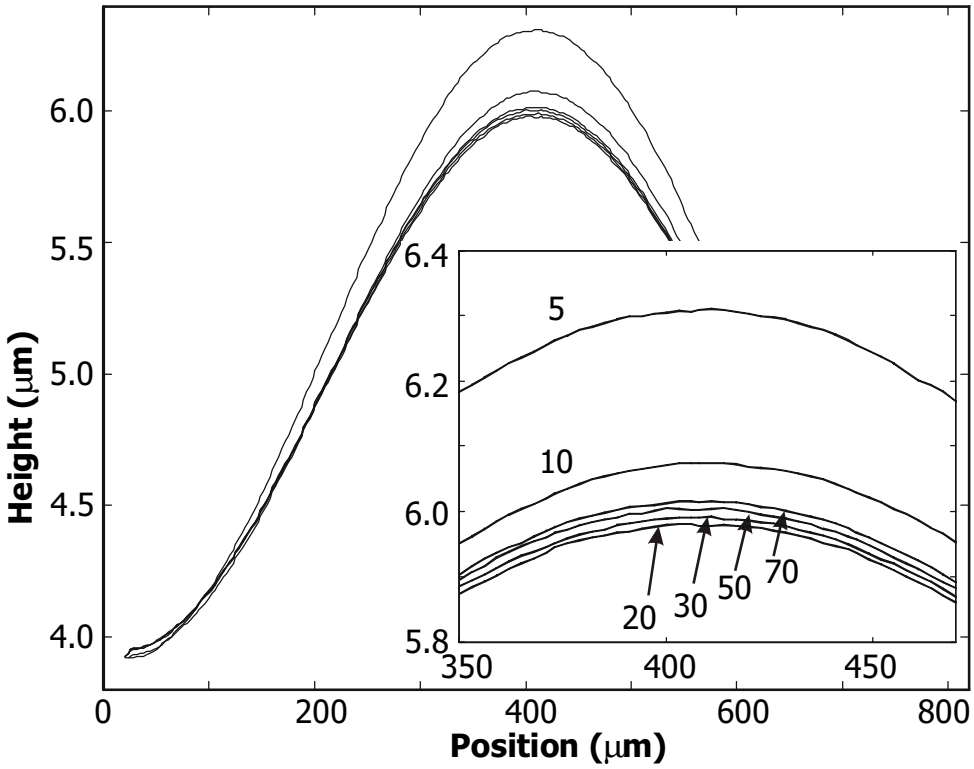

Figure 3-3. Profile of 780-μm-long fixed-fixed beams of various widths (as labeled in the inset). The 5- and 10-μm-wide beams buckle more than the other beams. The rest of the beams behave quite similarly. The inset is a closeup of the centers of the beams. Beams were fabricated in MUMPs 25 and do not have gold connections.

Cantilever beams are more difficult to characterize than fixed-fixed beams because they exhibit more variability. Among 30-μm-wide cantilevers of various lengths, each with a connection to a gold pad, the radii of curvature varies as shown in Figure 3-4. The shorter beams curl up more, presumably because the overetch due to the effect of gold is more significant. Figure 3-1 shows that cantilevers without connections to gold do not have uniform curvature throughout the length of the beam. Cantilevers were not used for parameter extraction because of the lack of uniformity among devices – each unique profile has to be characterized individually.

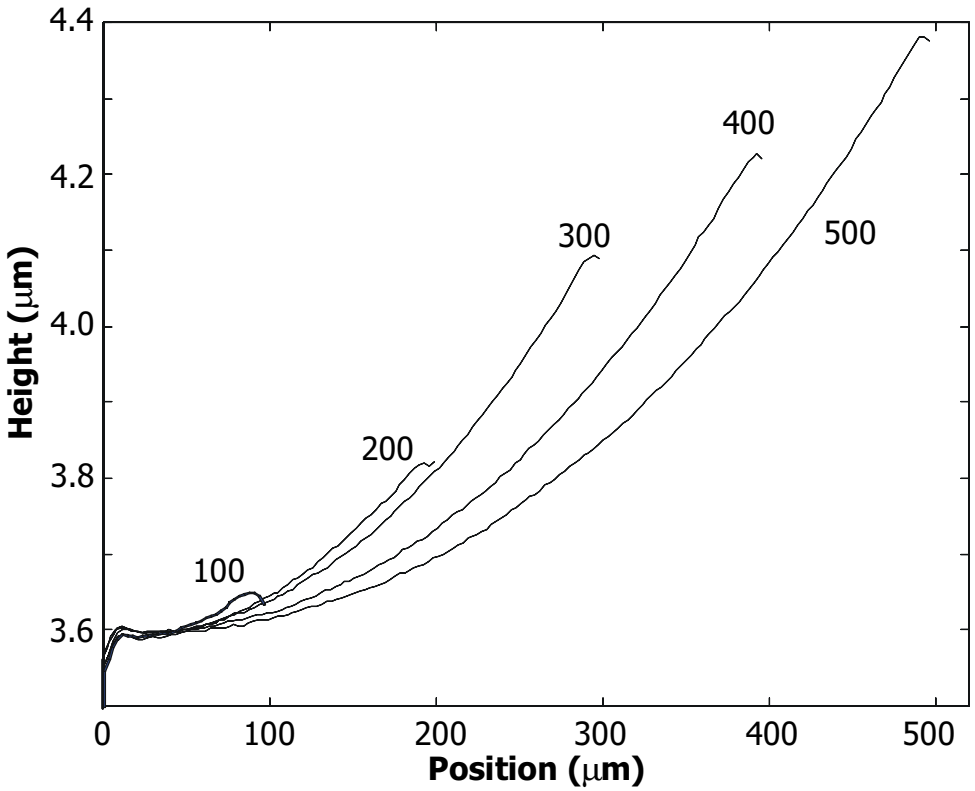

Figure 3-4. 30-μm-wide cantilevers of various lengths (as labeled in figure) showing different radii of curvature. The beams were fabricated in MUMPs 27 and have connections to gold pads.

The SEM of a POLY1 step over a POLY0 pad (Figure 3-2) reveals another interesting feature – a protrusion on the underside of the POLY1. This is probably due to notching in the sacrificial PSG on which the POLY1 was deposited. This sharp protrusion has a significant effect on electrostatic fields and affects electrostatic actuation. This defect was found on only a few beams on a particular die. Such defective structures were avoided.

3.7 Summary

This chapter covered the ground work necessary to obtain good geometrical measurements and defined the scope of characterization to avoid phenomena that is highly variable and difficult to quantify. Methods to obtain the true thickness after overetch, or at least to determine the bounds, were discussed. The effects of gold on thickness and stress that are design and area dependent were presented. A stress profile that explains the observed modifications in behavior due to increased etch rates was

proposed. The presence of gold, and presumably other noble metals such as platinum and copper, will cause single devices to behave differently from arrays of similar structures. Variations in beam profiles with width and length, particularly severe for cantilever beams, were also presented. With that foundation, the next chapter describes a very detailed and careful characterization methodology that produces a well-calibrated and verified simulation model.

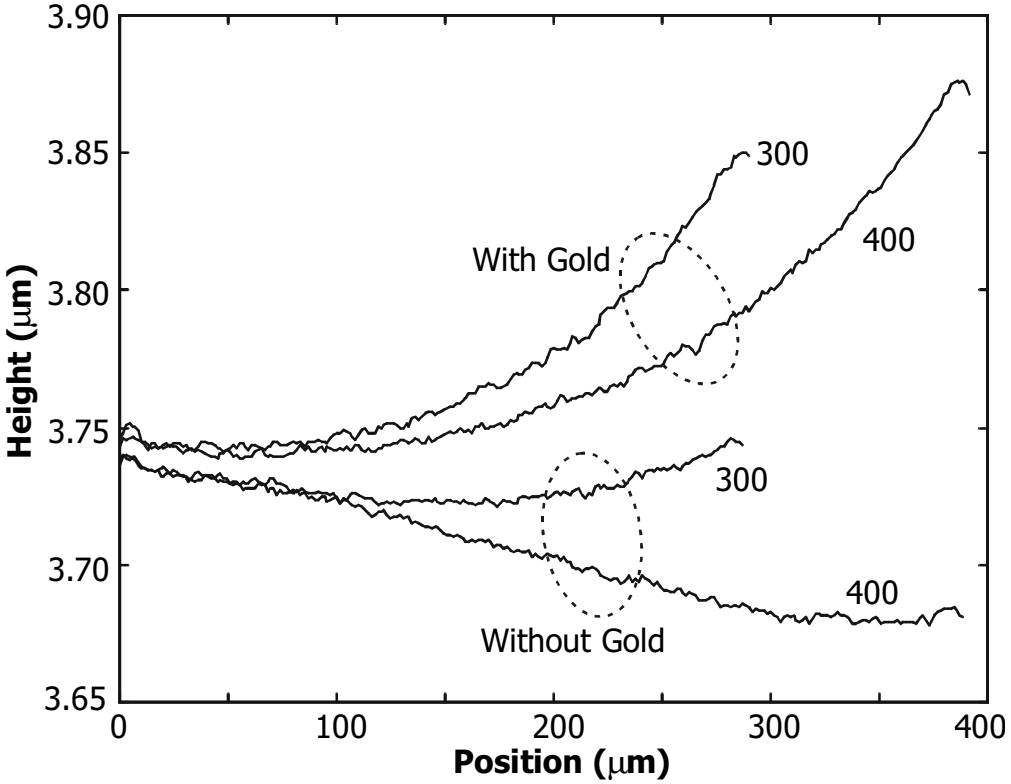

Figure 3-1. Cantilevers fabricated in MUMPs 29. The beams connected to gold curl up more. The 300- and 400-μm-long beams have different curvatures. The beams without gold connections do not have uniform curvatures throughout the length of the beams.

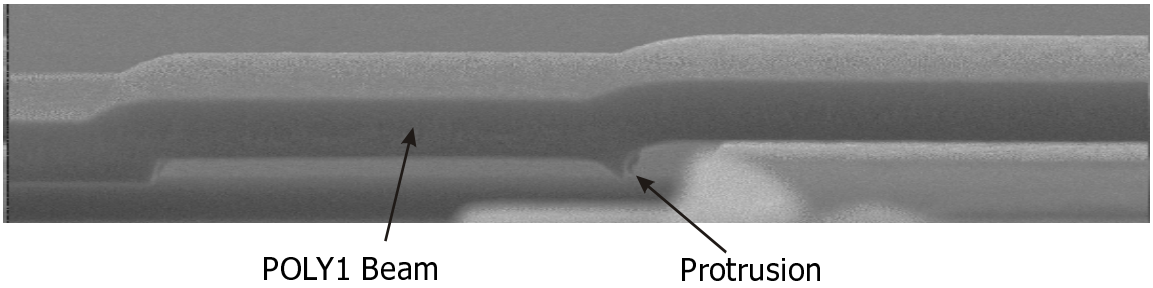

Figure 3-2. SEM of a protrusion at the bottom of a POLY1 beam stepping over POLY0 pad.

Chapter 4 Characterization of Pull-in

4.1 Overview

Using the geometrical dimensions determined in the previous chapter, the characterization procedure continues on to the extraction of material properties, specifically the elastic properties Young's modulus and residual stress. This work unifies two different parameter extraction methods to generate a consistent simulation model calibrated to the MUMPs process. After a brief introduction to parameter extraction methodologies, this chapter describes the design of the test structures used in this study. The characteristics of the 2-D Abaqus simulation model that captures measured behavior accurately over a wide range of beam dimensions are then detailed. Boundary conditions are discussed, particularly the effect of encapsulated PSG in backfilled anchors. Compressive residual stress is extracted first, from measurements and simulations of buckling amplitude, before Young's Modulus is extracted from pull-in voltages. The effects of multiple mechanical discontinuities are discussed subsequently. After some comments on the precision and consistency of these parameter extraction methods, a benchmark verification problem for coupled electromechanical simulators, with a demonstrated accuracy of better than 2%, is presented. Finally, secondary influences on fixed-fixed beam behavior such as stress gradients, substrate curvature and film coverage are investigated quantitatively.

4.2 Parameter Extraction Methods for Silicon

Accurate material property information is crucial to the design of high performance micromechanical devices. Researchers of polysilicon and single-crystal silicon, in particular, have been:

- measuring the vibrations and resonant frequencies of beams and comb drives [65], [66]
- observing the effects of stress on rotating or buckling structures [64], [67]-[69]
- probing beams with mechanical profilers [70], [71]
- measuring displacements under electrostatic forces [30], [34], [72]
- exciting films with ultrasonic surface waves [73]
- performing load-deflection measurements [74]
- performing traditional tensile tests [75]-[76]
- measuring wafer curvature [77]

to determine material properties, primarily Young's modulus and residual stress. Ideally, if all the methods are consistent, one researcher should be able to make the different measurements required by the different methods all on the same die and come up with a unique and universal set of parameters for a single analytic or computational model. This is hindered by the need for specialized measurement equipment, and by the difficulty in fitting all the different test structures onto a single die. In addition, comparisons among the different methods are difficult because each calibration method utilizes a model with its own set of assumptions, requirements, and uncertainties which can be difficult to quantify. Until full 3-D computations become fast and accurate, parameter extraction methods will have to rely on simplified models. Modeling approximations which are essential to making parameter extraction tractable lead to uncertainties in extracted parameters which are often significant enough to preclude authoritative comparisons among calibration results.

Van Drieenhuizen et al. [78] in their review of techniques to measure stress in thin films conclude that rotation or buckling structures are the most suitable. Other techniques are hampered by stress gradients, damping effects and cumbersome

measurement setups. However, the test structures suggested in that publication are still geometrically complicated. In one effort to compare and possibly standardize the characterization of MUMPs polysilicon, researchers at four institutions used different techniques to measure Young's modulus [52]. Sharpe et al. [75] and Knauss et al. [61] used tensions tests whereas Johnson et al. [70] and Brown et al. [65] performed flexural experiments. Measurements were made on dies from the same MUMPs run located close together on the wafer to minimize processing variations. Ultimately, because of uncertainty in modeling assumptions, no convincing conclusions could be reached about the variations in the extracted Young's modulus (from 132 GPa to 174 GPa). Issues of geometry, boundary conditions and metrology were not addressed thoroughly and uniformly. Thicknesses were measured only to within 0.1 μm in some cases. The geometries of some of the test specimens were quite involved, with numerous perforations, notches and narrow comb fingers, necessitating many modeling approximations.

This work unifies two different parameter extraction methods for MUMPs, to generate a consistent and comprehensive simulation model tailored towards the design of micromachined switches. This characterization expands in significant detail, accuracy and scope the suggestions of Zou et al. [72], who also compared results from pull-in voltage and buckling beam measurements, but relied on less-precise models and measurements. In this chapter, the simulation model is calibrated to optical (displacement and buckling amplitude) and electrical (pull-in voltage) measurements concurrently, not independently as in [34] and [64], thus increasing confidence in the extracted parameters. The voltage and displacement measurements are very precise offering good resolution in the extracted parameters as shown in Section 4.7. The detailed 2-D simulation model, which is the model that offers the best compromise between speed and accuracy at this time, captures the behavior of electrostatically actuated beams of a wide range of dimensions and topographies.

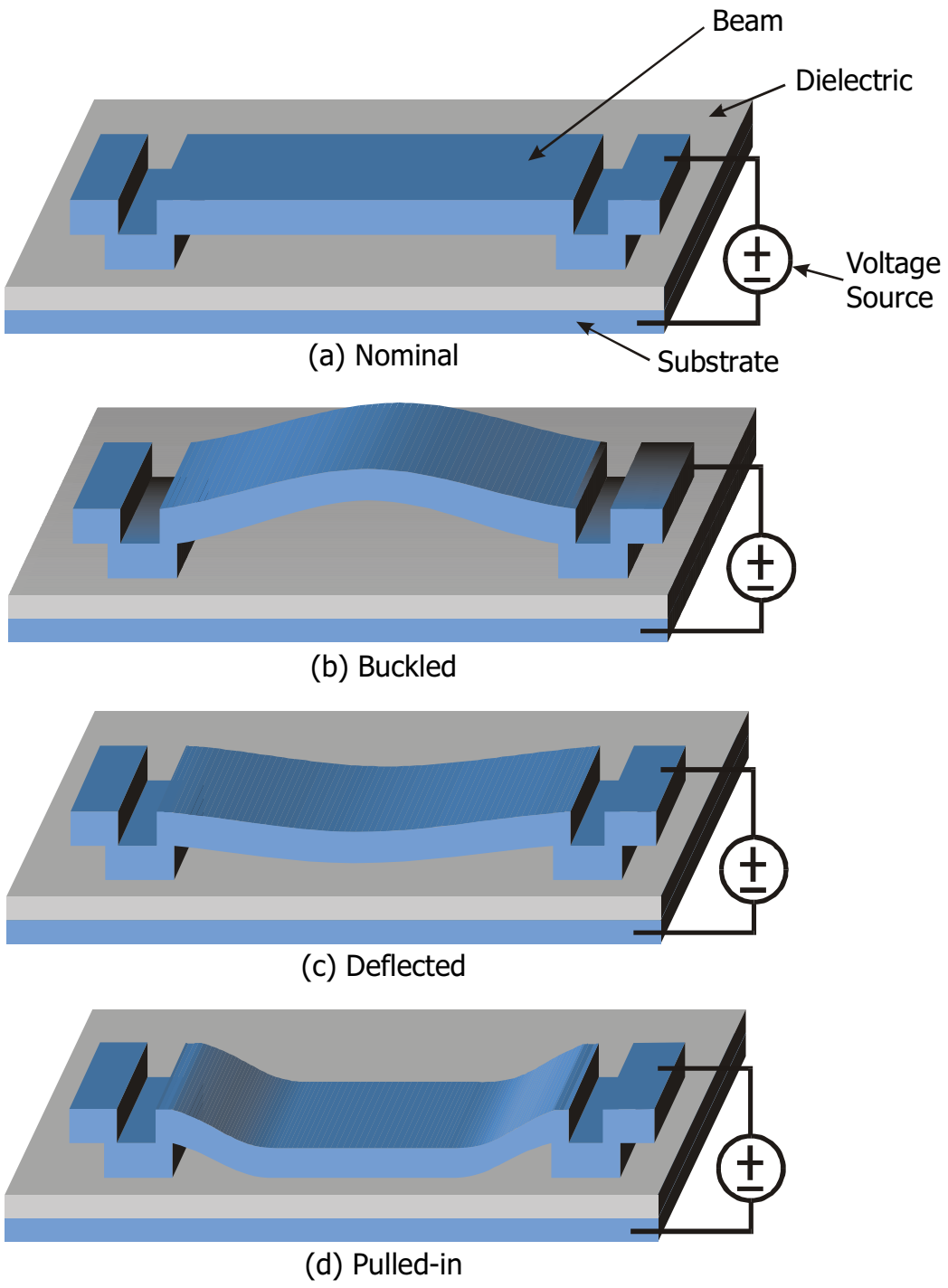

Figure 4-1. Test structures for materials characterization. The beams are essentially extrusions of 2-D profiles. **(a)** Initially flat. **(b)** Buckled due to as-deposited compressive stress. **(c)** Deflected under electrostatic actuation. **(d)** Pulled-in.

4.3 Design of Test Structures

A typical electrostatically actuated beam test structure fabricated in MUMPs is shown in Figure 4-1(a). The test structures are designed to be simple – essentially extrusions of 2-D profiles, in order to match simulations better. The principal set of test structures consists of relatively simple beams without any discontinuities except at the anchors. A critical assumption is that the only parameter or property that varies from device to device, among a given set of devices, is beam length – every other parameter is uniform. No gold pads were connected to the beams to prevent area-dependent nonuniformities as explained in the previous chapter.

The beams are designed to be flat when released as shown in Figure 4-1(a). However, after deposition and anneal, the polysilicon remains slightly compressive and hence wants to expand when the sacrificial PSG is etched away. Hence, beams beyond a certain threshold beam length buckle due to this stress as shown in Figure 4-1(b). This is similar to what happens when a beam is heated up and allowed to expand. When a voltage is applied between the beam and silicon substrate, electrostatic forces distributed along the underside of the beam pull the beam towards the silicon substrate (Figure 4-1(c)). As the beam deflects, the gap between the beam and substrate gets smaller which in turn increases the electrostatic forces. Eventually, this positive feedback mechanism overwhelms the mechanical restoring force and the beam collapses onto the nitride (Figure 4-1(d)). A dielectric sandwich is created by the beam, dielectric and substrate.

Three types of step-up boundary conditions are shown in Figure 4-1. The first one (Figure 4-1(a)) is used for calibration in this thesis because it is essentially an extruded 2-D profile that can be simulated very accurately. This design actually violates standard design rules which require that the anchor trench be completely enclosed by the POLY1 layer as shown in Figure 4-1(b). Obeying the design rules, however, can result in ambiguity in the definition of beam lengths especially if the enclosure lip is wider than the beam as in [30] and [34]. The third design, which encapsulates PSG (Figure 4-1(c)), will be detailed later in this chapter. To minimize the effects of variations related to width as described in the previous chapter, only 30-μm-wide beams are used in this calibration. In addition to the flat beams, beams with multiple mechanical discontinuities (steps) were

fabricated and measured to quantify the effects of these additional discontinuities.. The cross-sections of these beams are shown in Figure 4-2(a) and (b).

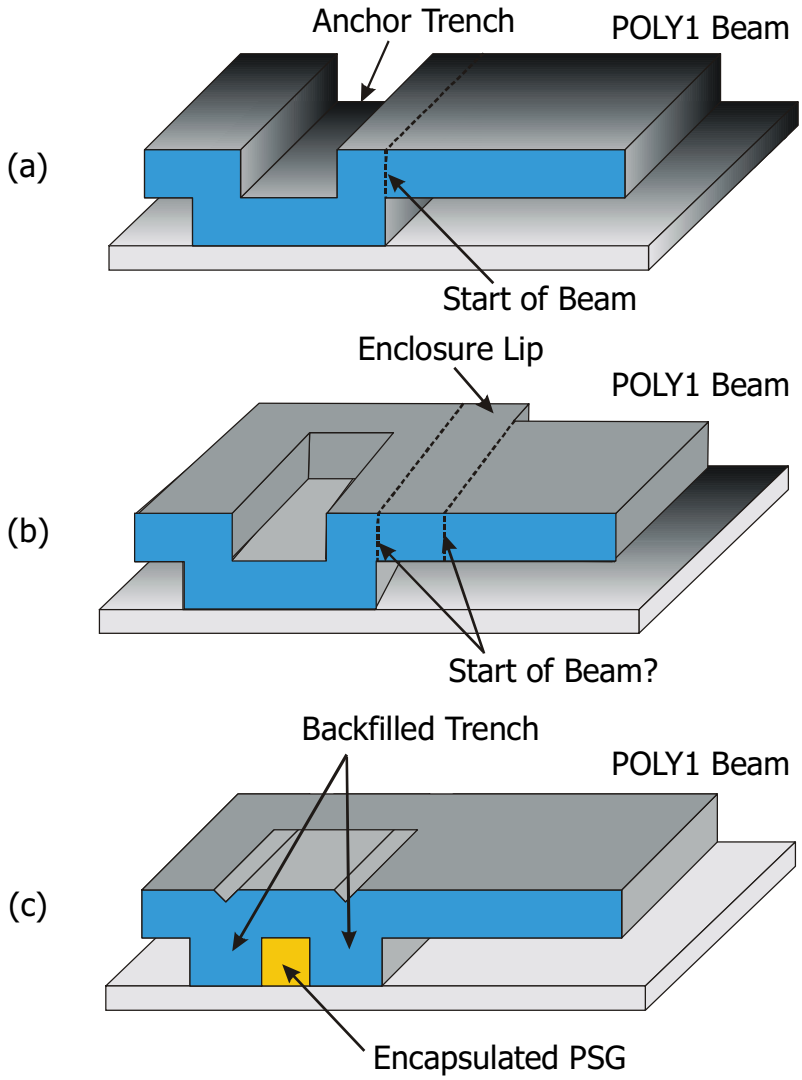

Figure 4-1. Longitudinal cut-away views through the center of the beam of commonly used step-up boundary conditions. **(a)** Extruded 2-D profile. Violates design rules. **(b)** Anchor with POLY1 enclosure lip around trench. Obeys design rules but can cause ambiguity in definition of beam length if enclosure lip is wider than beam. **(c)** Anchor with backfilled trenches and encapsulated PSG to increase the stiffness of the step-up.

The layout shown in Figure 4-3 of several elements of a test structure array show reference levels and tick marks fashioned of POLY0. The tick marks are at every 50 μm along the length of the beam, with a large mark indicating the center of the beam. Polysilicon makes a better reference level for Zygo measurements. It is much easier to consistently image the surface of polysilicon compared to nitride which has poor

reflectivity. This improves the reliability and repeatability of measurements. The tick marks allow measurements of the height of the beam at specific locations along the length of the beam, most commonly at the center of the beam. It is important to be able to make widthwise measurements across the beam rather than just lengthwise measurements because some of the longer beams can extend beyond the range of view of a given microscope objective. Furthermore, interferometric measurements from short cross-sections are less susceptible to the effects of vibrations or misalignments that can show up in large scanned images.

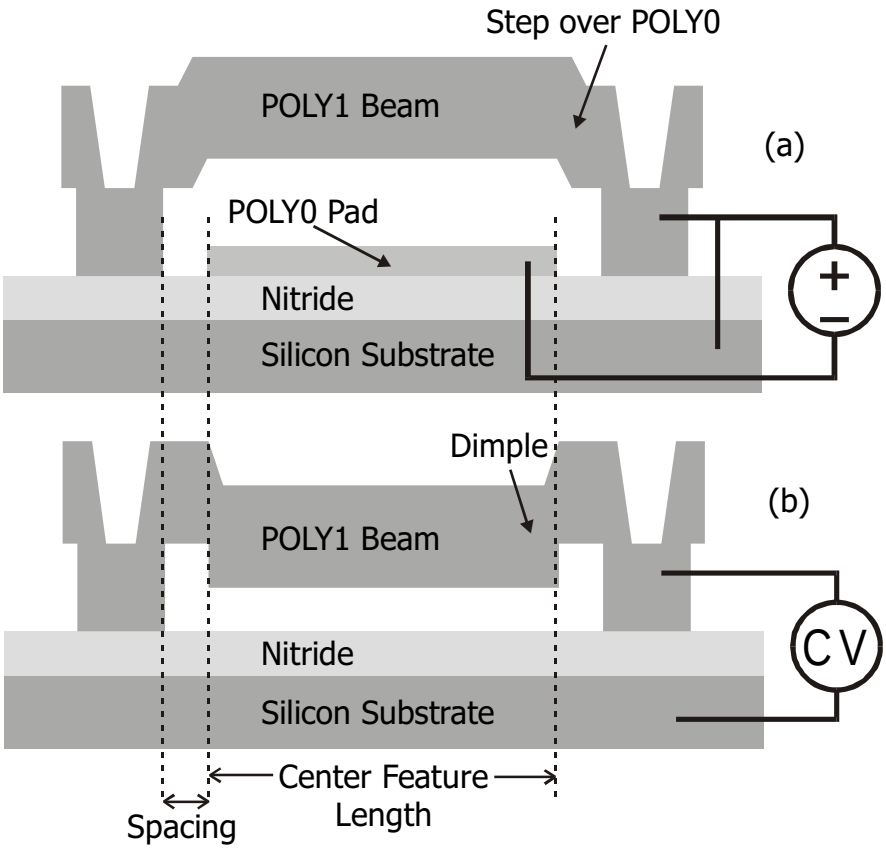

Figure 4-2. Profile of **(a)** beam over POLY0 pad, and **(b)** beam with dimple.

Two of every test structure were fabricated on a single chip for redundancy. The average of the two measurements are used unless one measurement is clearly erroneous. The MUMPs 29 dies were released in a short 1.5 minute HF etch and subsequently treated by the supercritical carbon dioxide drying process. All measurements discussed were on a single die on this MUMPs 29 run unless noted otherwise.

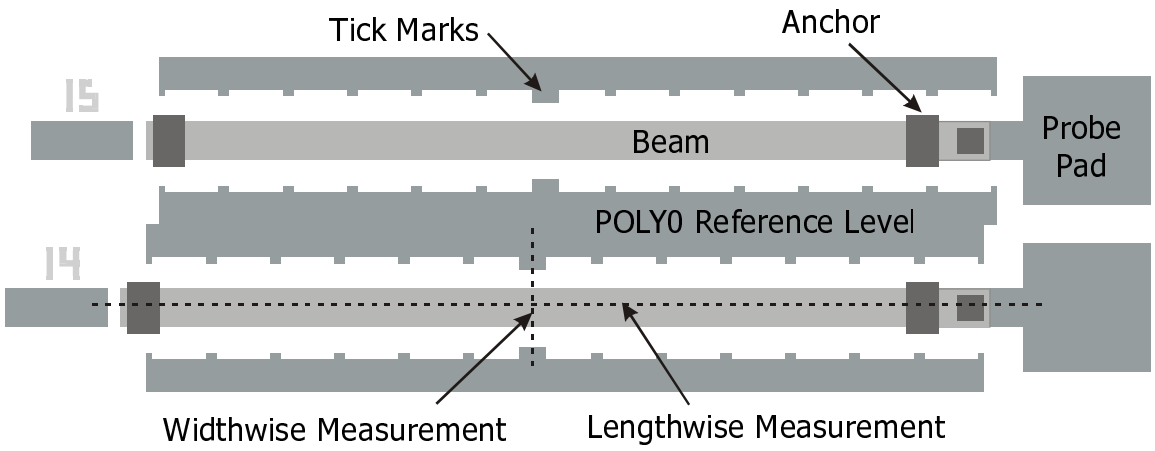

Figure 4-3. Layout of typical test structures. The beams are surrounded by POLY0 structures that serve as reference levels for the Zygo surface profiler. Tick marks are placed every 50 μm, with a wider mark indicating the beam center. This allows accurate widthwise as well as lengthwise measurements.

4.4 Abaqus 2-D Model

A 2-D Abaqus [17] simulation model is shown in Figure 4-1, highlighting the geometry of the step-up anchors and other mechanical discontinuities which correspond to the SEMs of Figure 3-4 and Figure 3-5. The rounded edge of the top of the step-up due to conformal deposition, and the sloping edge of the bottom of the step-up and dimple due to overetch are modeled. Currently, full 3-D simulations consume enormous computing resources, taking two to three orders of magnitude more time than 2-D simulations, making them infeasible for parameter extraction procedures which require the solutions of many variations of a given system of materials and parameters. 2-D models offer the best tradeoff between accuracy and speed at this moment. The input deck for the 2-D model, an example of which can be found in Appendix B, serves as an unambiguous repository of geometrical and material property information to be used by design engineers. As mentioned in Section 2.6, the Abaqus model captures all the mechanics accurately, incorporating the effects of stress stiffening, large rotations and compliant step-ups, making this extraction methodology wider in scope and more precise than others using quasi-2-D finite-difference models [30], [34] or analytic models [64], [72]. Furthermore, this model supports the analysis and simulations of post-buckled

structures, and contact. Stress gradients can be included but are neglected here because they have negligible impact, as detailed in Section 4.9.1

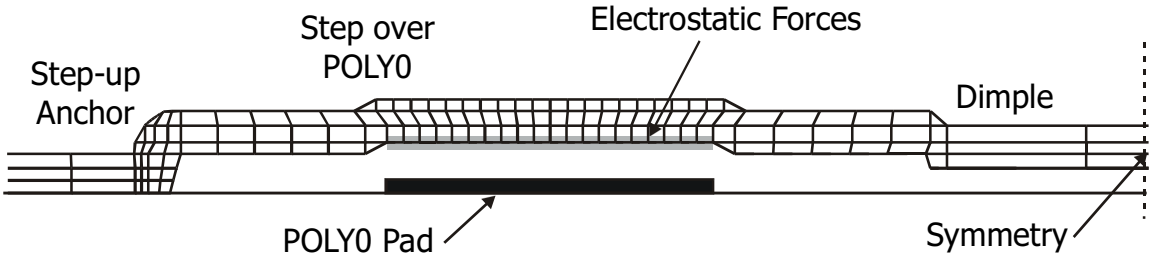

Figure 4-1. 2-D Abaqus model of a beam, capturing the essential features of the step-up anchor, the step over POLY0, and the dimple. Electrostatic forces are applied to the region of the beam directly above the POLY0 pad.

Electrostatic forces are applied to the bottom surfaces of the beam as user-defined loads as described in Section 2.5. For beams actuated by applying a voltage between the beam and silicon substrate, the electrostatic load is applied to the entire underside of the released portion of the beam. For beams actuated over POLY0 pads, the electrostatic force is applied only to the portion of the underside that is directly above the POLY0 pad as explained in Section 2.5 and shown in Figure 4-1. Poisson's ratio is assumed to be 0.23. The variation in fixed-fixed beam behavior as Poisson's ratio was varied between 0.15 and 0.35 was simulated and found to be negligible.

4.5 Calibration to Flat Beams

The fixed-fixed beams with no additional discontinuities besides the step-up anchors are characterized first. These beams will be referred to as "flat beams" from now on.

4.5.1 Buckling Amplitude

The POLY1 layer in MUMPs is deposited slightly compressive. As a result, beams fabricated in POLY1 tend to deform to relieve some of that stress. Equation (4-1) is an analytical expression for the buckling amplitude (displacement of the beam center) of fixed-fixed beams

$$u_{\max} = \sqrt{\frac{4\alpha L^2}{\pi^2} - \frac{k}{3}t^2}\ . \tag{4-1}$$

k is a constant that depends on boundary conditions, α is the initial (pre-buckled) strain, L is beam length, and t is beam thickness. k varies from 4 for beams with ideally clamped ends to 1 for beams with pinned boundary conditions. Equation (4-1) was derived assuming sinusoidal or cosinusoidal first buckling modes only, with all additional strain beyond the critical buckling strain contributing to buckling amplitude [79], [80]. The critical beam length for buckling is the value of L beyond which the term in the square root of (4-1) is positive, giving a real number for u_{max}. This critical length is the same as that derived using a slightly different approach in Section 2.3.

In contrast to the ideal case where deflection occurs only beyond a threshold buckling beam length, beams with step-up anchors begin to bow even at shorter lengths. This is shown in Figure 4-1 where the measured transition from the pre-buckled to the post-buckled state is not abrupt. Since the buckling amplitude depends strongly on initial strain but not at all on Young's modulus, the strain parameter can be extracted by fitting Abaqus simulations to the measured buckling amplitudes for various beams.

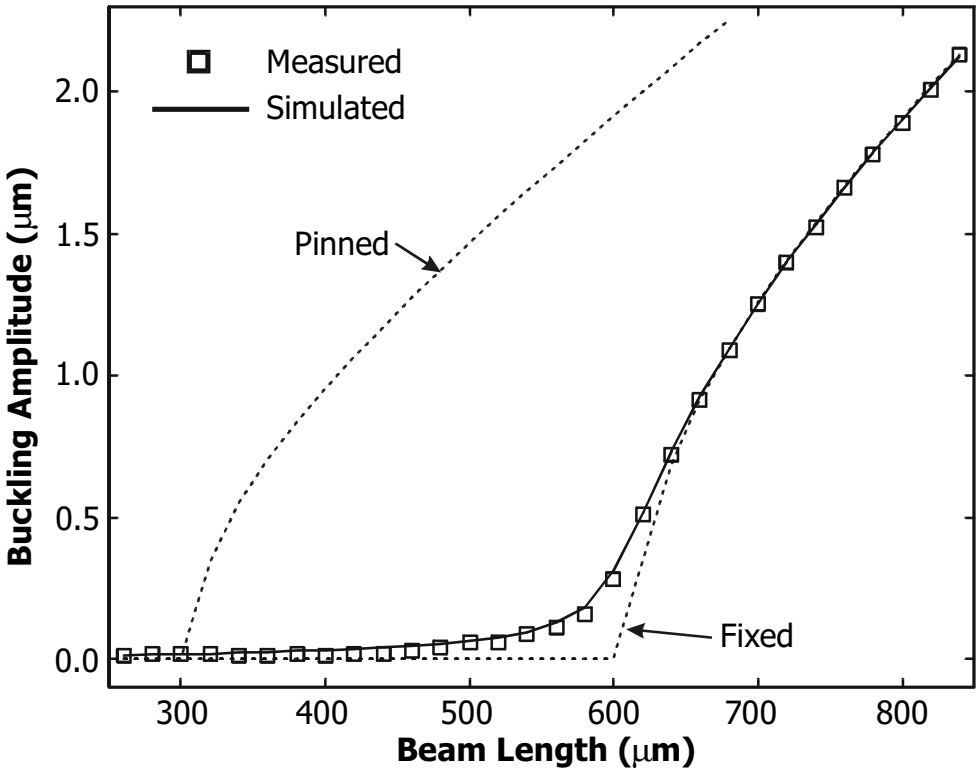

Figure 4-1. Measured and simulated buckling amplitudes of fixed-fixed beams of various lengths. The dotted lines are solutions from (4-1) for ideally pinned and ideally fixed boundary conditions.

The buckling amplitude measurements were made with the Zygo profiler using POLY0 as the reference level. Using a strain, α, of 3.40×10^{-5} in the Abaqus model gives the best fit to the measured data. The excellent fit capturing the gradual transition from the pre-buckled to the post-buckled state indicates that the other two parameters critical to buckling amplitude – boundary conditions and beam thickness – are modeled accurately from interferometric measurements and SEMs. For comparison, the analytic expression (4-1) gives the two dotted lines for $k = 4$ (ideally fixed ends) and $k = 1$ (pinned ends) using the extracted strain value. The step-up anchor closely resembles an ideally fixed boundary condition.

Beams with boundary conditions that have the POLY1 enclosure of the anchor as required by design rules (Figure 4-1(b)) behave quite similarly to beams that are strictly two-dimensional extrusions (Figure 4-1(a)). However, if the enclosure lip is much wider than the beam, the effective 2-D length of the beam would be rather ambiguous. Beams with backfilled anchors (Figure 4-1(c)) buckle downwards instead of upwards, and with larger amplitudes than beams with conventional stepups (Figure 4-1(a)). These anchors were proposed to reduce the compliance of the step-up [81]-[82]. However, the pressure exerted at the anchor by the encapsulated PSG forces the beam downwards as shown in the simulation model of Figure 4-2. A good fit to measurements, shown in Figure 4-3, is obtained using a compressive strain of 2.0×10^{-3} for the trapped PSG. In comparison, the strain in the POLY1 layer for this particular MUMPs run (MUMPs 25) is only $4.20\times10^{-5.}$ The strain value is only approximate because the simulation model is in 2-D whereas in reality the PSG is boxed in on all sides in 3-D. It is also difficult to accurately base this step-up anchor model on a SEM as lateral dimensions are difficult to determine to better than 0.05 μm. As noted earlier, this highly compressive PSG also forces the top surface of the POLY1 encapsulating it to rise about 0.01 μm higher than the surface of a POLY1 layer without PSG underneath. The Young's modulus for the polysilicon and PSG were assumed to be 140 GPa and 70 GPa, respectively, for the simulation.

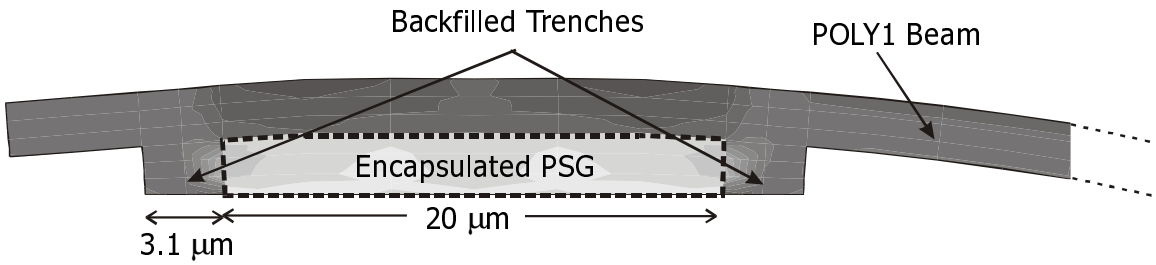

Figure 4-2. 2-D Abaqus model for backfilled anchor. The PSG expands against the POLY1 encapsulation and forces the beam to deflect downwards.

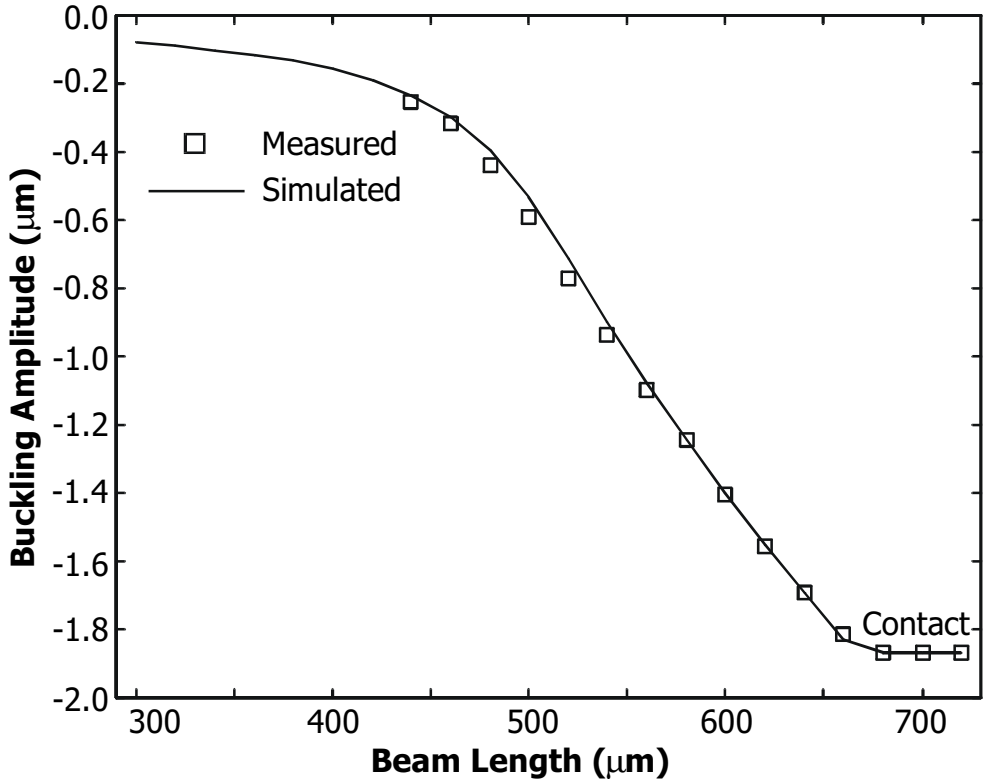

Figure 4-3. Buckling amplitude of beams with backfilled step-up anchors. Measurements were made on dies from MUMPs 25. Beams have connections to gold.

4.5.2 Pull-in Voltage

The next calibration is to pull-in voltages – the voltage required to pull a beam down beyond the point of instability onto the underlying layer. Figure 4-1 shows pull-in voltage as a function of beam length on a log-log scale for beams up to 520 μm long. Measurements were made using 3 different methods, all requiring electrical connections to the beam and substrate as shown in Figure 4-1(a). Electrical measurements must be

taken with care to avoid affecting substrate curvature and hence buckling amplitudes as described further in Section 4.9.2. The first measurement method utilizes an HP4275A LCR meter to apply a bias voltage and to sense the capacitance between the beam and substrate. At pull-in, the beam contacts the nitride and creates a large capacitance which is easily detected as an abrupt transition on a capacitance-voltage plot as shown in Figure 4-2. The second method is to actuate the beam with a voltage source (Tektronix PS5010 Programmable Power Supply) under the Zygo interferometer and observe the changes in optical fringes at the pull-in transition. The third technique employs an HP4155A Semiconductor Parameter Analyzer to source a small constant 20-pA current and sense the voltage on the beam. The current charges up the beam-substrate capacitor and increases the voltage on the beam. At pull-in, the capacitance increase abruptly and the voltage of the beam has to decrease momentarily due to charge conservation. All three methods give very similar results, with no systematic differences. The latter two measurement methods confirm that the 50 mV ac signal from the LCR meter does not cause resonance excitation that might affect the accuracy of the measurements.

Measurements were made using both positive and negative bias voltages to determine the effects of remnant or residual charge which offset voltage measurements as introduced in Section 2.3. Theoretically, the positive and negative V_{pi}'s should be of the same magnitude in the absence of remnant charge since the electrostatic force is proportional to the square of the applied voltage. Taking the average of the positive and negative measurements showed that the offset is less than 0.2 V for all the beams and hence is not a significant source of error. A more thorough description of residual charge is given in Section 5.2.2.

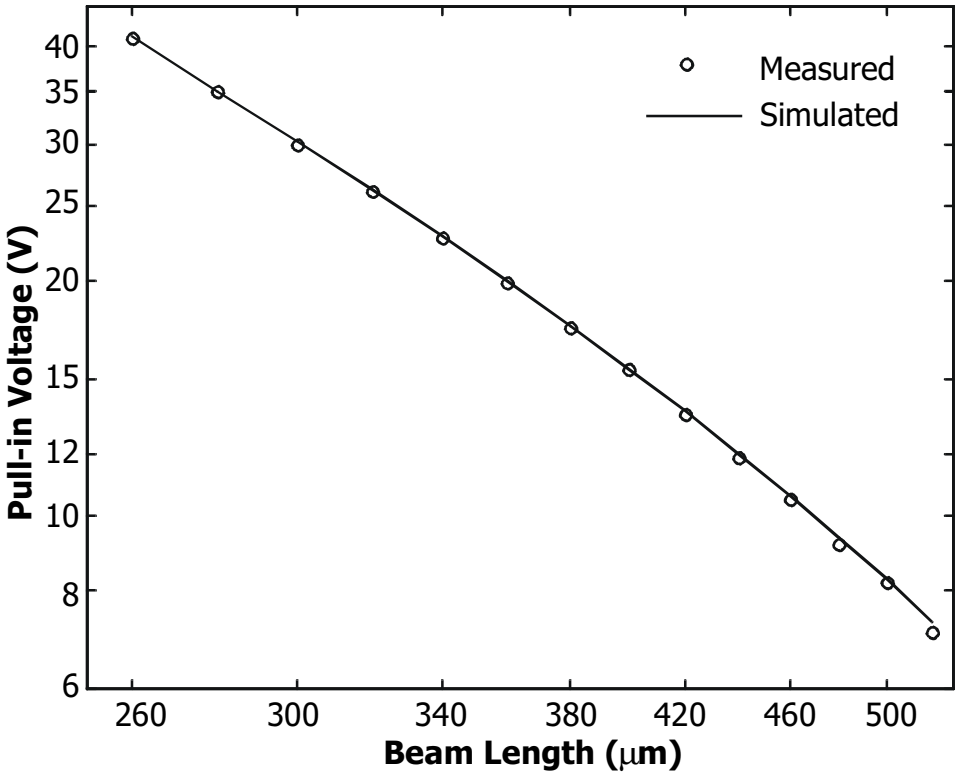

Figure 4-1. Log-log plot of the pull-in voltages of beams up to 520 μm long. The slope of the plot at any beam length is an indicator of the relative contribution of residual stress and bending stiffness to the overall stiffness of the beam.

The pull-in voltages decrease with increasing beam length. The magnitude of the slope at any point on the log-log curve provides an easy measure of the relative contributions of stress and bending stiffness to the overall stiffness of the beam. Semi-analytic expressions [30], [34], and numerical experiments for V_{pi} as a function of the lengths of fixed-fixed beams show that the magnitude of the slope should be two for stress-free beams dominated by bending stiffness, less than two for beams in tension and larger than two for beams in compression. This assumes ideally clamped boundary conditions. The more the slope deviates from two, the larger the influence of residual stress on the beam's overall stiffness. Hence, the slopes at the longer beams lengths are larger for these compressively stressed beams because the behavior of longer beams tend to be more heavily dominated by residual stress. For these measurements, the slope is 2.17 at 280 μm whereas the slope is 3.16 at 500 μm. Since the curve on the log-log plot is practically straight, only two parameters can be extracted with any confidence from V_{pi}

measurements, and only two measurements are needed if measurement noise is not a factor.

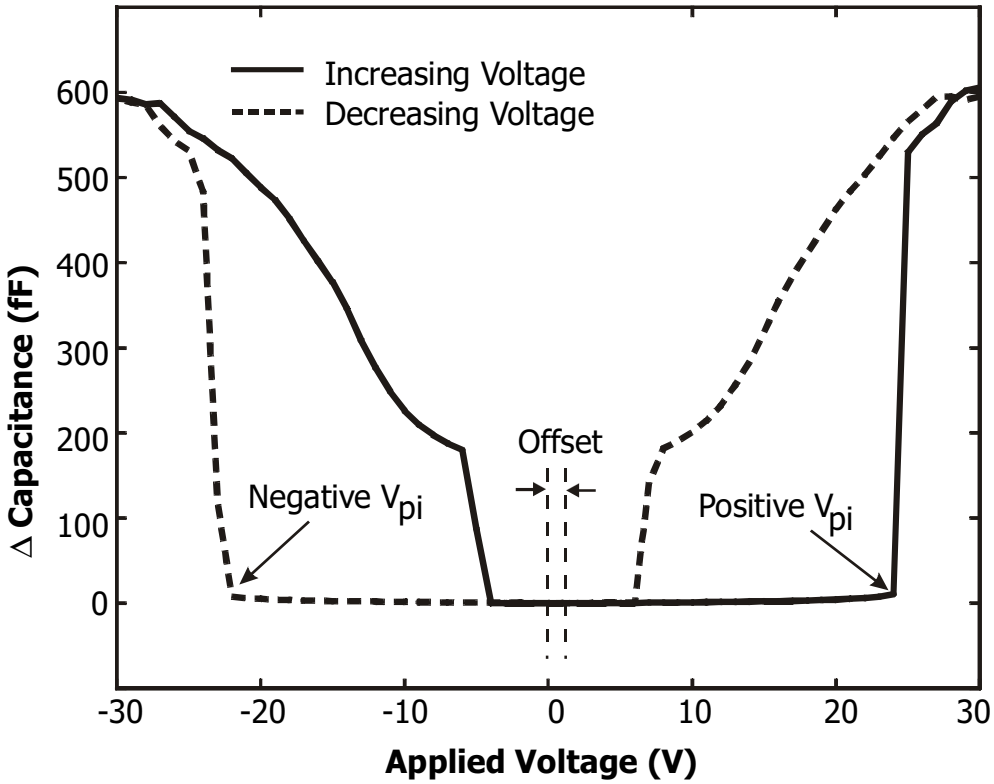

Figure 4-2. Capacitance-voltage (C-V) measurement of a fixed-fixed beam, showing positive and negative pull-in voltage measurements, and the offset voltage due to accumulated charge. The offset shown here is large because the beam is in contact with the nitride for a significant time as the voltage is swept from –35 V to +35 V and back to –35 V.

For beams longer than 620 μm, the pull-in voltage begins to rise with beam length as shown in the linear plot of Figure 4-3. The curve of buckling amplitude as a function of beam length also plotted in the same figure indicates why this happens. As the buckling becomes significant, the initial gap increases thus requiring higher voltages to pull the beam down since electrostatic forces are inversely proportional to the square of the gap. A Young's modulus of 140 GPa and an expansion coefficient, α, of 3.45×10^{-5} produce the simulated curves shown in Figure 4-1 and Figure 4-3. The simulation fit is excellent, with the kink at 620 μm captured accurately. This value for α is consistent with that determined from buckling amplitudes alone. The resultant uniaxial compressive stress in a beam due to this expansion coefficient and Young's modulus is 4.8 MPa and the resultant biaxial stress is 6.3 MPa. The extracted Young's modulus is similar to what

was obtained by Sharpe et al., Knauss et al., and Brown et al. in the MUMPs round robin publication [52] but lower than that obtained by Johnson et al. [52] and Gupta [34].

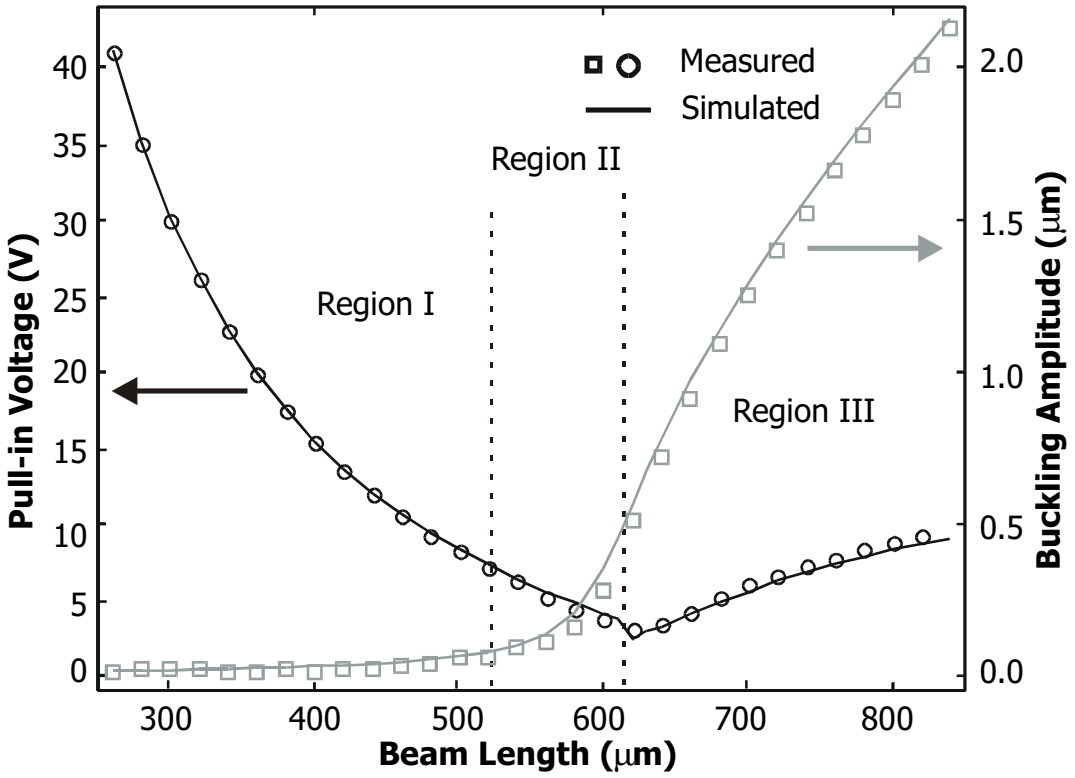

Figure 4-3. Pull-in voltages (left axis) of flat beams as a function of beam length, on a linear scale. Post-buckled behavior is captured by the simulation model. The behavior of beams in the three regions are elucidated in Figure 4-4. A plot of buckling amplitudes (right axis) is superposed. Young's modulus and strain were chosen to fit *both* the V_{pi} and buckling amplitude measurements well.

The three types of pull-in behavior corresponding to the three regions in Figure 4-3 are shown in Figure 4-4. Both displacement-voltage measurements and simulations are shown. A short beam in Region I will deflect continuously with increasing voltage until the gap decreases to about 0.9 μm (half the initial gap) then snap down to the nitride dielectric. The beam can travel more than the one-third of the gap predicted from simple theoretical calculations because of stress-stiffening. A longer beam in Region II that has an initial buckling displacement deflects continuously then snaps down to a stable state below the zero-displacement position. From there, it continues to deflect with increasing voltage before finally snapping down again, this time contacting the underlying nitride. After the first snap-through, the fact that buckling increased the initial gap is not significant anymore; hence the V_{pi}-length behavior continues along the same trajectory as

in Region I. This two-step pull-in does not occur for longer beams in Region III because there is no stable state below zero-displacement at the transition voltage, so the beams snap down all the way to the nitride. In contrast to beams in the first two regions, beams exhibiting this third type of behavior have pull-in voltages that increase with beam length because the gap throughout actuation is affected by the initial buckling amplitude. With the additional dependence of effective gap on initial stress, the pull-in voltages of these post-buckled beams are more sensitive to initial stress than the pull-in voltages of shorter beams. The slightly poorer simulation fit in Region II and III could be due to changes in substrate curvature due to probe pressure as discussed further in Section 4.9.2.

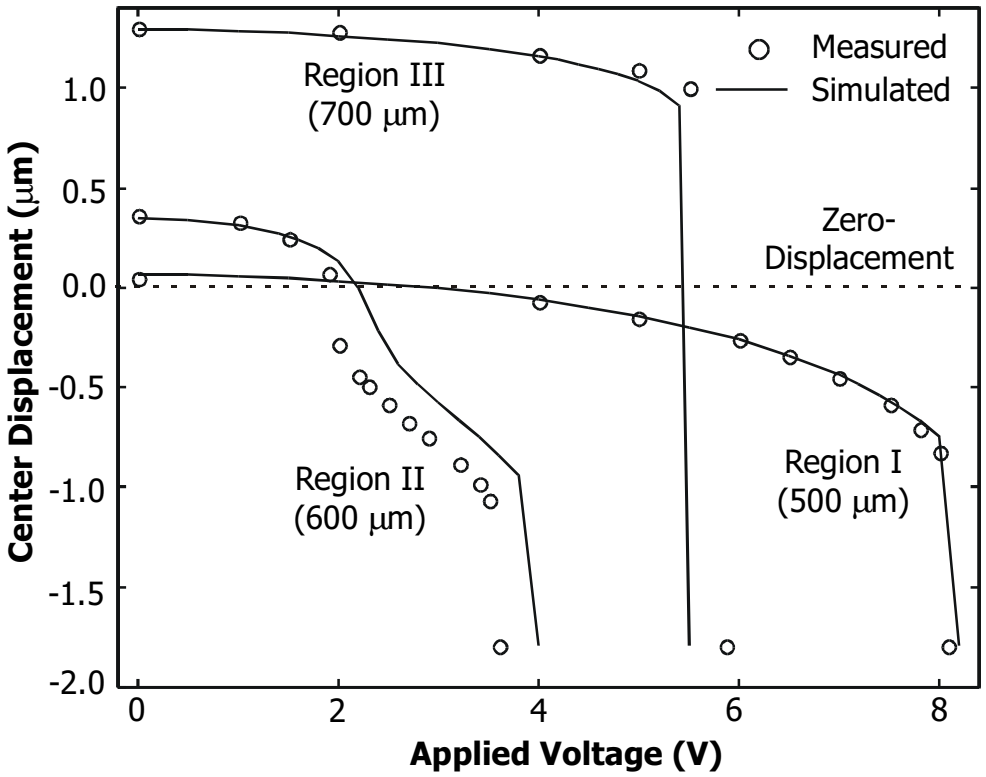

Figure 4-4. The distinct pull-in behaviors of beams in the three regions demarcated in Figure 4-3.

4.6 Calibration to Beams with Multiple Discontinuities

Beams fabricated out of conformal polysilicon can have dimples, and steps over POLY0 layers. Test structures with electrical connections as shown in Figure 4-2(a) and (b) were measured to examine the effects of these discontinuities. Once again, pull-in voltages and buckling amplitudes of beams of various lengths were measured. The pull-in

voltages of beams with dimples were measured using the HP4275A LCR meter whereas the pull-in voltages of beams over POLY0 were measured using the HP4155A Semiconductor Parameter Analyzer. When pull-in occurs for beams over POLY0, direct conductor-to-conductor contact is made and dc current will flow. This is usually a destructive measurement since fusing often occurs. Setting current compliance either on the HP4155A or by using a large resistor in series does not prevent fusing because the large current loops form at the contact surface between the beam and the POLY0 layer. The capacitor discharges locally at the contact surface when pull-in occurs, not through the external electrical circuit. On the other hand, pull-in can be difficult to determine if the beam discharges when it contacts the POLY0 pad and then pops back up. Therefore, the HP4155A measurements were confirmed by measurements on the second set of devices on the same die using a voltage source to actuate the beams under the Zygo. That way, the deflection of the beam can be observed continually until the first instance of pull-in instability.

V_{pi} and buckling amplitude are plotted as functions of beam length for beams over POLY0 in Figure 4-1 and for beams with dimples in Figure 4-2. The POLY0 or dimple features are spaced 20 μm from each anchor. The beams over POLY0 behave quite similarly to flat beams. The total effective gap is slightly smaller due to the absence of the nitride dielectric, resulting in marginally lower pull-in voltages. The transition in buckling amplitudes from the pre-buckled to post-buckled states is more gradual and begins earlier because of the increased compliance due to the additional step discontinuities. The amplitudes for longer beams are also slightly smaller. The same three regions of pull-in behavior are observed. The simulated V_{pi}'s agree closely with measured values but the simulated buckling amplitudes are slightly higher. The simulation model could not fit the measured buckling amplitudes even if the compliance of the step over POLY0 were modified arbitrarily. Since that step is the only modification to the previous simulation model for flat beams, this seems to indicate that the stress state of the beams over POLY0 pads are lower than beams over nitride by almost 0.3 MPa (uniaxial stress), possibly due to some processing-related effect.

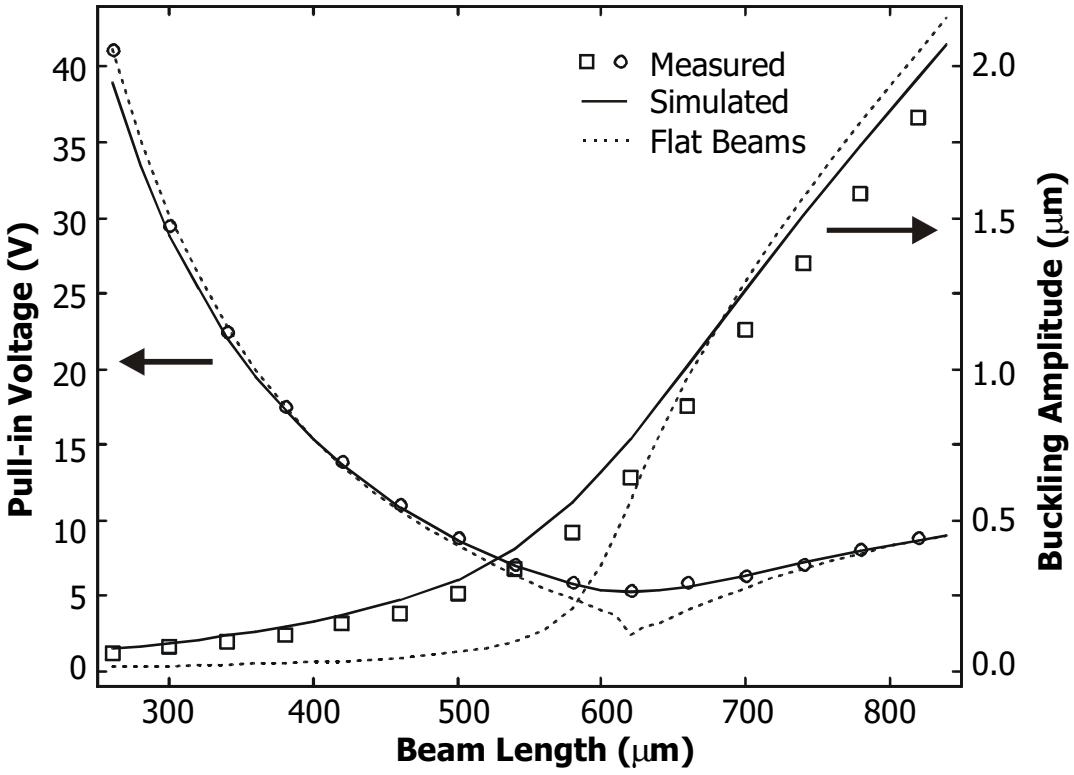

Figure 4-1. V_{pi} (left axis) and buckling amplitude (right axis) as a function of beam length, for POLY1 beams over POLY0. Simulated values for flat beams are indicated by the dotted lines for comparison.

On the other hand, the characteristics of beams with dimples deviate rather significantly from those of flat beams. The dimples cause the beams to buckle downwards systematically instead of upwards. Therefore, the post-buckled pull-in voltages do not rise with beam length but instead go to zero once the beams buckle into contact with the nitride. Similar to the beams over POLY0, the transition from pre-buckled to post-buckled states is more gradual and occurs earlier than for flat beams. The V_{pi}'s are lower compared to flat beams of similar length because the effective gap is smaller by the dimple depth. The measured dimple depth of 0.67 μm was used in simulations and gave a reasonably good fit as shown in Figure 4-2. A depth of 0.68 μm gives a slightly better simulation fit, decreasing the V_{pi} for the 220 μm beam, for example, from 31.1 V to 30.7 V which is closer to the measured value of 30.4 V. It is possible that the dimple etch of the PSG creates a rough PSG surface which then becomes the mold that creates some asperities on the underside of the POLY1 beam.

These asperities or small, sharp protrusions can reduce the effective electrical gap between the POLY1 beam and the silicon nitride surface.

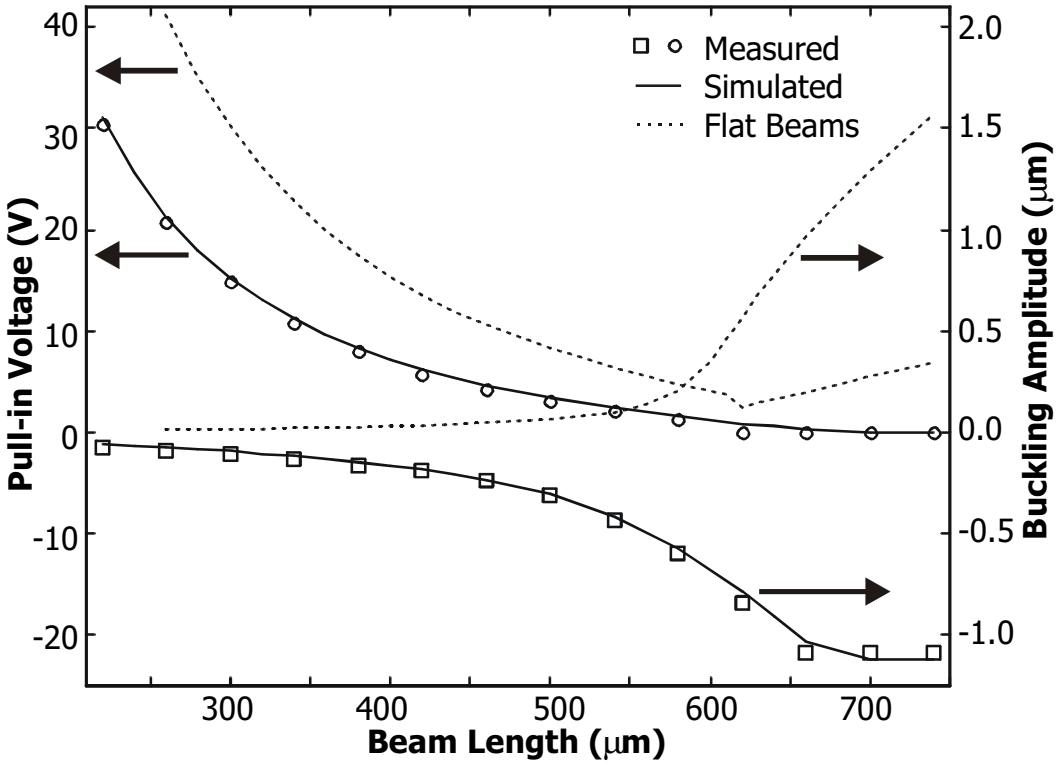

Figure 4-2. V_{pi} (left axis) and buckling amplitude (right axis) as a function of beam length for beams with dimples. Simulated values for flat beams are indicated by the dotted lines.

Pull-in voltages of beams with shorter center features – POLY0 pads or dimples (see Figure 4-2) – and thus with discontinuities closer to the beam center were measured to obtain the curves of Figure 4-3 and Figure 4-1. The pull-in voltages of beams over POLY0 and beams with dimples increase as the center feature decreases in length. The good simulation fit of V_{pi} shows that the parallel plate electrostatic approximation is still adequate, even in the presence of perturbations due to discontinuities that are close to the region of highest electric fields near the beam center.

The buckling amplitude of 600-μm beams – with dimples, and over POLY0 – vary as the discontinuity is moved from close to the anchor to close to the center. The magnitude of the buckling peaks when the discontinuities are half-way between the anchors and beam center i.e. when the center feature is 300-μm long. The simulation

model captures the trend well although the simulated magnitudes are larger in the case of the beams over POLY0, and smaller for the beams with dimples.

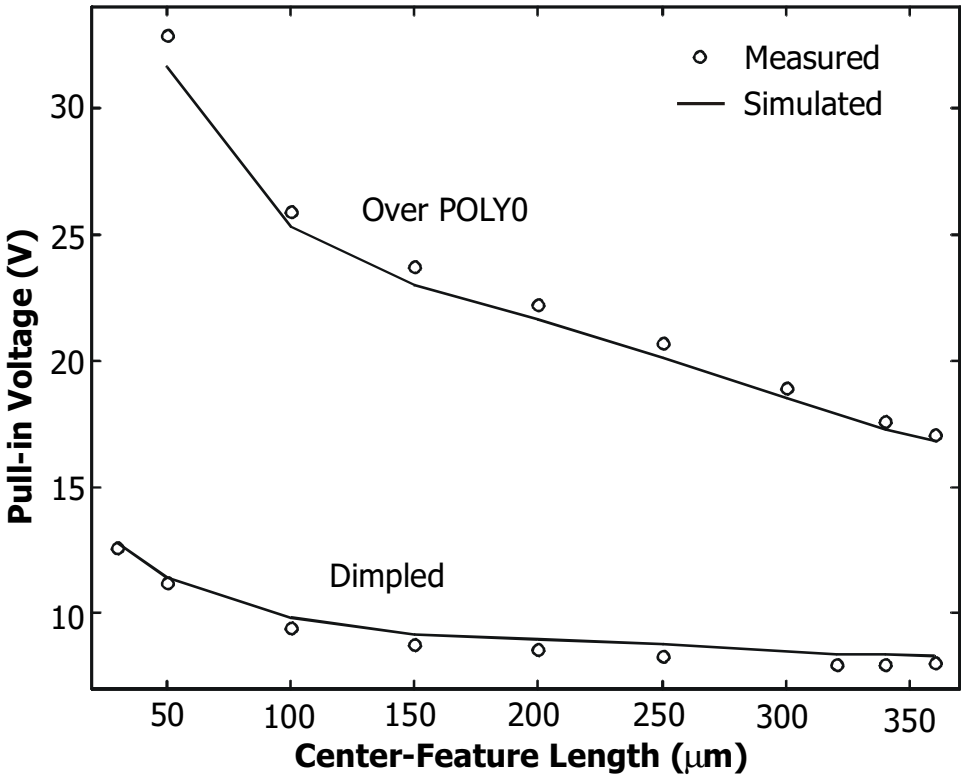

Figure 4-3. Pull-in voltage of 380-μm-long beams with dimples, and beams over POLY0 as a function of the center-feature length.

4.7 Precision and Consistency

4.7.1 Contours in *E*-σ Space

Contours in initial (undeformed state) uniaxial compressive stress (σ) vs. Young's modulus (E) space (Figure 4-2(a) and (b)) display the accuracy of the extracted parameters graphically. These are contours of the differences between simulated and measured values – V_{pi}'s or buckling amplitudes. In Figure 4-2(a), every pair of values of E and σ within the ±0.1 V contour gives simulation results within ±0.1 V of the measured V_{pi} for a 280-μm beam. This is an open-ended region, however, so the two parameters E and σ are not well-defined.

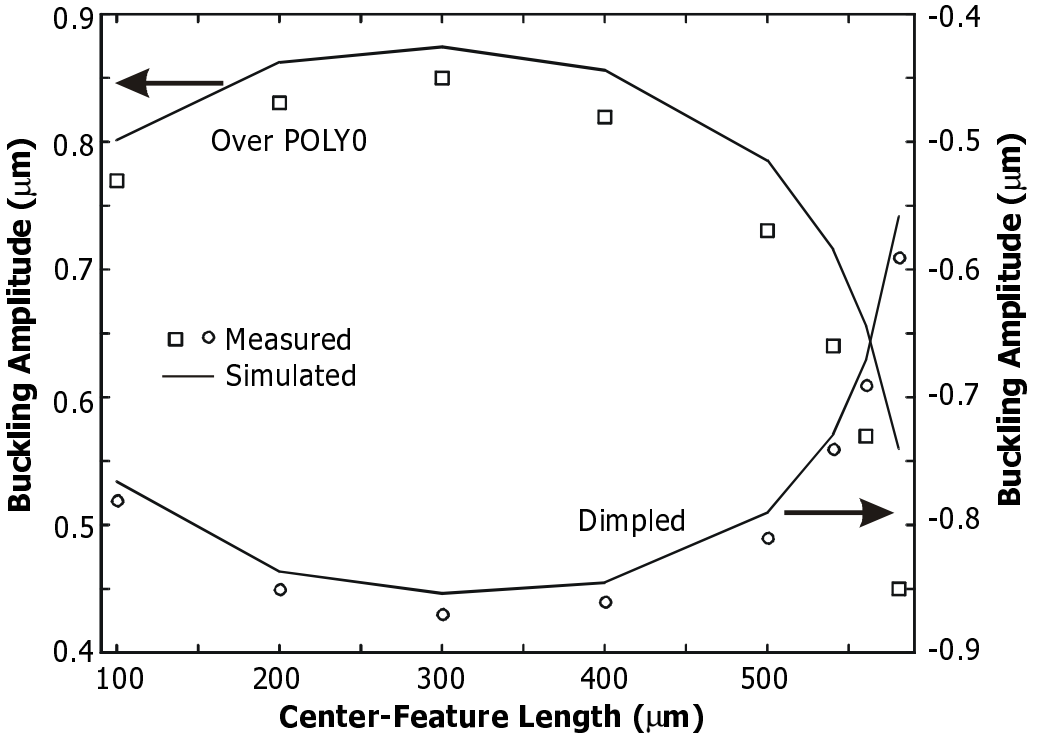

Figure 4-1. Buckling amplitude of 600-μm-long beams over POLY0 (left axis), and beams with dimples (right axis), as a function of the center-feature length.

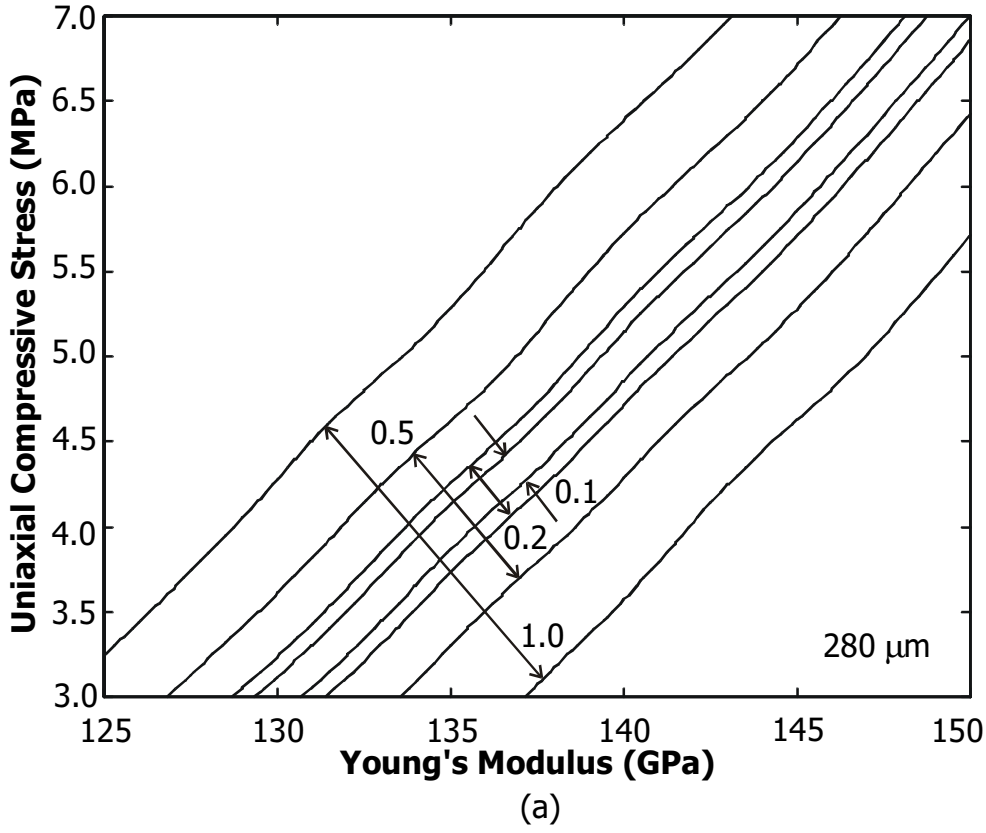

(a)

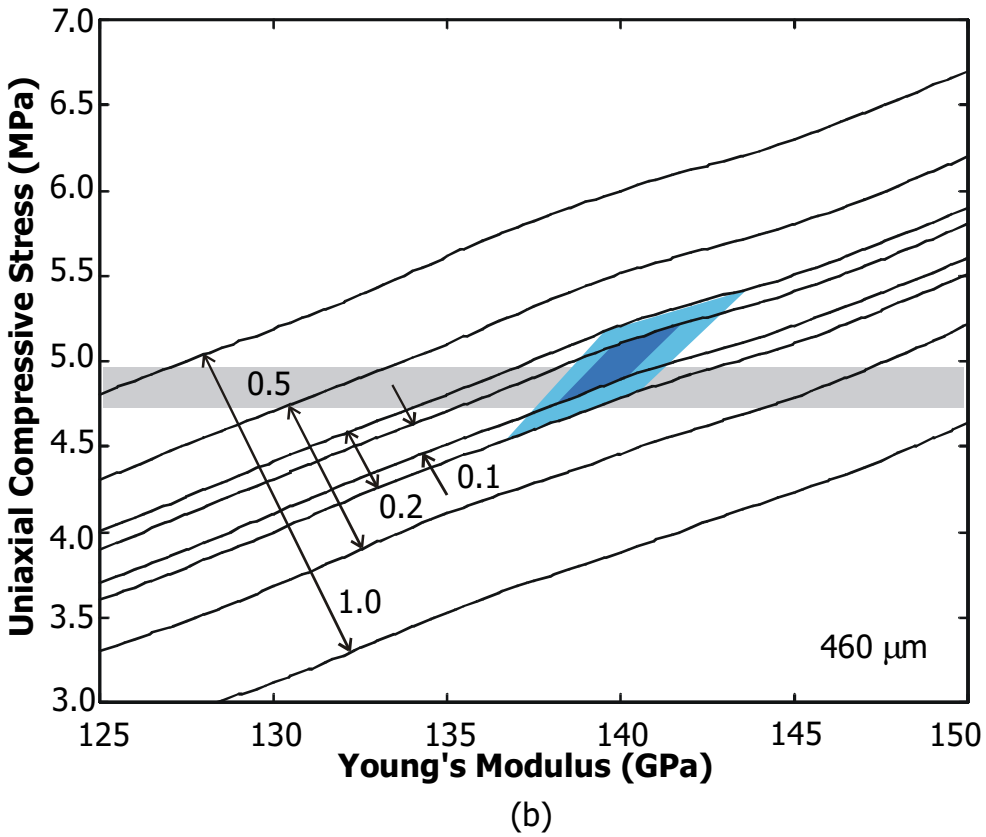

Figure 4-2. Contours in Young's modulus-uniaxial stress space of the difference between measured and simulated values. **(a)** V_{pi} contours [± 0.1, 0.2, 0.5, 1.0 V] for 280-μm-long beam. **(b)** V_{pi} contours for 460-μm-long beam. The shaded trapezoidal regions are the regions of overlap between the contours for the 280-μm and 460-μm beams. The darker trapezoid is the overlap of the ±0.1 V contours whereas the lighter trapezoid is the overlap of the ±0.2 V contours. The shaded horizontal bar indicates the precision of the extracted value of compressive stress corresponding to a measurement resolution of ±0.10 μm in the buckling amplitude of a 700-μm beam.

The shaded regions of overlap in Figure 4-2(b) are obtained by superposing the set of contours for a 460-μm beam with the contours for the 280-μm beam to obtain the regions in E-σ space which give simulation results within ±0.1 V or ±0.2 V of the measured V_{pi} for both beams, and actually for the entire range of beam dimensions. Assuming a resolution in V_{pi} of ±0.1 V, the uncertainty in E is ±1.8 GPa, and ±0.23 MPa in σ. If measurement repeatability is poor, due to charging effects for example, and the resolution is only ±0.2 V, the uncertainty increases to ±3.6 GPa in E and ±0.45 MPa in σ. The precision of the extracted parameters is limited by the repeatability of the measurements and the accuracy of the other parameters in the simulation model. This is quantified further in Section 4.7.2.

The horizontal shaded contour, 0.38 MPa wide, in Figure 4-2(b) comes from the calibration to the buckling amplitude of a 700-μm beam. The contour, which indicates the range of stress values that produces simulated amplitudes within ±0.10 μm of that measured, is horizontal because the buckling amplitude does not depend at all on Young's modulus. The region of overlap between the buckling amplitude contour for the 700-μm beam and the V_{pi} contour for the 280-μm beam overlaps the shaded trapezoidal regions, verifying the consistency of the two extraction methods. Another set of contours in E-σ space can be obtained from fitting simulations to the capacitance-voltage measurements of the next chapter, offering more redundancy among extraction methods. The C-V measurements are more sensitive to Young's modulus than the V_{pi} measurements, potentially offering better resolution in extracted parameters. However, as will be shown Chapter 5, this C-V measurement is beset by many uncertainties. This is a general problem that arises when attempting to reconcile various extraction methodologies. Each distinct measurement method brings its own unknowns, resulting in an underconstrained system in which there are, in mathematical terms, more unknowns than equations. Redundancy is limited to only a few variables or parameters – independent verification of all extracted parameters is difficult. The ideal of having a single research group fabricate, measure and characterize all the test structures is still difficult to achieve.

4.7.2 Corner Checking

To understand the dependence of pull-in voltage and buckling amplitude on the measured and extracted parameters, simulations were performed using parameters within the ranges of uncertainty in measurements or extraction as given in Table 4-1. The resolution in E and σ was obtained assuming a resolution of ±0.2 V in V_{pi} measurements, and a resolution of ±0.10 μm in buckling amplitude. The resolution in geometry was determined from experience with the repeatability of the measurements. The high and low corners in V_{pi} for a 280-μm beam and the variations in buckling amplitude for a 700-μm beam due to these uncertainties are shown in Table 4-1. Using the worst-case corner parameters, the V_{pi} can be 1.45 V larger or 1.55 V smaller than the nominal value of 35.05 V whereas the buckling amplitude can be 0.121 μm larger or 0.131 μm smaller

than the nominal 1.291 μm. The precision of the simulated V_{pi}'s, which is the step size used in the Abaqus simulations, is 0.05 V. The range of uncertainty in V_{pi} can be narrowed if the covariance between the extracted Young's modulus and residual stress is accounted for. Instead of defining the resolution of E and σ by the smallest bounding rectangle of the overlap space in Figure 4-2(b), the resolution can be defined by the exact shaded parallelograms. This covariance information, however, is difficult to incorporate into most simulation systems.

Table 4-1. Variation of V_{pi} and buckling amplitude within the precision of simulation parameters

Parameter	Nominal Value	Precision ±	V_{pi} (–)	V_{pi} (+)	Buckling Amplitude (–)	Buckling Amplitude (+)
POLY1 thickness	1.97 μm	0.01 μm	34.75 V	35.30 V	1.310 μm	1.271 μm
Initial air gap	1.79 μm	0.01 μm	34.75 V	35.30 V	1.291 μm	1.291 μm
Nitride thickness	0.077 μm	0.005 μm	34.90 V	35.20 V	1.291 μm	1.291 μm
Step-up sidewall angle	76°	3°	35.05 V	34.95 V	1.288 μm	1.295 μm
Step-up sidewall thickness	2.10 μm	0.10 μm	34.95 V	35.10 V	1.289 μm	1.293 μm
Young's modulus	140 GPa	3.6 GPa	34.50 V	35.55 V	1.291 μm	1.291 μm
Uniaxial compressive stress	4.83 MPa	0.19 MPa	35.15 V	34.90 V	1.185 μm	1.389 μm

The - (or +) values correspond to subtracting (or adding) the precision from the nominal value. Nominal V_{pi} is 35.05 V, and nominal buckling amplitude is 1.291 μm.

4.8 Extrapolation to Dual-Bias-Electrode Devices

The simulation model characterized in the previous section is now used to predict the behavior of more-complex dual-bias-electrode structures shown in Figure 4-1. Figure 4-2 is a 3-D solid model of the device, generated using a geometry generation program that incorporates the effects of conformal deposition and sloped sidewall etches [15]. Four probes are needed to measure the performance of the device as shown in Figure 4-1 – two to control the bias electrodes, and two to measure the capacitance between the beam and silicon substrate. An HP4155A applies a constant bias voltage to one electrode and a slow voltage ramp to the other electrode whereas the HP4275A monitors the capacitance. The two instruments share a common ground connection. The measurements of Figure 4-3 are of V_{pi} at one electrode as a function of the voltage, V_{bias}, applied to the other bias electrode. As the bias voltage is increased, the voltage required to pull the

dimple down decreases. The devices measured were designed with bias electrodes close enough to the center of the beam such that pull-in is still abrupt despite the fact that the center of the beam is being leveraged downwards by the electrodes [83]. This makes it easier to detect the abrupt change in capacitance as the beam snaps down onto the nitride. By having two bias electrodes, multiple precise pull-in voltage measurements can be used to characterize a single device. The dimple at the center of the beam prevents conductor-to-conductor contact between the POLY1 beam and POLY0 electrodes. Dielectric charging, which is covered in detail in Chapter 5, is avoided because there is no applied electric field across exposed (not covered by POLY0) regions of silicon nitride. The V_{pi} vs. V_{bias} curves for devices with left and right electrodes of equal length are symmetric about the $V_{pi} = V_{bias}$ line. By swapping the bias and pull-in connections, the integrity of the devices can be verified by checking symmetry.

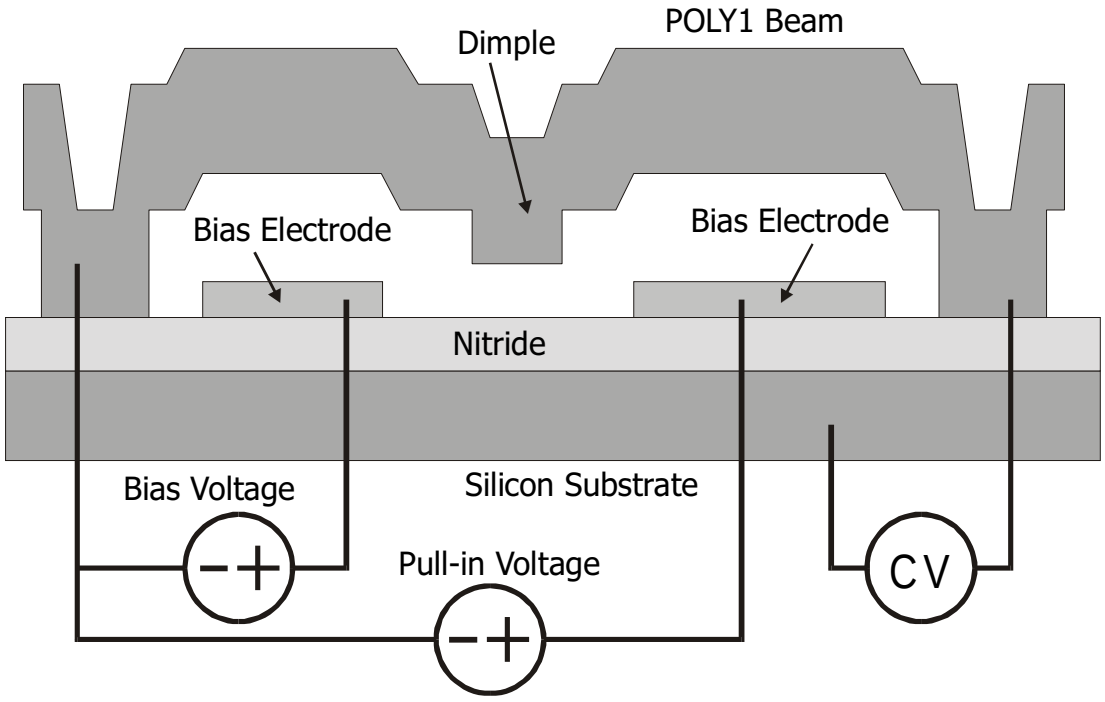

Figure 4-1. More-complex dual-bias-electrode structure with features such as dimples and steps over POLY0 that were well characterized in the previous sections. The voltage on the right bias electrode required to pull the dimple down to the nitride surface is measured as a function of the voltage applied to the left bias electrode.

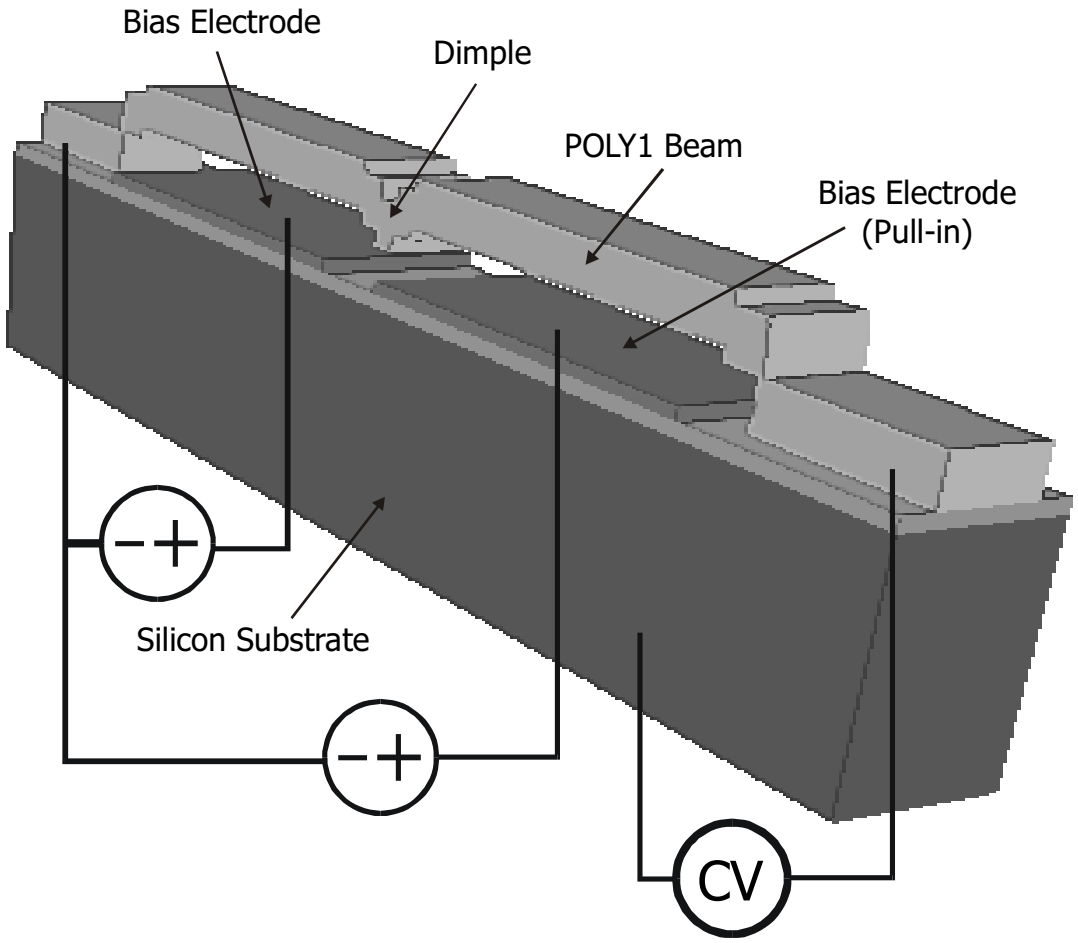

Figure 4-2. 3-D solid model of dual-bias-electrode structure.

The extrapolated behavior matches the measurements well. For curves such as these with segments that are primarily vertical, error norms should be calculated along the directions normal to the curves, as shown in Figure 4-3, rather than simply taking the differences between the measured and simulated pull-in voltages at a particular bias voltage. Using this normal-direction error metric, the simulations match the measured values to within 2%. To ensure that the simulation results are reliable for large bias voltages and small V_{pi}'s (less than 15 V), the bias on the pull-in electrode needs to be ramped up very gradually from 0 V in steps of 0.5 V or less to prevent the beam from pulling-in prematurely.

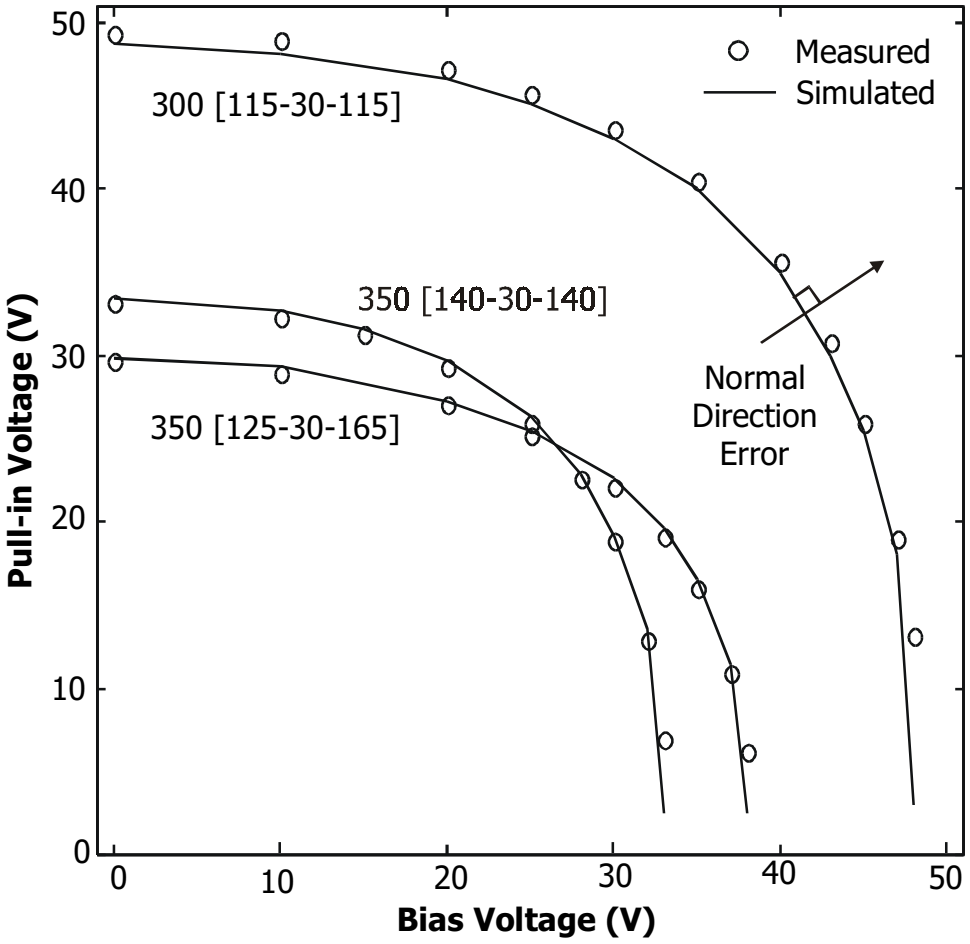

Figure 4-3. Measurements of dual-bias-electrode structures of different dimensions. Error between simulated and measured values are determined in the direction normal to the curve. Extrapolated simulations match measurements to within 2%. The labels indicate the lengths of the structural features: <total beam length> [<left electrode> <dimple> <right electrode>]. An additional 40 μm due to the spacings between each feature makes the numbers in the square bracket add up to the total beam length.

These comprehensive calibration procedures using simple test structures have produced simulation model parameters that predict the behavior of more complex devices very accurately. Therefore, the geometrical parameters in Table 3-1 and the extracted E and σ along with the measurement data in Figure 4-3 can serve as verification test cases to evaluate the accuracy of coupled electromechanical simulators. This can form a more meaningful tutorial example that encourages the understanding of mesh convergence and geometrical accuracy issues. For the most part, simulators have been compared on the basis of speed alone since accurate and verified benchmarks are not readily available. With those model parameters, we ran full 3-D simulations using the commercial

electromechanical simulator IntelliCAD. The geometry shown in Figure 4-4, generated automatically by the software, has sharp, right-angled edges instead of smooth rounded steps. The simulated pull-in voltages using this coarse model are slightly higher than those measured, or those simulated using the 2-D model.

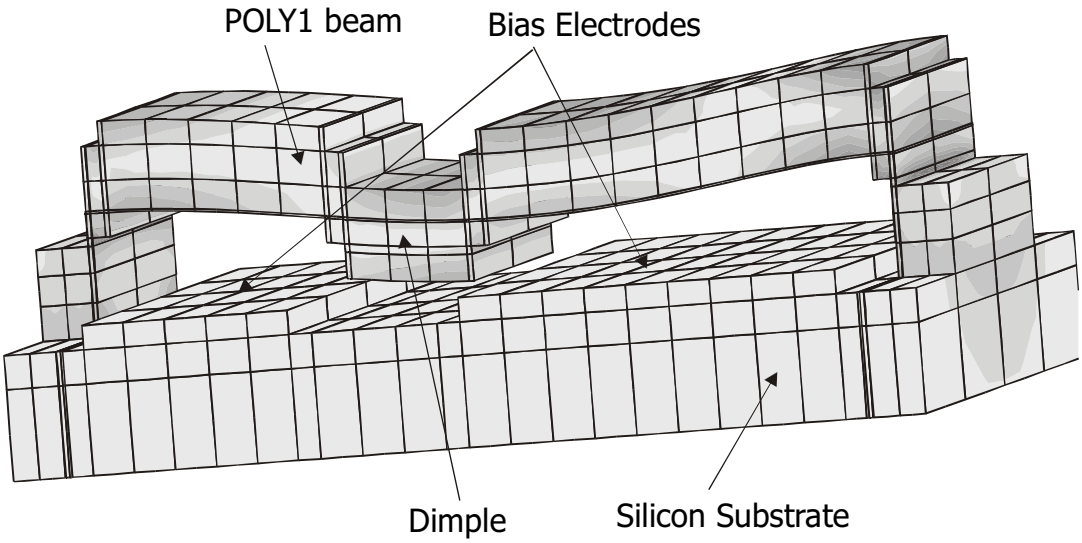

Figure 4-4. IntelliCAD model of dual-bias-electrode structure.

4.9 Secondary Effects

The excellent match of the simulation results to measurements indicates that the system of materials is very well characterized for the range of dimensions and actuation studied in this chapter. A few physical effects were mentioned along the way that affect beam behavior but their analyses were deferred until this section because the effects are small on the characterized devices. These effects are interesting in their own right and will affect the behavior of devices fabricated in other materials systems, or even other types of devices fabricated in MUMPs such as cantilevers or comb drives.

4.9.1 Stress Gradient

The stress in a polysilicon beam varies throughout its thickness and will cause a freestanding cantilever to curl upwards or downwards [84]. In the MUMPs dies measured, the degree of curling varies from cantilever to cantilever as shown in the Zygo profiles of Figure 3-2, Figure 3-4, and Figure 3-1. If the stress variation is uniform for all

beams, the profiles of cantilever beams of various lengths and widths should all lie on the same circle. As shown in Figure 3-4, each cantilever appears to have a different stress gradient. Furthermore, Figure 3-1 shows that some beams do not even have consistent curvatures throughout their lengths.

This section investigates the effects of stress gradients on fixed-fixed beams. The stress profile in a beam can be arbitrary [85]-[86], [87]-[88], such as the nonlinear profile proposed to explain the effects of gold on beam behavior in Section 3.5. In Abaqus, stress due to deposition is modeled by thermal stress. A stress gradient is imposed by either varying the effective temperature or the expansion coefficient through the thickness. In this section, the temperature was varied continuously from the top surface to the bottom surface as shown by the contours in Figure 4-1. The temperature contours are assumed to follow the conformal profile and are always parallel to the outer surfaces. The beam is 1.97 μm thick and suspended 1.79 μm above a ground plane (dimensions are similar to those measured in the previous section). Young's modulus is 140 GPa.

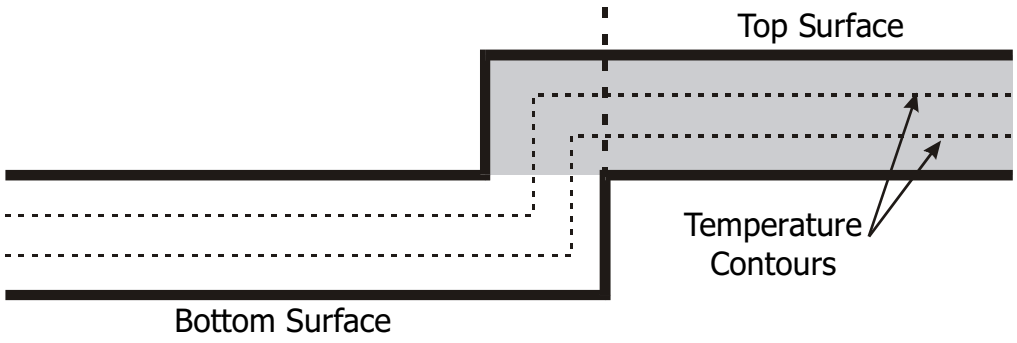

Figure 4-1. Profile of simulated beam near the step-up, showing temperature variation through the beam that gives rise to a stress gradient. Contours follow the conformal shape of the beam and are parallel to the outer surfaces. The nodes on the vertical dotted line can be fixed to eliminate the effect of the step-up in simulations. The stress states nearer the top surface occupy a larger portion of the shaded region and, hence, affect beam behavior more than the stress states nearer the bottom surface.

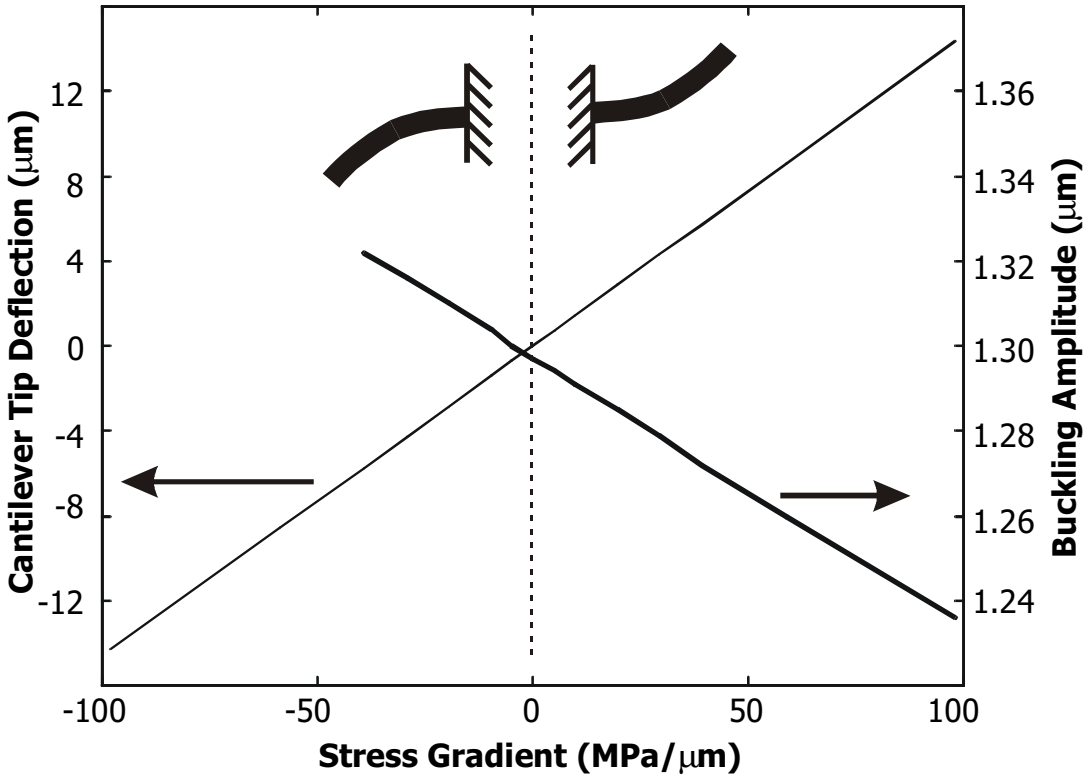

Figure 4-2. The deflection (left axis) of the tip of a 200-μm-long cantilever as a function of stress gradient. The corresponding buckling amplitude variation (right axis) of a 700-μm-long fixed-fixed beam is also shown. The insets show the direction of curling of cantilevers corresponding to the sign of the stress gradient.

The displacement of the tips of a 200-μm-long cantilever as a function of stress gradient is plotted in Figure 4-2 along with the corresponding variation of the buckling amplitude of a 700-μm-long fixed-fixed beam. The average uniaxial stress is kept constant at 4.83 MPa. The influence of stress gradients on the behavior of fixed-fixed beams is small unless the stress gradients are large. The change in buckling amplitude only becomes significant once the stress gradient is large enough to cause significant curling i.e. a deflection of several microns of the tip of the cantilever. Since such curling is not observed in MUMPs cantilevers, it can be safely assumed that the influence of stress gradients on the buckling amplitude of fixed-fixed beams is negligible.

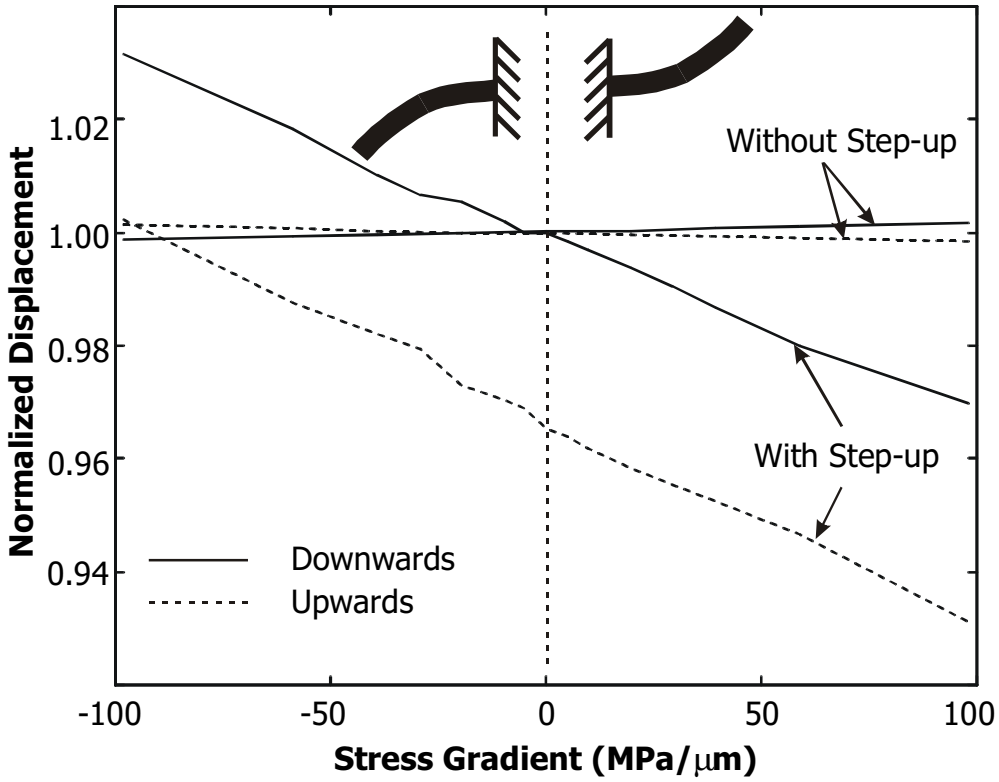

Figure 4-3. Normalized deflection magnitudes of 300-μm-long fixed-fixed beams under pressure loads in the upwards and downwards directions. The simulated deflections – both with and without step-ups – are normalized to the deflection of beams with zero stress gradient. Initial bowing is nulled out. The insets show the direction of curling of cantilevers corresponding to the sign of the stress gradient.

In the same way, the stiffness – determined from upwards and downwards pressure loading simulations – of a 300-μm beam is examined as a function of stress gradient. The magnitudes of the simulated deflections are normalized to the downwards deflection of a beam with uniform stress (no stress gradient) as shown in Figure 4-3. The initial unloaded deflection or bow of the beams are nulled out. Once again, the influence of the stress gradient only becomes meaningful when the stress gradient is large. The effect is especially small if the step-up anchor is eliminated. Without the step-up, the magnitude of the upwards deflection decreases as the stress gradient becomes more positive whereas the magnitude of the downwards deflection increases. There is a small asymmetry, or preferred direction of deflection, imposed by the stress gradient. With a step-up, the stress variation in the step-up alters the overall stress state of the beam, causing both upwards and downwards deflections to decrease as the stress gradient becomes more positive. As shown by the shaded region in Figure 4-1, the stress states

nearer the top surface occupy larger regions than the states nearer the bottom and, hence, have greater influence on the overall stiffness of the beam. Therefore as the stress gradient becomes more positive (top layer becomes more tensile), the overall average stress becomes less compressive causing the beam to become stiffer. Thus both upwards and downwards deflections are smaller in magnitude. There is a constant offset between the upwards and downwards deflection magnitudes indicating a preferred downwards direction of deflection due to the step-up.

4.9.2 Substrate Curvature

Pressure due to micropositioned probes alter the curvature of the silicon die and can change the buckling amplitude of beams as shown in Figure 4-1. As such, the probes must be positioned with the minimum amount of pressure required to make electrical contact. This is easier to do under the Zygo profiler because probe contact is easily detected from changes in fringe patterns, and the change in buckling amplitude can also be measured. Probe pressure control is more difficult under the optical microscope at the probe station setup for the HP4275A and HP4155A.

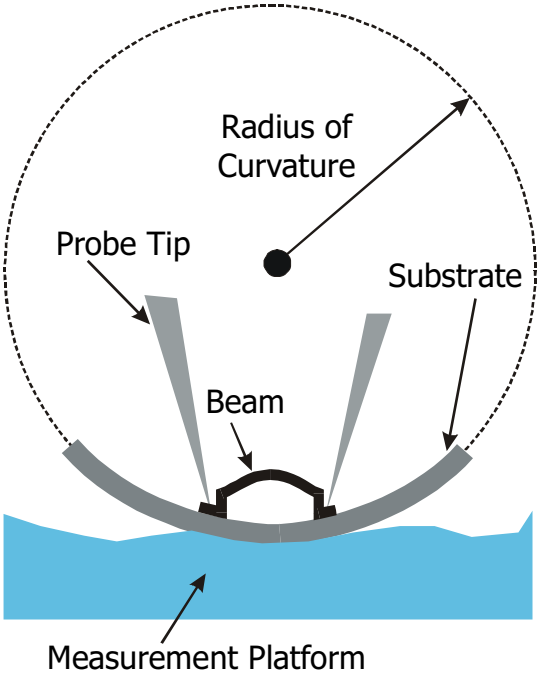

Figure 4-1. Schematic of a measurement setup. The pressure from the probes modifies the curvature of the substrate. The surface of the measurement platform is usually somewhat compressible, especially if the dies are placed in Gel-Pak containers. The curvatures are grossly exaggerated to show qualitative behavior clearly.

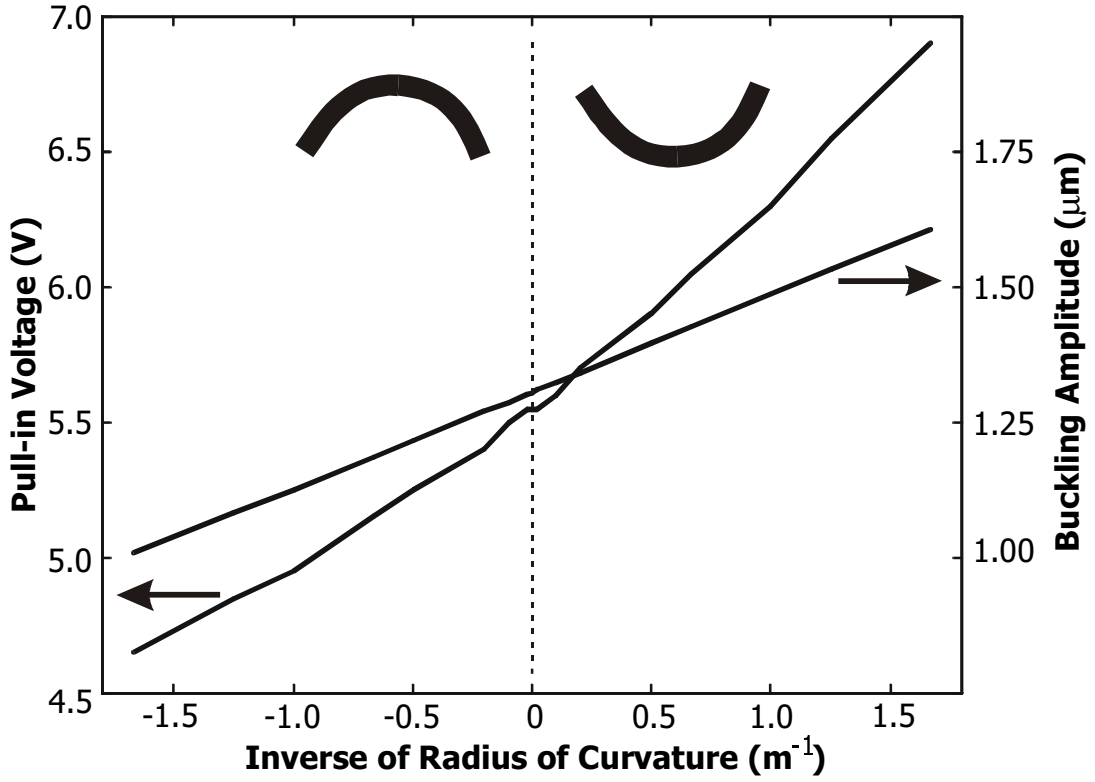

Figure 4-2. Variation in buckling amplitude (right axis) and pull-in voltage (left axis) of a 700-μm-long beam as the substrate curvature is varied. Substrate is initially flat. Kinks in V_{pi} curve are due to the limited precision of V_{pi}'s obtained from the simulation. The inset curves indicate the sign of substrate curvature.

Figure 4-2 shows how the buckling amplitude and pull-in voltage of a 700-μm beam changes as the substrate curvature varies. The buckling amplitude varies linearly with the inverse of the radius of substrate curvature. The effect of substrate curvature is modeled in Abaqus by displacing the anchor nodes in Figure 4-3 according to the degree of curvature. The electrical gap is also varied appropriately. The vertical displacement, u, imposed at each node is approximated from the equation of a large circle

$$u \approx r\left(1-\cos\frac{x}{r}\right) \tag{4-1}$$

where r is the radius of the circle (radius of curvature) and x is the distance of the node from the center of the beam. The center of the beam is vertically inline with the center of the circle. The substrate can have an arbitrary initial curvature. An initially flat substrate will have to curl up to a radius of curvature of about 2 m (or inverse radius of 0.5 m^{-1}) to induce a 0.10 μm increase in the buckling amplitude of the 700-μm beam, which in turn

increases the pull-in voltage by about 0.35 V. Such increases in buckling amplitude were observed for dies which were probed while on soft Gel-Pak trays. This could account for the slightly higher measured pull-in voltages in Section 4.5.2 compared to simulated results.

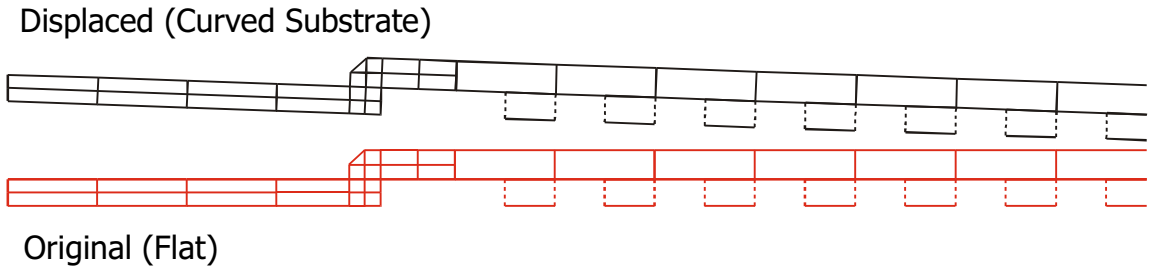

Figure 4-3. Displaced mesh to account for changes in curvature of the substrate. All bottom nodes lie on a circle.

4.9.3 Deposition Coverage

A layer of material deposited on a fixed-fixed beam or a diaphragm alters the properties of the system. If the deposited material covers the entire surface of the beam and extends all the way to the fixed boundaries, then the effects due to the additional material are simple additive and essentially independent of the underlying beam. If, however, the deposited material does not cover the entire surface of the beam, the material interacts with the beam and can cause unexpected results. Figure 4-1 shows the simulation model for a film deposited on a beam. The deposited film does not extend all the way to the clamped boundaries but is like an island on the beam. Figure 4-2 shows how the normalized upward and downward deflection magnitudes of the resulting system under pressure loading varies with deposition coverage. Unlike in the previous section, the initial deflections due to compressive stress are not nulled out because, here, the total deflection is the parameter of interest. Coverage, which is symmetric about the center of the beam, is measured as a percentage of the total beam length. The 2-μm-thick 400-μm-long beam has an initial tensile stress of 10 MPa. A 0.1-μm-thick film with a tensile or compressive stress of 10 MPa is deposited.

When a tensile film covers the entire beam and is clamped at the edges (100% coverage), it simply increases the total stiffness of the system as expected, and the normalized displacement is less than one. When the film covers only a portion of the

beam, the downward stiffness of the bilayer system is actually reduced (larger displacements) even though a highly tensile film was added to the system. This is because the film creates a localized region with a stress gradient that favors downwards displacement similar to the effects shown in Section 4.9.1. There is a preferred downwards deflection direction. This phenomena required that a stress sensor built to monitor thin film deposition be redesigned to eliminate the effect of incomplete coverage and ensure that the deposited films cover the entire underlying diaphragm [89]. When a compressive film is deposited, the converse happens. The compressive film interacts with the underlying beam creating a stress gradient that prefers upwards deflections. Hence the magnitudes of the upwards deflections increase with coverage whereas the magnitudes of the downwards deflections decrease. When coverage is 100%, the additional thickness causes the system to be stiffer than the original even though the additional film was compressively stressed.

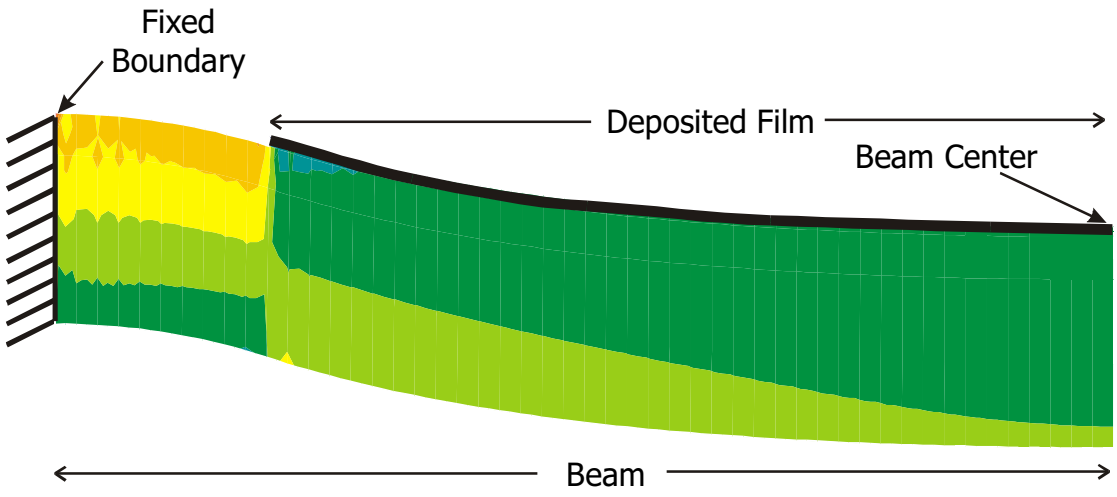

Figure 4-1. Simulation model of a thin film covering a percentage of an underlying beam. Only half the beam is simulated. The beam is 400 μm long and 2 μm thick whereas the film is 0.1 μm thick. The beam has an initial uniaxial tensile stress of 10 MPa. The deposited film has an initial tensile stress of 10 MPa. Both the film and beam have a Young's modulus of 100 GPa. The deformation is exaggerated to show the effects more clearly.

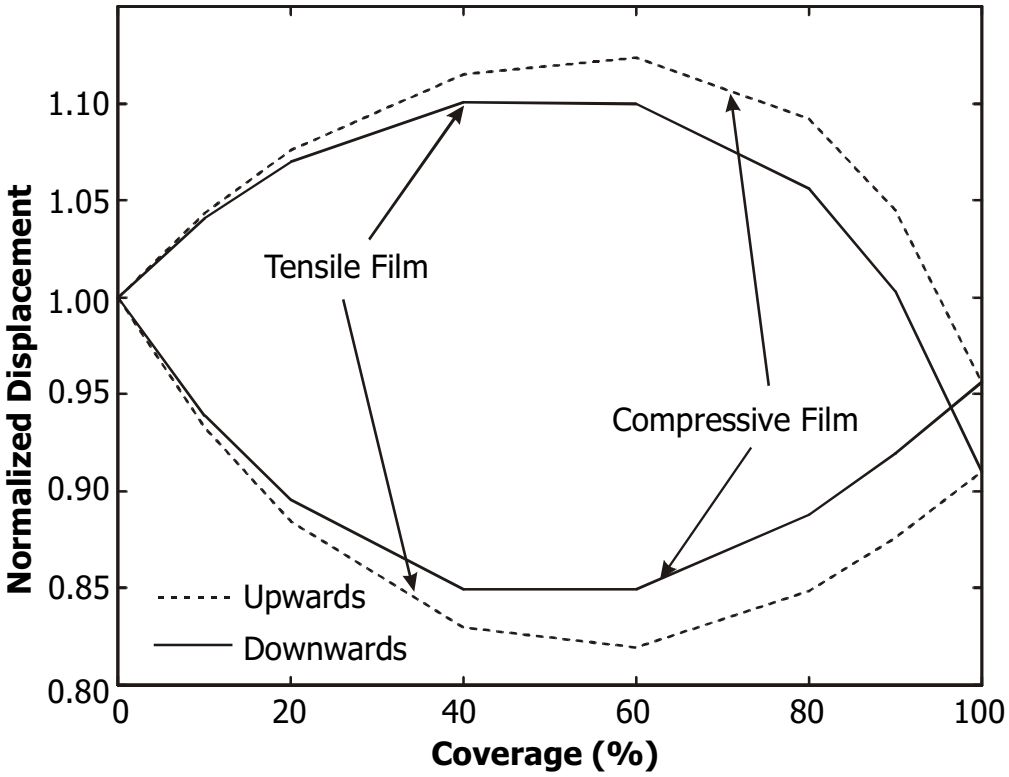

Figure 4-2. Upward and downward displacement magnitudes, normalized to the displacements of the original system with no additional films, as a function of film coverage. Geometry of the system is shown in Figure 4-1. Initial, unloaded deflection due to compressive stress is not nulled out.

4.10 Summary

The two main elastic properties of interest in polysilicon – Young's modulus and residual stress – were extracted from measurements of buckling amplitude and pull-in voltages. Three distinct boundary conditions were analyzed; the behavior of backfilled anchors was shown to be strongly influenced by stress in encapsulated PSG. Mechanical discontinuities were examined carefully. Consistency among extraction methods was demonstrated, and the precision illustrated graphically and through tabulated corner checking. The characterization methodology was verified by extrapolating the behavior of more-complex dual-bias-electrode structures. The well-calibrated model along with the measured data can serve as a verification test case to evaluate coupled electromechanical simulators. Finally, three interesting influences on beam behavior – stress gradients, substrate curvature, and deposition coverage – were investigated via computer simulations. The effects of stress gradients on fixed-fixed beams are minimal unless the

gradients are large enough to cause significant curling of cantilevers. Substrate curvature, which can be altered by probe pressure, causes measurable changes in buckling amplitude and hence V_{pi}. Deposition coverage must be considered when analyzing the overall stiffness of a composite system.

Chapter 5 Characterization of Contact Electromechanics

5.1 Overview

Beyond the pull-in voltage, the electrostatically actuated beam contacts the underlying silicon nitride layer creating a dielectric sandwich consisting of the beam, silicon nitride and silicon substrate. When the beam is in contact with the nitride, the capacitance between the beam and substrate is relatively large and changes considerably with changes in applied voltage. Measurements of capacitance as a function of voltage provide insight into contact mode behavior – a mode of operation important to capacitive microwave switches [9].

Fundamental capacitance-voltage characteristics are introduced in this chapter followed by a detailed analysis of the contact surface. The well-characterized flat beams of Chapter 4 are used as in-situ contact surface probes. There has been no prior work systematically addressing the effects of contact surfaces and dielectric charging on capacitance measurements. Simulations in 3-D of contact electromechanics were performed by Gilbert et al. [90] but no comparisons to measurements were made. Hung designed a variable capacitor based on contact electromechanical principles that avoided issues related to complex contact surface phenomena and dielectric charging [91]. The

effects of surface properties on conductor-to-conductor contact were analyzed in [92] and [93] whereas the phenomena of adhesion and friction have been studied in [94]-[95]. Effects of charge accumulation were alluded to in [9] and [34] but no quantitative descriptions were given. In this chapter, a compressible contact surface model captures effects indicated by C-V measurements. The electromechanical structures are strongly influenced by charge in the nitride, causing drift in voltage measurements, and both short-term and long-term reliability concerns. This drift or offset is exploited to monitor charge buildup over time which is modeled by a charge trapping model.

5.2 Capacitance-Voltage Characteristics

5.2.1 Theoretical Description

Figure 5-1 shows the behavior of an electromechanical system as a function of voltage applied between the beam and silicon substrate. At each stage or voltage range, the left diagram illustrates the shape of the beam and the region of the capacitance-voltage curve, indicated by the dot, corresponding to the beam position. The diagram on the right is a schematic plot of the total energy of the electromechanical system as a function of the displacement of a “quarter point” midway between the support post and center of the beam (see beam in Figure 5-1(a)). The circle on the energy curve indicates the position at static equilibrium. The contributions to the total energy of the system come from the mechanical restoring forces, the electrostatic forces, and the repulsive forces of contact. Only flat beams are studied in this chapter.

The capacitance of the system in the initial position is nulled out. At this starting point shown in Figure 5-1(a), the beam is in a minimum energy region at zero displacement. As the voltage increases, the beam deflects downwards and the capacitance increases slightly as shown in Figure 5-1(b). Another local energy minimum begins to form. There are two stable states at this applied voltage – one as shown by the beam position in Figure 5-1(b) and the other in-contact position shown in Figure 5-1(e). If the beam in the position of Figure 5-1(b) were pushed down mechanically, it would jump to the stable in-contact position of Figure 5-1(e). This is the basis of the measurement technique used in this chapter to minimize adhesion and charging effects. Moving from Figure 5-1(b) to Figure 5-1(c), a further voltage increase brings the system beyond the

pull-in threshold, where the beam snaps down abruptly and the capacitance increases dramatically. The beam is now in contact with the silicon nitride creating a dielectric sandwich along with the silicon substrate. Hysteresis is present because of the pull-in instability of this electromechanical system. The barrier between the two local energy minima in Figure 5-1(b) disappears at this point. As the voltage increases further, more of the beam comes into contact with the nitride, increasing the capacitance further as shown in Figure 5-1(d). This phenomenon is known as "zip up". Now as the voltage is decreased, the quarter-point moves away from the dielectric surface as shown in the energy diagram of Figure 5-1(e). The beam "peels off" and the system traverses the other branch of the hysteretic C-V curve. The other local energy minimum corresponding to the not-in-contact equilibrium position begins to form again. Adhesion of the beam to the nitride surface due to capillary forces can be significant here. These forces hold back the beam somewhat and can even prevent peeling off. When the voltage is reduced back towards zero, the beam continues to peel off until it pops back up to the initial state of Figure 5-1(a).

5.2.2 Measurements

Typical high-frequency small-signal C-V measurements, using an HP4275A LCR meter, of a cantilever and a fixed-fixed beam are shown in Figure 5-2(a) and Figure 5-2(b), respectively. The general shapes of the C-V curves match the theoretical hysteretic curves of Figure 5-1. The initial ($V_{applied} = 0$) capacitance is subtracted from all other measured capacitances.

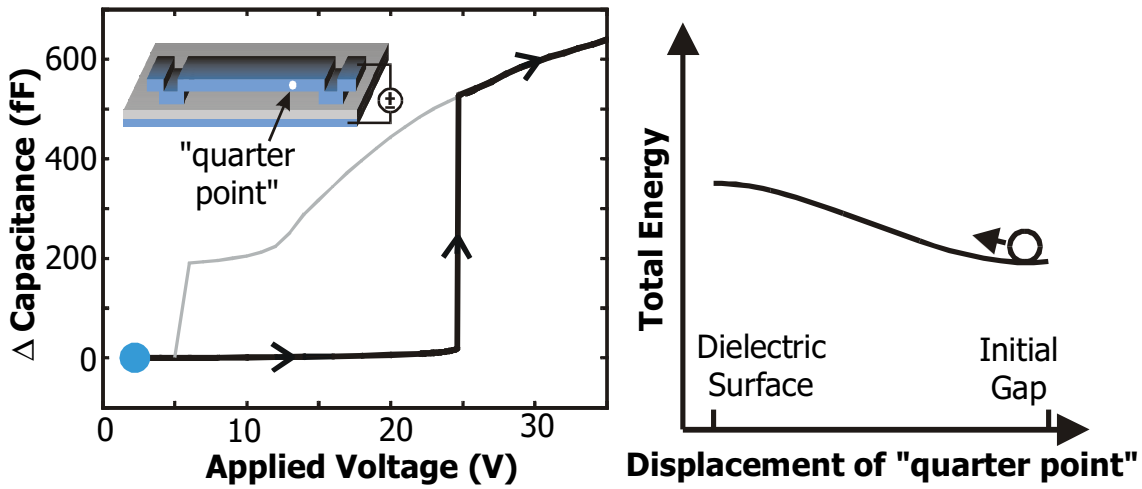

(a) Initial position

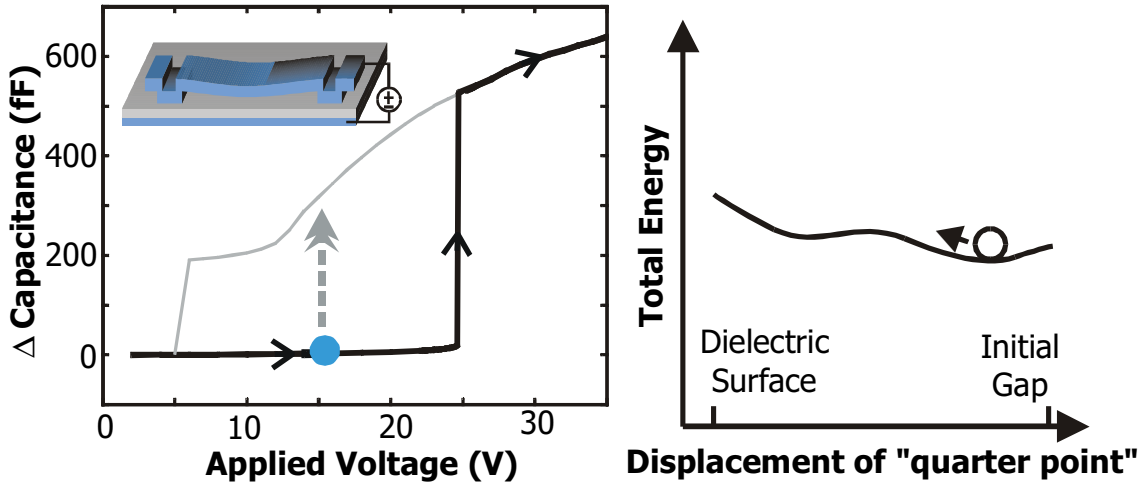

(b) Deflected

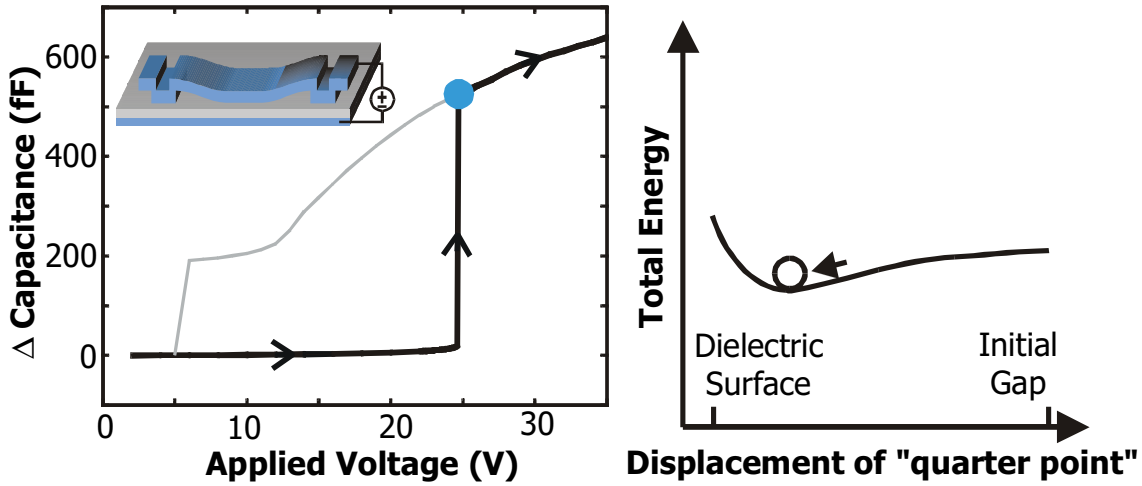

(c) Pulled-in

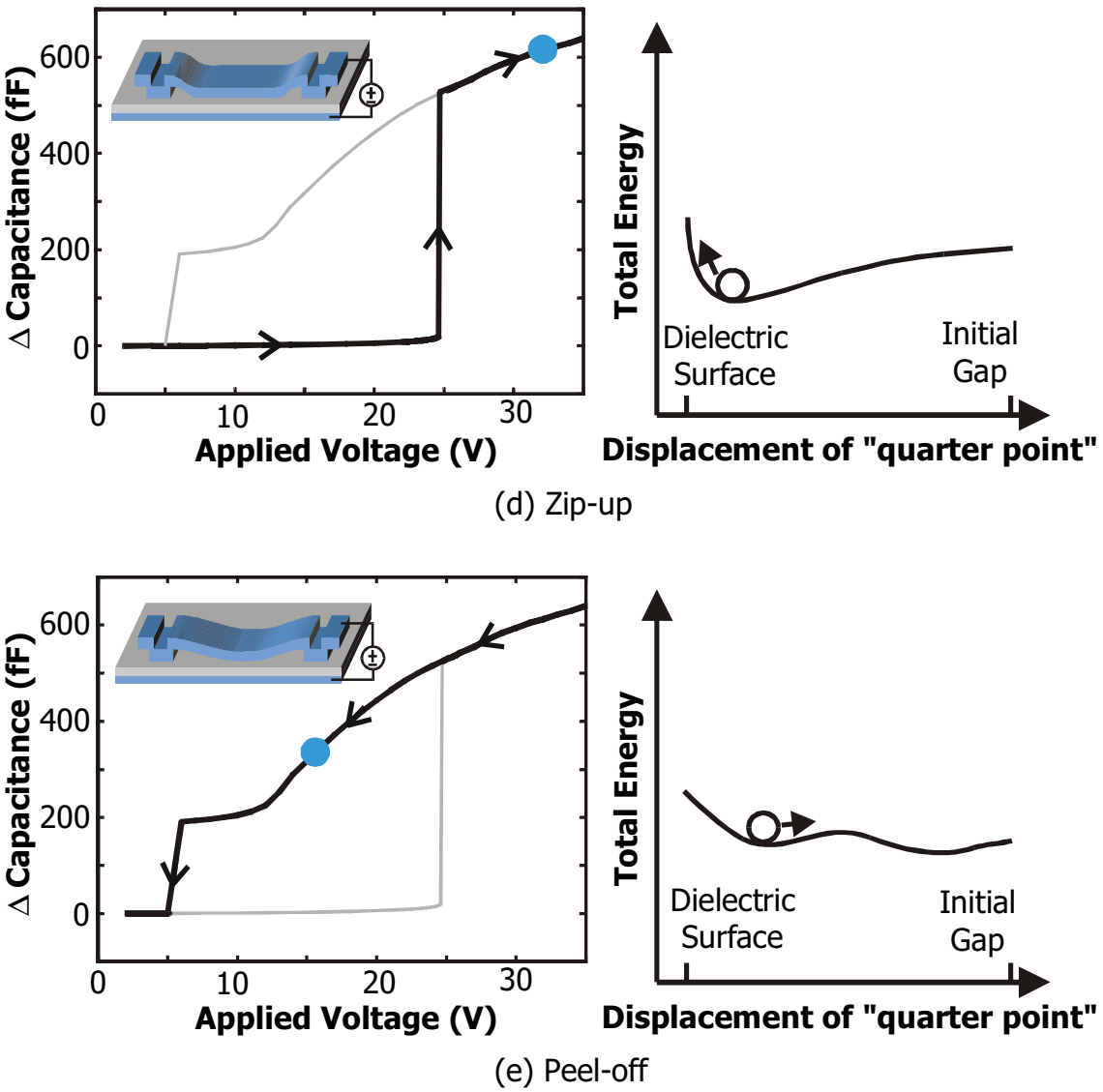

Figure 5-1. Beam deformation, capacitance-voltage (C-V) relationship, and energy diagram for electrostatically actuated beam. Position of dot on C-V curve corresponds to illustrated beam deformation. The "quarter-point" is located halfway between the beam center and beam anchor as shown in (a). The circle on the energy diagram indicates the equilibrium displacement. **(a)** Initial position. **(b)** Beam deflected by electrostatic force. Two stable solutions exist at this voltage – one in contact and one not. The gray arrow in the C-V plot shows that the beam can be bumped mechanically to position shown in (e). **(c)** Pulled-in. Capacitance increases abruptly. **(d)** Zipping up. Capacitance continues to increase with voltage. **(e)** Peeling off. Two solutions exist at this voltage as in (b).

There is a plateau in the peel-off portion of the cantilever C-V curve where most of the cantilever beam snaps off the nitride surface leaving only the tip touching, as shown schematically in the inset of Figure 5-2(a). This phenomenon during peel-off has

been replicated in simulations. The same deformation mode has been observed in measurements during the pull-in transition but has not been observed in simulations. Electrostatic fringing fields, friction and adhesion at the tip of the cantilever may not have been adequately modeled. In addition, the nonlinear solver in Abaqus might tend to skip this equilibrium solution and step right through to the lower-energy in-contact solution. Measurements under the Zygo profiler show that this tip-pull-in state is not stable and will transition to the flattened-out state after several seconds with the voltage held constant. Due to the inadequate accuracy of the electric field models for the tip of a cantilever, and to nonuniformities mentioned in Section 3.6, cantilever beams were not used for parameter extraction.

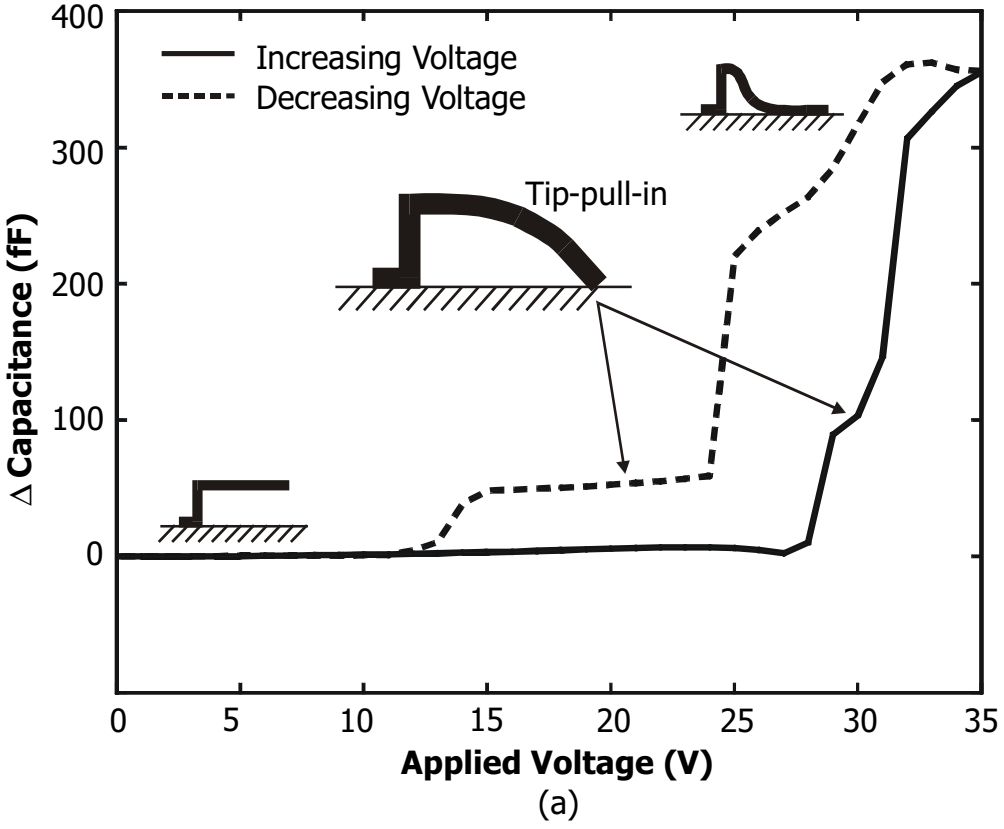

(a)

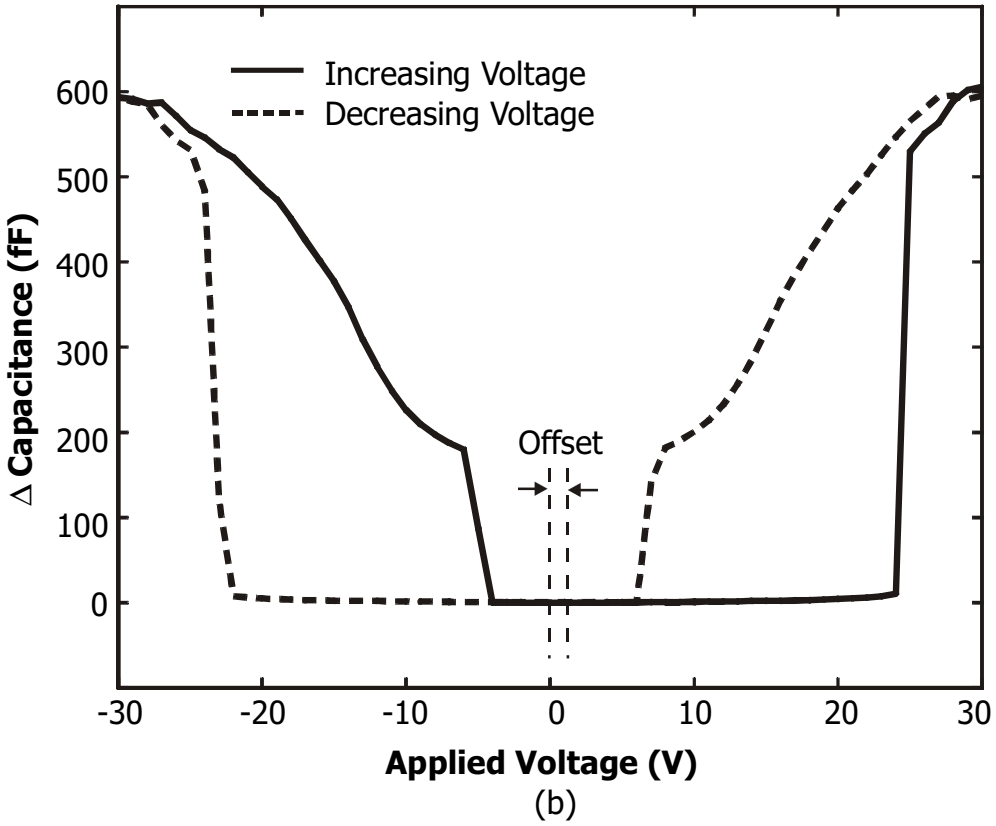

Figure 5-2. Typical measured C-V curves. Beams were fabricated in MUMPs 22. **(a)** Cantilever beam 130 μm long. Only the tip is in contact with the nitride in the regions indicated by the pointers. **(b)** Fixed-fixed beam 340 μm long. Offset voltage is due largely to charging during the voltage sweep.

Adhesion, which holds the beam down somewhat during peel-off, causes the capacitance during peel off to be larger than the corresponding capacitance during zip up as can be seen in Figure 5-2(a) and (b). Accumulated charge in the nitride, and possibly also on the surfaces of the polysilicon beam and nitride, shifts the measured V_{pi}'s and offsets the C-V curves along the voltage axis as shown in Figure 5-2(b). Assuming a sheet of charge in the nitride, the offset voltage was shown in Section 2.3 to be

$$V_{offset} = \frac{z\rho}{\varepsilon_n} \tag{5-1}$$

where ρ is the areal charge density, z is the distance of the charge sheet from the silicon nitride-silicon substrate interface, and ε_n is the permittivity of the nitride. To quantify this charge, V_{pi}'s were measured by applying both positive and negative voltages. Theoretically, the positive and negative V_{pi}'s should be of the same magnitude in the

absence of remnant charge since the electrostatic force is proportional to the square of the applied voltage. The measured differences between the magnitudes were less than 0.4 V after allowing more than 5 min between measurements. The voltage offsets are one-half of those differences. Assuming that all the charge is on the top surface of the nitride, ρ is about 10^{10} e cm^{-2} where e is the charge of an electron. This is roughly the same as the density of trapped charges in the thin-oxide layer of an MOS capacitor. Thus, fixed charge is not a major problem; each V_{pi} and C-V measurement can be adjusted by a small, fixed measured offset.

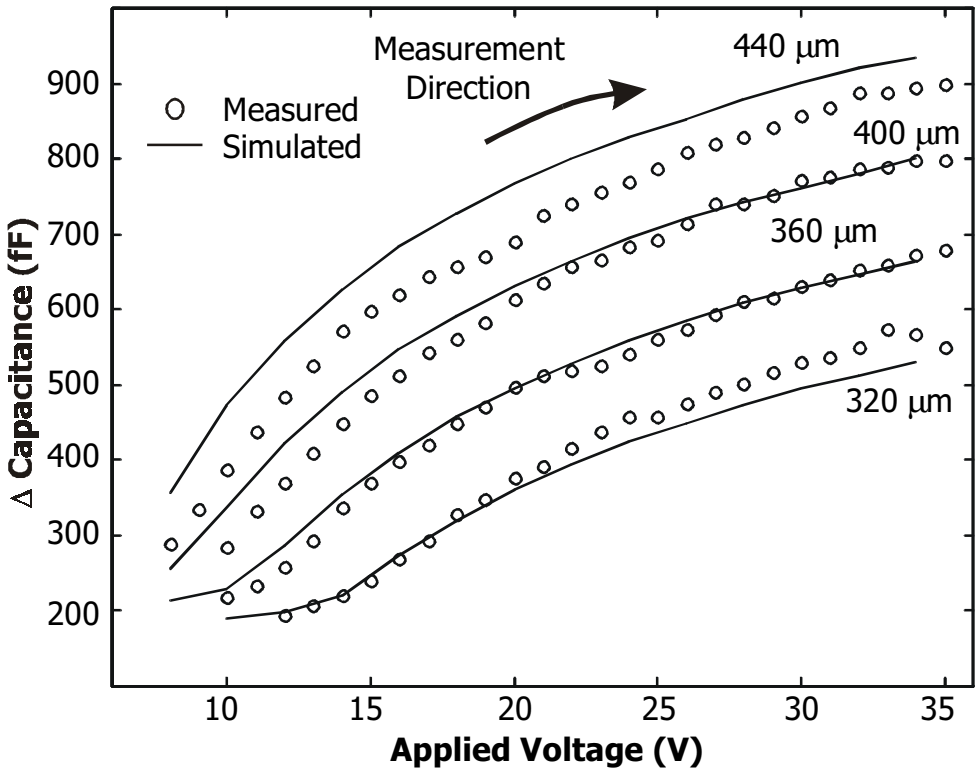

Figure 5-3. Measured and simulated C-V of several beams of different lengths fabricated in MUMPs 29. The general trend is captured by the simulation but the magnitudes are somewhat off.

Mobile charge, however, seriously distorts the measurements. The voltage offset shown in Figure 5-2(b) is rather large (about 2 V) because of charge accumulation during the voltage sweep starting from –35 V. The electric field across the nitride is high during most of the sweep because the beam is in contact with the nitride. For pull-in voltage measurements, however, the sweep starts with the beam in the initial (up) position at 0 V so the electric field is small until pull-in, and hence does not contribute appreciably to

mobile charge before pull-in. The magnitudes of V_{pi}'s measured in quick succession i.e. less than one minute between measurements are progressively either lower or higher. This indicates that charge is being accumulated in the nitride or on the surfaces with each measurement while the beam is in contact with the nitride, hence modifying the voltage required to pull the beam in. The further the charge is away from the silicon nitride-silicon substrate interface, the more influence it has as shown by Equation (5-1). There is no systematic indicator of why successive V_{pi} would increase for a particular beam but decrease for another. It is possible that for this type of measurement, where contact is made and broken several times, most of the charge accumulation occurs at the surfaces of the nitride and polysilicon beam that come into contact. Such surface charge is quickly neutralized when the conductive beam comes into contact with the nitride and is held there, as for the measurements in Section 5.4. As such, the mechanisms for charge buildup that affects pull-in measurements could be different from that affecting in-contact measurements characterized later in this chapter.

In order to avoid charge build up, especially at high voltages above V_{pi}, and to avoid adhesion effects, capacitance measurements were made quickly as the beams were zipping up instead of when the beams were peeling off. It is assumed that adhesion is a very short-ranged force which has no effect until surfaces are in contact, and therefore does not influence the zipping up process where electrostatic forces dominate. While holding the voltage steady at a value well below pull-in but still high enough to hold the beam down once the beam contacts the nitride surface, contact is induced by pushing the center of the beam down carefully with a probe tip. The transition from the state in Figure 5-1(b) to the state in Figure 5-1(e) is effected mechanically. The voltage is then ramped up while capacitance is measured. This zipping-up measurement takes about 10 seconds; results are shown in Figure 5-3.

5.3 Contact Surfaces

5.3.1 Rigid Contact Surface

Simulated C-V curves in Figure 5-3 were generated using the simulation model calibrated in the previous chapter, and assuming a perfectly rigid contact surface between the beam and silicon nitride. The thickness of the nitride was determined from

capacitance measurements of POLY0 pads deposited on the nitride. The simulated curves exhibit the same trends as the measured curves but the capacitance values are a little off. Since the beams and simulation model were well-characterized in the previous chapters, they can be used with confidence to investigate more involved contact electromechanical phenomena.

The simulated capacitances of the 320-μm beam are slightly lower than those measured at high voltages whereas the simulated values of the 440-μm beam are higher all around. A single set of simulation parameters, repeated here for convenience in Table 5-1, could not fit the measured V_{pi}'s and the C-V curves for the four beams, even if all the parameters were varied arbitrarily. Reducing the most influential parameter – the nitride thickness – would reduce all the capacitances, improving the fit for the 440-μm beam to the detriment of the fit for the 320-μm beam. No value of nitride thickness fits all four beams well. Investigations to determine an accurate effective nitride thickness follow.

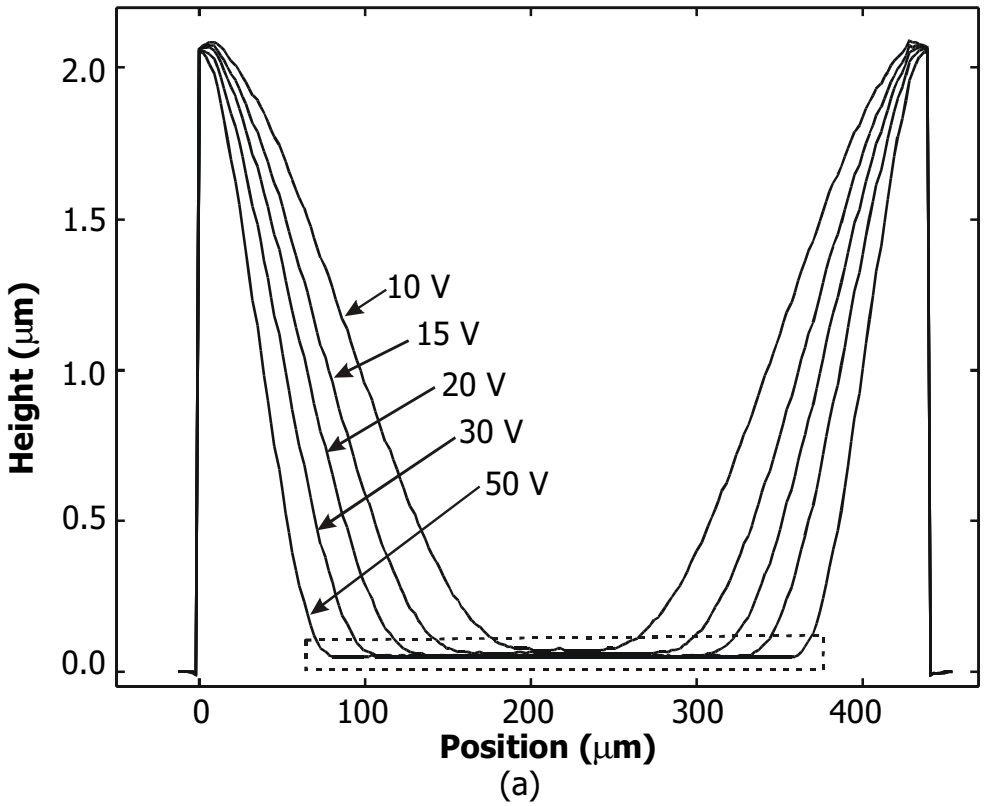

(a)

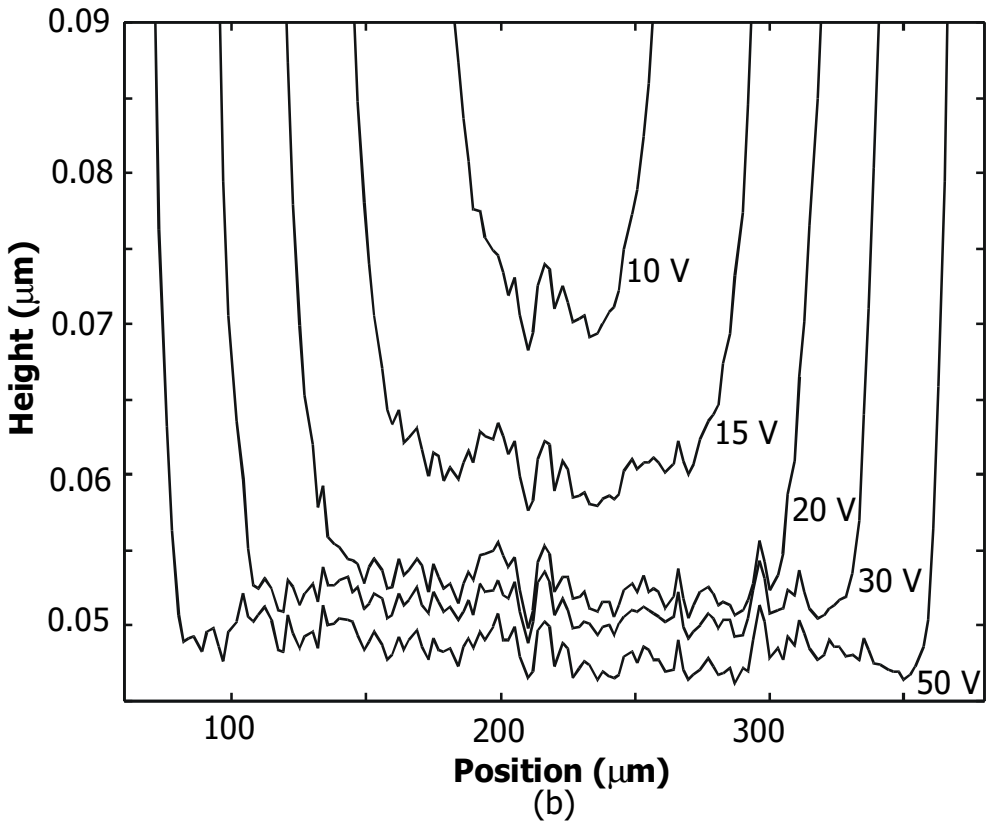

Figure 5-1. (a) Surface profile measurements of a 440-μm-long beam, showing zip-up as the applied voltage increases. **(b)** Close-up of the portion of the beam in contact with the nitride (indicated by the dotted-line box in (a)). The beam moves further downward as the applied voltage is increased. The shape of the roughness is repeatable from measurement to measurement, indicating that the measurement resolution is above the noise floor. The height is referenced to the anchors of the beam.

Table 5-1. Simulation model parameters

Parameter	**Nominal Value**
POLY1 thickness	1.97 μm
Initial gap	1.79 μm
Nitride thickness (electrical)	0.077 μm
Step-up sidewall angle	76°
Step-up sidewall thickness	2.10 μm
Young's modulus	140 GPa
Uniaxial compressive stress	4.83 MPa

5.3.2 Compressible Contact Surface

Surface profile measurements of the zipping up of a 440-μm-long beam are shown in Figure 5-1(a) with a close-up of the portion of the beam in contact with the nitride in Figure 5-1(b). The portion of the beam in contact with the nitride moves downwards as the voltage is increased. This indicates some compressibility of the contact surface and hence variability in the effective gap of the silicon nitride. The higher the voltage, the larger the force that the beam applies to the contact surface and hence the deeper the penetration into the surface. The travel range is almost 20 nm from 10 V to 30 V, beyond which the beam does not travel much more. Unfortunately, capacitance and surface profile measurements could not be made simultaneously because the LCR meter and the Zygo profiler are located in different rooms. The excellent repeatability of the roughness of the measurements indicate that the measurement resolution is above the noise floor. Each profile measurement, each made at exactly the same site, was carefully leveled to consistent reference points so that the profiles could be compared directly.

Measurements of a test structure consisting of a POLY1 beam suspended above the silicon nitride surface by POLY2 tethers, as shown in Figure 5-1, provide another perspective into the source of these discrepancies between measurements and simulations. Variations of this contact surface test structure include the square plates and untethered structures shown in Figure 3-1. A small voltage is required to pull the 400-μm-long by 30-μm-wide beam down to the nitride. Since the mechanical restoring forces of the thin POLY2 tethers are smaller than the surface adhesion forces, the POLY1 plate remains on the nitride even when the applied voltage is reduced back to zero. The capacitance is then measured using the HP4275A LCR meter. The bias voltage is swept from –35V to +35V and back to –35V again. As Figure 5-2 shows, after adjusting for the voltage offset, the capacitance increases as the magnitude of the applied voltage increases. This effect is not expected in theory because the entire beam, which is tethered at the center, should be resting on the nitride and no additional zipping should occur. Any initial curling of the plate due to small stress gradients should be flattened out by an applied voltage of less than 10 V because the electrostatic forces are very large when the plate is on the nitride and the electrical gap is small. Surface profile measurements show

that the POLY1 beam on the nitride is already uniformly flat to within 0.01 μm even without any applied voltage.

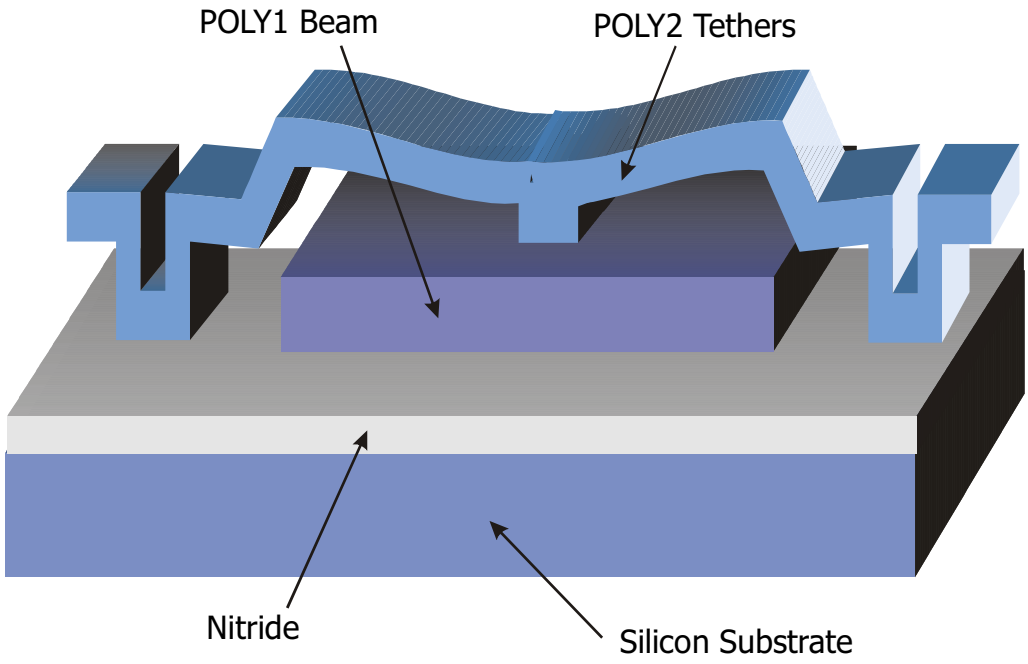

Figure 5-1. Test structure to measure contact surface properties. POLY1 beam is suspended by POLY2 tethers at the middle to eliminate zipping effects.

Assuming that in the absence of zipping, compressibility of the contact surface causes the variation of capacitance, the effective electrical gap between the POLY1 plate and silicon substrate as a function of applied voltage can be computed from the C-V curve, assuming an ideal parallel plate capacitor model. This is shown in Figure 5-3. Fringing fields are negligible at such small gaps. After adjusting for the voltage offset, the effective gap decreases from 100 nm to 91 nm, a change of about 9 nm, as the magnitude of the bias voltage is ramped up from 0 V to 35 V. This calculation assumes that the entire POLY1 plate remains completely flat and does not tilt or bend while moving closer towards the silicon substrate at higher voltages. The compression range is smaller than that shown in Figure 5-1(b). This could be because a flat plate cannot penetrate as deeply as can the center portion of a beam that is being leveraged downwards. The computed gap is larger than the gap computed from POLY0 pad capacitance measurements. This issue is addressed further later in this section.

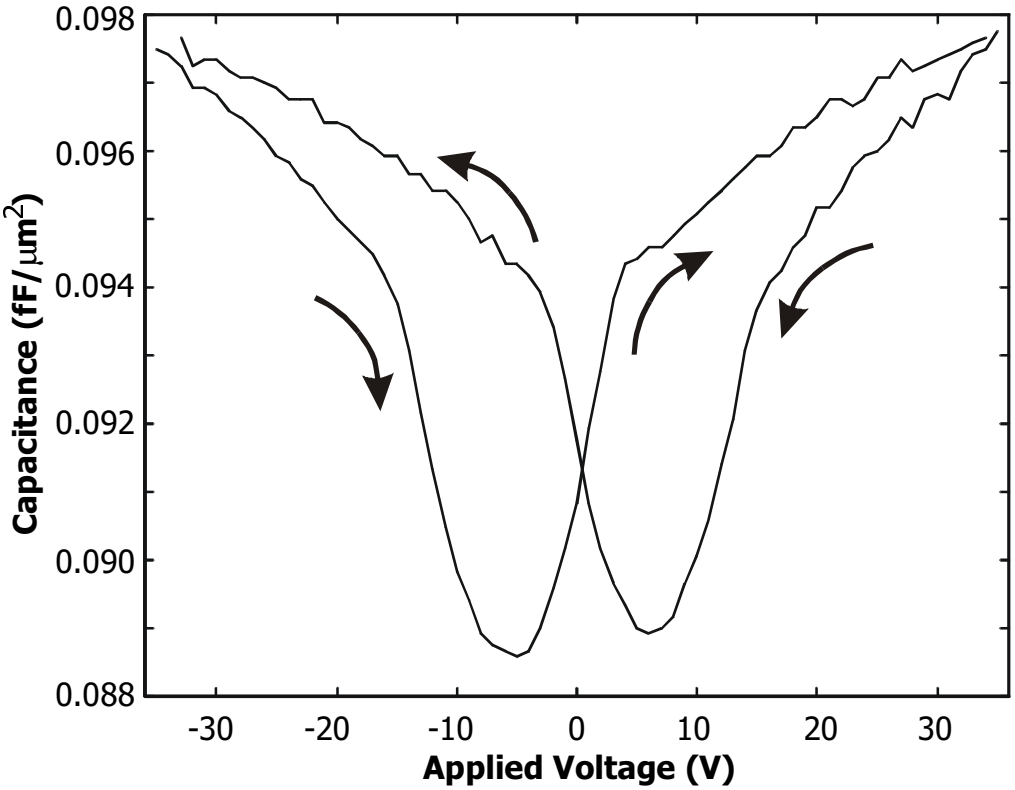

Figure 5-2. Capacitance–voltage measurement of the test structure shown in Figure 5-1. Adjusting for the voltage offset, capacitance increases with increasing magnitude of the applied voltage. The voltage sweep starts from –35 V and goes to +35 V before going back to –35 V as indicated by the arrows.

The illustrative closeup of the surface shown in Figure 5-4 suggests what might be going on. Surface residue – water molecules and microscopic dust – together with asperities increase the effective gap between the polysilicon beam and silicon nitride surface and, hence, with the silicon substrate. As the voltage is increased, the residue compresses and the effective gap decreases. Since polysilicon is a hard material, the asperities themselves are unlikely to deform but the regions between the highest asperities can deflect closer towards the substrate. The surface roughness on the underside of POLY1 depends on the roughness of the PSG on which it is deposited, which in turn depends on the roughness of the silicon nitride. The nitride surface was roughened by the RIE etch that removed the POLY0 layer. The final HF release etch can also contribute to surface roughness by overetching the POLY1 beam especially at grain boundaries [61], [74], [96]. Atomic Force Microscope (AFM) measurements of the underside of a polysilicon layer reveal roughness on the order of 20 nm [94]. Since the

deformation is assumed to occur between the highest asperities, the peak roughness value is of most interest and not the rms roughness. It is difficult to image movable residue such as dust and microscopic water droplets with an AFM, however.

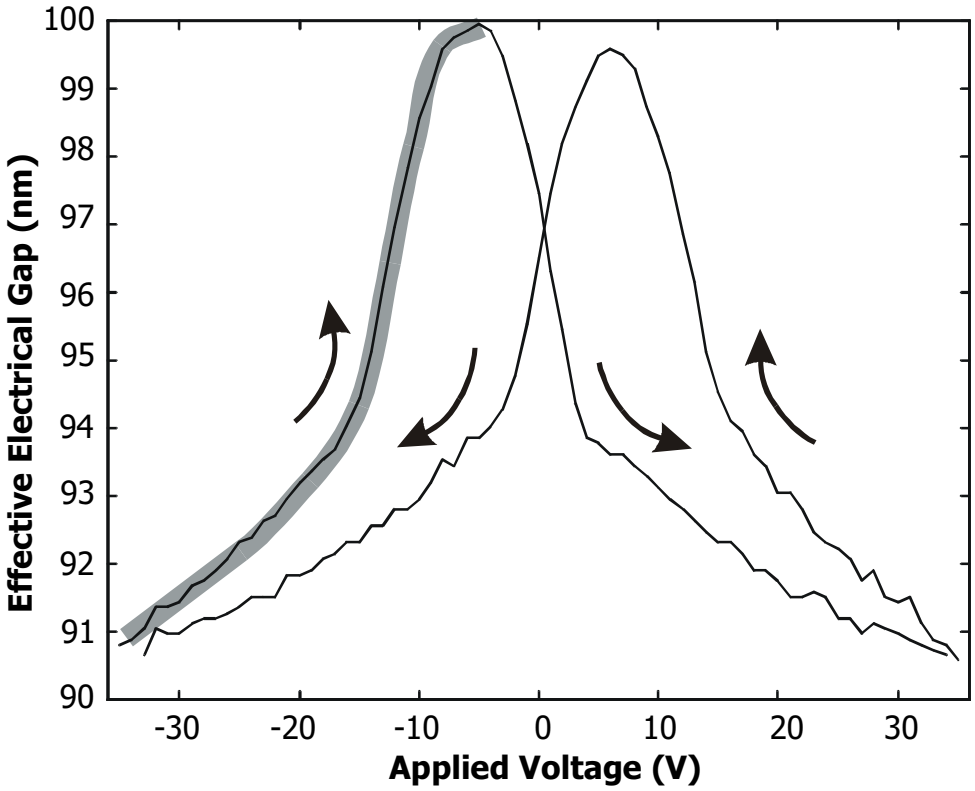

Figure 5-3. Gap-voltage plot derived from C-V measurement of Figure 5-2 assuming ideal parallel-plate capacitor model. The stiffness profile of Figure 5-7 corresponds to the shaded portion of this plot.

The contribution of electronic effects to the measured C-V characteristic is investigated via Medici [97] simulations. The high frequency C-V characteristics of a polysilicon-nitride-silicon capacitor (Figure 5-5) is shown in Figure 5-6. The three curves are of cases where the capacitor system consists of:

1. only the beam, nitride and substrate
2. the beam, surface layer, nitride and substrate
3. the beam with a connection to a p-well, surface layer, nitride, and substrate

As noted in Section 3.4, the capacitance between the silicon substrate and a POLY1 pad deposited directly on the nitride surface does not change as the bias voltage is swept from –35 V to +35 V. This corresponds to the first curve of the simulation which is almost flat.

The curve would be flatter if the doping density of the polysilicon were increased from the conservatively low 5×10^{18} cm^{-3} used in the simulations. If a thin (0.15 μm), more-lightly doped (5×10^{16} cm^{-3}) surface layer is included in the system, that surface layer can deplete leading to lower capacitances as indicated by the second dotted line. Such a surface layer could possibly occur in the unpassivated surface of the beam after the HF release etch. Unlike the measured C-V characteristic, this curve is not roughly symmetric about $V_{applied} = 0$. If the beam is connected to a p-well, the well can supply charge to the inversion layer producing the third curve. Although this curve resembles the measured C-V curve of Figure 5-2, this scenario is unlikely because the p-well will have to be connected to the portion of the beam that is in contact with the nitride. No p-type dopants were introduced into the system during fabrication. Hence the observed variation of capacitance with voltage must be due, at least primarily, to mechanical effects.

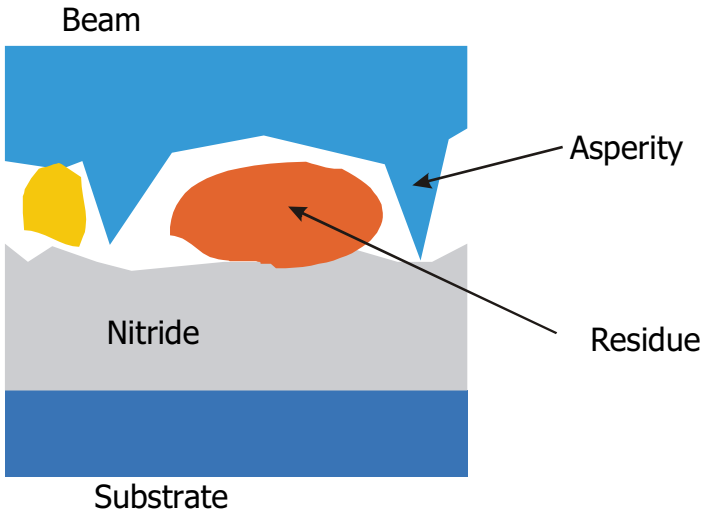

Figure 5-4. Closeup of surface showing residue and asperities. Effective stiffness of contact surface is due to the averaged hardness of distributed particles on the surface, not to the hardness of any particular material.

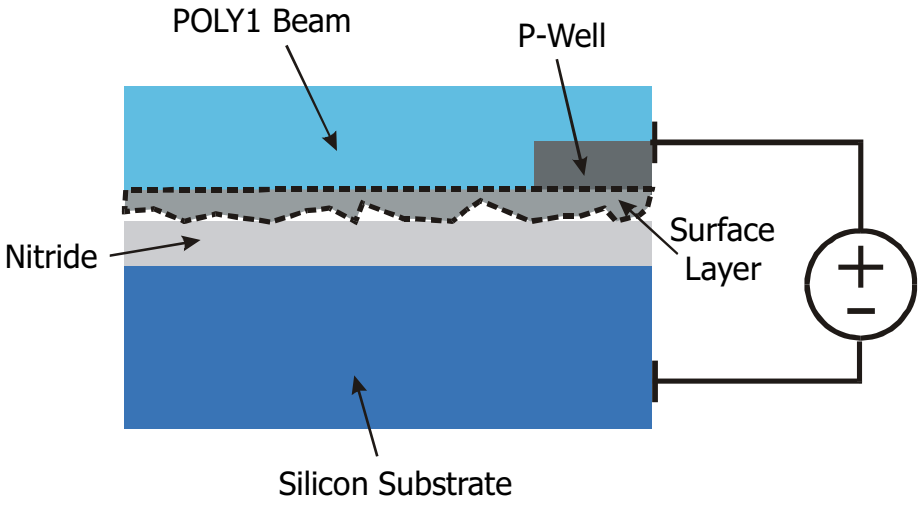

Figure 5-5. Polysilicon-nitride-silicon capacitor. An unpassivated surface layer could behave like a more lightly doped region, contributing to depletion effects shown in Figure 5-6. The location of the p-well is shown only schematically, and could be located anywhere near the region of the POLY1 beam that is in contact with the nitride.

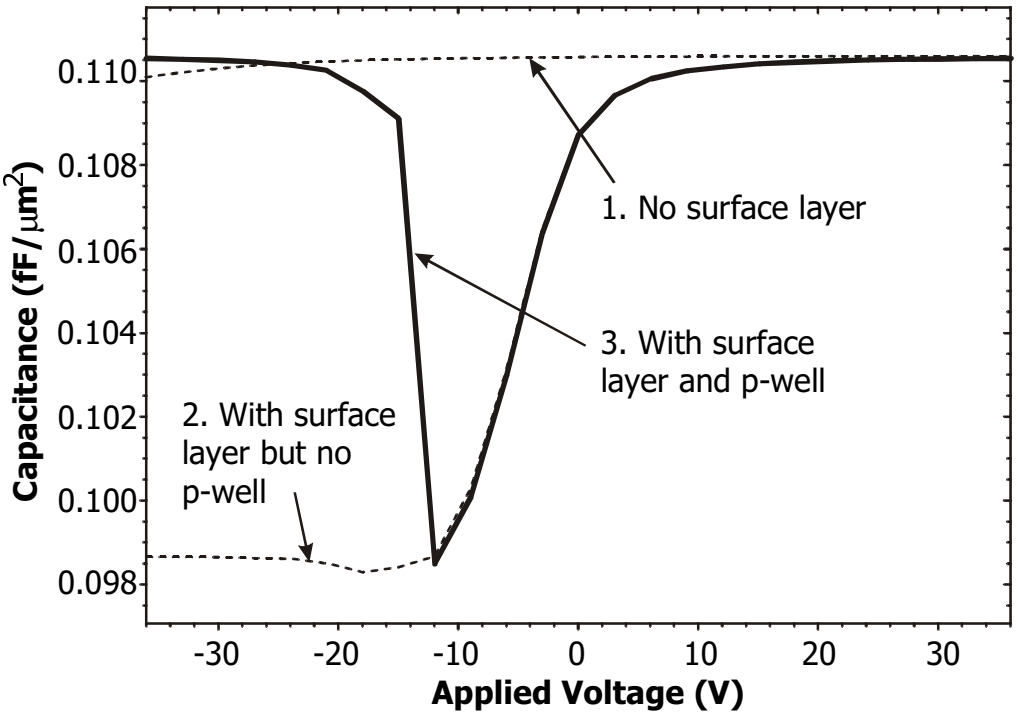

Figure 5-6. Capacitance-voltage characteristic of polysilicon-nitride-silicon capacitor. The nitride is 0.6 μm thick with a relative permittivity of 7.5. The polysilicon is doped n-type with a density of 5×10^{18} cm^{-3}. The surface layer, if present, has an n-type dopant density of 5×10^{16} cm^{-3}. The p-well, if present, has p-type dopants of density 5×10^{18} cm^{-3}.

Whatever the mechanisms behind this compressible behavior, the effects can be incorporated into the Abaqus simulation model as “softened” or compressible contact

surface behavior. The gap-voltage relationship of Figure 5-3 can be manipulated into a stiffness profile for the contact surface as shown in Figure 5-7 using the equation that describes electrostatic pressure, *P*, as a function of applied voltage, *V*, and effective electrical gap, *g*,

$$P = \frac{\varepsilon_0 V^2}{2g^2}. \tag{5-1}$$

Surface stiffness or reaction pressure is plotted as a function of the effective electrical gap. In the simulations, as the beam approaches the "true" rigid contact surface, which is the surface of the silicon nitride, the reaction forces increase, eventually stopping further penetration. For comparison, atmospheric pressure is on the order of 1×10^5 Pa. This surface reaction pressure does not describe the hardness of any particular material but is the effective hardness of a surface speckled with residue and asperities, much like the stiffness of a bed surface is the hardness of an array of steel coils distributed under the surface and not the hardness of steel itself.

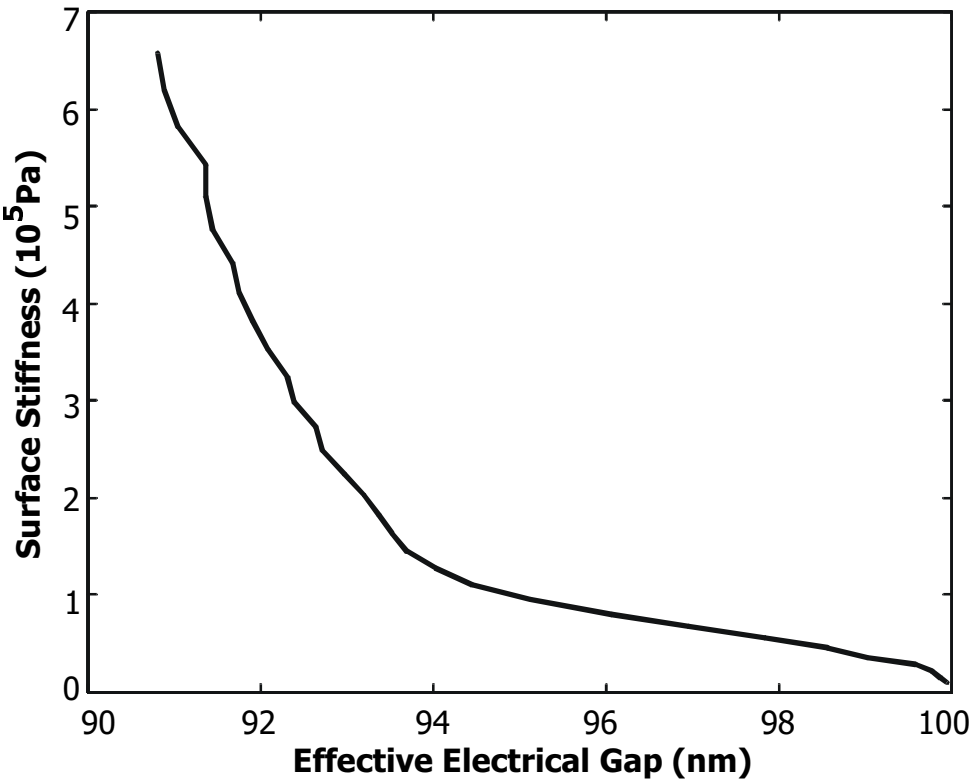

Figure 5-7. Compressible contact surface profile (surface stiffness vs. effective electrical gap) derived from C-V measurements.

The surface profile used in subsequent simulations is similar to that shown in Figure 5-7 but modified to obtain the best simulation fit to the measured C-V curves. The general shape of the profile is maintained but the effective gap shifted lower. The compressible surface model is easily incorporated into the Abaqus simulation and generates the C-V curves of Figure 5-8. The fit is much better in the lower voltage range (< 20 V) which is where most of the compression occurs. However, the spacing between the measured C-V curves for the various beams is smaller than the spacing in the simulations.

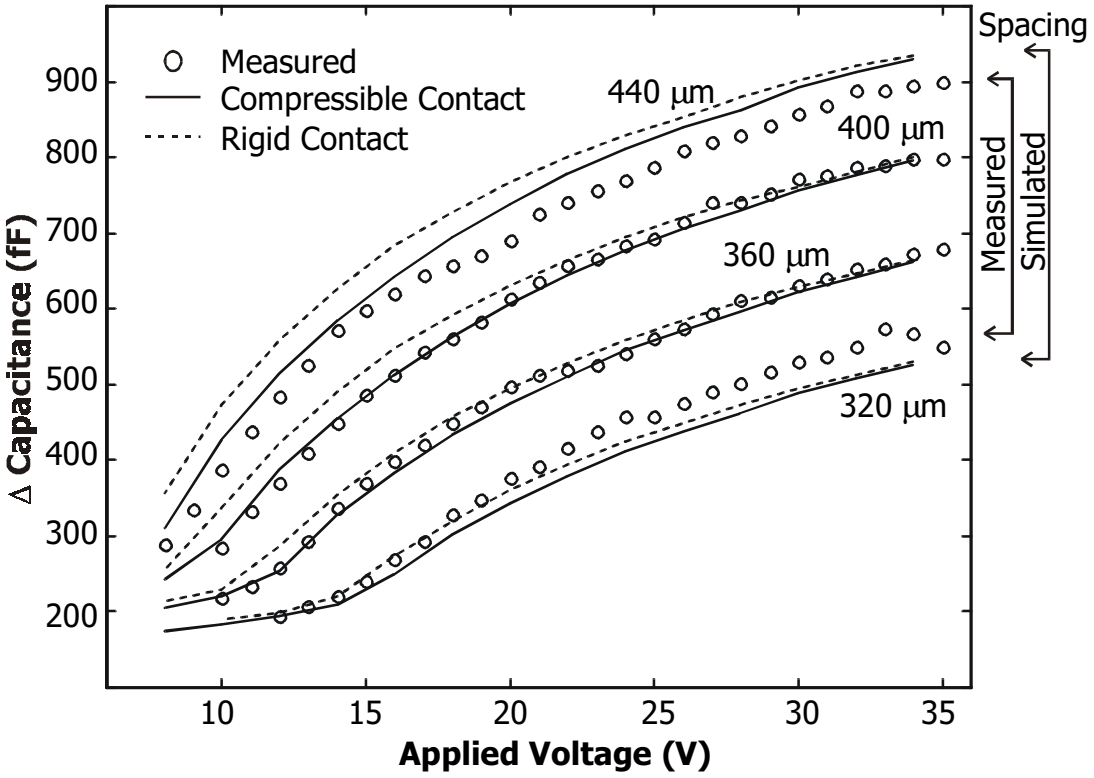

Figure 5-8. Simulated C-V of beams using compressible contact surface model. The fit is improved at the lower voltages. At higher voltages, the simulated spacing between the capacitance of the beams is larger than that measured.

The simulated profiles of the 320-μm, 360-μm, 400-μm and 440-μm-long beams at 34 V are shown in Figure 5-9, with the anchor step-ups aligned horizontally but the vertical displacements offset slightly. The profiles of all the beams near the step-ups are very similar (the profiles would overlap if not for the vertical offsets added) implying that the difference in capacitance between two beams at any given voltage is simply the capacitance due to the difference in length i.e.

$$\Delta C = \frac{\varepsilon_0 W \Delta L}{g_1}. \tag{5-2}$$

W is the width of the beam, ΔL is the difference in beam lengths, and g_1 is the electrical thickness of the nitride. As a result, the spacing between the simulated C-V curves for any two beams is constant with voltage after 20 V. The thickness of the nitride computed from C-V measurements using (5-2) is approximately 0.097 μm, which is in the ballpark of that shown in Figure 5-3. Using this value for nitride thickness produces the simulated curves of Figure 5-10. The fit is poor except that the simulated spacing between the C-V curves matches the measurements. Assuming that (5-2) provides an independent measure of the effective gap for capacitance at high voltages (> 20 V), this suggests that the effective gap for capacitance is larger than the effective gap for electrostatic force. This could be due to a parasitic series capacitance near the surface layer that effectively reduces the magnitudes of all the measured capacitances.

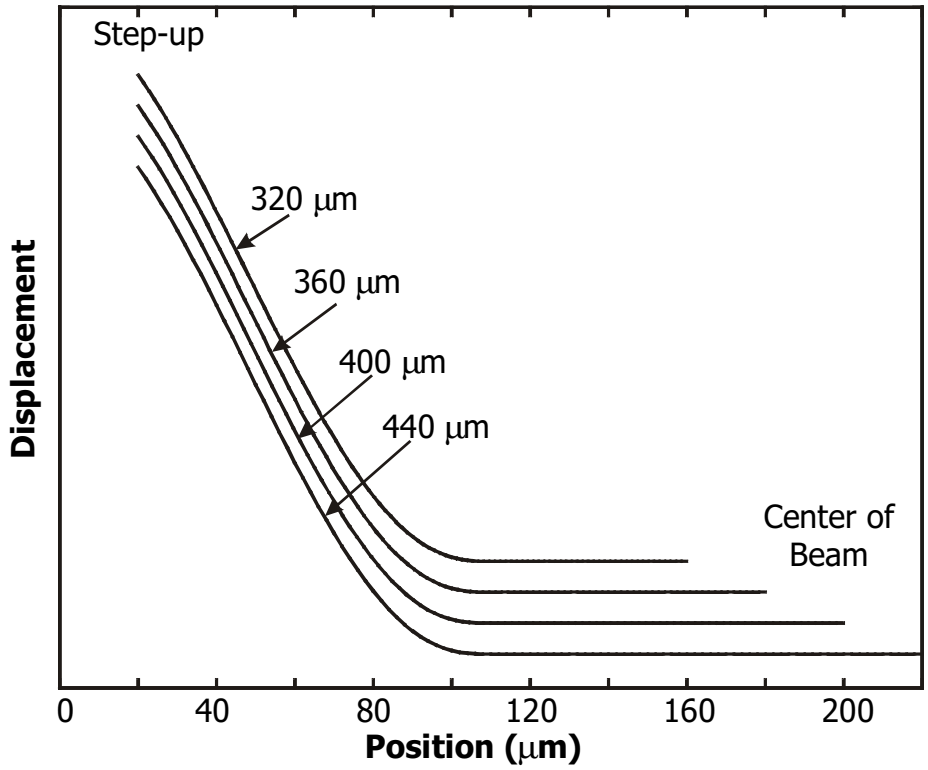

Figure 5-9. Profiles of the left halves of four beams of different lengths, at the same applied voltage (34 V). The profiles, which would otherwise all overlap, are offset vertically from one another. The profiles near the step-ups are exactly the same, indicating that differences in capacitance between beams at any voltage are directly proportional to the differences in beam lengths only.

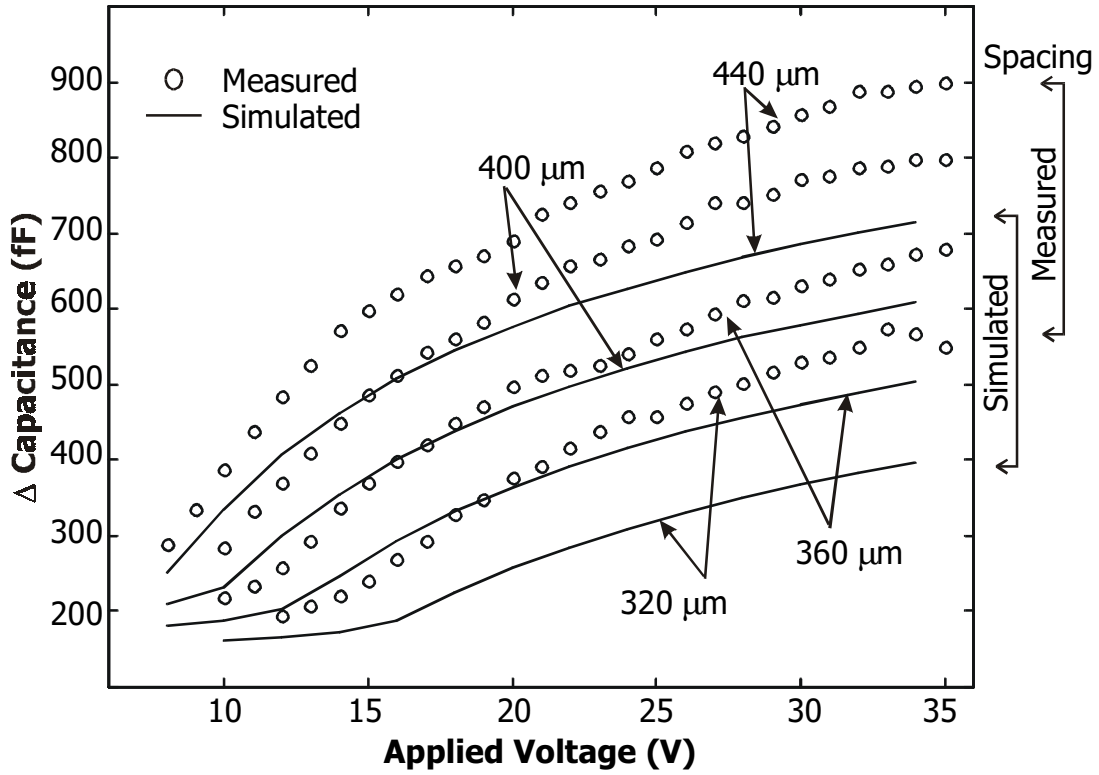

Figure 5-10. Simulated C-V using the larger nitride thickness which fits the measured spacing between the capacitance curves at high voltages. However, the overall slope of the curves are too gradual.

5.4 Dielectric Charging

The effects of mobile charge were introduced in Section 5.2.2 as causing pull-in voltages measured in quick succession to be progressively lower or higher. Another related effect is the increase in capacitance as a function of time as the beam is in contact with the nitride at a constant voltage, as shown in Figure 5-1. The curves for a 340-μm beam at three different applied voltages are shown. The measurements were made using a 100-kHz 50-mVrms sensing signal from the HP4275A LCR meter, but the measurements show no dependence on signal amplitude or frequency. Charge builds up over time in the nitride when the beam is in contact with the nitride surface. The polarity of the charge is opposite to that on the beam thus attracting more of the beam into contact i.e. increasing zipping, thus, increasing the capacitance of the system as illustrated in Figure 5-2. Continued zipping over time is shown in the measured profile of a 360 μm beam with a constant 16 V applied (Figure 5-3).

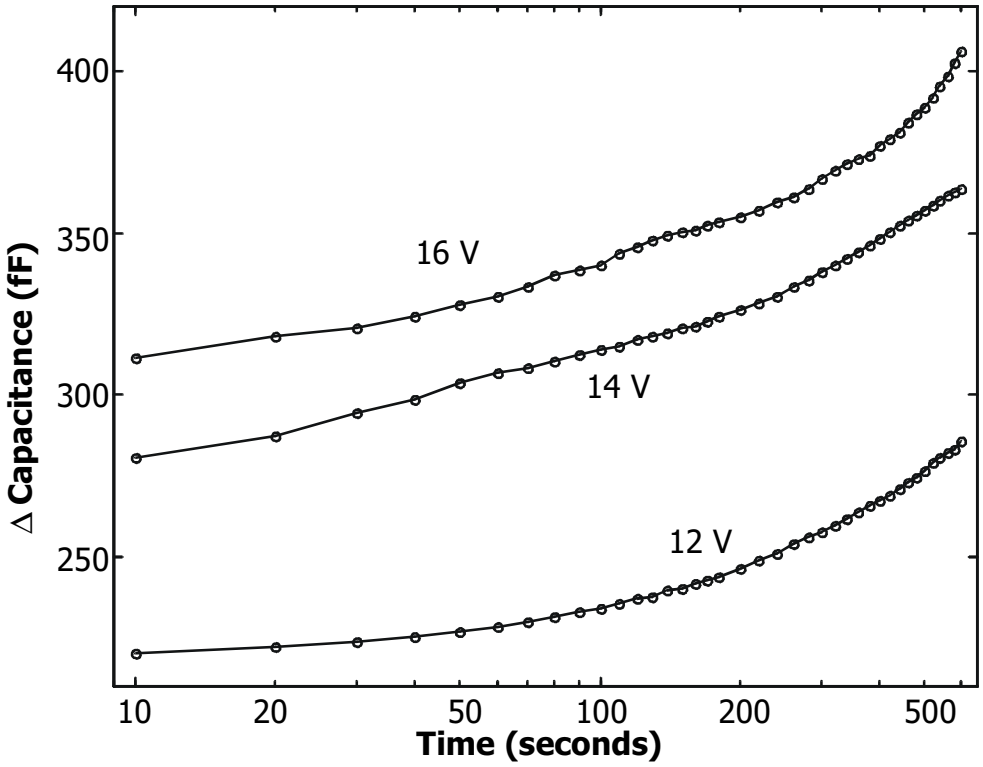

Figure 5-1. Measured capacitance increases over time at constant applied voltages. The beam is 340 μm long and fabricated in MUMPs 29.

The dependence of memory on polarity indicates that the continued deformation with time is due to electronic effects rather than mechanical creep. In an experiment to confirm this, +35 V was applied to the beam for about a minute causing the capacitance to increase. The capacitance was measured, and then the voltage removed to allow the beam to pop back up. When +35 V is applied again, the measured capacitance is close to the final capacitance measured previously, but if –35 V is applied, the measured capacitance is much lower. This can be explained by shielding due to accumulated charge. No such polarity dependence is expected if the deformation over time is due entirely to mechanical phenomena. If mechanical creep is the cause, applying the same electrostatic force by using different polarities should produce the same capacitance. Note that the electrostatic force is always attractive and proportional to the square of the applied voltage. Capacitance always increases with time in contrast to the V_{pi} measurements which can increase or decrease. This suggests that two different types of charge accumulation occur – accumulation at surfaces, which is highly variable, and

accumulation in the bulk of the nitride, which is governed by charge injection as will be shown later.

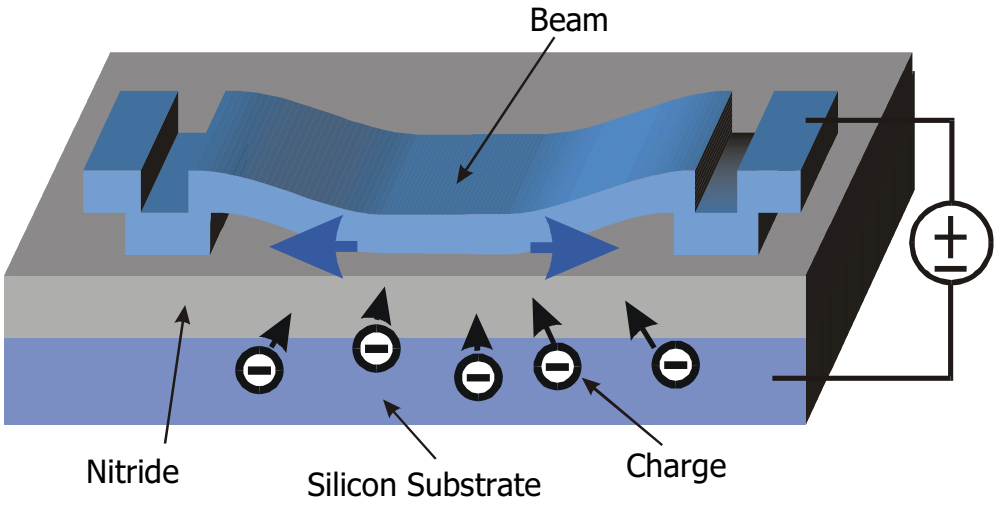

Figure 5-2. Charge buildup in the nitride increases the attractive force on the beam and increases zipping.

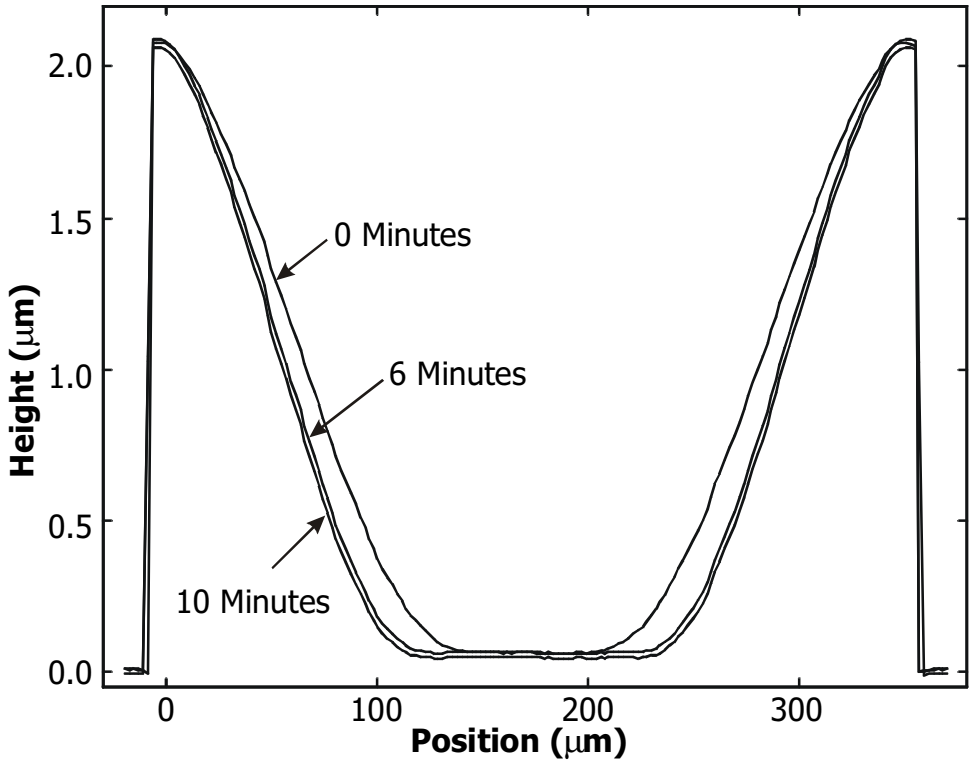

Figure 5-3. Measured profile of a 360-μm-long beam with a constant 16 V applied. The beam zips up more as time passes.

Ordinarily, determining the charge stored on the plates of a capacitor requires knowledge of both the capacitance and voltage across that capacitor. For this contact-electromechanical capacitor, however, the high-frequency small-signal capacitance has a one-to-one correspondence to the charge on the polysilicon beam, which in turn depends on the charge on the silicon substrate and nitride dielectric. The shape of the beam, and thus the capacitance of the system, depends on the charge on the polysilicon beam. The system functions as an electrometer. A more mathematical description can be found in [98]. Hence, the charge on the polysilicon beam can be determined from measurements of capacitance alone regardless of the applied voltage. It is important to note that the beam charge can change even when the applied voltage is held constant if charge accumulates in the dielectric. Knowing the charge on the polysilicon beam, charge in the nitride dielectric can be determined.

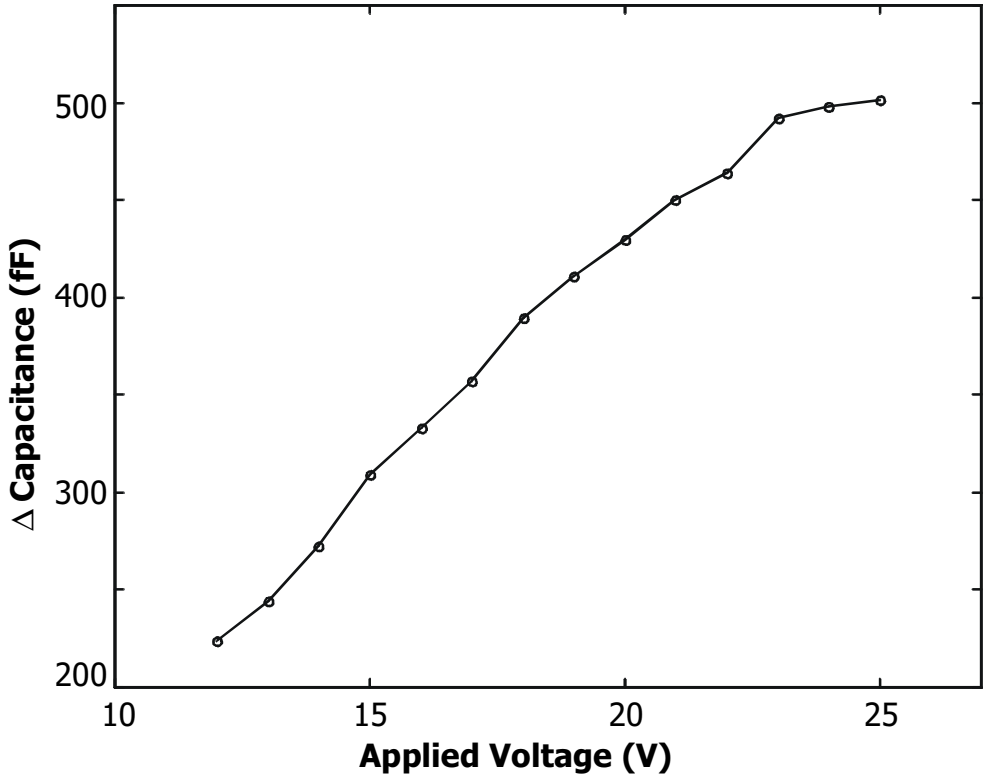

(a)

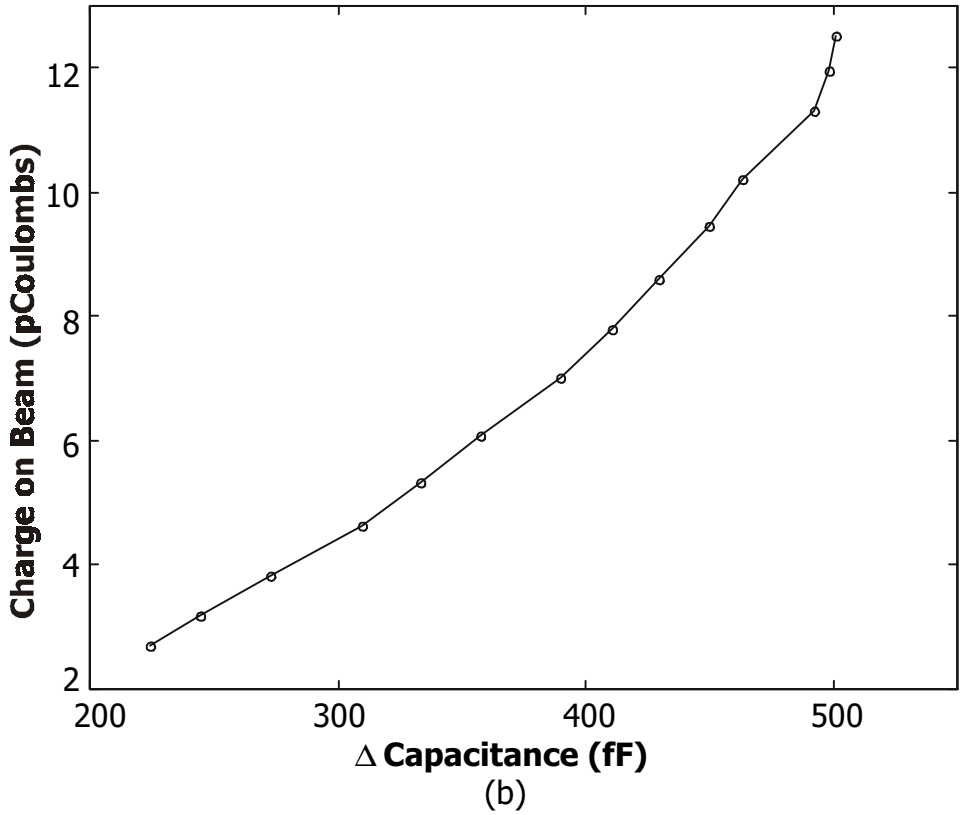

Figure 5-4. (a) Measured capacitance as a function of voltage for a 340-μm-long beam. **(b)** Charge vs. capacitance curve derived from (a).

Using the "push down" measurement technique described in Section 5.2.2, the C-V measurements of a 340-μm-long beam (Figure 5-4(a)) are assumed to be free from the influence of accumulated nitride charge. If dielectric charge can thus be neglected, the charge on the polysilicon beam at any voltage is simply the product of the capacitance and applied voltage. Therefore, beam charge can be computed as a function of voltage, and then as a function of capacitance (Figure 5-4(b)). The charge-voltage relationship only holds if dielectric charge is negligible. Assuming this is true, the resultant charge-capacitance relationship can then be used even in the presence of dielectric charge because capacitance is a unique function of beam charge. The capacitance measurements of Figure 5-1 are converted using the charge-capacitance relationship into the beam charge data shown in Figure 5-5. Since the charge-capacitance curve is obtained directly from data with no smoothing, all irregularities in beam behavior are faithfully preserved in the data transformation.

The increase in beam charge is directly proportional to the buildup of charge in the nitride dielectric – the contact electromechanical capacitor functions as a charge monitor. The effective voltage of the force acting on the beam is plotted in Figure 5-6. The voltage can drift by one to two volts over the course of a few minutes. The initial voltages are not exactly the applied voltages because of remnant charge in the nitride after several repeated charging measurements with both positive and negative voltages applied.

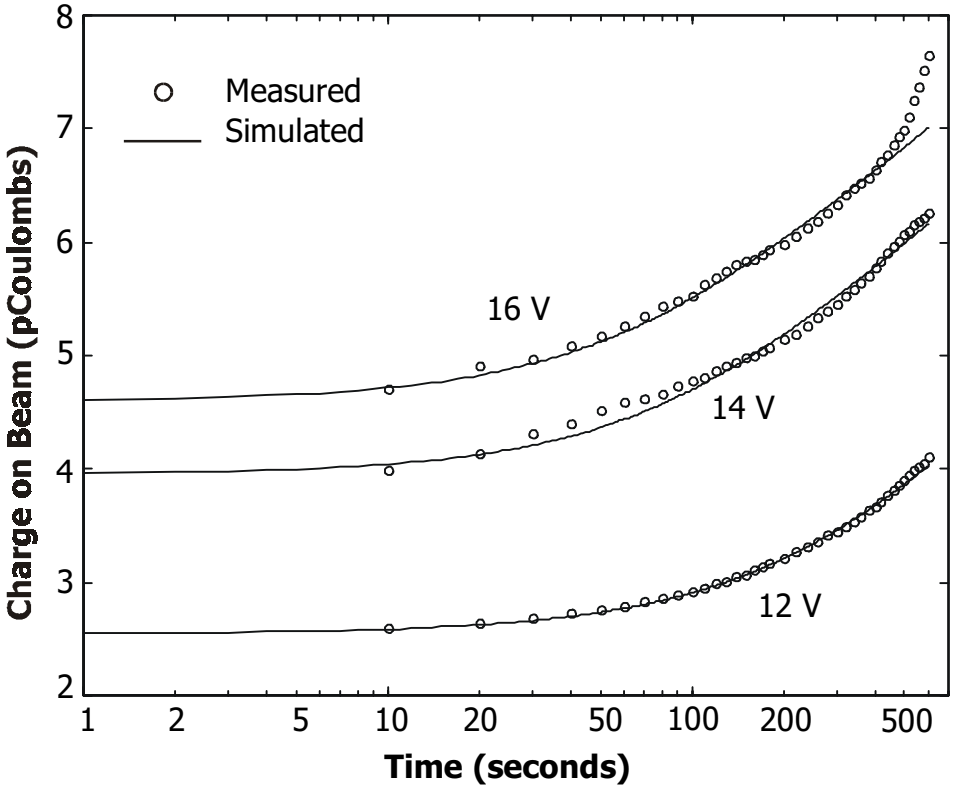

Figure 5-5. Charge buildup as a function of time. The curve fit comes from integrating (5-1), which describes charge accumulation through direct tunneling into the nitride.

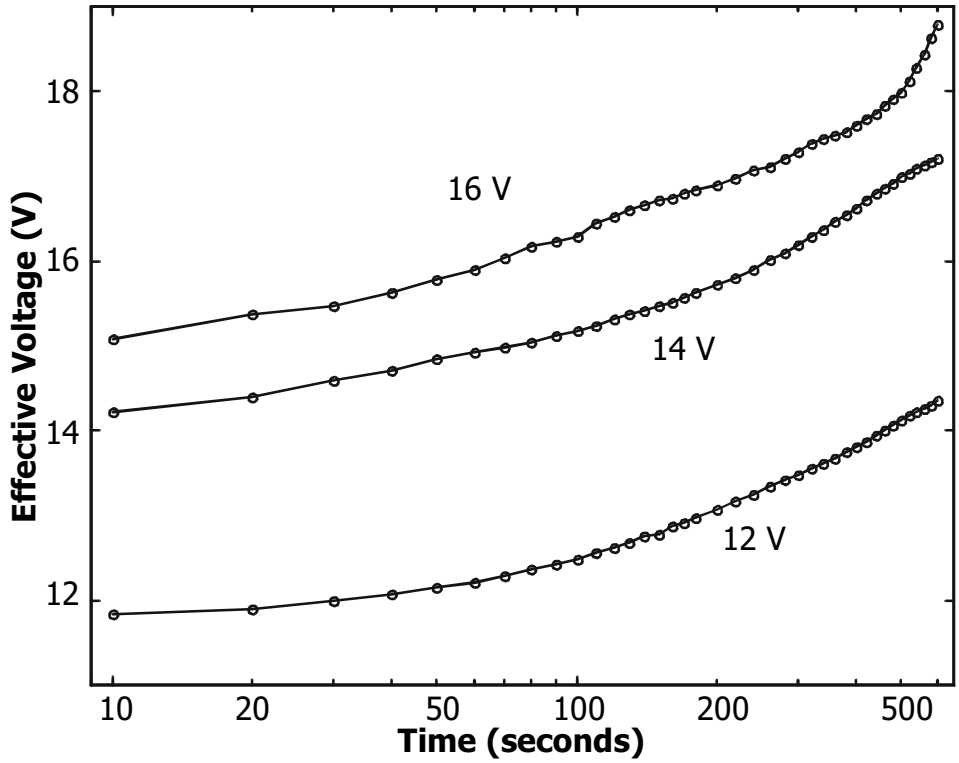

Figure 5-6. Effective voltage of electrostatic forces acting on beams as a function of time, parameterized by applied voltage. Charge buildup increases the attractive force and hence the effective voltage on the beam. The initial (time = 10 s) voltages are not exactly the applied voltages due to remnant charge in the system after repeated charging measurements with both positive and negative voltages applied.

The charge buildup can be modeled by a charge generation equation

$$\frac{dQ}{dt} = kA\left[\frac{1-\exp\left(-t/t_0\right)}{t}\right] \tag{5-1}$$

where k is a scaling parameter, A is the area of the beam that is in contact with the dielectric, t is time, and t_0 is a time constant. This equation describes the charge transfer rate by direct tunneling between either the conduction or valence bands of the silicon substrate into trap states in the nitride [99]. The energy band diagram of Figure 5-7 illustrates one possible tunneling process. Charge buildup is assumed to occur directly under the area of the beam that is in contact with the nitride, which is roughly proportional to the measured small-signal capacitance. The net charge is of polarity opposite to that of the polysilicon beam because the potential barrier to tunneling is

smaller on the silicon substrate-silicon nitride side compared to the silicon nitride-polysilicon beam side due to the finite air gap on the beam side, even after contact. The charging rate depends on charging history, remnant charge and applied electric field, and also on material properties such as stoichiometry and interface conditions. The integration constant resulting from integrating (5-1) quantifies the initial charge in the system including the remnant charge after repeated prolonged applied electric fields. It cannot be determined from these measurements whether the mobile species are electrons or holes. The time constants for (5-1) extracted from measurements of two beams at three different voltages are shown in Table 5-1. No general trends can be inferred from these constants since the same initial conditions of the system after repeated measurements cannot be reproduced, and the measurement data is very noisy.

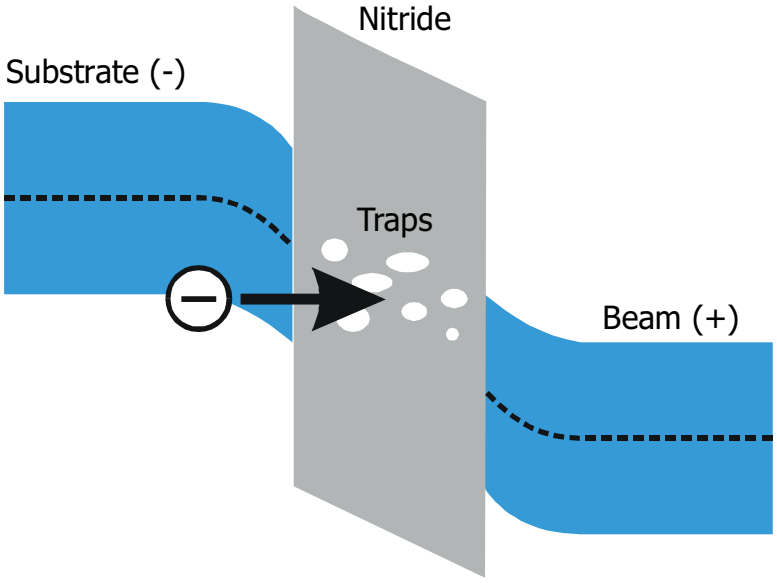

Figure 5-7. Energy band diagram describing direct tunneling of electrons from the valence band of the substrate into trap states in the nitride.

5.5 Summary

Well-characterized polysilicon beams were used as in-situ probes to understand contact electromechanical phenomena. Compressible surface behavior was demonstrated and measured using the Zygo surface profiler and test structures that eliminate zipping. The apparent compressible behavior was then incorporated into the Abaqus simulation model. The simulation fit to measurements improved at low voltages but the

discrepancies at higher voltages suggest that there could be additional series capacitance. Charge buildup over time was characterized using the beams as electrometers, and shown to correspond to charge injection through direct tunneling. The observed bipolar drift in pull-in voltages imply that another mechanism for charge accumulation exists, primarily at contact surfaces. All these surface effects are not easily nor precisely controllable, however, making them difficult to exploit in designs. As such, most electromechanical devices either avoid contact issues altogether or attempt to minimize the effects.

Table 5-1. Time constants of charge buildup

Beam Length (μm)	Applied Voltage (V)	Time constant (seconds)
340	12	190
340	14	80
340	16	60
360	12	55
360	14	60
360	16	80

Chapter 6 Electrostatic Actuator with Extended Travel

6.1 Overview

Micromechanical electrostatic actuators typically have a travel range limited to one-third to one-half of the initial gap. A method or mechanism to extend that travel range, preferably to the extent of the entire initial gap, is highly desirable, especially for optical applications. Such a method will increase the tunable range of an optical device such as a micromechanically-tuned laser [100]. This method will also enable the continuous analog control of a positioner instead of the limited on-off behavior that avoids teetering near the threshold of instability.

Several methods have been suggested that extend the usable range of electrostatic actuators, including closed-loop voltage control [101], series feedback capacitance [102]-[103] and "leveraged bending" [83]. Leveraged bending is the simplest method of the three, requiring that the electrostatic force be applied between the fulcrum (typically the anchor) and the segment of the beam that should be deflected. This is similar to the design of the dual-bias-electrode structure of Section 4.8 except that the electrodes are moved further away from the center of the beam to allow the center of the beam to touch down before pull-in occurs. Mechanical advantage and increased device area are traded

off for the increased range of motion. The closed-loop controller is much more complicated – requiring accurate and fast monitoring of the position of the movable element, and feedback control circuitry to stabilize the system in the unstable regime. No fabricated devices have been demonstrated to date. The series feedback capacitance method employs a capacitor in series with the electrostatic actuator to extend the effective electrical gap of the actuator. That way, the movable element can travel up to one-third of the new effective gap, which is larger than the entire initial gap of the original actuator. The concept is simple and the resultant device is compact – not any larger than a conventional device – but the practical design issues, neglected by Seeger et al., require attention.

In this chapter, the realistic design issues involved in designing a full-gap positioner are presented along with measurements of fabricated devices and analyses of their performance. After introducing the theory of operation of the device, the effects of parasitic capacitances, both from layout and from operation, are discussed. Over-stabilization is shown to improve dynamic or transient performance. A "folded capacitor" structure is introduced that limits parasitics, is easy to fabricate in MUMPs, and does not take up much more die area than a conventional device. The first measurements of an electrostatic actuator incorporating a series capacitor are presented. The actuator can travel beyond the conventional limit but is ultimately limited by tilting instabilities. This instability is analyzed further and shown to be a fundamental limit to performance. The idea for incorporating a series capacitor into an electrostatic actuator originated, independently of [102], albeit later, from measurements of POLY1 devices actuated over POLY0 pads. The goal was to exploit the capacitive coupling among devices in an array that was causing spurious actuation.

6.2 Series Capacitor Feedback

Figure 6-1(a) is a schematic of a conventional electrostatically actuated micromechanical actuator. The movable electrode moves under voltage control up to one-third of the initial gap. If actuated beyond that threshold, the movable electrode snaps down onto the bottom electrode. If the goal is to achieve a travel range of g_0, then the initial gap can be extended to 3 g_0 as shown in Figure 6-1(b) to have a stable region of up

to g_0. This design, however, is not very satisfactory because it requires a large gap that can be difficult to fabricate. Noting that this configuration is actually two capacitors in series, the additional 2 g_0 gap can be replaced with an equivalent series capacitor as shown in Figure 6-1(c). The electric field configuration is maintained; hence, the movable plate can traverse the entire g_0 gap stably. The voltage required to actuate the movable plate increases with the addition of the series capacitor because the total initial effective electrical gap is three times as large as the original. The expression for V_{pi} as a function of initial gap, (2-9), shows that this translates into a pull-in voltage $3^{3/2}$ times the original V_{pi}. Since the additional gap must be at least twice the original gap for stable full-gap travel, the equivalent series capacitance must be less than one-half the initial capacitance of the original actuator, c_0^i. The idea is simple, but the challenge is to maintain the simplicity in the face of nonidealities.

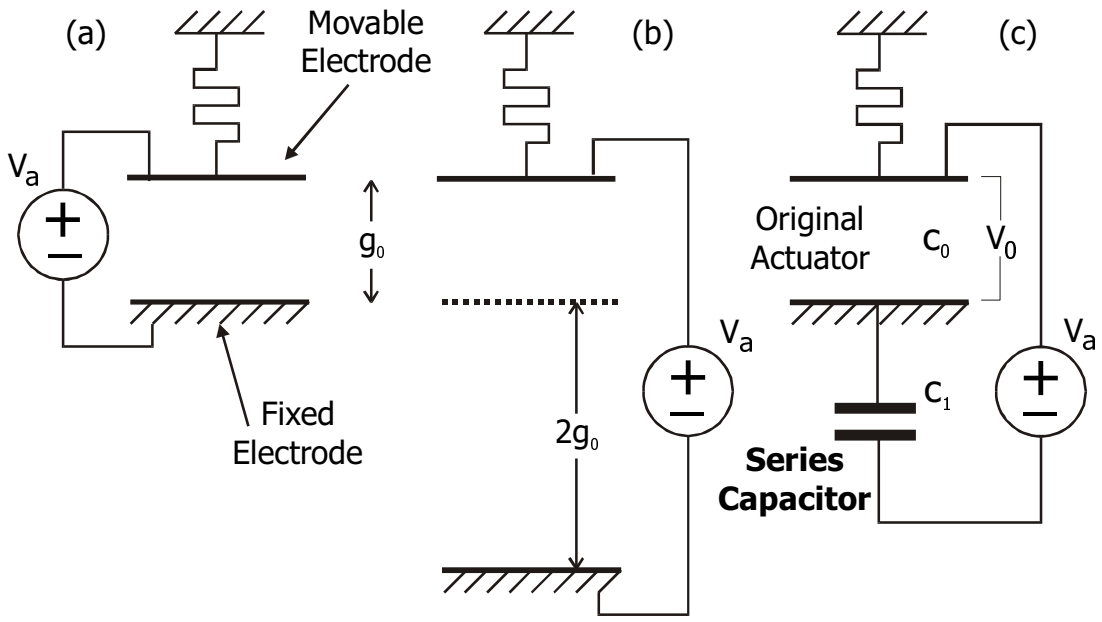

Figure 6-1. Electrostatic micromechanical actuator. **(a)** Conventional actuator with limited range of travel. **(b)** Actuator with extended gap and, hence, extended range of travel. **(c)** Actuator with series capacitor that is equivalent to design in (b). The series capacitor and original actuator form a voltage divider that provides negative feedback to stabilize the system.

The original actuator and series capacitor form a voltage divider circuit. As the movable electrode approaches the fixed electrode, the capacitance of the actuator increases, thus decreasing the fraction, V_0, of the total applied voltage, V_a, that is imposed across the actuator according to

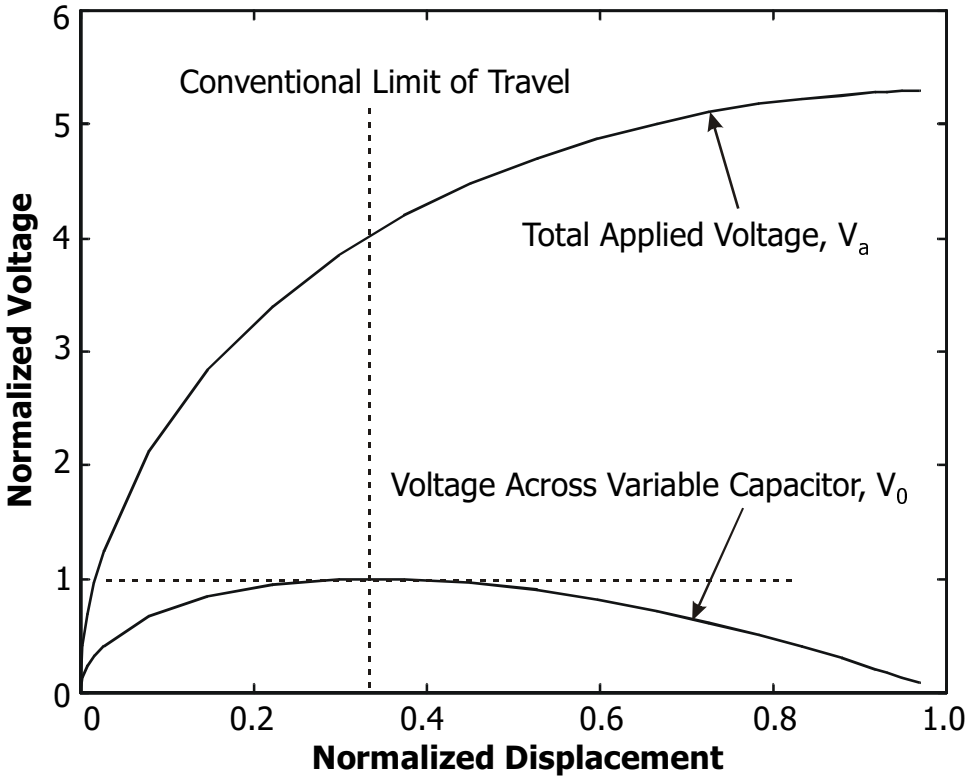

Figure 6-2. Voltage (normalized to original pull-in voltage) across variable capacitor (original actuator) and total applied voltage (also normalized) as a function of the displacement (normalized to the initial gap g_0). Series capacitor is one-half the original actuator capacitance. Actuator can travel the entire gap stably.

$$V_0 = \frac{c_1}{c_0 + c_1} V_a \tag{6-1}$$

where c_0 is the variable capacitance of the original actuator and c_1 is the series capacitance. When the movable electrode goes beyond one-third of the original gap, the rapid increase in capacitance provides the negative feedback necessary to stabilize the actuator so it can traverse the entire gap stably. Figure 6-2 shows how the voltage across the actuator changes as the total applied voltage is increased, assuming a linear mechanical restoring force. Initially, V_0 increases with V_a, with the rate of increase decreasing as c_0 increases, as indicated by (6-1). Beyond one-third of the initial gap where V_0 equals the original V_{pi}, V_0 actually starts to decrease since c_0 increases rapidly in this region, thus providing negative feedback. As the movable plate approaches the fixed plate, the capacitance c_0 goes towards infinity and V_0 goes towards zero. The electrostatic

force remains finite, however, since the electrostatic force is inversely proportional to the square of the gap which also goes towards zero. At all times, the mechanical and electrostatic forces are balanced and the system is stable.

6.3 Parasitic Capacitances

6.3.1 Parasitics from Layout

The cross section of a typical electrostatically actuated device fabricated in MUMPs is shown in Figure 6-1. c_0 and c_1 are the intrinsic or desired device capacitances whereas c_{p1}, c_{p2} and c_{p3} are parasitics. c_{p2} and c_{p3} are typically large because the dielectric layer is electrically thin. Depending on whether the substrate is left floating or grounded, the parasitic capacitances can be in parallel with either c_0 or c_1. The configuration of Figure 6-1(c) can be generalized to the circuit of Figure 6-2 which includes parasitic capacitances. Here, c_1 includes parasitics formerly in parallel with the desired series capacitance. c_3 is not important to static behavior since it is driven directly by the voltage source but it will affect dynamics.

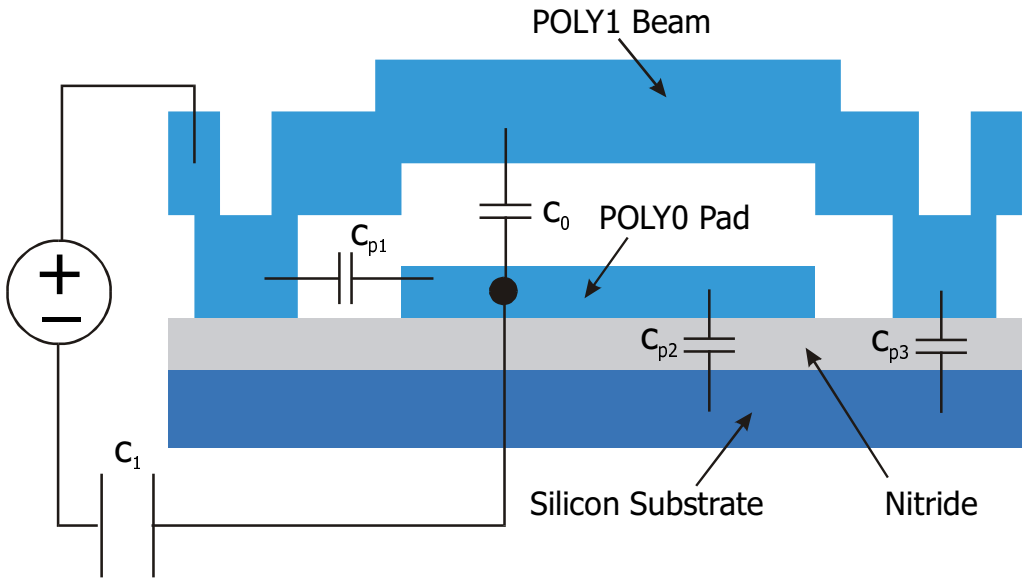

Figure 6-1. Cross section of a typical electrostatically actuated device designed for MUMPs. Large parasitic capacitances are connected to the POLY0 pad.

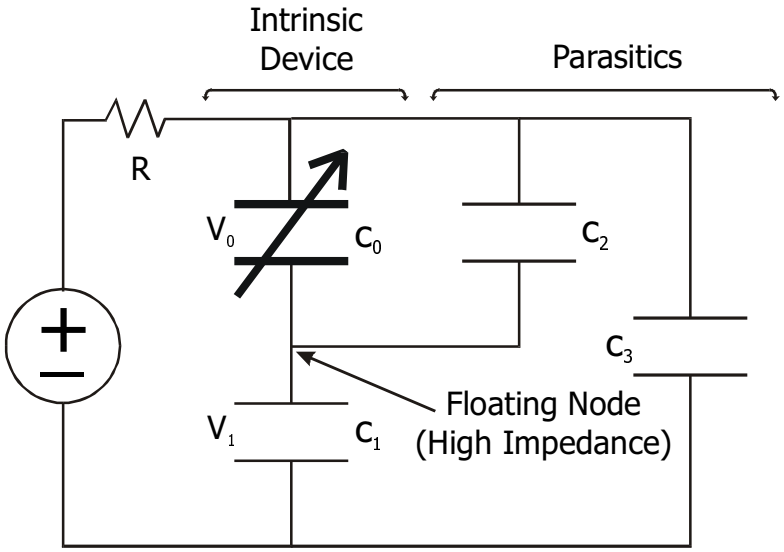

Figure 6-2. Circuit of actuator with series capacitor, augmented by parasitic capacitances in parallel and in series with the variable capacitor.

The expressions describing the static behavior of the actuator in the presence of a series feedback capacitor and parasitic capacitors can now be derived. Let

$$c_0 \propto \frac{1}{g_0 - u},\ c_1 \propto \frac{1}{ng_0} \text{ and } c_2 \propto \frac{1}{mg_0} \tag{6-1}$$

where g_0 is the desired travel range, u is displacement, and m and n are positive constants. The voltage across c_0 is determined by the capacitive voltage divider in Figure 6-2 to be

$$\begin{aligned} V_0 &= \frac{c_1}{c_0 + c_1 + c_2} V_a \\ &= \frac{m(g_0 - u)}{(m+n)(g_0 - u) + mng_0} V_a \end{aligned}. \tag{6-2}$$

The sum of the electrostatic and mechanical forces gives the total equilibrium force on the movable electrode

$$F_t = -ku + \frac{\varepsilon A}{2(g_0 - u)^2}\left[\frac{m(g_0 - u)}{(m+n)(g_0 - u) + mng_0} V_a\right]^2 = 0. \tag{6-3}$$

Following the method in Section 2.2, differentiating this expression with respect to u to determine the point at which the equilibrium solution becomes unstable gives

$$u_{\max} = \frac{g_0}{3}\frac{m+n+mn}{m+n} \tag{6-4}$$

as the maximum stable displacement of the movable electrode as a function of *m* and *n*. In the limit as $m \to \infty$ (no parasitic capacitor in parallel with c_0),

$$u_{\max} \to \frac{g_0}{3}(1+n) \tag{6-5}$$

implying that *n* should be larger than 2 for full gap travel ($u_{\max} \to g_0$) as noted previously. As $n \to \infty$ (infinitely small series capacitor for maximum feedback and stability),

$$u_{\max} \to \frac{g_0}{3}(1+m) \tag{6-6}$$

implying that c_2 must be no larger than $\frac{c_0^i}{2}$ if full gap travel is to be achieved. Thus, the electrostatic positioner must have well-controlled capacitances and parasitics.

6.3.2 Parasitics from Deformation

Another source of "parasitics" arises from the deformation of a beam in 2-D. When the beam in Figure 6-1 deforms, the displacement of the of the center portion is largest whereas the portions near the step-up supports hardly move at all. This 2-D nonuniform displacement is a subtle but significant source of parasitic capacitance in parallel with the intrinsic device. The 2-D beam/capacitor can be modeled as the sum of two 1-D capacitances – a variable capacitor in parallel with a fixed capacitor as shown in Figure 6-1. The total capacitance can be expressed as

$$c = c_0 + c_2 \propto \frac{1-q}{g_0 - u} + \frac{q}{g_0} \tag{6-1}$$

where c_0 and c_2 represent the same elements as in Figure 6-2, and *q* is a proper fraction that increases as *u*, the center displacement, increases. The larger the value of *q*, the more significant the effect of the parasitic fixed capacitance.

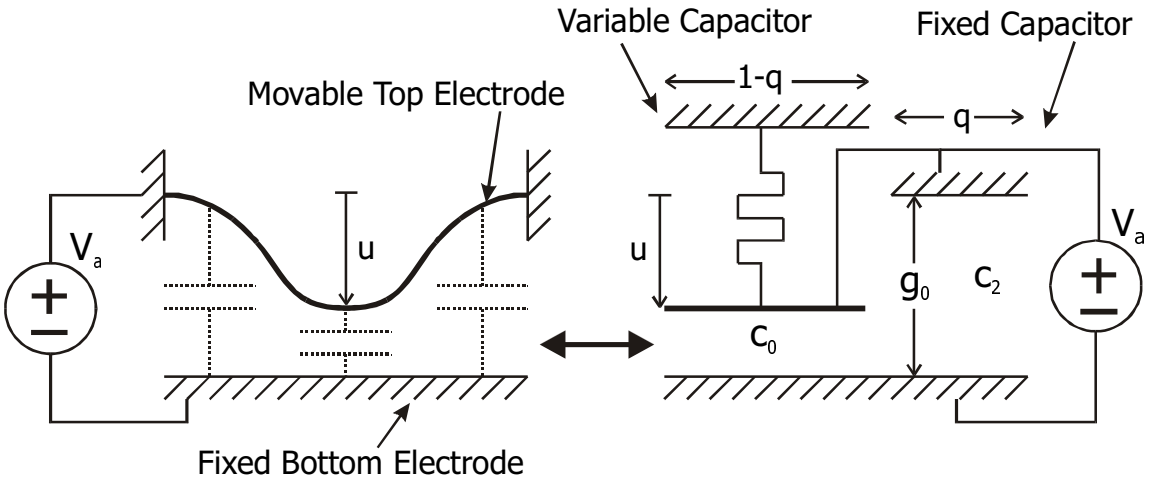

Figure 6-1. Ideal 2-D beam with nonuniform displacement and its 2-lump equivalent (variable + fixed capacitor).

Figure 6-2(a) shows the normalized simulated capacitances of several 2-D 400-μm-long electrostatically actuated beams. These beams are 2 μm thick and are suspended 2-μm above a ground plane – the nominal dimensions of a MUMPs device. The Young's modulus is 140 GPa whereas the uniaxial residual stress is a compressive 6 MPa. The 2-D capacitances are normalized to the capacitance of an ideal 1-D parallel plate capacitor, whose gap is equal to the distance between the center of the 2-D beam and ground plane. As shown, the capacitances of the 2-D devices are only fractions of the 1-D device as the center of the beam approaches the ground plane. If the length of the fixed bottom electrode under the 2-D beam is reduced (as a percentage of the beam length), the 2-D device approaches 1-D-like behavior because the deformation is more uniform over the more limited center region.

q is computed from the capacitance-displacement curves of Figure 6-2(a) using (6-1) and plotted in Figure 6-2(b) as a function of center displacement, *u*, and parameterized by bottom electrode length. The shorter the bottom electrode, the more 1-D-like the behavior of the system, and hence the smaller the value of *q*. *q* increases as the displacement increases because the diminishing gap amplifies the lack of flatness of the deformed beam. According to (6-1), the ratio of the variable capacitance to the fixed capacitance, $\frac{c_0}{c_2}$, is $\frac{mg_0}{g_0 - u}$. Equating this with the same ratio obtained from (6-1) gives *m* in terms of *q*,

$$m = \frac{1-q}{q}, \tag{6-2}$$

which when inserted in (6-6) gives

$$u_{\max} = \frac{g_0}{3q}. \tag{6-3}$$

Plotting $q = \frac{g_0}{3u}$ in Figure 6-2(b) gives the maximum q allowed for the desired range of motion, u. The displacement at the intersection of this line with the previous q-u curves indicates the maximum achievable stable travel. Beyond that, q is too large i.e. the parasitic is too large for effective stabilization. This assumes that the mechanical restoring force as used in (6-3) is still linear with displacement which is not true in real life due to stress-stiffening effects. Nonlinear stress-stiffening actually increases the range of stable travel, even without capacitive stabilization, to about one-half of the initial gap as shown in Section 4.5.2, up from the one-third of the linear case. Thus, all the 2-D devices shown in Figure 6-2 are stable up to about 1 μm of displacement. Beyond that, capacitive feedback can stabilize the device until the increasing displacement causes q to increase to the limit indicated by the dotted line. For example, for the device with a bottom electrode that is 30% of the upper electrode length, capacitive feedback will allow stable travel up to 1.8 μm or 90% of the 2-μm gap. This, according to (6-6), assumes an infinitely-small series feedback capacitor – a larger capacitor will reduce the stable travel range. Clearly, 2-D-like behavior must be avoided.

Referring back to the 1-D case shown in Figure 6-1(b), inserting a floating conductor into the gap at the dotted line does not perturb the electric field lines. When a 2-D beam deforms non-uniformly, however, the beam center moves the most, concentrating electrostatic forces near the center. Inserting a floating conductor into the gap in this case will distort the electric field lines since the conductor will enforce a flat, horizontal equipotential which did not previously exist. The series capacitor no longer extends the gap effectively and thus the efficacy of capacitive feedback is limited. Designs to maintain 1-D-like behavior are discussed later in this chapter.

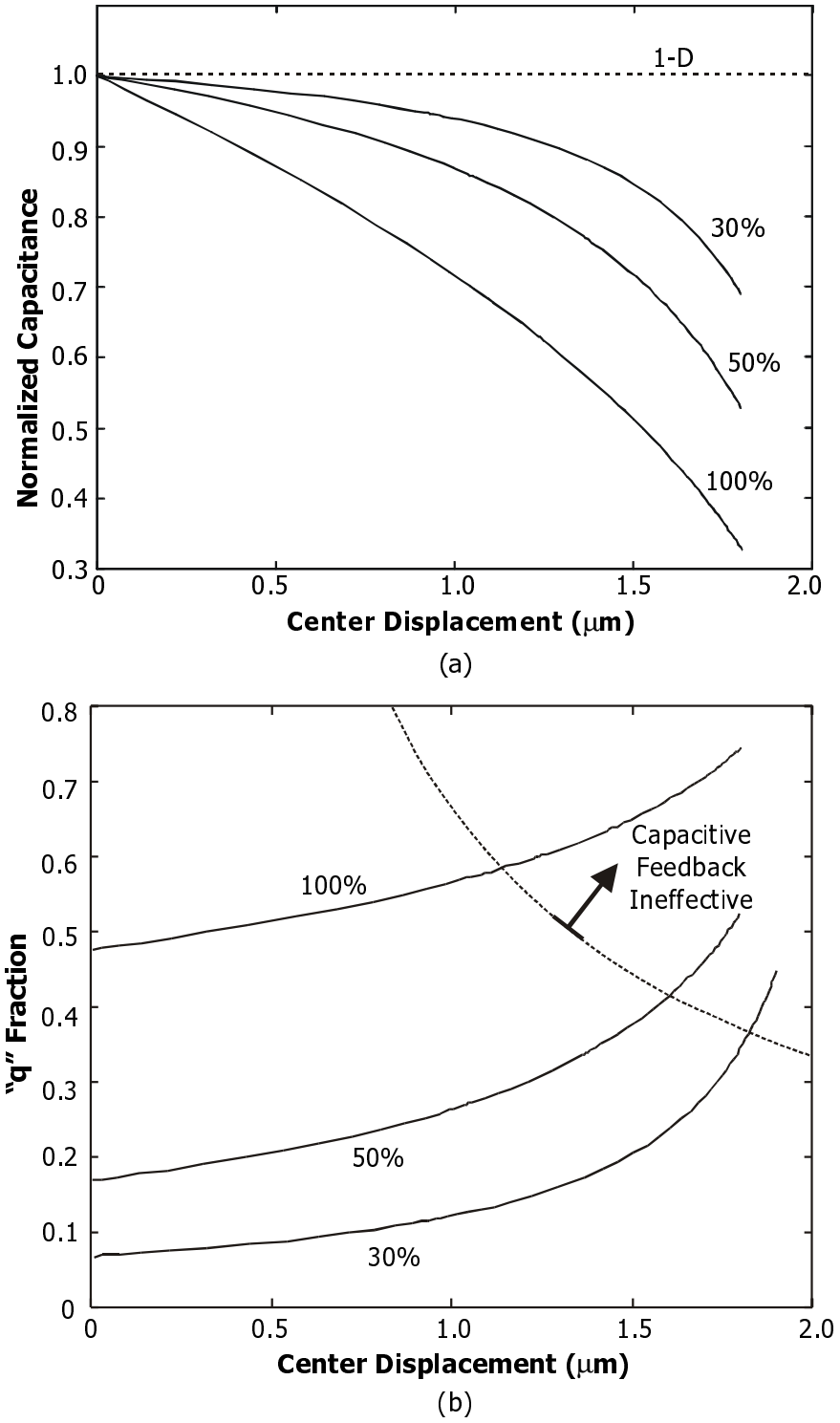

Figure 6-2. (a) Capacitance of 400-μm-long beams as a function of displacement, normalized to the capacitance of a 1-D device with displacement equal to the displacement of the beam center. The labels indicate the length of the bottom actuating electrode as a fraction of the upper beam length. **(b)** *q*-fraction as a function of displacement, computed from the capacitances in (a). Capacitive feedback is ineffective for displacements with *q*-fractions above the dotted line.

6.4 Residual Charge

Residual charge can accumulate in electrostatically actuated devices containing electrically isolated nodes such as the node between the original actuator and the series capacitor (Figure 6-2). Such charge was shown in Section 2.3 to shift the electrostatic forces by a voltage offset of $\frac{d_2\rho}{\varepsilon}$ which scales according to the amount of charge. This causes the displacement of the positioner to drift over time if charge accumulates. A high-impedance switch that can reset the voltage of the floating node from time to time is very desirable.

If charge lies on a plate that is free to move in an electric field, the effect is more complicated. Figure 6-1 shows one such configuration where a movable precharged floating conductor, like an electret foil, is inserted between two voltage-driven plates. The electrostatic force on the floating conductor – the product of charge on the conductor and the average of the electric fields on both sides of the conductor – is now

$$F_{electrostatic} = \rho\left[\frac{V_a}{d_1} - \frac{\rho}{\varepsilon}\left(\frac{d_2 - u}{d_1} - \frac{1}{2}\right)\right]. \tag{6-1}$$

The first thing to note is that unless the floating conductor is precharged, the net electrostatic force on the conductor is zero. Secondly, in contrast to (2-2), this force is linear with voltage and displacement. By equating the electrostatic and linear mechanical forces, we find the equilibrium displacement to be

$$u = \frac{\frac{V_a}{d_1} - \frac{\rho}{\varepsilon}\left(\frac{d_2}{d_1} - \frac{1}{2}\right)}{\frac{k}{\rho} - \frac{\rho}{\varepsilon d_1}}. \tag{6-2}$$

Here, the charge scales not just the voltage offset but the displacement as well. Since the inverse square behavior of (2-2) is absent, there is no abrupt pull-in effect, and actuation is always stable, potentially allowing for stable and linear electrostatic actuation. The main design issues are imparting a precharge to the floating node and then maintaining its electrical isolation. Parasitic capacitances affect linearity and the stable range of travel.

This design is practically impossible in MUMPs but might be achievable in SOI-based (Silicon On Insulator) micromachining processes.

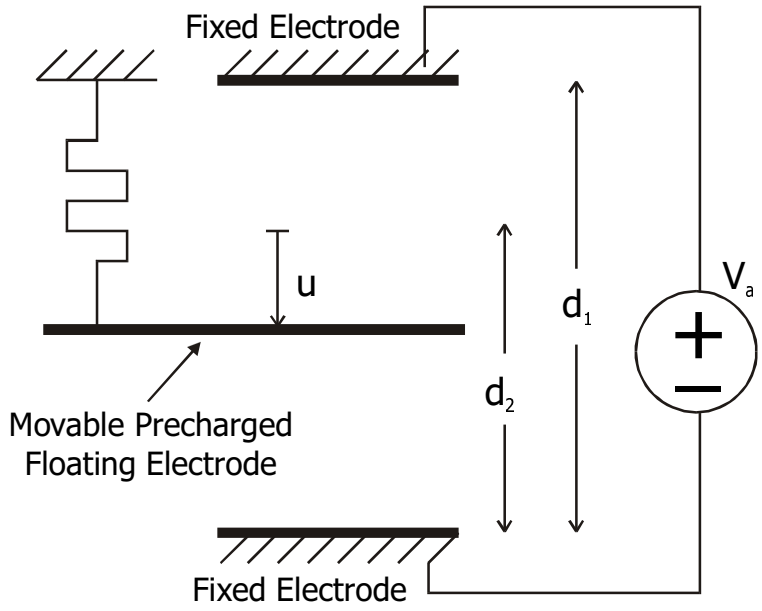

Figure 6-1. Movable precharged plate in an electric field. Displacement is linear with voltage in the absence of parasitics.

6.5 Dynamics

A good positioner or actuator should be well-damped so that rise times are fast, settling times are short and overshoots are small. The efficacy of two common damping mechanisms for micromechanical devices – resistive damping and compressible squeeze film damping – on stabilized electrostatic positioners are studied here using 1-D simulations. The simulation models are not calibrated to actual devices but serve to illustrate major damping characteristics. For conventional actuators, the only dynamic responses of interest are pull-in and release times since these devices are usually operated in ON-OFF modes. For analog positioners, the dynamic response from one position to another throughout the gap is of interest.

A resistor inserted in series with the voltage source in Figure 6-2 will help damp out oscillatory behavior by dissipating energy when current flows from the capacitor towards the voltage source during one-half of each oscillation cycle [104]. Figure 6-1(a) is an example of the damped step responses of an ideal, 1-D, critically stabilized

positioner ($c_1 = \frac{c_0^i}{2}$). The resistor damps out oscillations reasonably well for steps down from $u = 0$, especially for the larger steps ($u \geq 0.5\ g_0$). The size of the resistor was chosen so that the overshoot for the $u = 0.9\ g_0$ step would not cause the movable electrode to make contact with, and possibly stick to, the bottom electrode. The resistor performs poorly in damping out the oscillations stepping back up from $u = 0.9\ g_0$ to $u = 0.15\ g_0$. In fact, resistive damping alone can never damp out all the oscillations stepping back up all the way to $u = 0$ because the capacitors quickly discharge fully, leaving no voltage to drive current through the damping resistor. Hence, resistive damping – simple and easy to adjust – is attractive primarily for operating the positioner in the $u \geq 0.5\ g_0$ range.

Compressible squeeze film damping acts whenever the positioner is operated in air or other gases. It is more difficult to adjust – damping forces depend on air pressure and the geometry of the device. Figure 6-1(b) shows the performance of the positioner under squeeze film damping forces modeled by (2-8). In general, the larger steps (to $u \geq 0.75\ g_0$) are overdamped, with the approach to $u = 0.9\ g_0$ being almost asymptotic. This slow approach is probably overestimated by the simulation because (2-8) neglects the transition from spring-like behavior to incompressible viscous damping at lower actuation speeds [105]. The damping at small deflections i.e. near $u = 0.15\ g_0$ is generally better than can be achieved with resistive damping because it works for both halves of every oscillation cycle. Under either resistive or squeeze film damping, the oscillations are difficult to damp out near $u = 0$. Increasing the damping forces will increase the rise time to $u = 0.9\ g_0$ significantly, especially for the squeeze film damping case. Over-stabilizing the positioner i.e. making $c_1 << \frac{c_0^i}{2}$ improves the rise time for the larger steps while leaving settling times and overshoots roughly unchanged as shown in Figure 6-1(c). Decreasing c_1, to $\frac{c_0^i}{8}$ in this example, provides a more constant electrostatic driving force that is less dependent on the actuator gap, especially as u approaches g_0, thus reducing asymptotic behavior. In the critically-stabilized case, the electrostatic force and the gap are more strongly interdependent and hence both approach steady state asymptotically.

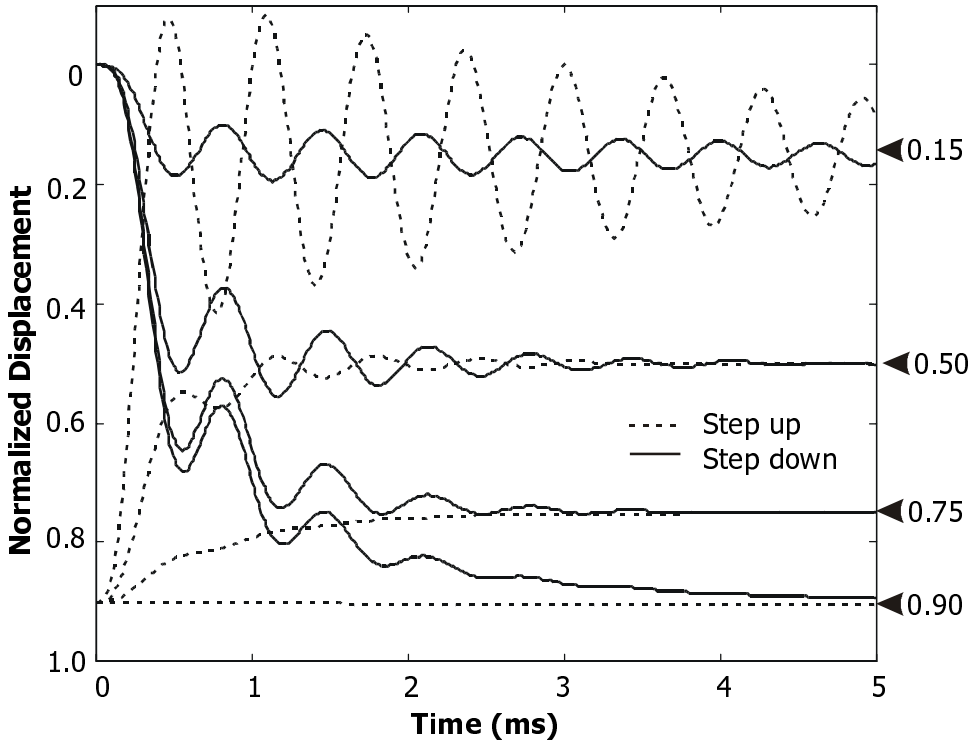
Normalized Displacement
Time (ms)
0
0.2
0.4
0.6
0.8
1.0
0
1
2
3
4
5
0.15
0.50
0.75
0.90
Step up
Step down

(a)

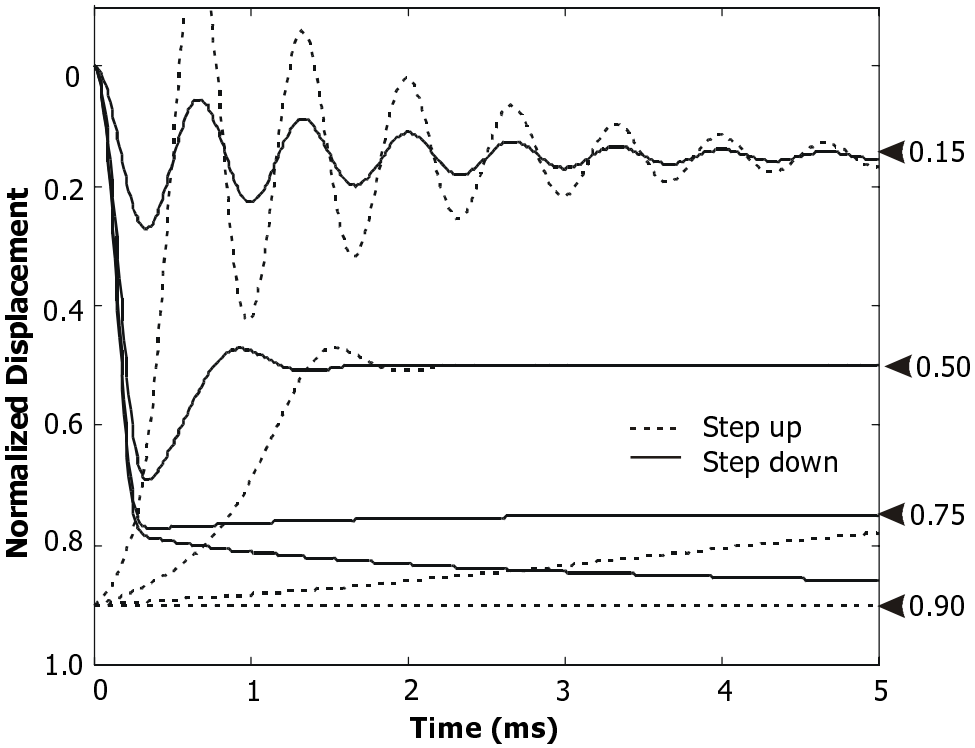
Normalized Displacement
Time (ms)
0
0.2
0.4
0.6
0.8
1.0
0
1
2
3
4
5
0.15
0.50
0.75
0.90
Step up
Step down

(b)

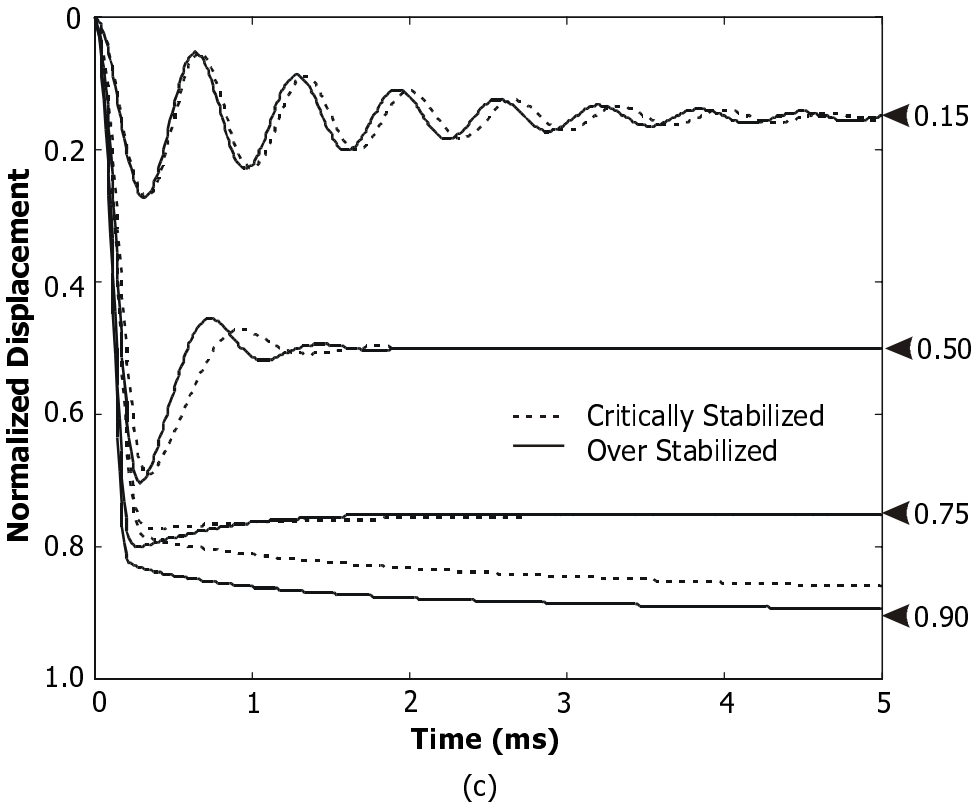

Figure 6-1. Simulated transient damping characteristics (step response) of electrostatic actuator with extended travel. **(a)** Resistive damping. **(b)** Compressible squeeze film damping. **(c)** Over-stabilized actuator with compressible squeeze film damping.

6.6 Folded Capacitor Design

Fabricating a device based on a straightforward implementation of the actuator with series feedback capacitor as shown in Figure 6-1(a) would require a dielectric spacer many times the thickness of the travel gap to maintain the proper $\frac{c_0^i}{c_1}$ ratio. This device cannot be realized in MUMPs. The desired configuration is Figure 6-1(d) where the series capacitor is alongside the original actuator, not stacked underneath it. The series capacitor is connected to the actuator by flexible tethers. Figure 6-1(b) and (c) conceptualize the transformation of the initial three conductor stack (Figure 6-1(a)) into the equivalent two layer design more suitable for surface micromachining. First, the floating conductor/electrode is extended, as shown in Figure 6-1(b), so that the moving elements and the series capacitor can eventually be placed side by side. The electric field configuration is maintained because the floating electrode is an equipotential. Next, the

left-hand side is folded over the floating electrode creating the "folded capacitor" configuration of Figure 6-1(c). By doing so, the original actuator is now alongside the series capacitor thus requiring only two conductive layers instead of the original three layer stack, while maintaining low parasitic capacitances. The actuated part must now be put back on top to be free to move. To get to the final configuration, the electrical connections are maintained while the mechanical elements on the left-hand side are swapped. The electrostatic force configuration on the movable electrode in Figure 6-1(d) is exactly the same as that in the initial design of Figure 6-1(a). No additional parasitics were introduced, and this two-conductive-layer configuration can be translated directly into a MUMPs design.

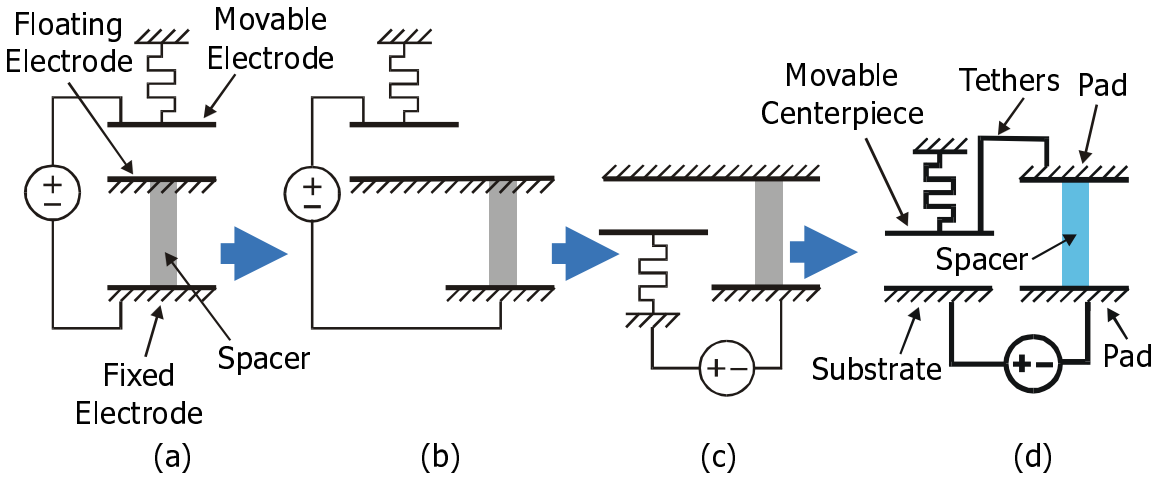

Figure 6-1. Transformation of three-conductor stack into side-by-side configuration. **(a)** Original, straightforward three-conductor stack. **(b)** Floating electrode is elongated to separate variable capacitor from series capacitor. **(c)** The left-hand side is folded over to place the capacitors side-by-side. **(d)** The movable portion is flipped back on top to get the final two-conductive-layer configuration.

Profiles of two designs fabricated in MUMPs are shown in Figure 6-2(a) and (b). The essential elements of the designs are labeled corresponding to Figure 6-1(d). The profiles match the simple 1-D schematic of Figure 6-1(d) closely, with the main difference being that the actual physical device has tethers on each side of the centerpiece to help maintain balance and symmetry. The device consists of a nominally rigid centerpiece fabricated in POLY1 suspended by tethers of either POLY1 or POLY2. These designs are not much different from a conventional actuator shown in Figure 6-1,

except for the addition of dielectric spacers under the tether anchors. The gap between the POLY1 centerpiece and POLY0 pad was reduced with a dimple etch as shown in Figure 6-2(a) to increase c_0^i and hence relax the constraints on achieving the desired capacitance ratio, $\frac{c_0^i}{c_1}$. Small series capacitors, c_1, are difficult to design in the MUMPs process because the dielectrics are electrically thin.

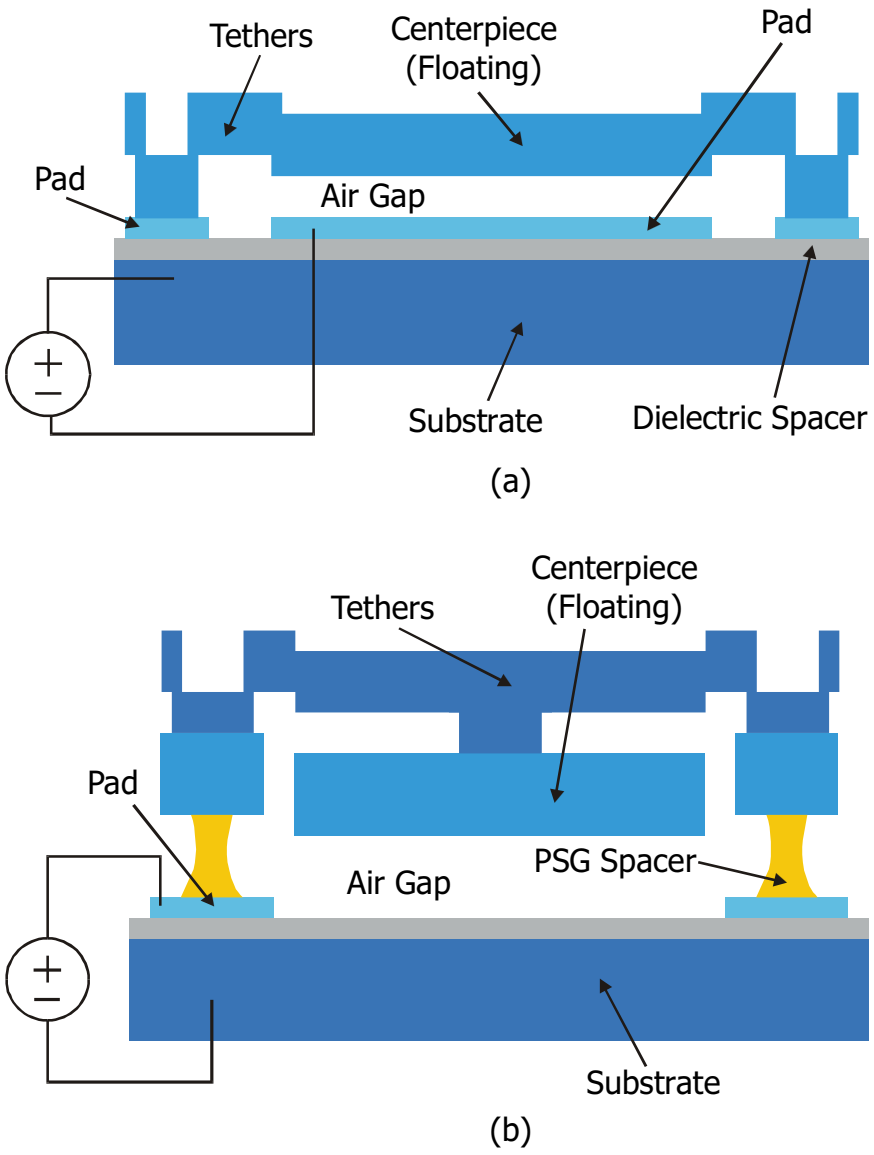

Figure 6-2. Cross sections of folded capacitor structures. **(a)** Structure using the nitride layer as the dielectric spacer. Centerpiece and tethers are made from POLY1. **(b)** PSG forms the dielectric spacer after a controlled HF etch. The tethers, made from POLY2, are shielded from the substrate electrode by the centerpiece, thus reducing parasitics.

In the Figure 6-2(a) design, the series capacitor is formed by the POLY0 pad under the anchor and silicon substrate, sandwiching the nitride. The actuator capacitance, c_0, is between the POLY1 centerpiece and POLY0 pad directly beneath it. The tethers are formed in POLY1 and have parasitics associated with nonuniform deformation similar to that described in Section 6.3.2. For the design of Figure 6-2(b), a controlled HF etch of the sacrificial PSG creates dielectric spacers, which form the series capacitors and electrically-isolate the tethers and centerpiece, leaving them floating. The actuator capacitance is between the centerpiece and the silicon substrate. The POLY2 tethers are shielded from the substrate by the POLY1 centerpiece thus reducing associated parasitics.

Top views and 3-D views of these two designs along with yet another design are shown in the Zygo interferometric images of Figure 6-3. In all cases, the movable centerpieces are large compared to the areas of the series capacitors due to the constraints of the thin MUMPs dielectrics. The centerpieces range from 140 μm × 140 μm to 260 μm × 260 μm. In Figure 6-3(a), the series capacitors at the anchors are very small, only 23-μm by 25-μm, because the nitride is electrically thin. The capacitance ratios, $\frac{c_0^i}{c_1}$, for these devices range from 1.5 to 8.1. A ratio larger than 2 is required for full-gap travel. The tethers are designed with flexures for maximum compliance to compensate for the increase in actuation voltage due to the addition of the series capacitor. The flexures also provide stress relief to prevent buckling. POLY2 rails are deposited on the POLY1 centerpieces to help maintain flatness during actuation that is essential to the proper operation of these devices.

The structure in Figure 6-3(b) uses PSG as the dielectric spacer for the series capacitors, and POLY2 as tethers. The series capacitors have larger area than those in Figure 6-3(a) because the PSG is thicker than the nitride. This design requires careful control of the PSG etch in HF. The undercut of PSG in HF is roughly 30 μm per minute. Proper release of the 30-μm-wide beams studied in the previous chapters requires an etch time of at least 1 minute, preferably 1.5 minutes. Thus the smallest PSG spacer that can be fabricated is 60-μm × 60-μm. Square POLY1 pads with edges of 80 μm or 110 μm were designed to form the series capacitors. The capacitances of these series capacitors were computed assuming some mixture of air and PSG dielectrics under the POLY1 pads

resulting from an undercut of exactly 30 μm (1 minute etch) or 45 μm (1.5 minute etch). For example, the capacitance of a 110 μm × 110 μm series capacitor after a 1.5 minute etch is

$$c_1 = \frac{\varepsilon_{PSG} A_1}{g_{PSG}} + \frac{\varepsilon_0 A_2}{g_{PSG}} \tag{6-1}$$

where

$$A_1 = (110 - 2\times 45)^2 \ \mu\text{m}^2, \tag{6-2}$$

$$A_2 = 110^2 \ \mu\text{m}^2 - A_1, \tag{6-3}$$

and g is the thickness of the PSG (geometrical, not electrical, thickness). The relative permittivity of PSG is about 4. The capacitance ratios for this range of devices were designed to be between 1.3 and 7.2.

In yet another effort to minimize the series capacitance, a structure with only a single anchor was designed (Figure 6-3(c)). The movable element, still labeled the centerpiece, surrounds a single series capacitor in the center. This essentially halves the total series capacitance allowing greater feedback stability. The tethers are made from POLY2. Such techniques and efforts to create the proper capacitance ratios would not be necessary in an optimized process with the desired dielectric thicknesses. A thicker dielectric layer would make smaller series capacitances easier to fabricate and, hence, allow smaller centerpieces or larger anchors.

The performance of the design of Figure 6-3(b) was simulated in Abaqus (Figure 6-4) using beam elements for the tethers and shell elements for the centerpiece. The POLY2 stiffener frame was not modeled explicitly. The effects of capacitive feedback could not be included in the Abaqus simulation because global solutions, necessary for computing voltages on floating conductors, are not available in user-defined subroutines; therefore, the results are of direct actuation of just the original conventional actuator. At a deflection close to one-third of the initial gap of 2 μm, the centerpiece was flat to within 0.02 μm. This variation was further reduced when the simulated centerpiece thickness was increased from 2 μm to 3 μm to mimic the effect of a POLY2 stiffener frame. This suggests that the desirable 1-D-like behavior can be achieved.

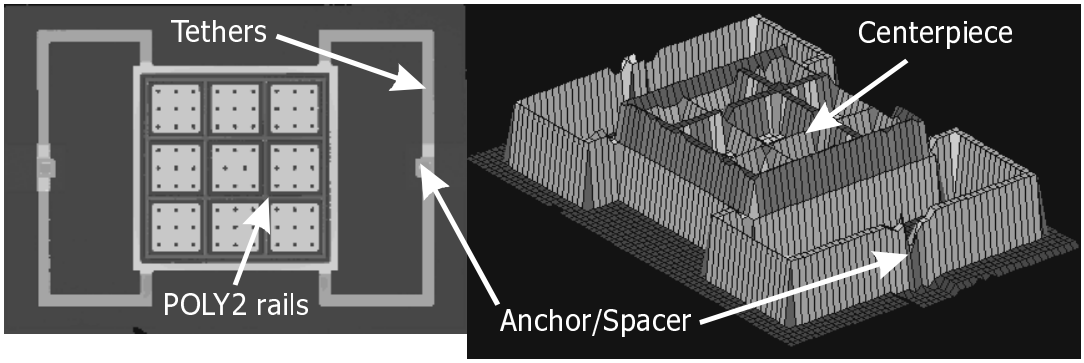

(a)

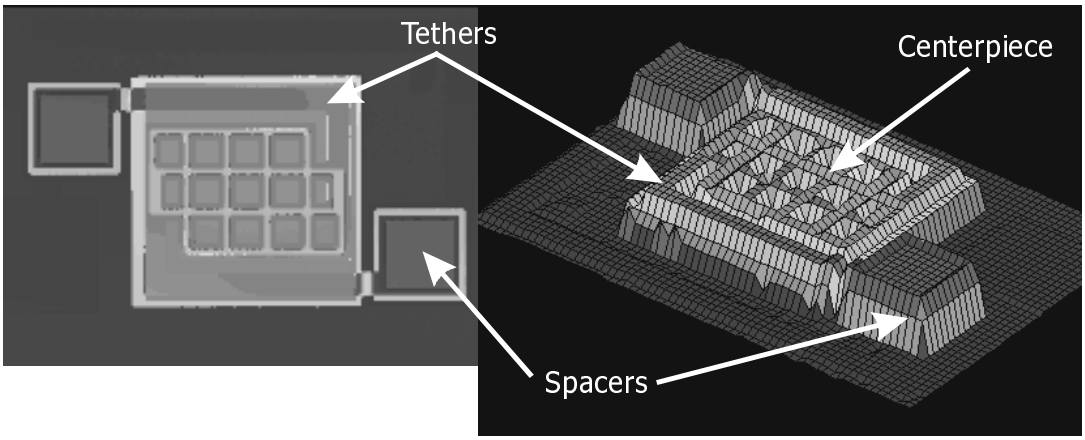

(b)

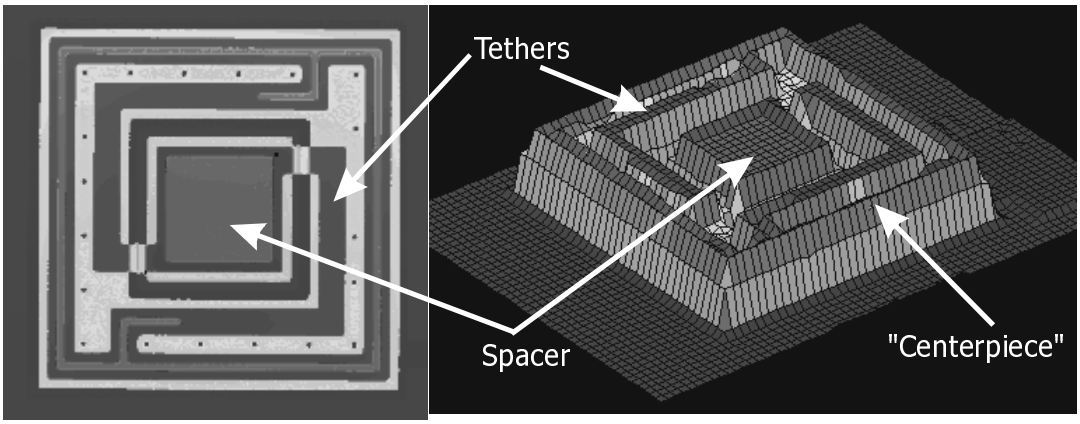

(c)

Figure 6-3. Interferometric views of three folded-capacitor designs. The images on the left are top views whereas the images on the right are 3-D views. Interferometry only provides the shape of the top surface so the sacrificial gap and other underlying structures are not visible. **(a)** POLY1 is used for both the centerpiece and tethers. Nitride forms the spacer. **(b)** POLY2 forms the tethers, which are shielded from the bottom electrode to minimize parasitics. PSG forms the spacer. **(c)** Only one anchor/spacer is used in order to minimize the series capacitance. PSG forms the spacer and POLY2 forms the tethers.

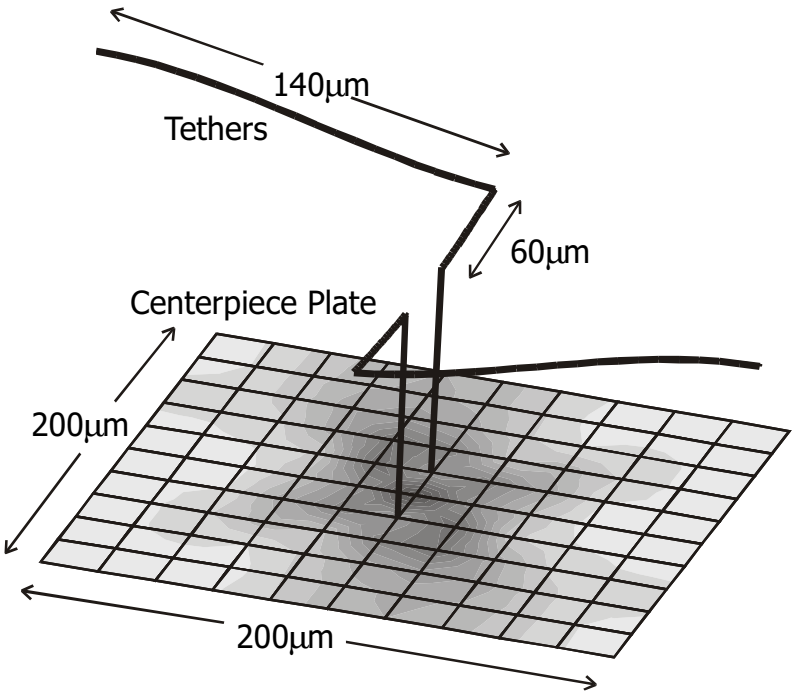

Figure 6-4. Abaqus quasi-3-D model of a POLY1 plate with POLY2 tethers. Plate remains quite flat under electrostatic actuation.

6.7 Performance

The performance of several permutations of folded capacitor structures fabricated in the MUMPs 29 run were analyzed under the Zygo interferometer. After a 1 minute HF etch, most of the large centerpieces were still not released because the HF could not undercut the PSG through the arrays of 3 μm × 3 μm etch holes. Thus, dies released in a 1.5 minute etch were used; but even then, some dies had unreleased parts. Measurements of the device shown in Figure 6-3(a) are shown in Figure 6-1. The first curve actually shows the performance of a conventional actuator. The measurement was made on exactly the same structure except that the electrical probes bypassed the series capacitor. One probe was positioned at the top center of an anchor/series capacitor, making sure that the rest of the structure was not perturbed. The plot of the normalized displacement of the centerpiece as a function of voltage shows that the actuator travels up until the theoretical limit then collapses to the bottom. The measurements match theory because the mechanical stiffness of the slender tethers is linear with displacement. The actuator

with the series capacitor can go beyond the theoretical limit, almost twice the conventional range, before collapsing. The increase in actuation voltage confirms that the fundamental principles of capacitive voltage division and negative feedback are operational.

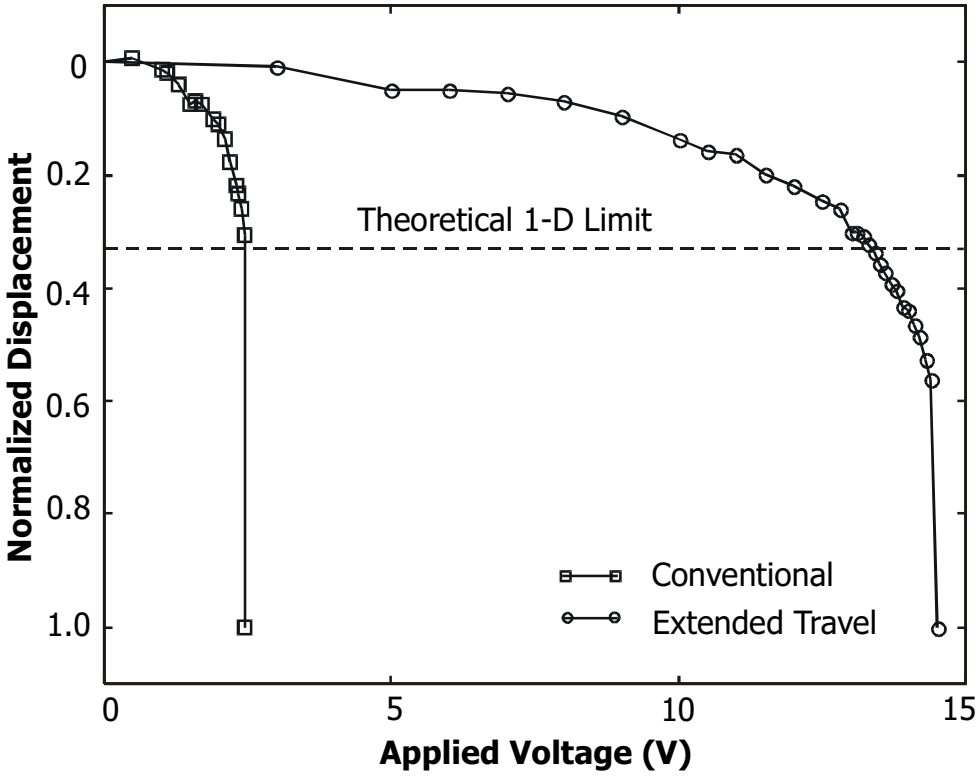

Figure 6-1. Measured displacement-voltage characteristic of a conventional actuator, and an actuator with extended travel. Both measurements were made on the same device – the measurements of a conventional actuator were obtained by bypassing the series capacitance with the probes. Displacement shown is that of the center of the centerpiece.

Further analyses reveal that pull-in still occurs, even though the designed capacitance ratio is sufficient, because tilting occurs. 1-D-like behavior should be maintained at all times for proper operation but asymmetry in the device causes tilting to occur as shown in Figure 6-2. As the centerpiece deflects beyond the conventional theoretical limit, any asymmetries are amplified. When one side of the plate deflects more than the other, the capacitance change due to this tilting is insufficient to adjust the voltage of the plate to maintain stability. Electrostatic forces concentrate on that side of the plate causing positive feedback, which snaps that side down. This tilting was

observed on all the other folded capacitor designs at travel ranges close to that shown in Figure 6-1.

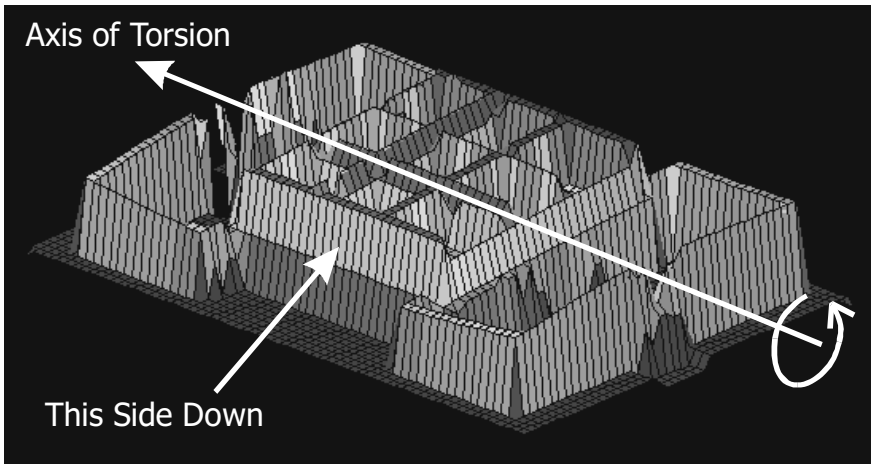

Figure 6-2. Surface profile of a folded capacitor device tilted at pull-in. A preferred axis of torsion exists, spanning the two anchors.

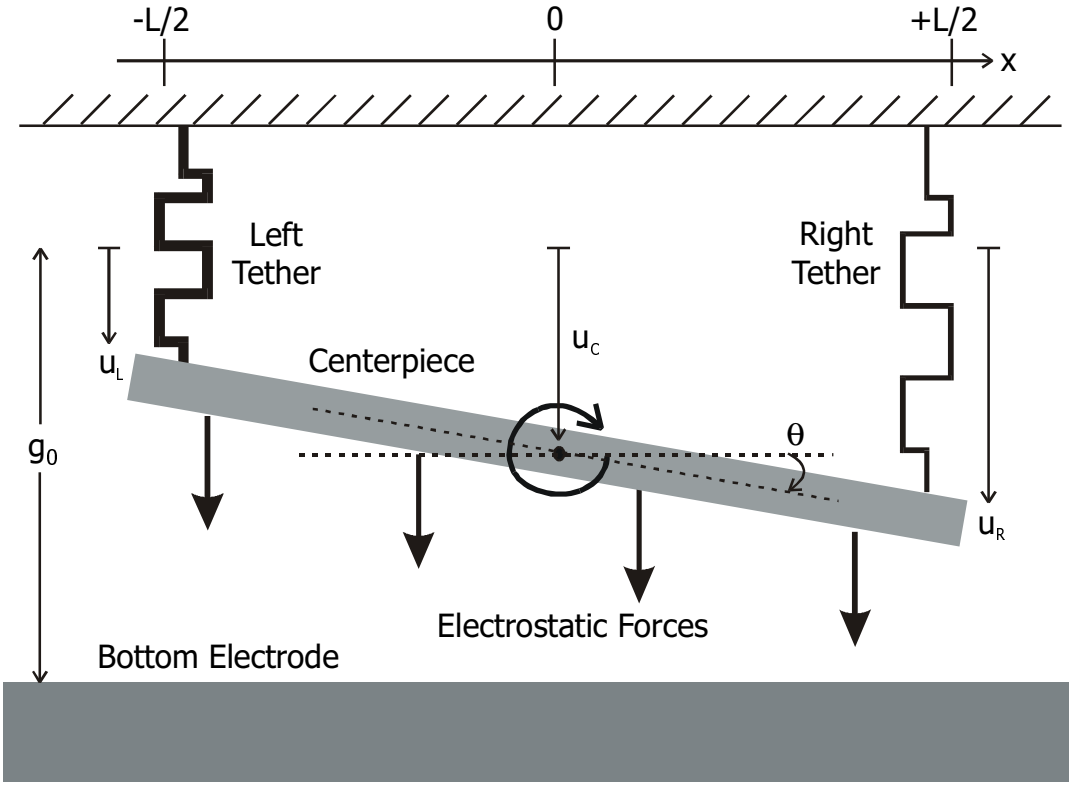

Figure 6-3. Rigid-body model of actuator with series capacitor. The torsional degree of freedom is introduced to analyze effects of asymmetry between the right and left tethers.

6.8 Tilting

This phenomenon was analyzed in 2-D using rigid body simulations. The model consists of a rigid centerpiece suspended by tethers at the ends as shown in Figure 6-3.

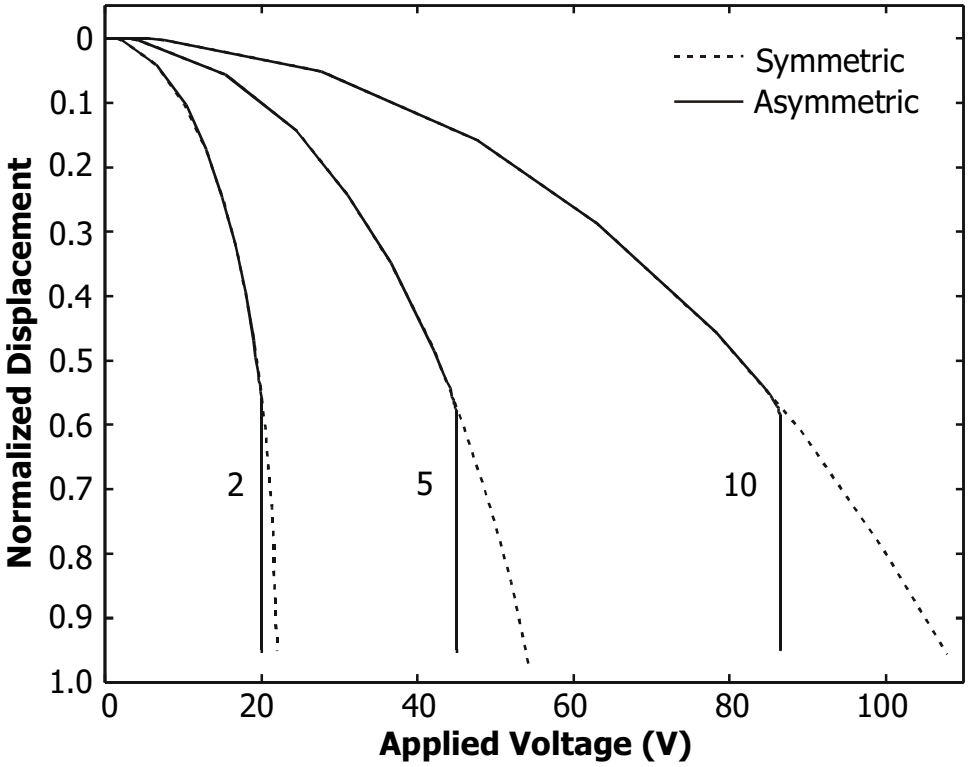

Figure 6-1. Normalized displacement of the centerpiece as a function of applied voltage, showing the range of travel that can be achieved. The displacement shown is the maximum displacement, which is of the right-hand side of the centerpiece. The labels are the original-to-series capacitance ratios. At close to a normalized deflection of 0.6, asymmetry causes the devices to tilt and snap down. The ranges of travel do not seem to depend on the ratio of the capacitances.

The equations of motion that describe the centerpiece are

$$m\frac{d^2u_C}{dt^2} = -k_L u_L - k_R u_R + \frac{W\Delta x\varepsilon_0 V^2}{2}\sum_{x=-L/2}^{+L/2}\frac{1}{[g_0 - u(x)]^2} \tag{6-1}$$

for the vertical displacement of the center, and

$$I\frac{d^2\theta}{dt^2} = \frac{L}{2}k_L u_L - \frac{L}{2}k_R u_R + \frac{W\Delta x\varepsilon_0 V^2}{2}\sum_{x=-L/2}^{+L/2}\frac{x}{[g_0 - u(x)]^2} \tag{6-2}$$

for the rotation of the centerpiece. The centerpiece is discretized into small segments of length Δx. Damping terms are added to help quasi-static simulations converge quickly. For the centerpiece, m is the mass, I is the moment of inertia, W is the width, and L is the length. k_L and k_R are the stiffnesses of the left and right tethers, respectively. Asymmetry is introduced by increasing the relative stiffness of the left tether. The stiffnesses of the tethers are roughly those of 200-μm-long and 30-μm-wide polysilicon beams. Thicknesses, stress and other properties used are nominal MUMPs parameters.

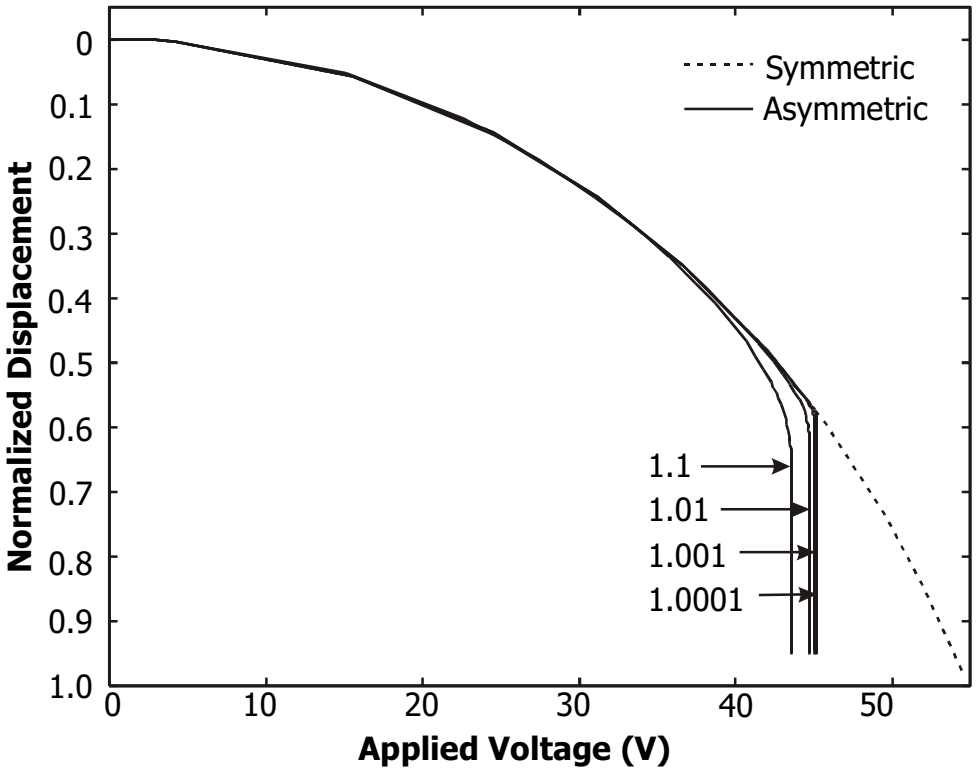

Figure 6-2. Normalized displacement of centerpiece as a function of voltage for devices with different degrees of asymmetry. The four labeled curves correspond to the cases where the tether on the left-hand side is stiffer by 10, 1, 0.1 or 0.01%. The displacement shown is the maximum displacement, which is of the right-hand side of the centerpiece. For asymmetries resolvable by the simulation tolerance, the device tilts and pulls-in close to a normalized displacement of 0.6. The capacitance ratio is 5 in all cases.

Figure 6-1 shows the quasi-static simulated displacement of an actuator with a series capacitor, as a function of voltage, and parameterized by capacitance ratio $\frac{C_0^i}{C_1}$. With perfect symmetry, the actuator can travel the entire gap stably for any capacitance ratio more than or equal to 2. With the introduction of a 0.1% asymmetry, the device tilts

and pulls-in after deflecting close to 60% of the initial gap. This is very close to the measured range of travel. The effect of the degree of asymmetry is investigated in Figure 6-2. $\frac{c_0^i}{c_1}$ was fixed at 5. Here, all asymmetries that are resolvable within the tolerance of the simulation cause tilting at about 60% of the initial gap. This range of travel does not seem to depend on the ratio of the capacitances, or the degree of asymmetry (within the tolerance of the simulation), potentially indicating a fundamental limit to the performance of this technology. The profile of the centerpiece as the actuation voltage is increased is shown in Figure 6-3. The left tether is 10% stiffer than the right tether causing the right side to move down more than the left side. At about 43.54 V, the system becomes unstable and the right side of the centerpiece tilts and pulls-in.

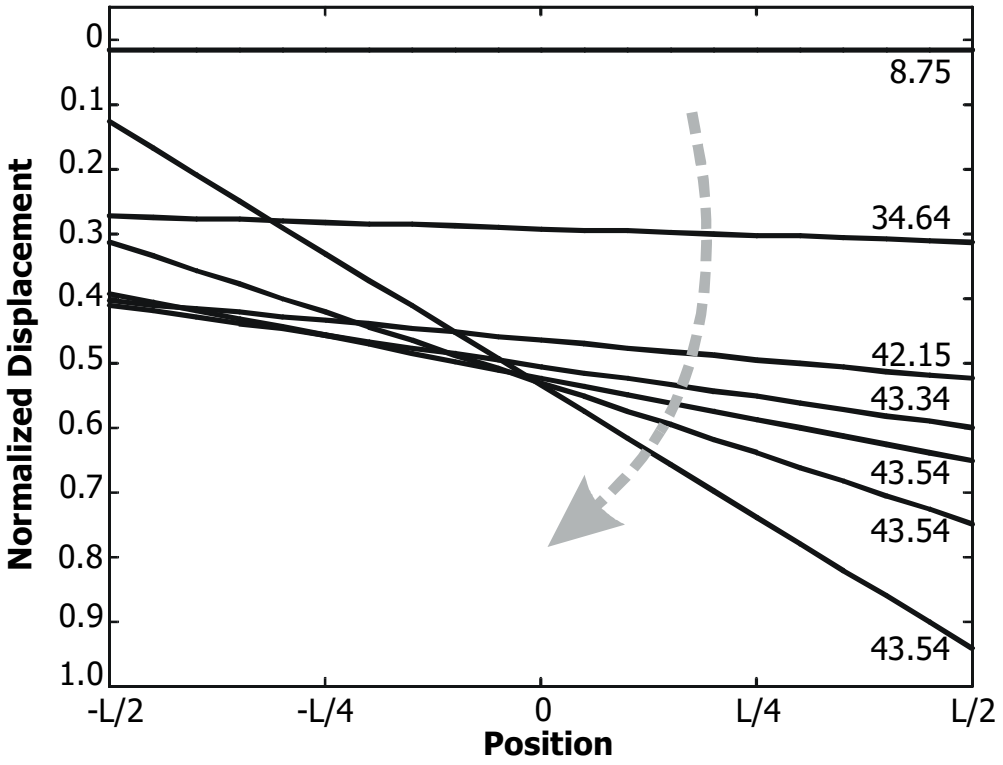

Figure 6-3. Profile of centerpiece as the actuation voltage is increased. The left tether is 10% stiffer than the right tether. Labels are of applied voltage. The last three profiles are essentially at the same voltage, indicating a sharp descent due to tilting.

6.9 Summary

This chapter discussed the practical and realistic design requirements for an actuator with an extended range of travel. The effects of parasitic capacitances from layout and from nonuniform deformation were discussed. Residual charge causes voltage drift, but can also be exploited to create a linear electrostatic actuator. Analyses of dynamic performance show that over-stabilization can mitigate asymptotic slow down at large deflections close to contact. Three “folded capacitor” designs that attempt to meet these practical design challenges were fabricated. Extended travel, almost twice the conventional range, was achieved but ultimately limited by tilting instabilities. These were the first measurements of devices incorporating series capacitors. Simulation analyses show that such tilting due to asymmetries might pose a fundamental limit to the performance of this technology. Designs using long, slender beams instead of wide plates might be more tilt resistant. An optimized fabrication process that provides good electrical isolation of nodes will allow more design flexibility. Such designs can be smaller than devices based on other extended-travel technologies, making them attractive for applications that require high fill-factors such as micromirror arrays.

Chapter 7 Conclusions

7.1 Contributions

Computer simulators are powerful tools that can help in the design of electromechanical devices, and aid in the understanding of material and device behavior. A wide range of simulation models was used in this thesis, with the appropriate models chosen to describe and characterize phenomena ranging from buckling to pull-in to charging to tilting.

Chapter 2 presented contributions towards improving the accuracy and applicability of 1-D models in simulating electrostatically actuated beams. The accuracy of electrostatic fringing fields in 2-D models was augmented by including the effects of finite beam thickness. Quasi-2-D simulations utilized time integrators to produce quasi-static solutions instead of relying on slower relaxation methods. The 2-D mechanical model in Abaqus was tailored to capture geometry and contact accurately. All 2-D assumptions and approximations were validated to obtain a good simulation basis for the characterization work in Chapters 4 and 5. Practical simulation know-how on issues such as convergence and boundary conditions was also conveyed. The strengths and weaknesses of the various simulation models, ranging from 1-D to 3-D, were compared and contrasted.

A comprehensive calibration methodology was introduced in Chapter 3. Techniques to measure geometry and true thicknesses accounting for effects of overetch, gold and stress in PSG were described. Important geometrical features that influence device performance were pointed out. Gold was shown to influence the electrochemistry of the HF release etch and, consequently, affect the thicknesses and stress states of polysilicon structures. This effect is dependent on the area of gold relative to the rest of the polysilicon structure and, hence, affects single devices differently than arrays. A through-thickness stress profile was proposed to describe the observed behavior. Variations with width and length, and other nonuniformities, especially among cantilevers, were discussed to define a well-characterized scope for calibration.

A thorough analysis of the electrostatic pull-in behavior of beams was the subject of Chapter 4. Post-buckled behavior, the effects of mechanical discontinuities, and three step-up anchor designs were examined. The expansion of PSG was shown to cause backfilled anchors to be highly stressed and beams to buckle downwards. Young's modulus and residual stress were extracted from measurements of both buckling amplitude and pull-in voltages, leading to more confidence in the extracted parameters. Three distinct types of pull-in behavior were highlighted. The simulation model parameters along with measurements of dual-bias-electrode structures were proposed as benchmark verification cases to evaluate coupled electromechanical simulators. The chapter closed with a quantitative description of the influences of stress gradients, substrate curvature and multi-layers. It was demonstrated that stress gradients do not affect fixed-fixed beams appreciably, that buckling amplitude is affected by probe pressure, and that the coverage of deposited films needs to be considered carefully.

Contact electromechanical phenomena were the issues addressed in Chapter 5. Well-characterized beams were used as in-situ surface probes to monitor charge buildup in the nitride, and apparent compressibility of the contact surface. Zygo profile measurements and test structures that eliminate zipping confirm compressible surface behavior. Electronic effects were investigated and subsequently discounted. However, a discrepancy between simulations and measurements at high voltages suggest the presence of additional series capacitance. Despite ambiguity in the mechanisms behind the compressible contact surface behavior, their effects on capacitance-voltage measurements

can be captured in simulations using a "softened" contact profile. Charge buildup over time was shown to correspond to charge injection through direct tunneling into the nitride. The observed drift in pull-in voltages implies that another mechanism for charge accumulation exists, primarily at contact surfaces.

The practical design issues of an electrostatic actuator that can travel beyond the trademark limitation of conventional actuators were presented in Chapter 6. Sources of parasitics, from layout and from 2-D non-uniform deformation, were discussed along with three "folded capacitor" designs that minimize their deleterious effects. The designs are straightforward to implement in MUMPs. The effects of residual charge were analyzed, and a linear electrostatic actuator proposed. Transient simulations showed that over-stabilization improves actuation speeds at deflections close to contact. Extended travel was achieved but ultimately limited by tilting instabilities. Simulations of asymmetries suggest that tilting could fundamentally limit the performance of this technology.

7.2 Suggestions for Future Work

The goal is always to progress towards the ultimate objective of characterizing a full three-dimensional model valid over a wide range of dimensions and actuation regimes. In practice, however, calibration work needs to be driven by real device applications, with detailed work usually viable only for widely-used foundry processes such as MUMPs. In this thesis, effects due to gold connections, width-wise variations, and other nonuniformities were described but not thoroughly quantified. The influence of gold and other noble metals on the electrochemistry of the HF release etch, and subsequently on the properties of polysilicon, need further study. Cantilever-like structures – comb drive fingers, for example – should also be examined further. These devices are more susceptible to variations in material properties, especially stress gradients and, hence, demonstrate more nonuniformities among ostensibly similar devices. Cantilevers of different widths and lengths behave quite differently. Accurate and general electrostatic models in 2-D and 3-D are always desirable due to the high cost of solving electrostatics problems in 3-D. Accurate models for the tip of a cantilever will allow accurate characterization of electrostatically actuated cantilever beams. The use of

well-characterized structures as in-situ probes can be extended to investigate other surface phenomena such as adhesion and friction. Careful control and monitoring of surfaces is needed to improve the repeatability of contact surface measurements. Installing an LCR meter near the Zygo surface profiler will allow some direct corroboration between optical and capacitance measurements. Finally, the electrostatic actuator with extended travel can be redesigned with better symmetry to avoid tilting. More analyses are required to uncover why tilting always occurs at around the same point. The design should be ported over to fabrication processes, such as SOI processes, that allow for high impedance nodes, potentially enabling the fabrication of a linear electrostatic actuator.

7.3 Take Home Message

As stated at the beginning of this thesis, the foundation of this work is the belief that accurate computer simulations in conjunction with careful physical measurements is one of the best ways to understand device behavior and physical properties. Only with good confidence in the accuracy of the simulations could subtle phenomena such as surface compressibility be uncovered. Sources of error in models must be identified and avoided to understand what is really being examined. Simulation just for simulation's sake, without careful calibration, has limited use. The characterization of fabrication processes is very important but will always remain incomplete due to the expansive range of processes, physical domains, and applications. Nevertheless, consistency among device behavior, test structure measurements, and computer simulations must be the goal. Only then will computer simulation tools gain credibility and contribute towards the growth of the field of sensors, actuators, transducers, microsystems and MEMS. The continued miniaturization and multiplicity of micromachined devices will greatly improve the interactivity and performance of computers and other appliances of the future.

Appendix A Matlab Quasi-2-D Scripts

These are the Matlab scripts to simulate the behavior of an electrostatically actuated beam. They run on Matlab version 5.0 and higher. Comments are sprinkled liberally throughout the script. “quasi2d.m” is the main program and requires an additional function file “quasi2d_outfun.m” to produce text and graphics output during the simulation.

quasi2d.m

```
function [out1,out2,out3] = quasi2d(t,temp,flag,p1,p2)

% quasi2d.m
%
% Solve the distributed ODE describing beam actuation
% using the Matlab ODE integrators
%
% Only solve for one-half of beam
% Assume dw/dx = d2w/dx2 = 0 at center
%
% Equation is:
%
% Fbend + Fstress + Fstretch + Felec - Fvisc = m a
%
% Finite-difference approximation
%
% State vector is [wdot w] where wdot and w are vectors
% usage:>>[t,w]=ode23s('quasi2d',[0 200])

% all units are MKS

format long g
format compact
global vpi lc wc yy ss thth gap0 gap1 N g0 width disc e fraction
```

```
lc=400*1e-6;  %length of beam
wc=30e-6;  %width of beam
yy=140e9; %Young's modulus
ss=-6.16e6; %residual stress
thth=2.0e-6; %thickness of beam
gap0=1.0e-6; %gap between beam and nitride
gap1=0.5e-6; %thickness of nitride

t0=0; tstep=1; tf=1000;  % time range

% Constants
e=8.854e-12; %free space constant
k=1; %effective dielectric constant of nitride
N=100; %number of discretization points
disc=lc./(2*N+1); % finite-difference discretization size of beam

% Distributed parameters
pts=ones(1,N+4); %include boundaries
nu=0.23.*pts; %Poisson's ratio
y=yy./(1-0*nu.^2).*pts; %plane strain Elasticity (E/(1-nu^2)) of beam
sigma=ss.*pts; %residual stress

g0=(gap0+gap1/k).*pts; %effective electrical gap
th=thth.*pts; %Thickness of beam
width=wc.*pts; %Width of beam

m=th*2330; %mass
i=(th.^3)/12; %moment of inertia per unit width

if nargin < 3 | isempty(flag)

% Return "dy/dt = F(t,y)"

% expand to include 4 boundary condition points
w=temp(N+1:2*N);
w=[w(1) 0 w' w(N) w(N-1)]; %ideal clamped + symmetry
%w=[w(1) 0 w' 0 w(N)]; %ideal clamped-clamped BC
%w=[1*w(1) 0 w' 0 1*w(N)]; %compliant clamped-clamped BC (?)
%w=[1*w(1) 0 w' 2*w(N)-w(N-1) 4*w(N)-4*w(N-1)+w(N-2)]; %cantilever BC (?)

n=1.8e-5.*(width.^2)./((gap0-w+0.1e-6).^3);%squeeze film damping coefficient
%n=2000;

dwdx=(w-[w(3:N+4) w(N) w(N-1)])./(2*disc); %central differencing
dwdx=[-dwdx(2) dwdx(1:N+3)];

%compute elongation
strain=sum (0.5 .* dwdx(3:N+2).^2 .* disc) .* ones(1,N+4);
nstr=strain./sum(disc./(y(3:N+2).*width(3:N+2).*th(3:N+2)));
nres=sigma.*width.*th;

%force due to stress and stretching Fn = d/dx (N dw/dx)
Fn = (nres+nstr) .*  dwdx;
Fn = (Fn-[Fn(3:N+4) Fn(N) Fn(N-1)])./(2*disc);
Fn = [0 Fn(1:N+3)];

%force due to bending Fb = d2/dx2 (E I d2w/dx2)
aaa=diff(w,2)./(disc^2);
d2wdx2 = [aaa(2) aaa aaa(N+1)];
Fb = - [0 diff(y .* i .* width .* d2wdx2,2)./(disc^2) 0];

% voltage source
```

```
v=1*t; %steady-state ramp
%v=30; %step
%v=14*sin(2*pi*10000*t); %sinusoidal

tempdot = 1 ./ (m .* width) .* ( ...
   + Fb ...
   + Fn ...
   + e.*v.^2.* width .*  (1.006 + 0.95 .* (g0-w)./width)./(2 * (g0-w).^2) ...
   - n .* width .* [0 0 temp(1:N)' 0 0] ...
   );

wdot(1:N)=tempdot(3:3+N-1); %acceleration
wdot(N+1:2*N)=temp(1:N); %velocity

out1 = wdot';

else
   switch(flag)
   case 'init'                         % Return default [tspan,y0,options].
%      out1 = [t0:tstep:tf];
      out1 = [t0 tf];
      out2 = zeros(1,2*N);
      out3 = odeset('reltol',1e-3,'abstol',[1e-4*ones(1,N) 1e-8*ones(1,N)],...
         'outputfcn','quasi2d_outfun','jpattern','on','refine',1);

   case 'jacobian'                     % Return matrix J(t,y) = dF/dy.
      out1 = [];

   case 'jpattern'                     % Return sparsity pattern matrix S.
      % Generate sparse matrix
%      spas=zeros(2*N,2*N);
      spas(1:N,N+1:2*N) = spdiags(ones(N,N),-2:2,N,N);
      spas(N+1:2*N,1:N) = spdiags(ones(N,1),0,N,N);
      spas(1:N,1:N) = spdiags(ones(N,1),0,N,N);
      %spy(spas); %view Jacobian matrix sparsity
      out1 = spas;

   case 'events'                       % Return event vector and information.
      out1 = [];
      out2 = [];
      out3 = [];

   otherwise
      error(['Unknown flag ''' flag '''.']);
   end
end
```

quasi2d_outfun.m

```
function status = outfun(t,w,flag)
% quasi2d_outfun.m
%
% Output function for ODE solver

global gap0 gap1 N width disc e wd g0

if nargin < 3 | isempty(flag)

l=length(t);

%plot only the latest time and position
time=t(l)

w=w(:,l);

max_defl=max(w(N+1:2*N))
max_vel=max(w(1:N));
min_vel=min(w(1:N));

status = 0;
if min((g0-max_defl)./g0)<0.05, status=1, end; %termination criterion for sim.

plot([1:N]*disc,g0(3:N+2)'-w(N+1:2*N),'o-');
axis([0 (N)*disc -0.1*(gap0+gap1) 1.2*(gap0+gap1)]); hold off;
title('Gap vs Position')

%plot(t,max(w'));
drawnow;
%disp('press key');pause

else
   switch(flag)
   case 'init'               % outfun(tspan,w0,'init')

      clc;clf
      disp('initialize');

   case 'done'               % outfun([],[],'done')
      disp('done');
      fprintf('\n\n');

   end
end
return;
```

Appendix B Abaqus Input Deck

This is the Abaqus input deck for the dual-bias-electrode structure described in Section 4.8. Comments are included in the deck. This file works under Abaqus 5.6 and 5.7-7.

```
*heading
beam loaded with electrostatic force
refined mesh
*node
********** define all nodes
*** bottom level
1000, -25, 0.00
1016, -1.60, 0.00
1020, -1.0, 0.00
1024, 0, 0.00
1034, 9.0, 0.00
1036, 10.0, 0.00
1076, 135.0, 0.00
1078, 136.0, 0.00
1088, 145, 0.00
1090, 145.75, 0.00
1130, 174.25, 0.00
1132, 175, 0.00
1142, 184.0, 0.00
1144, 185.0, 0.00
1184, 340.0, 0.00
1186, 341.0, 0.00
1196, 350, 0.00
1200, 351.0, 0.00
1204, 351.60, 0.00
1220, 375, 0.00
*** dimple level
3000, -25, 1.12
3016, -1.60, 1.12
3020, -1.0, 1.12
3024, 0.3, 1.12
3034, 9.0, 1.12
```

```
3036, 10.0, 1.12
3076, 135.0, 1.12
3078, 136.0, 1.12
3088, 145, 1.12
3090, 145.75, 1.12
3130, 174.25, 1.12
3132, 175, 1.12
3142, 184.0, 1.12
3144, 185.0, 1.12
3184, 340.0, 1.12
3186, 341.0, 1.12
3196, 349.7, 1.12
3200, 351.0, 1.12
3204, 351.60, 1.12
3220, 375, 1.12
*** gap level
4000, -25, 1.79
4016, -1.64, 1.79
4020, -1.0, 1.79
4024, 0.5, 1.79
4034, 9.0, 1.79
4036, 10.0, 1.79
4076, 135.0, 1.79
4078, 136.0, 1.79
4088, 144.8, 1.79
4090, 145.75, 1.79
4130, 174.25, 1.79
4132, 175.2, 1.79
4142, 184.0, 1.79
4144, 185.0, 1.79
4184, 340.0, 1.79
4186, 341.0, 1.79
4196, 349.5, 1.79
4200, 351.0, 1.79
4204, 351.64, 1.79
4220, 375, 1.79
*** gap + poly0 level
5000, -25, 2.32
5016, -1.60, 2.32
5020, -0.7, 2.32
5024, 0.5, 2.32
5034, 9.0, 2.32
5036, 10.0, 2.32
5076, 135.0, 2.32
5078, 136.0, 2.32
5088, 145, 2.32
5090, 145.75, 2.32
5130, 174.25, 2.32
5132, 175, 2.32
5142, 184.0, 2.32
5144, 185.0, 2.32
5184, 340.0, 2.32
5186, 341.0, 2.32
5196, 349.5, 2.32
5200, 350.7, 2.32
5204, 351.60, 2.32
5220, 375, 2.32
*** gap + poly1 - dimple level
6000, -25, 3.09
6016, -1.60, 3.09
6020, -0.7, 3.09
6024, 0.5, 3.09
6034, 9.0, 3.09
```

```
6036, 10.0, 3.09
6076, 135.0, 3.09
6078, 136.0, 3.09
6088, 145, 3.09
6090, 145.75, 3.09
6130, 174.25, 3.09
6132, 175, 3.09
6142, 184.0, 3.09
6144, 185.0, 3.09
6184, 340.0, 3.09
6186, 341.0, 3.09
6196, 349.5, 3.09
6200, 350.7, 3.09
6204, 351.60, 3.09
6220, 375, 3.09
*** gap + poly1 level
7000, -25, 3.76
7016, -1.60, 3.72
7020, -0.3, 3.72
7024, 0.5, 3.76
7034, 8.5, 3.76
7036, 9.5, 3.76
7076, 135.5, 3.76
7078, 136.5, 3.76
7088, 145, 3.76
7090, 145.75, 3.76
7130, 174.25, 3.76
7132, 175, 3.76
7142, 183.5, 3.76
7144, 184.5, 3.76
7184, 340.5, 3.76
7186, 341.5, 3.76
7196, 349.5, 3.76
7200, 350.3, 3.72
7204, 351.60, 3.72
7220, 375, 3.76
*** gap + poly0 + poly1 level
8000, -25, 4.29
8016, -1.60, 4.29
8020, -0.3, 4.29
8024, 0.5, 4.29
8034, 8.5, 4.29
8036, 9.5, 4.29
8076, 135.5, 4.29
8078, 136.5, 4.29
8088, 145, 4.29
8090, 145.75, 4.29
8130, 174.25, 4.29
8132, 175, 4.29
8142, 183.5, 4.29
8144, 184.5, 4.29
8184, 340.5, 4.29
8186, 341.5, 4.29
8196, 349.5, 4.29
8200, 350.3, 4.29
8204, 351.60, 4.29
8220, 375, 4.29
**********************************************
*** define node sets at each level
*ngen, nset=l1
1000,1016,1
1016,1020,1
1020,1024,1
```

```
1024,1034,1
1034,1036,1
1036,1076,1
1076,1078,1
1078,1088,1
1088,1090,1
1090,1130,1
1130,1132,1
1132,1142,1
1142,1144,1
1144,1184,1
1184,1186,1
1186,1196,1
1196,1200,1
1200,1204,1
1204,1220,1
*ngen, nset=l3
3000,3016,1
3016,3020,1
3020,3024,1
3024,3034,1
3034,3036,1
3036,3076,1
3076,3078,1
3078,3088,1
3088,3090,1
3090,3130,1
3130,3132,1
3132,3142,1
3142,3144,1
3144,3184,1
3184,3186,1
3186,3196,1
3196,3200,1
3200,3204,1
3204,3220,1
*ngen, nset=l4
4000,4016,1
4016,4020,1
4020,4024,1
4024,4034,1
4034,4036,1
4036,4076,1
4076,4078,1
4078,4088,1
4088,4090,1
4090,4130,1
4130,4132,1
4132,4142,1
4142,4144,1
4144,4184,1
4184,4186,1
4186,4196,1
4196,4200,1
4200,4204,1
4204,4220,1
*ngen, nset=l5
5000,5016,1
5016,5020,1
5020,5024,1
5024,5034,1
5034,5036,1
5036,5076,1
```

```
5076,5078,1
5078,5088,1
5088,5090,1
5090,5130,1
5130,5132,1
5132,5142,1
5142,5144,1
5144,5184,1
5184,5186,1
5186,5196,1
5196,5200,1
5200,5204,1
5204,5220,1
*ngen, nset=l6
6000,6016,1
6016,6020,1
6020,6024,1
6024,6034,1
6034,6036,1
6036,6076,1
6076,6078,1
6078,6088,1
6088,6090,1
6090,6130,1
6130,6132,1
6132,6142,1
6142,6144,1
6144,6184,1
6184,6186,1
6186,6196,1
6196,6200,1
6200,6204,1
6204,6220,1
*ngen, nset=l7
7000,7016,1
7016,7020,1
7020,7024,1
7024,7034,1
7034,7036,1
7036,7076,1
7076,7078,1
7078,7088,1
7088,7090,1
7090,7130,1
7130,7132,1
7132,7142,1
7142,7144,1
7144,7184,1
7184,7186,1
7186,7196,1
7196,7200,1
7200,7204,1
7204,7220,1
*ngen, nset=l8
8000,8016,1
8016,8020,1
8020,8024,1
8024,8034,1
8034,8036,1
8036,8076,1
8076,8078,1
8078,8088,1
8088,8090,1
```

```
8090,8130,1
8130,8132,1
8132,8142,1
8142,8144,1
8144,8184,1
8184,8186,1
8186,8196,1
8196,8200,1
8200,8204,1
8204,8220,1
**************************************************************
*** fill in the nodes
*nfill, nset=beam
l1, l3, 4, 500
l3, l4, 2, 500
l4, l5, 2, 500
l5, l6, 2, 500
l6, l7, 2, 500
l7, l8, 2, 500
**************************************************************
*** create elements
*** element numbers correspond to lower left node numbers
*** brick elements first
*element, type=cpe8r, elset=beam
1000,1000,1002,2002,2000,1001,1502,2001,1500
*elgen,elset=e1
1000,12,2,2
*elcopy,element shift=1000, old set=e1, shift nodes=1000, new set=beam
*elcopy,element shift=2000, old set=e1, shift nodes=2000, new set=beam
*****
*element, type=cps8r, elset=beam
4020,4020,4022,5022,5020,4021,4522,5021,4520
*elgen,elset=e2
4020,7,2,2
*elcopy,element shift=1000, old set=e2, shift nodes=1000, new set=beam
*elcopy,element shift=2000, old set=e2, shift nodes=2000, new set=beam
*****
*element, type=cps8r, elset=beam
5036,5036,5038,6038,6036,5037,5538,6037,5536
*elgen,elset=e3
5036,20,2,2
*elcopy,element shift=1000, old set=e3, shift nodes=1000, new set=beam
*elcopy,element shift=2000, old set=e3, shift nodes=2000, new set=beam
*****
*element, type=cps8r, elset=beam
4078,4078,4080,5080,5078,4079,4580,5079,4578
*elgen,elset=e4
4078,5,2,2
*elcopy,element shift=1000, old set=e4, shift nodes=1000, new set=beam
*elcopy,element shift=2000, old set=e4, shift nodes=2000, new set=beam
*****
*element, type=cps8r, elset=beam
3088,3088,3090,4090,4088,3089,3590,4089,3588
*elgen,elset=e5
3088,22,2,2
*elcopy,element shift=1000, old set=e5, shift nodes=1000, new set=beam
*elcopy,element shift=2000, old set=e5, shift nodes=2000, new set=beam
*****
*element, type=cps8r, elset=beam
4132,4132,4134,5134,5132,4133,4634,5133,4632
*elgen,elset=e6
4132,5,2,2
*elcopy,element shift=1000, old set=e6, shift nodes=1000, new set=beam
```

```
*elcopy,element shift=2000, old set=e6, shift nodes=2000, new set=beam
*****
*element, type=cps8r, elset=beam
5144,5144,5146,6146,6144,5145,5646,6145,5644
*elgen,elset=e7
5144,20,2,2
*elcopy,element shift=1000, old set=e7, shift nodes=1000, new set=beam
*elcopy,element shift=2000, old set=e7, shift nodes=2000, new set=beam
*****
*element, type=cps8r, elset=beam
4186,4186,4188,5188,5186,4187,4688,5187,4686
*elgen,elset=e8
4186,7,2,2
*elcopy,element shift=1000, old set=e8, shift nodes=1000, new set=beam
*elcopy,element shift=2000, old set=e8, shift nodes=2000, new set=beam
*****
*element, type=cpe8r, elset=beam
1196,1196,1198,2198,2196,1197,1698,2197,1696
*elgen,elset=e9
1196,12,2,2
*elcopy,element shift=1000, old set=e9, shift nodes=1000, new set=beam
*elcopy,element shift=2000, old set=e9, shift nodes=2000, new set=beam
******** odds and ends (connectors)
*element,type=cps6,elset=beam
5016,5016,5018,6018,5017,5518,5517
5018,5018,5020,6020,5019,5520,5519
6018,6018,6020,7020,6019,6520,6519
4034,4034,5036,5034,4535,5035,4534
7034,7034,7036,8036,7035,7536,7535
4076,5076,4078,5078,4577,4578,5077
7076,7076,7078,8076,7077,7577,7576
6088,6088,6090,7088,6089,6589,6588
6130,6130,6132,7132,6131,6632,6631
4142,4142,5144,5142,4643,5143,4642
7142,7142,7144,8144,7143,7644,7643
7184,7184,7186,8184,7185,7685,7684
4184,5184,4186,5186,4685,4686,5185
6200,6200,6202,7200,6201,6701,6700
5202,5202,5204,6202,5203,5703,5702
*element,type=cps8r,elset=beam
4016,4016,4018,5018,5016,4017,4518,5017,4516
4018,4018,4020,5020,5018,4019,4520,5019,4518
5018,5018,5020,6020,6018,5019,5520,6019,5518
5034,5034,5036,6036,6034,5035,5536,6035,5534
6034,6034,6036,7036,7034,6035,6536,7035,6534
5076,5076,5078,6078,6076,5077,5578,6077,5576
6076,6076,6078,7078,7076,6077,6578,7077,6576
6142,6142,6144,7144,7142,6143,6644,7143,6642
5142,5142,5144,6144,6142,5143,5644,6143,5642
5184,5184,5186,6186,6184,5185,5686,6185,5684
6184,6184,6186,7186,7184,6185,6686,7185,6684
5200,5200,5202,6202,6200,5201,5702,6201,5700
4200,4200,4202,5202,5200,4201,4702,5201,4700
4202,4202,4204,5204,5202,4203,4704,5203,4702
**********************************
*elset,elset=beam
beam,e1,e2,e3,e4,e5,e6,e7,e8,e9
*elset,elset=center,generate
3088,3132,2
*elset,elset=elec1,generate
5036,5074,2
*elset,elset=elec2,generate
5144,5182,2
```

```
*solid section, elset=beam, material=poly
30
*material, name=poly
*elastic, type=isotropic
**** poly properties
140e9, 0.23
*expansion
3.45e-05
*****************************************************************
****** interface / gap element method
*element,type=inter2,elset=gaps
1036,1036,1037,5036,5037
1078,1078,1079,4078,4079
1088,1088,1089,3088,3089
1133,1133,1134,4133,4134
1145,1145,1146,5145,5146
*elgen,elset=gaps
1036,20,2,1
1078,5,2,1
1088,23,2,1
1133,5,2,1
1145,20,2,1
*interface,elset=gaps
**** interface properties
30
*surface behavior, no separation
**surface behavior, softened, tabular
**0, -0.020
**1.2e5, -0.015
**2.5e5, -0.010
**4.5e5, -0.002
**13e5, +0.005
**20e5, +0.007
**50e5, +0.009
*****************************************************************
**** anchor node for contact surface
**node
**40000, 0,0
****** contact surface method
**rigid surface, type=segments, name=bsurf, ref node=40000
**start, 0, 0
**line, 300, 0
**surface definition, name=asurf
**center
**contact pair, small sliding, interaction=simple
**asurf,bsurf
**surface interaction,name=simple
*****************************************************************
*nset,nset=bottom,generate
1000,1220,1
*nset,nset=monitor
3088,3110,3132
*boundary
bottom,encastre
*restart,write,frequency=1
*preprint, echo=no, model=yes, history=no, contact=no
*nset,nset=beam,elset=beam
*****************************************************************
**** electrostatic pressure routine
**** forces are per unit length
*user subroutines
         subroutine dload (f,kstep,kinc,time,noel,npt,layer,kspt,
     1   coords,jltyp)
```

```
c
         include 'aba_param.inc'
c
         dimension time(2), coords(3)
c
         voltage=time(2)
c voltage steps
         if (voltage .gt. 100 ) then
            voltage =200 - voltage
         end if
         if (coords(1) .lt. 160) then
            voltage = time(2) * 20
            if (voltage .gt.   38) then
               voltage=   38
            end if
         end if
c take TOTAL time; go back down after v=maxvolt
         gap=coords(2)-0.53
c make sure electrostatic force does not go to infinity
         if (gap .lt. 0.1) then
            gap=0.1
         end if
c must multiply by width of beam if using beam elements
c force computation
         f=-8.854e-12*(voltage)**2/(2*(gap*1e-6)**2)
     1   *1*(1.006+0.95*gap/30)
         return
         end
**************************************************************
*step,nlgeom,inc=50
allow initial stress state due to temperature
*static,direct
.0001,0.001
*controls, parameters=time incrementation
30,30,20,30,20,20,200
*temperature
beam,1
*monitor,node=3110,dof=2
*el print, frequency=0, totals=yes, elset=beam
s11
*node print, nset=monitor, frequency=10
u
*end step
**************************************************************
*step,inc=500
ramp up
*static,direct
**** voltage ramp
2,20
*controls, parameters=time incrementation
60,60,20,60,20,20,200
*dload
elec1,p1nu,1
elec2,p1nu,1
**print,residual=no
*el print, frequency=0
*node print, nset=monitor
u
*restart,write,frequency=1
*end step
**************************************************************
*step,inc=500
ramp up
```

Appendix B Abaqus Input Deck

```
*static,direct
**** voltage ramp
0.1,2
*controls, parameters=time incrementation
60,60,20,60,20,20,200
*dload
elec1,p1nu,1
elec2,p1nu,1
**print,residual=no
*el print, frequency=0
*node print, nset=monitor
u
*restart,write,frequency=1
*end step
```

Appendix C MUMPs Runs

Run #	Date Received	Release	Structures and Devices
19	8/1997	2.5 min HF	30-μm-wide beams with enclosed anchors Various switch geometries – centerpiece geometry, tether flexures, etch-hole patterns POLY0-POLY1-POLY2 sandwich structures POLY2 designs All single devices have gold connections
22	2/1998	2.5 min HF	Arrays (10 beams each) of fixed-fixed beams and cantilevers of various lengths and widths Single beams placed next to arrays Pull-in structures with various interesting geometries Ladder of beams of different lengths, with single actuation electrode All with gold connections
25	8/1998	2.5 min HF + CO_2 drying	Arrays of beams of different lengths with 3 different step-ups – no enclosure lip, backfilled anchor, with enclosure lip Pitch, width, and orientation variations Square spirals Tilting and laterally actuated electrostatic devices Thickness measurement structures Arrays have no gold connections; individual beams do Bondwire pads around die
26	10/1998	5 min HF +	Arrays of beams widely-spaced apart Arrays to examine effect of pitch

		CO_2 drying	POLY1 beams over POLY0 (no gold connections) POLY1 beams with dimples Most devices with gold connections Untethered test structures Thickness measurement structures
27	12/1998	2.5 min HF + CO_2 drying	Extended array of fixed-fixed beams with no-enclosure and backfilled step-up anchors Arrays of beams over POLY0, and beams with dimples Effect of pitch and gold connections Buckling structures with varied geometries Dual-bias-electrode structures Folded capacitor structures Thickness measurement structures
29	4/1999	1, 1.5 min HF + CO_2 drying	Arrays of fixed-fixed beams, beams over POLY0 and beams with dimples, all with no-enclosure step-ups Center-tethered test structures Several folded capacitor designs, including those with POLY2 tethers POLY1-POLY2 “linear” actuator Dual-bias-electrode structures Thickness measurement structures Release-etch measurement structures

MUMPs 29 Die Layout

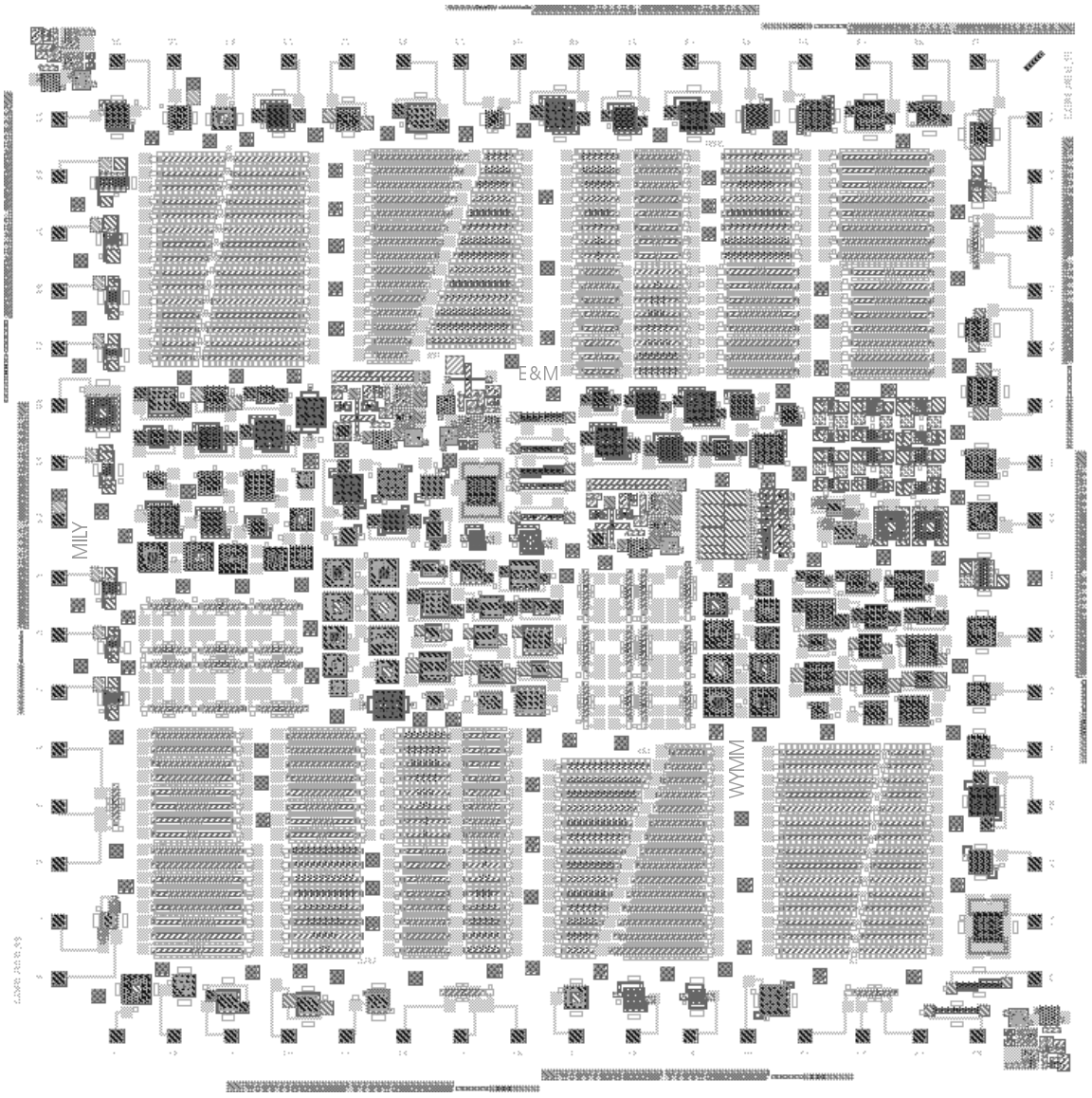

Bibliography

[1] K. J. Gabriel, "Microelectromechanical Systems," *Proc. IEEE*, vol. 86, no. 8, pp. 1534-5, Aug. 1998.

[2] J. Bryzek, K. Petersen, W. McCulley, "Micromachines on the march," *IEEE Spectrum*, vol. 30, no. 5, pp. 20-31, May 1994.

[3] P. Saffo, "Sensors: The next wave of infotech innovation," http://www.saffo.org/sensors.html, Oct. 13, 1999, 4:15pm PDT.

[4] S. F. Brown, "Big jobs are going to micromachines," *Fortune*, May 10, 1999.

[5] P. F. Van Kessel, L. J. Hornbeck, R. E. Meier, M. R. Douglass, "A MEMS-based projection display," *Proc. IEEE*, vol. 86, no. 8, pp. 1687-704, Aug. 1998.

[6] M. M. Athavale, H. Y. Li, H. Q. Yang, A. J. Przekwas, C. Cabuz, W. Herb, "Coupled electrostatics-structures-fluidic simulations of a BEAD mesopump," to be presented at *ASME Int. Mech. Engr. Congress. Expo.*, Nashville, TN, Nov. 1999.

[7] C. Goldsmith, T.-H. Lin, B. Powers, W.-R. Wu, B. Norvell, "Micromechanical membrane switches for microwave applications," in *Dig. IEEE MTT-S Int. Microwave Symp.*, Orlando, FL, May 1995.

[8] C. Goldsmith, J. Randall, S. Eshelman, T.-H. Lin, D. Denniston, S. Chen, B. Norvell, "Characteristics of micromachined switches at microwave frequencies," in *Dig. IEEE MTT-S Int. Microwave Symp.*, San Francisco, CA, May 1996.

[9] Z. J. Yao, S. Chen, S. Eshelman, D. Denniston, C. Goldsmith, "Micromachined low-loss microwave switches," *J. Microelectromechanical Systems*, vol. 8, no. 2, pp. 129-34, June 1999.

[10] XFDTD ver. 5.0, Remcom Inc., State College, PA, http://www.remcom.com.

[11] Ansoft HFSS, Ansoft Corp., Pittsburgh, PA, http://www.ansoft.com.

[12] G. Cornella, "Monotonic and cyclic testing of thin film materials for MEMS applications," Ph.D. Thesis, Stanford University, CA, July 1999.

[13] J. Gilbert, T. Ray, "The next big thing: Next-generation silicon chips", Smart Money, July 20, 1999, http://www.smartmoney.com/smt/stocks/index.cfm?story=199907201d.

[14] P. M. Osterberg, S. D. Senturia, "MemBuilder: An automated 3D solid-model construction program for microelectromechanical structures," in *Proc. Transducers'95*, Stockholm, Sweden, June 1995, vol. 2, pp. 21-4.

[15] N. M. Wilson, R. W. Dutton, P. M. Pinsky, "Utilizing existing TCAD simulation tools to create solid models for the simulation based design of MEMS devices," in *ASME Int. Mech. Engr. Congress Expo.*, Anaheim, CA, Nov. 1998, DSC-Vol. 66, pp. 565-70.

[16] Z. K. Hsiau, "Boundary movement in semiconductor etching and deposition simulation," Ph.D. Thesis, Stanford University, CA, June 1997.

[17] Abaqus ver. 5.7, Hibbitt, Karlsson & Sorensen, Inc., Pawtucket, RI, http://www.hks.com.

[18] MEMCAD ver. 4.5, Microcosm Technologies, Inc., Research Triangle, NC, http://www.memcad.com.

[19] IntelliSuite, IntelliSense Corp., Wilmington, MA, http://www.intellisense.com.

[20] J. M. Funk, J. G. Korvink, J. Buhler, M. Bachtold, H. Baltes, "SOLIDIS: A tool for microactuator simulation in 3-D," *J. Microelectromechanical Systems*, vol. 6, no. 1. pp. 70-82, Mar. 1997.

[21] ANSYS/Multiphysics ver. 5.5, Ansys, Inc., Canonsburg, PA, http://www.ansys.com.

[22] CFD-ACE+ and add-on modules, CFD Research Corporation, Huntsville, AL, http://www.cfdrc.com.

[23] Star-HSPICE, Avant! Corp., Fremont, CA, http://www.avanticorp.com.

[24] Simulink ver. 3.0, The Mathworks, Inc., Natick, MA, http://www.mathworks.com.

[25] SaberDesigner, Analogy, Inc., Beaverton, OR, http://www.analogy.com.

[26] N. Zhou, J. V. Clark, K. S. J. Pister, "Nodal analysis for MEMS design using SUGAR v0.5," in *Proc. Modeling and Simulation of Microsystems (MSM'98)*, Santa Clara, CA, Apr. 1998, pp. 308-13.

[27] Working Model Motion ver. 5.0, MSC.Working Knowledge, San Mateo, CA, http://www.workingmodel.com.

[28] L. L. Howell, A. Midha, T. W. Norton, "Evaluation of equivalent spring stiffness for use in a pseudo-rigid-body model of large-deflection compliant mechanisms," *ASME Journal of Mechanical Design*, vol. 118, pp. 126-31, Mar. 1996.

[29] L. G. Salmon, D. B. Gunyan, J. M. Derderian, P. G. Opdahl, L. L. Howell, "Use of the pseudo-rigid body model to simplify the description of compliant micro-mechanisms," in *Proc. Solid-State Sensor and Actuator Workshop,* Hilton Head, SC, June 1996, pp. 136-9.

[30] P. M. Osterberg, "Electrostatically actuated microelectromechanical test structures for material property measurement," Ph.D. Thesis, Massachusetts Institute of Technology, MA, Sep. 1995.

[31] P. M. Osterberg, S. D. Senturia, "M-TEST: A test chip for MEMS material property measurement using electrostatically actuated test structures," *J. Microelectromechanical Systems*, vol. 6, no. 2, pp. 107-18, June 1997.

[32] B. E. Artz, L. W. Cathey, "A finite element method for determining structural displacements resulting from electrostatic forces," in *Proc. Solid-State Sensor and Actuator Workshop*, Hilton Head, SC, June 1992, pp. 190-3.

[33] R. J. Roark, W. C. Young, *Formulas for Stress and Strain*, 6th Edition, New York, McGraw-Hill, 1989.

[34] R. K. Gupta, "Electrostatic pull-in test structure design for in-situ mechanical property measurements of microelectromechanical systems (MEMS)," Ph.D. Thesis, Massachusetts Institute of Technology, MA, June 1997.

[35] J. B. Starr, "Squeeze-film damping in solid-state accelerometers," in *Proc. Solid-State Sensor and Actuator Workshop*, Hilton Head, SC, June 1990, pp. 44-7.

[36] E. S. Hung, Y. J. Yang, S. D. Senturia, "Low-order models for fast dynamical simulation of MEMS microstructures," in *Proc. Transducers'97*, Chicago, IL, June 1997, pp. 1101-4.

[37] E. S. Hung, S. D. Senturia, "Generating efficient dynamical models for microelectromechanical systems from a few finite-element simulation runs," *J. Microelectromechanical Systems*, vol. 8, no. 3, pp. 280-9, Sep. 1999.

[38] C. Kittel, *Introduction to Solid State Physics*, 6th edition, New York, John Wiley and sons, Chapter 3, 1986.

[39] Matlab ODE Suite, The Mathworks, Inc., Natick, MA, http://www.mathworks.com/access/helpdesk/help/pdf_doc/otherdocs/ode_suite.pdf, Oct. 13, 1999, 10pm PDT.

[40] S. Lewis, Analog Devices, private communication.

[41] G. K. Fedder, "Simulation of microelectromechanical systems," Ph.D. Thesis, University of California at Berkeley, CA, Sep. 1994.

[42] B. D. Jensen, M. P. de Boer, S. L. Miller, "IMAP: Interferometry for material property measurement in MEMS," in *Proc. Modeling and Simulation of Microsystems (MSM'99)*, Puerto Rico, USA, Apr. 1999, pp. 206-9.

[43] Matlab PDE Toolbox ver. 1.03, The Mathworks, Inc., Natick, MA, http://www.mathworks.com.

[44] Raphael RC2 ver. 98.4, Avant! Corp., Fremont, CA, http://www.avanticorp.com.

[45] G. Strang, *Introduction to Applied Mathematics*, Wellesley, Wellesley-Cambridge Press, 1986.

[46] K. Nabors, J. White, "FastCap: A multipole accelerated 3-D capacitance extraction program," *IEEE Trans. Computer-aided Design of Int. Circuits and Systems*, vol. 10, no. 11, pp. 1447-59, Nov. 1991.

[47] N. R. Aluru, J. White, "An efficient numerical technique for electromechanical simulation of complicated microelectromechanical structures," *Sensors and Actuators A (Physical)*, vol. A58, no. 1, Jan. 1997, pp. 1-11.

[48] N. R. Aluru, J. White, "A multi-level Newton method for static and fundamental frequency analysis of electromechanical systems," in *Proc. SISPAD'97*, Cambridge, MA, Sep. 1997, pp. 125-8.

[49] N. R. Aluru, J. White, "A multilevel Newton method for mixed-energy domain simulation of MEMS," *J. Microelectromechanical Systems*, vol. 8, no. 3, pp. 299-308, Sep. 1999.

[50] H. B. Palmer, "The capacitance of a parallel-plate capacitor by the Schwartz-Christoffel transformation," *Electrical Engineering*, 56, pp. 363-6, Mar. 1937.

[51] D. A. Koester, R. Mahadevan, A. Shishkoff, K. W. Markus, *MUMPs Design Handbook*, Rev. 4, Research Triangle, NC, Cronos Integrated Microsystems, Inc., 1999, http://mems.mcnc.org/mumps.html, Oct. 13, 1999, 10:30pm PDT.

[52] W. N. Sharpe, Jr., S. Brown, G. C. Johnson, W. Knauss, "Round-robin tests of modulus and strength of polysilicon," in *Mat. Res. Soc. Symp. Proc.*, vol. 518, 1998, pp. 57-65.

[53] J. C. Marshall, N. R. Swart, D. A. Koester, M. Gaitan, "Determination of layer thickness in two surface micromachining MEMS processes," *MUMPs user group meeting*, Santa Clara, CA, Sep. 24, 1998.

[54] Q. Meng, M. Mehregany, R. L. Mullen, "Theoretical modeling of microfabricated beams with elastically restrained supports," *J. Microelectromechanical Systems*, vol. 2, no. 3, pp. 128-37, Sep. 1993.

[55] V. L. Rabinovich, R. K. Gupta, S. D. Senturia, "The effect of release-etch holes on the electromechanical behavior of MEMS structures," in *Proc. Transducers'97*, Chicago, IL, June 1997, pp. 1125-8.

[56] W. N. Sharpe, Jr., R. Vaidyanathan, B. Yuan, G. Bao, "Effect of etch holes on the mechanical properties of polysilicon," *J. Vac. Sci. Tech.*, B 15(5), pp. 1599-603, Sep./Oct. 1997.

[57] J. M. Bustillo, R. T. Howe, R. S. Muller, "Surface micromachining for microelectromechanical systems," *Proc. IEEE*, vol. 86, no. 8, pp. 1552-74, Aug. 1998.

[58] D. A. Koester, Microelectronics Center of North Carolina/Cronos Integrated Microsystems, Inc., private communication.

[59] Zygo Corporation, Middlefield, CN, http://www.zygo.com.

[60] Step Height Standard, Model SHS 1.8 QC, Serial #4343-27-24, VLSI Standards, Inc., San Jose, CA, http://www.vlsistd.com.

[61] I. Chasiotis, W. Knauss, "Mechanical properties of thin polysilicon films by means of probe microscopy," in *Proc. SPIE*, vol. 3512, Santa Clara, CA, Sep. 1998, pp. 66-75.

[62] L. Torcheux, A. Mayeux, M. Chemla, "Electrochemical coupling effects on the corrosion of silicon samples in HF solutions," *J. Electrochem. Soc.*, vol. 142, no. 6, pp. 2037-2046, June 1995.

[63] W. D. Nix, B. M. Clemens, "Crystallite coalescence: A mechanism for intrinsic tensile stress in thin films," *J. of Materials Research*, (14), no. 8, pp. 3467-73, Aug. 1999.

[64] J. C. Marshall, D. T. Read, M. Gaitan, "Analysis of fixed-fixed beam test structures," in *Proc. SPIE*, vol. 2880, Austin, TX, Oct. 1996, pp. 46-55.

[65] W. W. Van Arsdell, S. B. Brown, "Subcritical crack growth in silicon MEMS," *J. Microelectromechanical Systems*, vol. 8, no. 3, pp. 319-27, Sep. 1999.

[66] R. I. Pratt, G. C. Johnson, R. T. Howe, D. J. Nikkel, "Characterization of thin films using micromechanical structures," in *Mat. Res. Soc. Symp. Proc.*, vol. 276, 1992, pp. 197-202.

[67] H. Guckel, T. Randazzo, D. W. Burns, "A simple technique for the determination of mechanical strain in thin films with applications to polysilicon," *J. App. Phys.*, vol. 57 (5), pp. 1671-5, 1 Mar. 1985.

[68] H. Guckel, D. W. Burns, C. C. G. Visser, H. A. C. Tilmans, D. DeRoo, "Fine-grained polysilicon films with built-in tensile strain," *IEEE Trans. Elec. Dev.*, vol. 35, no. 6, June 1988, pp. 800-1.

[69] H. Guckel, D. W. Burns, H. A. C. Tilmans, D. W. DeRoo, C. R. Rutigliano, "Mechanical properties of fine grained polysilicon – the repeatability issue," in *Proc. Solid-State Sensor and Actuator Workshop*, Hilton Head, SC, June 1988, pp. 96-9.

[70] P. T. Jones, G. C. Johnson, R. T. Howe, "Fracture strength of polycrystalline silicon," in *Mat. Res. Soc. Symp. Proc.*, vol. 518, 1998, pp. 197-202.

[71] Y. C. Tai, R. S. Muller, "Measurement of Young's modulus on microfabricated structures using a surface profiler," in *Proc. IEEE Workshop Micro Electro Mechanical Systems (MEMS'90)*, Napa Valley, CA, Feb. 1990, pp. 147-52.

[72] Q. Zou, Z. Li, L. Liu, "New methods for measuring mechanical properties of thin films in micromachining: beam pull-in voltage (V_{PI}) method and long beam deflection (LBD) method," *Sensors and Actuators A (Physical)*, vol. A48, no. 2, May 1995, pp. 137-43.

[73] D. Maier-Schneider, A. Koprululu, S. B. Holm, E. Obermeier, "Elastic properties and microstructure of LPCVD polysilicon films," *J. Micromechanics and Microengineering*, vol. 6, no. 4, Dec. 1996, pp. 436-46.

[74] J. A. Walker, K. J. Gabriel, M. Mehregany, "Mechanical integrity of polysilicon films exposed to hydrofluoric acid solutions," in *Proc. IEEE Workshop Micro Electro Mechanical Systems (MEMS'90)*, Napa Valley, CA, Feb. 1990, pp. 56-60.

[75] W. N. Sharpe, Jr., K. Turner, R. L. Edwards, "Polysilicon tensile testing with electrostatic gripping," in *Mat. Res. Soc. Symp. Proc.*, vol. 518, 1998, pp. 191-6.

[76] W. N. Sharpe, Jr., K. Turner, R. L. Edwards, "Measurements of the effect of specimen size on Young's modulus and tensile strength of polysilicon," in *Late news poster session, Supplemental digest, Solid-State Sensor and Actuator Workshop*, Hilton Head, SC, June 1988, pp. 17-8.

[77] C. L. Yu, P. A. Flinn, S. H. Lee, J. C. Bravman, "Stress and microstructural evolution of LPCVD polysilicon thin films during high temperature annealing," in *Mat. Res. Soc. Symp. Proc.*, vol. 441, 1996, pp. 403-8.

[78] B. P. van Drieenhuizen, J. F. L. Goosen, P. J. French, R. F. Wolffenbuttel, "Comparison of techniques for measuring both compressive and tensile stress in thin films," *Sensors and Actuators A (Physical)*, vol. A37-38, June-Aug. 1993, pp. 756-65.

[79] W. Fang, J. A. Wickert, "Post-buckling of micromachined beams," *J. Micromechanics and Microengineering*, vol. 4, no. 3, Sep. 1994, pp. 116-22.

[80] J. E. Shigley, L. D. Mitchell, *Mechanical Engineering Design*, 4th edition, New York, McGraw-Hill, Chapter 3, 1993.

[81] L. V. Ngo, P. Nelson, C. J. Kim, "Surface-micromachined beams without spring effect of an anchor step-up," in *Proc. Solid-State Sensor and Actuator Workshop*, Hilton Head, SC, June 1996, pp. 140-3.

[82] J. J. Y. Gill, L. V. Ngo, P. R. Nelson, C. J. Kim, "Elimination of extra spring effect at the step-up anchor of surface-micromachined structure," *J. Microelectromechanical Systems*, vol. 7, no. 1, pp. 114-21, Mar. 1998.

[83] E. S. Hung, S. D. Senturia, "Leveraged bending for full-gap positioning with electrostatic actuation," in *Proc. Solid-State Sensor and Actuator Workshop*, Hilton Head, SC, June 1998, pp. 83-6.

[84] T. A. Lober, J. Huang, M. A. Schmidt, S. D. Senturia, "Characterization of the mechanisms producing bending moments in polysilicon micro-cantilever beams by interferometric deflection measurements," in *Proc. Solid-State Sensor and Actuator Workshop*, Hilton Head, SC, June 1988, pp. 92-5.

[85] M. S. Benrakkad, M. A. Benitez, J. Esteve, J. M. Lopez-Villegas, J. Samitier, J. R. Morante, "Stress measurement by microRaman spectroscopy of polycrystalline silicon structures," *J. Micromechanics and Microengineering*, vol. 5, no. 2, June 1995, pp. 132-5.

[86] M. S. Benrakkad, J. M. Lopez-Villegas, J. Samitier, J. R. Morante, M. Kirsten, P. Lange, "Stress gradient and structural properties of atmospheric and reduced pressure deposited polysilicon layers for micromechanical sensors," *Sensors and Actuators A (Physical)*, vol. A51, no. 1, Oct. 1995, pp. 9-12.

[87] P. Krulevitch, G. C. Johnson, R. T. Howe, "Stress and microstructure in LPCVD polycrystalline silicon films: experimental results and closed form modeling of stresses," in *Mat. Res. Soc. Symp. Proc.*, vol. 239, 1992, pp. 13-8.

[88] P. Krulevitch, G. C. Johnson, R. T. Howe, "Stress and microstructure in phosphorus doped polycrystalline silicon," in *Mat. Res. Soc. Symp. Proc.*, vol. 276, 1992, pp. 79-84.

[89] P. Zhang, R. P. Vinci, J. C. Bravman, T. W. Kenny, "Thin film stress measurement with a tunneling sensor," in *Mat. Res. Soc. Symp. Proc.*, vol. 546, 1998, (in press).

[90] J. R. Gilbert, G. K. Ananthasuresh, S. D. Senturia, "3D modeling of contact problems and hysteresis in coupled electro-mechanics," in *Proc. IEEE Workshop Micro Electro Mechanical Systems (MEMS'96)*, San Diego, CA, Feb. 1996, pp. 127-32.

[91] E. S. Hung, S. D. Senturia, "Tunable capacitors with programmable capacitance-voltage characteristic," in *Proc. Solid-State Sensor and Actuator Workshop*, Hilton Head, SC, June 1998, pp. 292-5.

[92] S. Majumder, N. E. McGruer, P. M. Zavracky, G. G. Adams, R. H. Morrison, J. Krim, "Measurement and modeling of surface micromachined, electrostatically actuated microswitches," in *Proc. Transducers'97*, Chicago, IL, June 1997, pp. 1145-8.

[93] E. J. J. Kruglick, K. S. J. Pister, "Lateral MEMS microcontact considerations," *J. Microelectromechanical Systems*, vol. 8, no. 3, pp. 264-71, Sep. 1999.

[94] M. P. de Boer, M. R. Tabbara, M. T. Dugger, P. J. Clews, T. A. Michalske, "Measuring and modeling electrostatic adhesion in micromachines," in *Proc. Transducers'97*, Chicago, IL, June 1997, pp. 229-32.

[95] M. P. de Boer, J. M. Redmond, T. A. Michalske, "A hinged-pad test structure for sliding friction measurement in micromachining," in *Proc. SPIE*, vol. 3512, Santa Clara, CA, Sep. 1998, pp. 241-50.

[96] T. A. Lober, R. T. Howe, "Surface-micromachining processes for electrostatic microactuator fabrication," in *Proc. Solid-State Sensor and Actuator Workshop*, Hilton Head, SC, June 1988, pp. 59-62.

[97] Medici ver. 4.1, Avant! Corp., Fremont, CA, http://www.avanticorp.com.

[98] E. R. Konig, G. Wachutka, "Analysis of unstable behavior occurring in electro-mechanical microdevices," in *Proc. Modeling and Simulation of Microsystems (MSM'99)*, Puerto Rico, USA, Apr. 1999, pp. 330-3.

[99] D. A. Buchanan, R. A. Abram, M. J. Morant, "Charge trapping in silicon-rich Si_3N_4 thin films," *Solid-state electronics*, vol. 30, no. 12, Dec. 1987, pp. 1295-1301.

[100] F. Sugihwo, M. C. Larson, J. S. Harris, Jr., "Micromachined widely tunable vertical cavity layer diodes," *J. Microelectromechanical Systems*, vol. 7, no. 1, pp. 48-55, Mar. 1998.

[101] P. B. Chu, K. S. J. Pister, "Analysis of closed-loop control of parallel-plate electrostatic microgrippers," in *Proc. IEEE Int. Conf. Robotics and Automation*, San Diego, CA, May 1994, pp. 820-5.

[102] J. I. Seeger, S. B. Crary, "Stabilization of electrostatically actuated mechanical devices," in *Proc. Transducers'97*, Chicago, IL, June 1997, pp. 1133-6.

[103] J. I. Seeger, B. E. Boser, "Dynamics and control of parallel-plate actuators beyond the electrostatic instability," in *Proc. Transducers'99*, Sendai, Japan, June 1999, pp. 474-7.

[104] M. Varghese, R. Amantea, D. Sauer, S. D. Senturia, "Resistive damping of pulse-sensed capacitive position sensors," in *Proc. Transducers'97*, Chicago, IL, June 1997, pp. 1121-4.

[105] Y. J. Yang, S. D. Senturia, "Numerical simulation of compressible squeeze-film damping," in *Proc. Solid-State Sensor and Actuator Workshop*, Hilton Head, SC, June 1996, pp. 76-9.

Related Publications by the Author

[1] E. K. Chan, E. C. Kan, R. W. Dutton and P. M. Pinsky, "Nonlinear dynamic modeling of micromachined microwave switches," in *Dig. IEEE MTT-S Int. Microwave Symp.*, Denver, CO, June 1997, pp. 1511-4.

[2] E. K. Chan, K. Garikipati, Z. K. Hsiau, R. W. Dutton, "Characterization of electrostatically-actuated beams through capacitance-voltage measurements and simulations," in *Proc. Modeling and Simulation of Microsystems (MSM'98)*, Santa Clara, CA, Apr. 1998, pp. 180-5.

[3] E. K. Chan, R. W. Dutton, "Effects of capacitors, resistors and residual charges on the static and dynamic performance of electrostatically-actuated devices," in *Proc. SPIE*, vol. 3680, Paris, France, Mar. 1999, pp. 120-30.

[4] E. K. Chan, K. Garikipati, R. W. Dutton, "Complete characterization of electrostatically-actuated beams including effects of multiple discontinuities and buckling," in *Proc. Modeling and Simulation of Microsystems (MSM'99)*, Puerto Rico, USA, Apr. 1999, pp. 194-7.

[5] E. K. Chan, K. Garikipati, R. W. Dutton, "Characterization of contact electromechanics through capacitance-voltage measurements and simulations," *J. Microelectromechanical Systems*, vol. 8 no. 2, pp. 208-17, June 1999.

[6] E. K. Chan, K. Garikipati, R. W. Dutton, "Comprehensive static characterization of vertical electrostatically actuated polysilicon beams," *IEEE Design and Test of Computers*, vol. 16, no. 4, pp. 58-65, Oct.-Dec. 1999.

[7] E. K. Chan, R. W. Dutton, "Effects of surface properties on the effective electrical gap of microelectromechanical devices operating in contact," submitted to *Modeling and Simulation of Microsystems (MSM2000)*, San Diego, CA, Mar. 2000.

[8] E. K. Chan, R. W. Dutton, "Electrostatic micromechanical actuator with extended range of travel," submitted to *J. Microelectromechanical Systems*.